UNIVERSITY OF CALIFORNIA
RIVERSIDE

Exploring Dwarf Galaxies and Their Dark Matter Halos in Diverse Cosmic Environments

A Dissertation submitted in partial satisfaction
of the requirements for the degree of

Doctor of Philosophy

in

Physics

by

Niusha Ahvazi

September 2024

Dissertation Committee:

Dr. Laura Sales, Chairperson
Dr. Andrew Benson
Dr. Bahram Mobasher

The Dissertation of Niusha Ahvazi is approved:

Committee Chairperson

University of California, Riverside

Acknowledgments

First and foremost, I would like to express my deepest gratitude to my family and friends for their unwavering support and encouragement throughout my academic journey. Their belief in me has been a constant source of motivation and strength.

I am profoundly grateful to my advisors, Laura Sales and Andrew Benson, for their invaluable guidance, mentorship, and support. Their expertise and insights have been instrumental in shaping the content of this dissertation and my development as a researcher.

I would also like to extend my heartfelt thanks to all the collaborators who contributed to my research, papers and, consequently, this dissertation. Your contributions and feedback have been indispensable.

The faculty and community of the Astronomy Department at UCR, along with the community at Carnegie Observatories, have provided exceptional mentorship, advice, and encouragement, all of which have been crucial for my progress along the academic career path. I am especially grateful to my committee members at UCR, Bahram Mobasher and Brian Siana, for their wisdom and support. Additionally, a special thanks to all the graduate students, undergraduates, and postdocs associated with Laura and Andrew's groups; you have been a constant source of knowledge, inspiration, and support.

A very special thanks to Omid Tavakol for his unwavering moral support throughout my PhD, even from afar. His constant encouragement, especially during the challenging times, has been invaluable in guiding me through this journey.

I would like to acknowledge the financial support provided by UCR's Chancellor's Distinguished Fellowship, the UCR-Carnegie Fellowship, and the Dissertation Year Program Fellowship. Your support has made this research possible.

This work utilizes the IllustrisTNG suite of simulations and the Galacticus semi-analytical model, which are publicly available[1]. I also acknowledge several open-source Python packages that have been utilized for my analyses: Matplotlib (Hunter 2007), NumPy (Harris et al. 2020a), Scipy (Virtanen et al. 2020), Astropy (Astropy Collaboration et al. 2013, 2018, 2022), and illustris_python (Nelson et al. 2015).

Finally, the text of this dissertation, in part, is a reprint of materials that have appeared or will appear in journal articles. Chapters 2 and 3 have been accepted for publication by Oxford University Press in the Monthly Notices of the Royal Astronomical Society, and Chapter 4 is submitted for publication by the Open Journal of Astrophysics. These works were written by myself and my collaborators: Niusha Ahvazi, Laura Sales, Andrew Benson, Jessica E. Doppel, Julio Navarro, Richard D'Souza, Vicente Rodriguez-Gomez, Ethan O. Nadler, Sachi Weerasooriya, Xiaolong Du, Mia Sauda Bovill, and Alessandro Boselli.

[1]IllustrisTNG simulation: https://www.tng-project.org, Galacticus semi-analytical model: https://github.com/galacticusorg

To my parents, for their unwavering support, encouragement, and love throughout every step of this journey.

ABSTRACT OF THE DISSERTATION

Exploring Dwarf Galaxies and Their Dark Matter Halos in Diverse Cosmic Environments

by

Niusha Ahvazi

Doctor of Philosophy, Graduate Program in Physics
University of California, Riverside, September 2024
Dr. Laura Sales, Chairperson

A comprehensive study on the formation and evolution of dwarf galaxies, their environments, and corresponding dark matter halos is presented within the framework of the Lambda Cold Dark Matter (ΛCDM) model. Using advanced cosmological hydrodynamical simulations, and semi-analytic models, this work addresses several critical questions in galaxy formation and evolution. These include the mechanisms driving intra-cluster light (ICL) formation, the role of dwarf galaxies as building blocks of ICL, its reliability as a tracer of the underlying dark matter, and the relation between the dwarf galaxy properties and their corresponding dark matter halo.

This research demonstrates that dwarf galaxies exhibit a wide range of relevance in contributing to ICL, with significant implications for upcoming deep observations from the Euclid and Roman space telescopes. Findings show that systems with minimal contributions from dwarf galaxies ($M\star < 10^{10}$ $M\odot$) display shallower ICL metallicity profiles. Moreover, intra-cluster globular clusters (ICGCs) are identified as valuable tracers of halo assembly histories, particularly when observing ICL is challenging. The shape and orientation of ICL

and ICGCs show a reasonable correlation with those of the dark matter in the outskirts of halos, underscoring their common origin and potential as luminous tracers.

In addition, this dissertation explores the ICL component of Virgo-like clusters by analyzing ICL fractions, density profiles, and star formation rates. The simulation results predict an ICL component comparable to the brightest cluster galaxy in mass and star formation rate, with an in-situ stellar component present at all redshifts. The in-situ component, accounting for approximately 8–28% of the ICL stellar mass at $z = 0$, is attributed to widespread star formation along filamentary structures tracing the distribution of neutral gas in the cluster host halo.

Additionally, a modified semi-analytic model, Galacticus, was developed to reproduce the properties of Milky Way dwarf galaxies. This model incorporates H_2 cooling, an updated UV background radiation model, and a metal content model for the intergalactic medium. The model shows that the fraction of subhalos hosting a galaxy with MV < 0 drops to 50% by a halo peak mass of approximately 8.9×10^7 $M_\odot$, aligning with recent observations.

The findings of this dissertation allows for integrating observational data from forthcoming telescopes/surveys to refine models and enhance our understanding of dwarf galaxies' roles within the broader cosmic structure.

Contents

List of Figures

List of Tables

Chapter 1

Introduction

In the vast expanse of the universe, understanding the formation and evolution of galaxies is a fundamental quest in astronomy. This dissertation examines the universe under the assumption of the Lambda Cold Dark Matter (ΛCDM) model, which posits that dark matter is cold (non-relativistic) and that the cosmological constant (Λ) drives the accelerated expansion of the universe. Within this framework, the focus is on dwarf galaxies, the most prevalent type of galaxy in the universe, which play a crucial role in testing cosmological models. Dwarf galaxies, characterized by their small size, low gravitational potential, and high susceptibility to environmental influences, serve as essential probes for dark matter physics (Simon 2019). They can constrain our cosmological models through their abundances, luminosity function, and mass content, posing challenges such as the core vs. cusp problem[1] and the diversity of rotation curves problem[2] (Sales et al. 2022).

[1]Refers to the discrepancy between the observed flat central density profiles (cores) of dwarf galaxies and the steep density profiles (cusps) predicted by ΛCDM simulations (Flores and Primack 1994; Moore 1994).

[2]Refers to the observed variation in the shapes of rotation curves of dwarf galaxies, which show a wide range of inner density slopes. In the ΛCDM model, dark matter halos of a given mass are predicted to have similar density profiles, resulting in less diversity in their rotation curves (Santos-Santos et al. 2018, 2020).

Understanding the formation and disruption of dwarf galaxies in various environments is vital for testing and refining these models.

The formation of dark matter structures in the ΛCDM model posits that halos are forming from the *hierarchical* growth of high-density fluctuations in the early universe, where low-mass halos collapse first and subsequently merge to form more massive ones (White and Rees 1978). Consequently, within larger halos, such as those in galaxy groups and clusters, numerous mergers and interactions with smaller galaxies are expected. These environments exert significant influence on smaller galaxies through processes such as ram-pressure stripping, which removes gas and quenches star formation (Hester 2006), and tidal stripping, where larger galaxies pull stars and stellar material from smaller galaxies due to strong gravitational forces (Mihos et al. 2005). These processes can result in the production of stellar halos and intra-cluster light (ICL).

To fully understand the environmental effects on dwarf galaxies, it is essential to study their evolution within their environment or host halo. Given the long-term implications of these effects, simulations become a crucial tool in capturing their influence over time. This work utilizes a combination of large cosmological simulations, which model millions of particles influenced by gravitational and hydrodynamical forces to create a representation of the universe, and semi-analytical models, which employ simplified, parameterized equations to efficiently simulate complex astrophysical processes and explore galaxy formation and evolution over cosmological timescales. This approach allows for testing the ΛCDM model on a statistically significant set of dwarf galaxies in different environments, providing a comprehensive framework for exploring their long-term evolution, the impact of past ac-

cretion events, and environmental effects on present-day observable properties of halos and galaxies within them.

Excitingly, ongoing and upcoming observations are expected to provide unprecedented measurements of both large-scale and small-scale structures. The Euclid[3] and Roman[4] space telescopes are set to push the boundaries of surface brightness limits, allowing for deeper observations of intra-group/intra-cluster light (see Kluge et al. 2024 for an example using early Euclid results). Meanwhile, the Rubin Observatory Legacy Survey of Space and Time (LSST)[5] is anticipated to discover hundreds of dwarf and ultra-faint galaxies within the entire virial radius of the Milky Way halo and extend our knowledge of dwarf galaxies at greater distances. Interpreting these results statistically will require extensive halo realizations across various mass ranges.

Studying dwarf galaxies, their environments, and corresponding dark matter halos with the methods presented in this thesis allows us to address several open questions in the field of galaxy formation and evolution. *What mechanisms drive the formation of the ICL? What role do dwarf galaxies play as contributors and building blocks of the ICL? Are the ICL and its globular cluster components reliable tracers of the underlying dark matter*, and *how effectively can they trace the formation history of halos?* Furthermore, *what is the relationship between dwarf galaxy properties and their corresponding dark matter halos*, and *what predictions can be made about the mass of halos that host the faintest observed galaxies?* This thesis investigates these questions by studying several observables, including

[3] https://www.esa.int/Science_Exploration/Space_Science/Euclid

[4] https://roman.gsfc.nasa.gov

[5] https://www.lsst.org

intra-cluster light and its globular cluster component, and the abundance of ultra-faint dwarf galaxies. Each of these observables is described in more detail in what follows.

1.1 Intra-cluster light

Intra-cluster light (ICL) is the diffuse light found between galaxies within galaxy clusters. It can reveal the history of galaxy interactions and stripping processes and serve as a luminous tracer to map the underlying dark matter component in the halos (see the review by Montes 2022, and references therein). Remarkably, past merger events that occurred billions of years ago can be reconstructed from present-day ICL properties such as mass fraction and metallicity profile. These characteristics make ICL a powerful tool for reconstructing the accretion histories of halos. The stellar content in the ICL can either form "in situ" from gas bound to the central galaxy (and its main progenitor) or be brought in "ex situ" by merging satellite galaxies. The exact fraction of stars contributed by these mechanisms remains uncertain but is a crucial constraint for cosmological and galaxy formation models.

In Chapters 2 and 3, we use the large-volume cosmological simulation IllustrisTNG50 (Pillepich et al. 2019; Nelson et al. 2019a) to investigate the properties and build-up of ICL. In Chapter 2, we compare observational estimates of the ICL's mass fraction and radial extension. We show that about half of the merged ICL in all our systems is contributed by galaxies within a narrow stellar mass range ($M_\star = 10^{10} M_\odot - 10^{11} M_\odot$). However, the contribution of low-mass (dwarf) galaxies ($M_\star < 10^{10} M_\odot$) to the ICL's build-up varies widely from system to system, ranging from approximately 5% to 45%. This vari-

ability can potentially be traced through observable properties of the ICL at present, such as its metallicity profile. By utilizing a post-processing globular cluster tagging method applied to the IllustrisTNG50 simulation, we also investigate intra-cluster globular clusters (ICGCs). These ICGCs, found in the space between galaxies within a cluster, can serve as a good proxy for reconstructing the build-up of ICL, especially when the diffuse light of the ICL is not detectable. Overall, ICGCs prove to be valuable tools for reconstructing the assembly history of dark matter halos and constraining their shape and orientation.

In Chapter 3, we explore the formation of in situ ICL and the conditions under which these stars are born. We find that the diffuse star-forming component of the ICL is filamentary in nature, extends for hundreds of kilo parsecs, and traces the distribution of neutral gas and dark matter within the cluster's host halo.

1.2 Ultrafaint dwarf galaxies

Ultrafaint dwarf galaxies are the faintest and smallest galaxies known, with stellar masses less than $10^5 M_\odot$ or $M_V \gtrapprox -7$ (Bullock and Boylan-Kolchin 2017). In these systems, star formation is highly suppressed by reionization and stellar feedback, leading to mass-to-light ratios that are hundreds of times larger than the universal average (Simon 2019). This makes ultrafaint dwarfs pristine laboratories for studying dark matter, as they can be used to set constraints on the properties of dark matter in different models. The abundance of these systems is particularly sensitive to any dark matter physics that suppresses the formation or present-day abundance of small halos (see Nadler et al. 2021 and references therein).

In Chapter 4, we use the semi-analytic model GALACTICUS to study the formation of dwarf galaxies down to the ultrafaint regime within larger halos of various masses, under the assumption of cold dark matter. We compare the predictions from our model, which incorporates different assumptions regarding the physical processes involved, with current observational data available for the Milky Way galaxy and its satellites. This model can be further refined to explore alternative dark matter physics, potentially providing constraints on these models based on its predictions for the abundances of dwarf galaxies.

Chapter 2

The progenitors of the intra-cluster light and intra-cluster globular clusters in galaxy groups and clusters[1]

2.1 Abstract

We use the TNG50 from the IllustrisTNG suite of cosmological hydrodynamical simulation, complemented by a catalog of tagged globular clusters, to investigate the prop-

[1]This chapter is based on a draft of an article that has been accepted for publication in March 2024 by Oxford University Press in the Monthly Notices of the Royal Astronomical Society written by Niusha Ahvazi, Laura V. Sales, Jessica E. Doppel, Andrew Benson, Richard D'Souza, and Vicente Rodriguez-Gomez. While this chapter includes significant content from the accepted article, it also incorporates additional results and modifications not present in the original publication.

erties and build up of two extended luminous components: the intra-cluster light (ICL) and the intra-cluster globular clusters (ICGC). We select the 39 most massive groups and clusters in the box, spanning the range of virial masses $5 \times 10^{12} < \mathrm{M_{200}/M_{\odot}} < 2 \times 10^{14}$. We find good agreement between predictions from the simulations and current observational estimates of the fraction of mass in the ICL and its radial extension. The stellar mass of the ICL is only $\sim$ 10%–20% of the stellar mass in the central galaxy but encodes useful information on the assembly history of the group or cluster. About half the ICL in all our systems is brought in by galaxies in a narrow stellar mass range, $M_* = 10^{10}$–$10^{11}\mathrm{M_{\odot}}$. However, the contribution of low-mass galaxies ($M_* < 10^{10}\mathrm{M_{\odot}}$) to the build-up of the ICL varies broadly from system to system, $\sim 5\% - 45\%$, a feature that might be recovered from the observable properties of the ICL at $z = 0$. At fixed virial mass, systems where the accretion of dwarf galaxies plays an important role have shallower metallicity profiles, less metal content and a lower stellar mass in the ICL than systems where the main contributors are more massive galaxies. We show that intra-cluster GCs are also good tracers of this history, representing a valuable alternative when diffuse light is not detectable.

2.2 Introduction

One of the most striking features of high density environments is the intra-cluster light (ICL), a diffuse component of light that originates from populations of stars that are not associated with individual galaxies and are instead gravitationally bound to the host dark matter halo. The ICL is thought to be a product of the tidal stripping of stars from galaxies as they traverse the cluster or group environments and was first proposed

and subsequently discovered by Zwicky (1937, 1951, 1952, 1957) in the Coma cluster. The direct link between the ICL and satellite galaxies makes the formation of this diffuse light a natural prediction of the hierarchical assembly model in Cold Dark Matter (CDM, White and Rees 1978; Conroy et al. 2007; Montes and Trujillo 2018; Contini 2021).

The ICL has cosmological relevance primarily in two aspects. First, it represents a visible tracer of the unseen dark matter distribution, with several theoretical works supporting a good correlation between the shape and orientation of the ICL and those of the underlying dark matter halo (Montes and Trujillo 2019; Alonso Asensio et al. 2020; Contini and Gu 2020; Deason et al. 2020; Gonzalez et al. 2021a). Second, and the main focus of this paper, the ICL is built by the tidal disruption of many satellite galaxies, some of which do not survive until today. As such it can help unravel the past formation history of the host group or cluster halo (Contini 2021; Montes 2022, and references therein), in a similar way that stellar halos can help reconstruct the merger histories of smaller mass halos in the Milky Way-like (MW-like) regime (e.g., Bullock and Johnston 2005).

The stellar mass content of the ICL is directly related to the stellar mass-halo mass relation and serves as a probe of the past assembly history of galaxy clusters. A number of observational constraints on the amount of ICL have been reported in the literature, with studies using deep imaging to estimate the total amount of ICL in galaxy clusters (e.g. Zibetti et al. 2005; Krick and Bernstein 2007; McGee and Balogh 2010; Mihos et al. 2017; Morishita et al. 2017; Jiménez-Teja et al. 2019). These studies have found that the ICL typically makes up a significant fraction of the total light in galaxy clusters, ranging from

<10% to 50% depending on the cluster and the methods used to estimate the ICL (see Montes 2022).

Numerical simulations predict that the bulk of the ICL mass comes from the tidal stripping of massive satellites ($10 < \log(M/M_{\odot}) < 11$) (Puchwein et al. 2010; Contini et al. 2013; Cui et al. 2014; Cooper et al. 2015a; Contini et al. 2019; Montenegro-Taborda et al. 2023). Particularly, disk-like massive satellites are thought to significantly contribute to building the ICL through a large number of small stripping events (Contini et al. 2018). However, other less-dominant mechanisms may also contribute stars to the ICL including the total disruption of low mass satellites (Purcell et al. 2007), stars ejected into the inter-cluster medium after a major merger (Murante et al. 2007) and the pre-processing of accreted groups (Rudick et al. 2006). Due to the well established relation between stellar mass and metallicity in galaxies, the nature of the progenitors that build up the ICL can be observationally constrained from stellar metallicities. Furthermore, each of these mechanisms are expected to leave distinct patterns on the metallicity and their gradients.

Constraining the contribution of each mechanism can be extremely challenging due to the faint ($\mu_V \sim 26.5$ mag/arcsec^2) and extended characteristics of the ICL, which can often only be probed by broad-band photometry. Yet, over the last two decades, significant progress has been made. A number of observational studies have highlighted the presence of clear negative radial color gradients (Krick and Bernstein 2007; Rudick et al. 2009; Melnick et al. 2012; DeMaio et al. 2015) in the ICL of the majority of clusters studied at $z \sim 0.5$. While such gradients could potentially arise due to changes in metallicity (Montes and Trujillo 2014; DeMaio et al. 2015) or variations in the ages of the stars (Morishita et al.

2017; Montes and Trujillo 2018), it suggests that violent relaxation after major mergers with the BCG cannot be the dominant source of ICL. Although the observed metallicities of the ICL ($[Fe/H]_{ICL} \sim -0.5$) align with the notion that the ICL stars likely originate either from stars located in the outer regions of galaxies with stellar masses approximately 5×10^{10} $M_{\odot}$ (DeMaio et al. 2018; Montes and Trujillo 2018; Montes et al. 2021) or from the dissolution of dwarf galaxies, the amount of ICL is often used as an argument against the latter as this would dramatically alter the faint end of the cluster galaxy luminosity function (e.g. Zibetti et al. 2005; DeMaio et al. 2018). Only a small number of clusters have been identified with flat color gradients (e.g., Abell 370) - indicating an ICL formed through the expulsion of stars into the intra-cluster medium during a major merger event (Krick and Bernstein 2007; DeMaio et al. 2015, 2018). While the vast variety of observations point to the progenitors of the ICL being the tidal stripping of massive satellites ($10 < \log(M/M_{\odot}) < 11$) consistent with theoretical predictions, the ICL of the two closest well-studied clusters, the Virgo and Coma, which can be studied in significant detail, suggest very different assembly mechanisms. A study by Williams et al. (2007), examining the RGB populations of the Virgo cluster ($\sim$15 Mpc) using a single and deep HST pointing, found that 70% of the stars have a metallicity of $[M/H] \sim -1.3$ indicating that the ICL was built up primarily through the disruption of dwarf galaxies. Similarly, Gu et al. (2020) spectroscopically studied the ICL of the Coma cluster in the low S/N regime finding it to be old and metal-poor ($[M/H] \sim -1.0$) – consistent with the accretion of low-mass galaxies or the tidal stripping of the outskirts of massive galaxies that have ended their star formation early on. The low metallicity of the ICL of the Virgo and the Coma cluster

clearly suggests that the contribution of dwarf galaxies to the ICL can be significant. This is clearly in tension with the observations of clusters further away as well as the current theoretical paradigm, requiring further study and perhaps a revision of understanding of the contribution of dwarf galaxies to the ICL.

One way to observationally disentangle the various formation mechanisms is to study how the ICL correlates with the mass of the cluster and with redshift. However, as we probe deeper into the universe and examine systems at earlier redshifts, the low surface brightness of the intra-cluster light becomes increasingly difficult to capture. In such cases, an alternative path to study the dark matter halos may be offered by globular clusters (GCs). These ancient, dense clusters of stars are commonly found in nearly all types of galaxies and are thought to be among the oldest and (often) metal-poor stellar populations in the universe (Gratton et al. 2019). They are believed to have formed before the majority of galaxies and are relatively luminous (Schauer et al. 2021), making them easily detectable at large distances and earlier redshifts and a powerful tool to study the distribution of dark matter and ICL in the early universe.

GCs can be very numerous in groups and clusters. While for MW-like galaxies they populate host halos by the hundreds, in the Virgo cluster more than 10,000 have been cataloged around M87 (Durrell et al. 2014). Studies have shown that the abundance of GCs is closely related to the amount of dark matter in the halos (Spitler and Forbes 2009; Harris et al. 2013; Hudson et al. 2014; Harris et al. 2015). Therefore, GCs can offer an alternative path to study the dark matter halos in galaxy groups and clusters, especially when the ICL is not easily captured.

A large fraction of GCs associated with a given system are members of the intra-cluster globular cluster (ICGC) component, which has been observationally confirmed in Fornax (Schuberth et al. 2008), Coma (Madrid et al. 2018), Abell 1689 (Alamo-Martínez and Blakeslee 2017), Virgo (Lee et al. 2010; Ko et al. 2017; Longobardi et al. 2018), Centaurus A (Taylor et al. 2017), Perseus (Harris et al. 2020b) and Abell 2744 (Harris and Reina-Campos 2023) for example. This intra-cluster component is expected to arise mostly by the gravitational removal of GCs from satellite galaxies that interacted with the groups, and predominantly from satellites that did not survive until today (Ramos-Almendares et al. 2020). In this way, the origin of the ICGCs and the ICL are therefore expected to be strongly linked, and one might naively expect similar properties and building blocks for both components. However, the way stars and GCs occupy halos is different, in particular in the low mass end of dwarf galaxies, and it is as yet unclear how this may impact the way GCs and the ICL trace each other.

In this study, we take advantage of the recently published catalog of GCs[2], which are tagged post-processing into the cosmological hydrodynamical simulation TNG50 to explore the properties of the ICL and GC components of groups and clusters. The paper is organized as follows: in section 2.3, we present a brief description of the simulation and definitions used in our study. In section 2.4, we introduce the general properties of the ICL component predicted by the simulation. In section 2.5, we analyze the progenitors of the ICL component, and in section 2.6, we investigate the use of GCs as tracers of the formation history of ICL. Finally, in section 2.8, we summarize the main results of our study.

[2] www.tng-project.org/doppel22

2.3 Simulation

We use the TNG50 of the IllustrisTNG suite of cosmological hydrodynamical simulation (Pillepich et al. 2019; Nelson et al. 2019a), which is part of the suite of cosmological boxes from the IllustrisTNG project[3] (Marinacci et al. 2018; Naiman et al. 2018; Nelson et al. 2018; Springel et al. 2018; Pillepich et al. 2018a; Nelson et al. 2019b). TNG50 is the highest resolution baryonic run of the IllustrisTNG suite, which has a volume of approximately $50^3\,\mathrm{Mpc}^3$ and 2×2160^3 resolution elements, with an average mass per baryonic particle $8.5 \times 10^4 \mathrm{M}_\odot$, and dark matter mass with $4.5 \times 10^5 \mathrm{M}_\odot$ per particle. The IllustrisTNG cosmological parameters are consistent with ΛCDM model determined by Planck XIII (Collaboration et al. 2016b) to be $\Omega_\mathrm{m} = 0.3089$, $\Omega_\mathrm{b} = 0.0486$, $\Omega_\Lambda = 0.6911$, $H_0 = 100\,h$ km s^{-1} Mpc^{-1} with $h = 0.6774$, $\sigma_8 = 0.8159$, and $n_\mathrm{s} = 0.9667$.

The evolution of gravity and hydrodynamics are followed using the AREPO moving mesh code (Springel 2010). The galaxy formation baryonic treatment is based on its predecessor simulation suite, Illustris (Vogelsberger et al. 2013, 2014b,a; Genel et al. 2014; Nelson et al. 2015), with modifications implemented to better track the formation and evolution of galaxies, as described in Weinberger et al. (2017); Pillepich et al. (2018b).

The updated IllustrisTNG sub-grid models accounts for star formation, radiative metal cooling, chemical enrichment from SNII, SNIa, and AGB stars, stellar feedback, and super-massive black hole feedback (Weinberger et al. 2017; Pillepich et al. 2018b). These models are shown to reproduce several of the $z = 0$ basic galaxy scaling relations, including the stellar mass - size (Genel et al. 2018), the color bimodality (Nelson et al. 2018) and

[3] https://www.tng-project.org

galaxy clustering (Springel et al. 2018), among others. As such, they are representative of the present day population of galaxies in the universe and reproduce the main environmental trends observed in satellites. Of particular relevance to this work, the abundance of low-mass and intermediate mass galaxies seems consistent with observationally estimated stellar mass functions (e.g. Pillepich et al. 2018b; Vázquez-Mata et al. 2020; Engler et al. 2021).

2.3.1 Identification of groups and clusters

Groups are identified using spatial information based on a Friends-of-Friends (FoF) algorithm (Davis et al. 1985). Individual self-gravitating subhalos and galaxies are later found in these groups using SUBFIND (Springel et al. 2001; Dolag et al. 2009). The object at the center of the gravitational potential of each group is called the "central" galaxy, while all other substructures are "satellites" (or "subhalos"). SUBFIND identifies substructures with a minimum of 32 particles and we additionally apply $M_{DM} \geqslant 5.4 \times 10^7$ $M_\odot$ (at the time of infall) to remove the chances of including spurious baryonic clumps that are not bonafide galaxies. The time evolution of galaxies and halos through the 99 snapshots of the simulation is followed by using the SUBLINK merger trees (Rodriguez-Gomez et al. 2015).

We identify groups and low mass clusters in TNG50 by selecting all host halos with virial masses $M_{200}/M_\odot \geqslant 5 \times 10^{12}$, where virial quantities are measured within the virial radius, or r_{200}, defined as the radius of a sphere where the mean density of the group is 200 times the critical density of the Universe. This selection results in 39 groups and clusters, containing 3305 and 5020 satellite galaxies with $M_* > 10^7$ $M_\odot$ within the virial radius and FoF group boundaries, respectively.

2.3.2 The intra-cluster light (ICL) in groups and clusters

For the purpose of this work we define the ICL as all stellar particles that belong to the group and are not bound to any satellite, and are located within a radial range of $0.15\,r_{200} < r < r_{200}$ from the host galaxy, where r_{200} is the virial radius of the group. Different definitions of ICL are commonly assumed in the literature, both in simulations and observational work. We have experimented with several of these definitions and explicitly checked that none of our main conclusions depends qualitatively on the specific criteria adopted here. For a more detailed view, we collect in Appendix A some examples on how the exact definition of ICL affects some of our reported results.

Further inspection of our selection of ICL particles revealed an excess of stars located on the periphery of several satellites. These stellar particles are considered unbound by SUBFIND (and therefore included as ICL candidates) but are still clearly part of the satellite or substructure in the 6D space of positions and velocities. We therefore applied two extra requirements in order to "clean" our ICL sample. Each stellar particle needs to be at least $10 \times r_{h_*}$ away from any massive satellite (the ones larger than $M/M_\odot > 10^{10}$), where r_{h_*} is the stellar half mass radius of the satellite. In addition, we ensure that the velocity of the particles satisfy $V/V_C > 2.5$ to be considered part of the ICL, where V_C is the circular velocity at $2 \times r_{h_*}$ of the satellite. This procedure satisfactorily removes extra stellar particles with positions and velocities strongly correlated with the local substructure. Note that similar methods are used in observations of the ICL to reduce the light contamination from the central galaxy and the satellite galaxies.

2.3.3 In-situ vs. ex-situ

In this paper, we frequently use the terms "in-situ" and "ex-situ" to distinguish between different types of stellar populations: those born from gas bound to the main branch progenitor in the SUBLINK merger tree of a galaxy ("in-situ") versus those born in external galaxies and later brought in to the descendant object during mergers or tidal stripping events ("ex-situ").

To classify stars as ex-situ or in-situ, we use the stellar assembly catalogs, offered as auxiliary data in the TNG database. The classification method was introduced in detail in Rodriguez-Gomez et al. (2016) and is based on the SUBFIND association of the newly formed stars (at the time of birth) to either the main progenitor of the central galaxy (in-situ) or to a substructure that later merges into the system (ex-situ). Main or secondary progenitors are defined using the SUBLINK merger trees.

2.3.4 Globular Clusters

We use the catalog of GCs presented in Doppel et al. (2023) for our TNG50 systems. GCs are tagged for all galaxies with $M_{*,max} \geq 5 \times 10^6$ $M_\odot$ that infall or interact with our groups and clusters. The tagging is done at infall time for all galaxies, after which the dynamics of the GCs is followed naturally by tracking the positions and velocities of the particles flagged as GC candidates. The simulated GCs are shown to follow known scaling relations for galaxy-GCs and, in addition, to give rise to a population of intra-cluster GCs (ICGCs) as a combination of tidal stripping of GCs from merging galaxies and a native GC population tagged onto the central galaxy (Ramos-Almendares et al. 2020; Doppel et al.

2023). The slope and normalization of this ICGC component is in rough agreement with current observational constraints (see Fig. 5 in Doppel et al. 2023). GCs are tagged to selected dark matter particles and are assigned masses $M_{\rm GC} = 7 \times 10^3$ - $5 \times 10^6 {\rm M}_\odot$ as described in more detail in Appendix B. For additional information we refer the reader to Doppel et al. (2023).

For this work, we use from this catalog the ICGCs, identified as tagged GCs that are currently not associated to any substructure according to SUBFIND and "cleaned" with the same method described in section 2.3.2 for the ICL. As an example of how these GCs are distributed in our systems, we show in Fig. 2.1, projected maps of multiple groups from our sample. These plots show the stellar component (gray-scale in the background) with the position of the ICGCs highlighted by the cyan dots. These few examples illustrate interesting differences in size, shapes and concentration of the GC and ICL components, suggesting a link to their different formation histories.

2.4 The mass and extent predicted for the ICL

2.4.1 ICL mass content

In order to quantify the amount of mass in the ICL we define the fraction of mass in the ICL as:

$$f_{\rm ICL} = \frac{M^*_{ICL}}{M^*_{BCG}}, \tag{2.1}$$

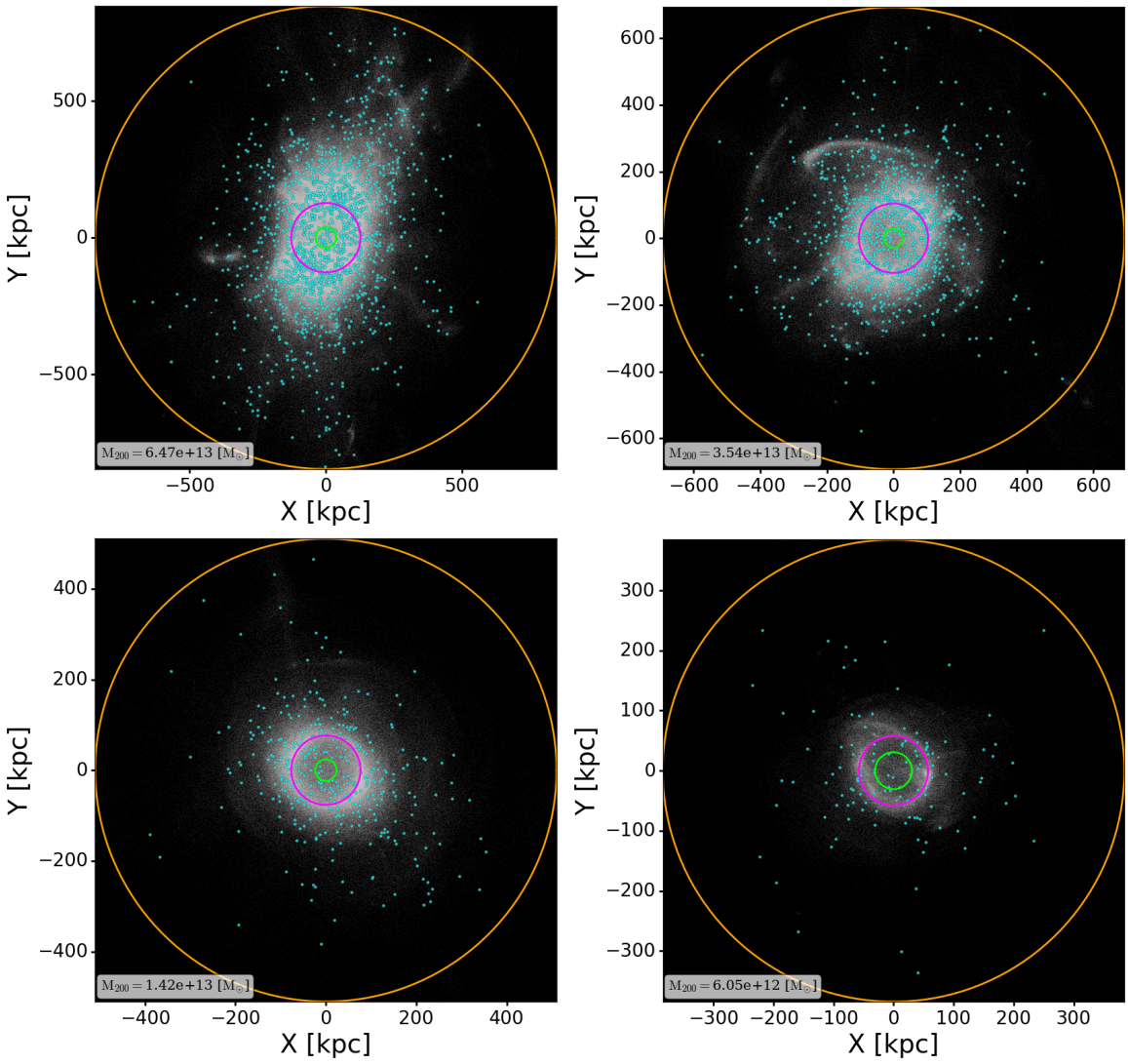

Figure 2.1: Projected position of the luminous (stellar (gray-scale background) + ICGCs (cyan dots)) components in the ICL of 4 randomly selected groups from our sample (the virial mass of each group is quoted on the bottom left of each panel). Orange, magenta, and lime circles show the position of r_{200} for the group, and $0.15 \times r_{200}$, and $2 \times r_{h_*}$, respectively.

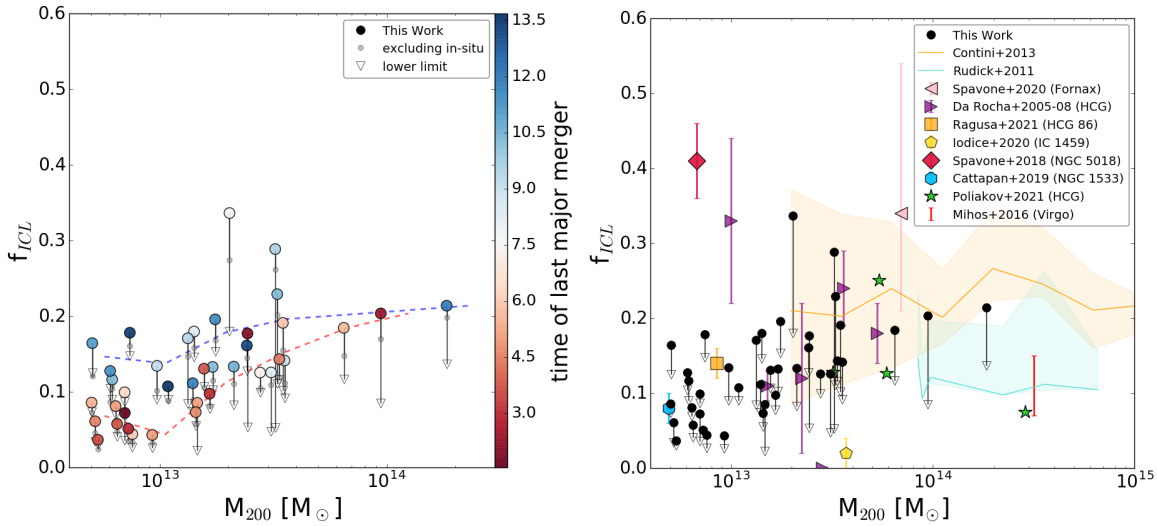

Figure 2.2: Left panel: ICL fraction as a function of virial mass of our groups and clusters color codded by the time of the last major merger of the central galaxy. Predictions from TNG50 are shown with large filled circles (upper limit), and empty downward triangles (lower limit). Small gray circles indicate the fraction if only ex-situ or accreted stars are considered. Right panel: comparison of the predicted ICL fraction in TNG50 with results from previous simulations (shaded areas) and several observational studies (different markers). References along with the reported quantities are presented in table D.1 in Appendix D.

where M^*_{ICL} is the stellar mass in the ICL and M^*_{BCG} is the stellar mass within $2 \times r_{h_*}$ of the central galaxy. Solid circles with black outlines in Fig 2.2 show f_{ICL} for our sample of groups and clusters plotted against the virial mass of each group. We note that various definitions of this fraction have been used in the literature. In particular, a lower limit to f_{ICL} might be found by dividing the mass of the ICL by the total mass of stars within the virial radius $f_{ICL,tot} = M_{ICL}/M_{*,r_{200}}$. For comparison, we show $f_{ICL,tot}$ in Fig. 2.2 with downward triangles connected to the solid symbols. In general we find that the ICL fraction can change by more than a factor of two by adopting common definitions in the literature (see Appendix A). In this work, f_{ICL} will refer to Eq. 2.1 unless specified otherwise.

Our systems span from 5×10^{12} to nearly 2×10^{14} $M_{\odot}$ in virial mass, sampling the range from isolated elliptical galaxies comparable to Centaurus A to moderate mass galaxy clusters such as Fornax, and conservative mass estimates of the Virgo cluster. The ICL mass fraction shows a subtle increase with virial mass, with typical values 5-10% in our low mass systems and $\sim 20\%$ for our more massive clusters. The relation also exhibits a substantial degree of dispersion at a given mass (results are comparable to the best-fit relation in Ragusa et al. 2023, albeit with lower scatter).

We trace back the dispersion in this relation to the assembly history of each group. The color coding in the left panel of Fig. 2.2 shows that, at fixed halo mass, groups with a longer time since their last major merger tend to show lower ICL mass fractions than groups where the last major merger was more recent. This trend has been quantified by categorizing the systems into "red" and "blue" groups, based on whether their last major merger occurred within 7.5 Gyr or after. Major mergers are here defined as merger events of the central galaxy with satellites of stellar mass ratios greater than 0.25 measured at the time of maximum stellar mass of the companion merging galaxy (Rodriguez-Gomez et al. 2015).

This correlation between mass in the ICL and the assembly history of the system is consistent with being an extension into the larger mass regime of the trend found for stellar halos in MW-like galaxies (e.g., Elias et al. 2018) and is also in agreement with findings in other simulations of MW-like and groups and cluster systems using the Horizon-AGN simulations (Cañas et al. 2020). Similarly, several observational studies at low and intermediate redshift find a consistent pattern where higher ICL fractions are common in

systems undergoing active mergers while lower fractions are characteristic in more passive or relaxed objects (Jiménez-Teja et al. 2018, 2019, 2021; de Oliveira et al. 2022; Dupke et al. 2022).

On the right panel of Fig. 2.2 we explore how TNG50 predictions compare to available theoretical and observational constraints to validate our systems. On the theoretical side, our results seem to agree, within the dispersion at a given mass, with semi-analytical models from Contini et al. (2013; shaded orange) and N-body + stellar tagging simulations of Rudick et al. (2011; shaded cyan).

Our results seem to also agree well with several observational constraints available in the literature (symbols with error bars), in particular, bearing in mind that the definition of ICL, band-width and depth of the observational data varies from system to system. We discuss in more detail the compilation of individual measurements in Appendix D and also summarize the information in table D.1.

Most observational constraints seem to suggest that the ICL has less than $\sim 30\%$ of the light of the BCG, in good agreement with our results. Only NGC 5018 (red diamond), HCG 79 (highest purple triangle) and the Fornax cluster (pink triangle) have $f_{\rm ICL} > 0.3$. While in general we do not reproduce such large ICL fractions in our simulated systems, two of our groups have $f_{\rm ICL} \geq 0.3$. A careful look into the formation history of these systems (with FoF group IDs 4 and 12 in TNG50) revealed that their large ICL fractions can be attributed to two different factors. Group 4 presents a central galaxy that is under-massive compared to what is expected of its virial halo mass, such that when computing the ICL fraction it appears larger than other systems. Closer inspection revealed that this group

had a rather late major merger (time $\sim$ 12.3 Gyr) that significantly increased its total mass but has not yet propagated into the central galaxy yet. Reassuringly, this group has several large mass satellites that presumably will merge soon with the central bringing its mass into agreement with its halo mass, at which point we expect $f_{\rm ICL}$ to align with the lower values found in the sample. The second group, FoF group 12, is currently undergoing a major merger with a large satellite companion and the stripped material of this interaction is actively increasing the ICL mass without contributing yet to the central galaxy. Both of these examples are expected to decrease their $f_{\rm ICL}$ after the current interactions are settled.

Our analysis of the groups in TNG50 also revealed the presence of a substantial in-situ stellar component within the ICL, in agreement with previous studies of stellar halos in the predecessor Illustris simulation (D'Souza and Bell 2018; Elias et al. 2018) for smaller mass systems and a more recent study of cluster mass halos using TNG300 simulation by Montenegro-Taborda et al. 2023 (see Sec. 2.3.3 for a description of the in-situ definition). We highlight in Fig. 2.2 where the ICL fraction would fall if one only considers the accreted component (gray filled circles), indicating that the inclusion or not of this component does not strongly modify our results. A more detailed study of the in-situ ICL is deferred to Ahvazi et al. (2024). In what follows, we include only the accreted component of the ICL in the analysis, unless otherwise stated.

2.4.2 ICL radial extent

The physical radius at which the density profile of the ICL reaches a given surface brightness limit is an observable that may help constrain theoretical models on the formation of galaxies and their associated diffuse stellar component. In order to establish a

fair comparison between observations and simulations, we randomly project our simulated groups and clusters generating their 2D surface brightness maps. Following Rich et al. (2019), we measure the radius at which the surface brightness reaches 28 mag/arcsec^2 in the r-band, using the available stellar particle magnitudes from TNG50.

We characterize the radial extension of the ICL in our simulated systems by defining two different radii, R_{28} and a_{28}, an ellipsoid-base and a circle-based definition following common practice in the field. First, we measure the average surface brightness in circular bins and find the (circular) radius R_{28} where the surface brightness is closest to 28 mag/arcsec^2. Second, we measure the surface brightness map with a 3 kpc $\times$ 3 kpc resolution and fit an ellipse to the regions of this map exhibiting a surface brightness of 28 magnitudes per square arcsecond (excluding any low surface brightness features that may result from interactions of subhalos). The semi-major axis of this ellipse was then used as a proxy of radial extension (a_{28}). Note that, on average, this surface brightness limit is predicted to occur at $\sim [0.2 - 0.3]\mathrm{r}_{200}$ in our systems, extending significantly beyond the central galaxy. Next generation surveys using Euclid or JWST are expected to reach several magnitudes fainter, mapping further out regions at $\sim [0.3 - 0.9]\mathrm{r}_{200}$ (see Fig. C.1 in Appendix C).

Fig. 2.3 shows the size of our simulated systems as a function of the stellar mass of the central (left panel) and the virial radius of the group (right panel). As expected, the elliptical semi-major axis tends to be slightly larger than the circularly-averaged radius R_{28}, but they both trace similar trends. The ICL size follows a power law relation with the

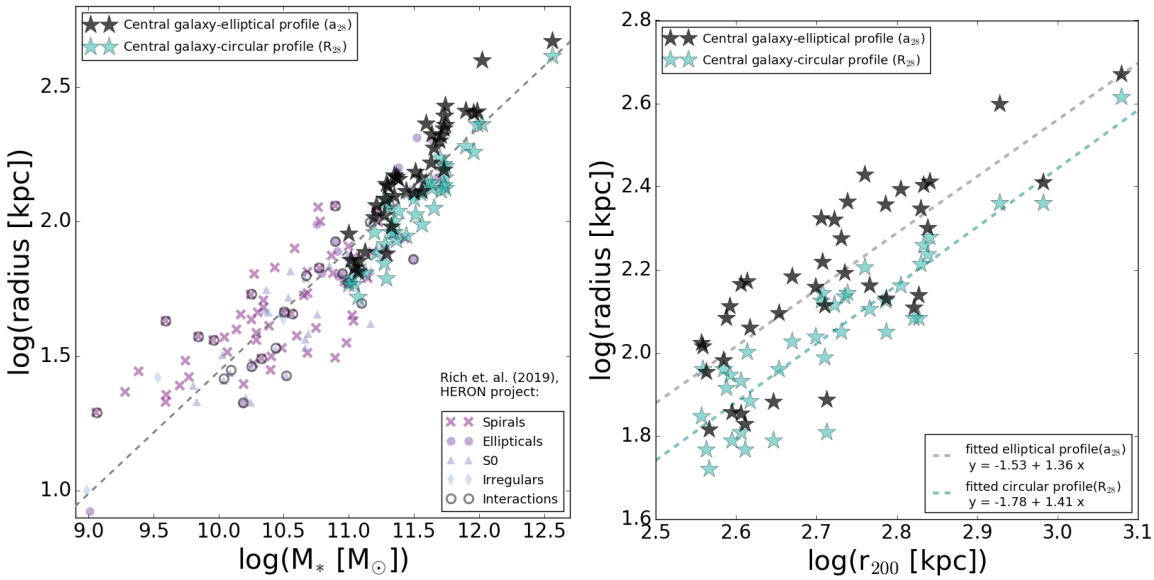

Figure 2.3: Size of the extended stellar halo measured by fitting ellipses to the surface brightness maps (black stars), and by measuring radius from radial binning of surface brightness maps (turquoise stars). Left panel: Size-stellar mass relation, compared to observations from Rich et al. (2019) (colored markers) and relation from Muñoz-Mateos et al. (2015) (gray dashed line). Right panel: Size as a function of virial radius of the group. Grey and turquoise dashed lines correspond to measurements of semi-major axis of the best fit ellipse and radius of the circular profile, respectively.

mass of the central galaxy, consistent with observational constraints available at the low mass end of our sample.

The left panel of Fig. 2.3 shows this good agreement by including observational results for the stellar halo of galaxies in the HERON survey (Rich et al. 2019) (magenta, purple and gray symbols) and also the fit provided in Muñoz-Mateos et al. (2015) (gray dashed line). Our sample, while in agreement in the low mass end, seems to predict a slightly steeper increase in size with stellar mass for the highest mass objects than expected from the gray dashed line.

The right panel of Fig. 2.3 indicates that the size of the ICL also shows a good correlation with the virial radius of the system, although with significant scatter. The gray and cyan dashed lines are best-fit linear relations (y = a + b x) between the logarithmic sizes of the ICL and the halos, characterized by the parameters a and b. For the elliptical radius a_{28}, we find the parameter values to be $a = -1.57$ and $b = 1.41$ with r.m.s scatter of ~ 0.1 dex, while for the circular radius R_{28}, the values are $a = -1.81$ and $b = 1.45$ with a scatter measured to be ~ 0.1 dex. The existence of a correlation between the radial extension of the ICL and the virial radius of the host halo demonstrates that the assembly of these two components is intertwined and reaffirms the validity of the ICL as observational tracer of the distribution of dark matter in these objects.

2.5 The progenitors of the ICL in groups and clusters

A myriad of disrupted satellites are expected to contribute to the build up of the ICL as a consequence of the hierarchical formation scenario, making it a unique probe of the particular assembly history of a given object. Yet, while the individual formation histories may vary from halo to halo, common trends arise that may be used to infer details of the formation and assembly of a given object from the properties of their diffuse stellar component. For instance, in the case of MW-mass galaxies, simulations suggest that the properties of the stellar halos are dominated by one or two most massive progenitors, which naturally explains the correlation between stellar halo mass and metallicity (e.g., Deason et al. 2016; D'Souza and Bell 2018). We explore in what follows what are the typical building

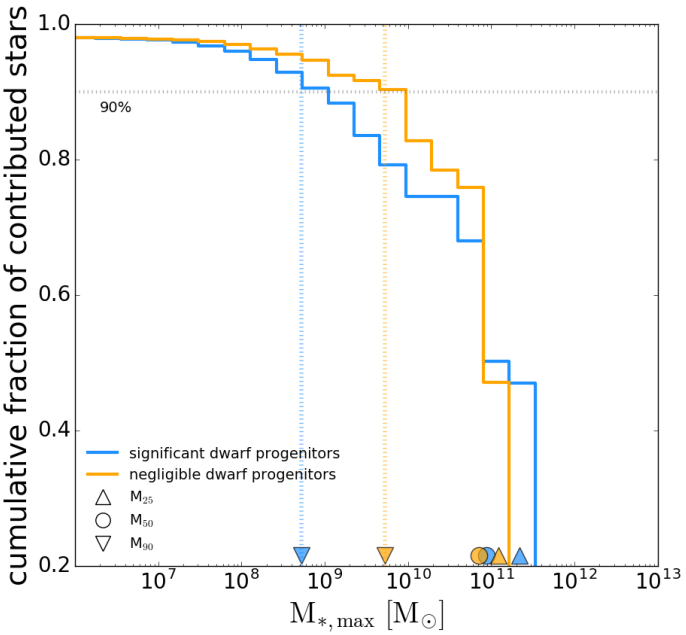

Figure 2.4: Example of two groups with different ICL progenitor mass functions. The vertical axis shows the cumulative fraction of stellar mass deposited in the ICL (the accreted stellar component) by galaxies with maximum stellar mass $> \mathrm{M}_{*,\mathrm{max}}$. Markers on the x-axis correspond to the measured M_{25} (triangle), M_{50} (circle), and M_{90} (pointing down triangle), and horizontal and vertical lines correspond to the measurement of the M_{90} for the groups highlighted here. The group in orange has an ICL contributed mostly by massive progenitors with $M_{*,\mathrm{max}} \sim 10^{10}$ $\mathrm{M}_{\odot}$ while the one in blue has significant contributions from lower mass dwarf galaxies with $M_{*,\mathrm{max}} \sim 5 \times 10^{8}$ $\mathrm{M}_{\odot}$, as shown by their different M_{90} values.

blocks of the ICL in more massive objects like groups and clusters, and what observational signatures may be useful to decode details of their assembly.

Fig 2.4 shows the fractional contribution of stars to the ICL of two different groups (orange and blue curves) that come from progenitors of a given stellar mass $M_{*,\mathrm{max}}$. Both groups are selected to have comparable mass, $M_{200} \sim 3.2 \times 10^{13}$ $\mathrm{M}_{\odot}$, but different accretion histories. Here we choose to characterize the mass of the progenitors using their maximum stellar mass $M_{*,\mathrm{max}}$, and we build the cumulative histogram of stellar particles brought in by progenitors more massive than a given $M_{*,\mathrm{max}}$. The group depicted in orange corresponds

to a case where most of the mass in the ICL is contributed by relatively massive galaxies while the group shown in blue allows for significant contribution of progenitors in the regime of dwarf galaxies.

We quantify this by means of M_{25}, M_{50} and M_{90}, which are defined as the mass of the progenitors in such cumulative distribution contributing 25%, 50% and 90% of the mass in the accreted ICL. For illustration, we highlight M_{90} in Fig. 2.4 with vertical dotted lines and an inverted triangle, computed as the intersection of the cumulative distribution of accreted stars in each group and the 0.9 horizontal line. M_{50} and M_{25} are also denoted by a circle and a triangle for each group along the horizontal axis. The larger contribution of dwarf galaxies to the build up of the ICL in the group shown in cyan is now clearly shown by its lower mass $M_{90} = 5.2 \times 10^8$ $M_\odot$ compared to $M_{90} = 5.2 \times 10^9$ $M_\odot$ in the case of the group in orange. Differences for M_{50} and M_{25} between these two groups are smaller, but systematic.

The typical progenitors of the ICL for the full sample of groups and clusters are shown in the left panel of Fig. 2.5. Our results suggest that the predominant contributors to their ICL are massive galaxies with $M_{50} \geq 10^{10} M_\odot$, regardless of the host halo mass in this somewhat narrow M_{200} range. This is in agreement with previous works in the literature which identify $M_* \sim 10^{10}$-$10^{11} M_\odot$ as the main progenitors of the ICL in groups (e.g., Contini et al. 2013; Montes and Trujillo 2018; Contini et al. 2019; Montes et al. 2021). However, a comparison of the M_{90} values uncovers a larger variability of contributions of dwarf galaxies from halo to halo, with some systems having $M_{90} \sim 10^{10} M_\odot$ –and therefore

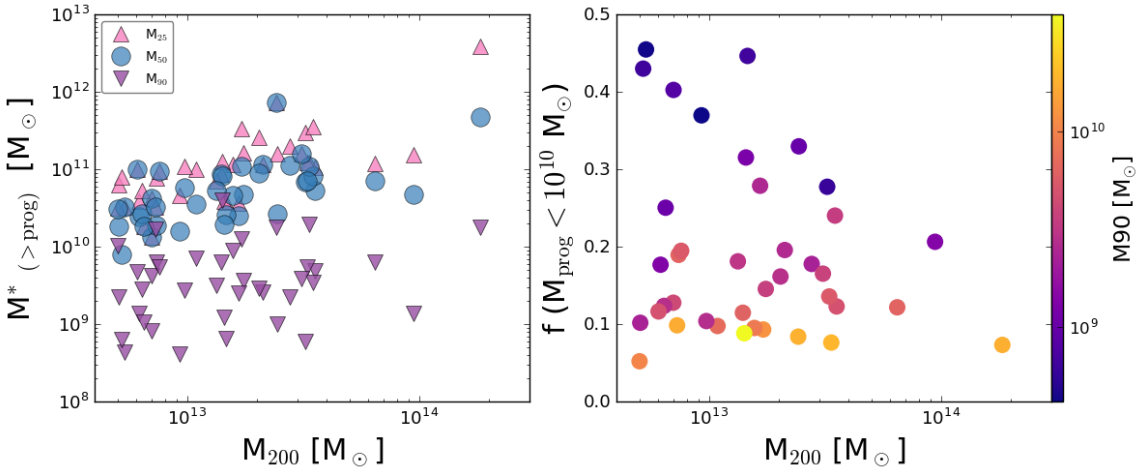

Figure 2.5: Left panel: Stellar mass of the progenitors that brought a percentile of accreted stellar mass to the ICL as a function of virial mass of the groups. Pink triangles, blue circles, and purple pointing down triangles correspond to M_{25}, M_{50}, and M_{90}, respectively. Note the large scatter in M_{90} indicating a varied contribution of dwarf galaxies to the build up of the ICL. Right panel: fraction of the accreted ICL that was contributed by (dwarf) galaxies with stellar masses below $M_{*,\rm max} = 10^{10}$ M$_\odot$. Symbols are colored by M_{90} for each group (from the left panel) and highlight the good correspondence between the two metrics. At similar halo mass, some groups have about half of their ICL built by low mass galaxies with $M_{*,\rm max} = 10^{10}$ M$_\odot$ while others show less than 10% contribution from these dwarfs.

having negligible mass brought in by dwarf galaxies with $M_* \sim 10^9$M$_\odot$ and below– while other systems show a more significant contribution by dwarfs with typical $M_{90} < 10^9$M$_\odot$.

This is further illustrated in the right panel of Fig. 2.5, which depicts the fraction of ICL mass contributed by galaxies with $M_{*,\rm max} < 10^{10}$ M$_\odot$ as a function of the halo virial mass. As anticipated, these fractions can be quite different from system to system, even in the case of similar halo masses. For instance, for groups with $M_{200} \sim 10^{13}$M$_\odot$, the fraction of mass brought into the ICL by low mass galaxies with $M_{*,\rm max} < 10^{10}$ M$_\odot$ varies from 10% to 40%, these extremes being examples of systems where dwarf galaxies play little to a significant role, respectively. Symbols in the right panel of Fig. 2.5 are colored according to the previously introduced M_{90} and highlights the good correlation between both indicators:

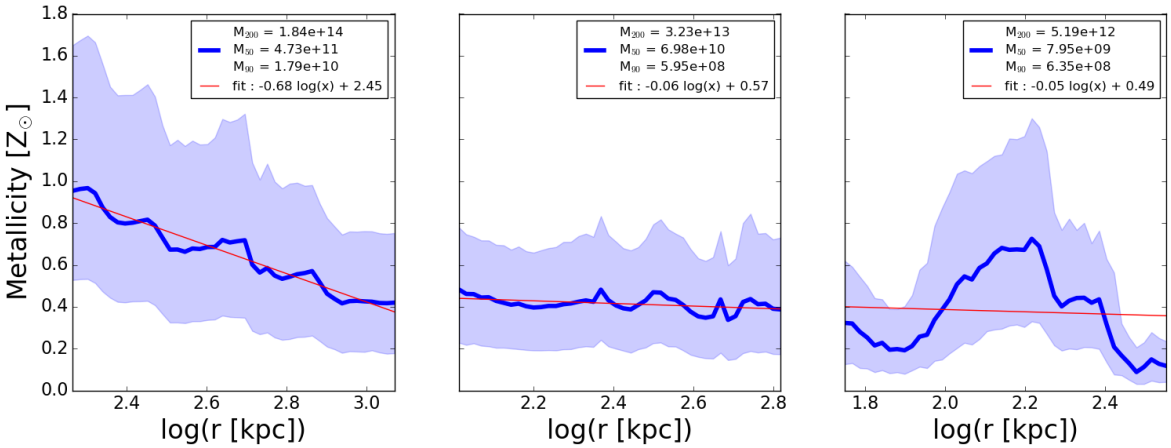

Figure 2.6: Illustration of the metallicity profiles for the accreted stellar component of three randomly selected groups from our sample, with the median and 25-75 percentile depicted by the blue line and shaded region, respectively. The best-fit linear relation (in log) is highlighted in red and quoted in each panel. Most systems show a negative metallicity profile with radius, but the slope changes substancially from system to system.

systems with a substantial contribution from low mass galaxies have a high fraction of stars brought in by progenitors with $M_{*,\rm max} < 10^{10}$ M$_\odot$ and a low M_{90} value while systems built up mostly by large galaxies have a small fraction f and large M_{90} values.

This opens up the possibility to use different observables to attempt determine the kind of accretion history of a halo given the observed properties of their ICL. One such key observable is the metallicity profile. Fig 2.6 illustrates the metallicity profile for three representative groups with differing formation histories and virial masses (as indicated by the legends). The blue curve in each panel depicts the median metallicity of the merged stellar particles in the ICL at each radius, while the blue shaded region represents the 25th and 75th percentiles. A linear fit of the form $Z = a\log(\rm r) + \rm b$ is in general a roughly good description of our profiles (see red lines) and allow us to quantify for each object the slope of the metallicity profile (a) and its intercept (b).

Fig. 2.7 shows interesting correlations in the ICL observables that imprinted by the kind of progenitors that built each individual object. At a given host halo mass, systems with a larger contribution from dwarfs (blue-ish purple points) show less total mass in the ICL (left panel), a lower average metallicity (middle panel) and also flatter metallicity profile slopes (right-hand panel). Systems with mostly massive progenitors (yellow-ish orange colors) tend to show strongly declining metallicity profiles. Not shown here for brevity, the metallicity profile intercepts correlates well with the median metallicity. In all panels points have been color-coded by M_{90} and only the accreted component of the ICL is being considered here. However, our main results would not substantially change if, instead, we would show the total ICL (in-situ plus accreted, gray triangles on the right panel). We have explicitly checked that similar trends exist with the stellar age profiles, with most systems displaying decreasing age profiles with radius, and some showing considerably flatter age distributions. However ages seemed less well correlated with the assembly history of the group and cluster than the information provided by metallicity.

The ICL mass and metallicity should then be considered a valuable tool to reconstruct details on the past merger history of systems assembled within ΛCDM. Similar correlations on amount of mass, overall metallicity and metallicity gradients with the diffuse component build-up have been found in the regime of stellar halos for MW-like galaxies (D'Souza and Bell 2018; Monachesi et al. 2019). Our results extend upwards the range of halo masses over which these correlation are expected, including now the regime of groups and clusters.

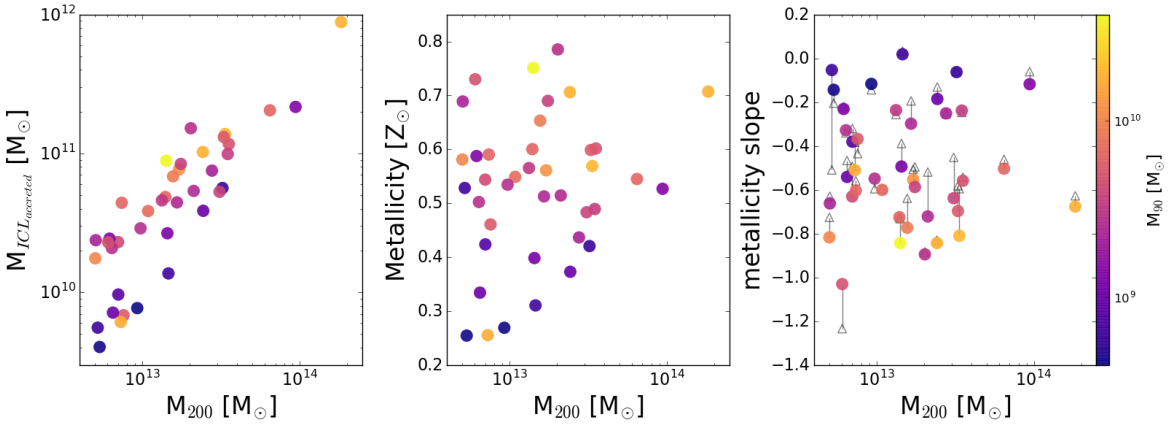

Figure 2.7: Left panel: stellar mass of the accreted component in the ICL as a function of the virial mass. Middle panel: median metallicity of the accreted stars in the ICL as a function of the virial mass. Right panel: the slope of the metallicity profile as a function of virial mass for the accreted (merged) component, with black triangles representing the results for all the stellar components (accreted + in-situ components). All panels are color-coded by the M_{90} of each group. Systems where dwarf galaxies play a role in building the ICL (low M_{90}) tend to have lower ICL mass, lower overall metallicity and shallower metallicity profiles than systems with accretion dominated by more massive galaxies.

2.6 Tracing the formation history of the ICL through globular clusters

We investigate how well the GCs can trace the ICL in our systems using the GC catalog presented in Doppel et al. (2023). As detailed in section 2.3.4, we use only intra-cluster GCs (ICGCs)—GCs not gravitationally bound to any structure according to SUBFIND and that satisfy the cleaning criteria in section 2.3.2. As briefly discussed in Doppel et al. (2023), the GC tagging model predicts that the ICGC component forms via the tidal stripping of GCs from their host galaxies as they interact with their new host environment after infall. The buildup of ICGCs is thus, in a similar fashion to the ICL, a result of the hierarchical assembly of their host systems. The GC catalog follows the population of surviving GCs with mass $M_{\rm GC} > 7 \times 10^3$ $M_\odot$, and while we do not make the

distinction between "red" and "blue" GCs as in Doppel et al. (2023), their Fig.5 shows that the mass density of the simulated ICGC is in good agreement with available observational constraints.

As in the case of the ICL, we find a large spread on the distribution of progenitors that build the the intra-cluster GC component in our groups. Using a similar concept to that introduced for M_{25}, M_{50} and M_{90}, we define similar quantities but considering only the stellar mass that brought in the 25%, 50% and 90% of the mass in GCs in the ICGC component. Fig. 2.8 compares the progenitors for the ICL and the GCs. We find that GCs can be very good tracers of the most massive contributors to the ICL, in particular M_{25} and M_{50} for the stars or GCs in the diffuse component are very similar, indicating that the progenitors that build up to half of the ICL also bring along about half of the GCs in the ICGC. However, we find a clear bias in the contributors as quantified by M_{90}: taking the progenitors that bring 90% of the GCs mass typically leads to smaller masses than the progenitors contributing 90% of the stellar mass in the ICL (left panel Fig. 2.8).

This means that when using GCs to reconstruct the merger history of groups and clusters, one should keep in mind that the contribution from dwarf galaxies will be over-represented compared to the contribution of the same dwarfs to build the diffuse light component. This result can be intuitively understood from the different scaling of GCs and stellar mass with the halo mass. In the considered GC model, the mass of GCs scales as a power-law of halo mass (Doppel et al. 2023) while abundance matching results suggest a more steep decrease in the efficiency of low mass halos to form stars compared to more massive galaxies like the MW (abundance matching is better described by a double

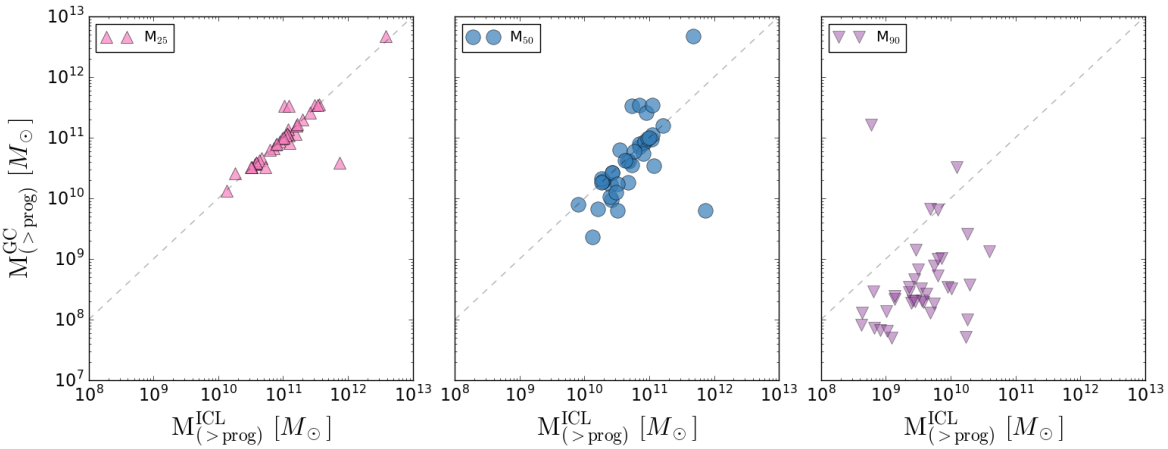

Figure 2.8: Typical mass of progenitors that build the ICL (x-axis) and the intracluster-GCs (y-axis) as quantified by M_{25} (left), M_{50} (middle), and M_{90} (right) of each population. The gray dashed line corresponds to the one to one relation. Our findings indicate that GCs can serve as a good tracers of the most massive contributors to the ICL, although it is important to note that the contribution from dwarf galaxies may be over-represented when looking at GCs in comparison to the ICL (right panel).

power-law). As a result, dwarfs contribute *fractionally* more GCs than stars to the diffuse components. Interestingly, as found for the case of the ICL, there is a sizable range in the typical contributor of the ICGC. For some of our GC systems, M_{90} is found to be galaxies with $M_* \sim 10^{10}\mathrm{M}_\odot$, indicating little role played by low mass galaxies. However, there are also cases with $M_{90} \sim 5 \times 10^7\mathrm{M}_\odot$, indicating dwarfs with masses typical of dSph galaxies playing a role. These differences in the accretion histories of these objects are likely to remain imprinted in the metallicity of their intra-cluster GC component and offer an avenue to constrain formation histories of massive hosts in cases where measurements of diffuse light becomes too challenging or implausible. Future GC models that are able to follow the formation and evolution of individual GC metallicities are necessary to quantify the strength of the signal expected and whether or not such signatures are to be detectable with current or future observations.

2.7 Intra-cluster light and its globular cluster component as luminous tracers of dark matter

Fig. 2.9 shows the 3D density profiles of the ICGCs, ICL and dark matter components in our systems (corresponding to the red, blue, and gray colors on this plot). Thin lines corresponds to individual objects and the median density at a given radius is highlighted with the thick lines. The grey shaded region indicates the ICL region based on our definition. We find that the ICGCs exhibit profiles similar to the dark matter in terms of the slope, whereas the ICL is more centrally concentrated than the dark matter, as evidenced by the steeper radial profiles. Within satellites, stellar profiles are also biased toward the inner regions of their own dark matter halos at infall. Consequently, during the tidal stripping that forms the ICL components, these stars are deposited more efficiently toward the inner regions, creating the more centrally concentrated profiles for the stellar component. Previous numerical simulations have reported similar results when comparing the ICL with the dark matter in groups and clusters (e.g., Pillepich et al. 2018a; Alonso Asensio et al. 2020).

In order to quantify shapes of our simulated dark matter halos, ICL, and ICGCs we use the commonly adopted "reduced inertia tensor" method. In brief, we follow Allgood et al. (2006) and fit ellipsoids to the dark matter and stellar particles in the ICL region. We define the normalized tensor as:

$$I_{ij} = \sum_{x_k \in V} \frac{x_k^{(i)} x_k^{(j)}}{d_k^2}, \tag{2.2}$$

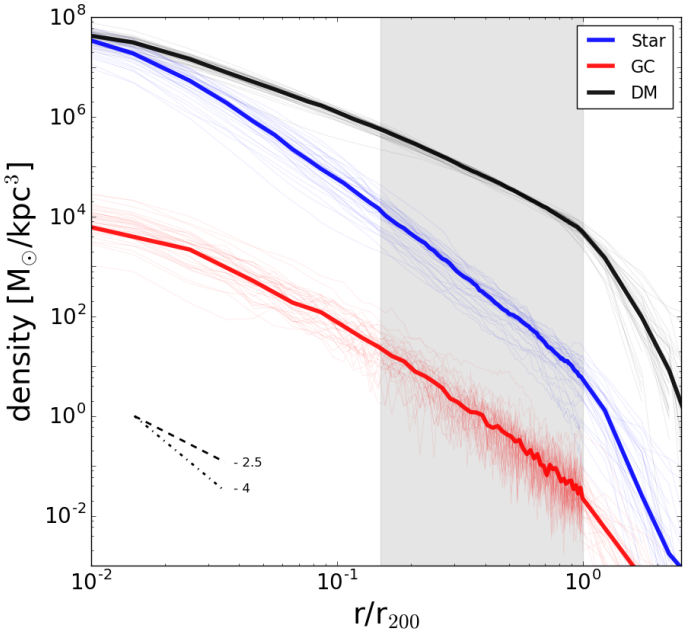

Figure 2.9: Density profiles of stellar, ICGC, and dark matter components for each group in our sample are represented by the thin blue, red, and black lines, respectively. The thick lines show the median density profiles for each component. The shaded grey region depicts the region corresponding to the ICL on the plot.

where x_k denotes the position of the k^{th} particle (either dark matter or stellar particle) within the volume V in each iteration, and d_k represents a scaled distance to the k^{th} particle, taking into account the axis ratios of the ellipsoid (the definition of d_k is detailed in the next paragraph). We find the best fitting ellipsoid at any given radius of interest, which is represented by its axis lengths; $a \geqslant b \geqslant c$. From those we can define axis ratios $q = b/a$ and $s = c/a$ that are the ratios of the square-roots of the eigenvalues of **I**, and the directions of the principal axes given by the corresponding eigenvectors. We measure the shape of the dark matter and stellar halos at the virial radius.

To find the best fitting ellipsoid we utilize an iterative method, which starts the calculation by considering all the particles in between concentric spheres that encompass the ICL region ($0.15 \times r_{vir} \leqslant r \leqslant r_{vir}$) and in each step there is a reshaping of the outer sphere using the eigenvalues of **I**. Note that the distance measured to each particle is $d_k^2 = x_k^2 + y_k^2/q^2 + z_k^2/s^2$, and is updated at each iteration based on the eigenvalues for **I**.

The comparison between the shapes and orientations of the best fitting ellipsoids representing the ICL, ICGC and dark matter components are shown in Fig 2.10. The left panel displays the shapes of ICL (blue dots), ICGC (red dots), and dark matter (gray dots), highlighting a reasonable agreement, with dark matter exhibiting slightly more spherical morphologies. This is better seen by looking at the histogram distributions, showing higher median values by ~ 0.1 dex in both axis ratios b/a and c/a for the dark matter compared to the luminous tracers (see dashed lines in histograms along both axes).

The right panels of Fig. 2.10 explores the orientations of the best fitting ellipsoids, comparing the dark matter with ICL (bottom right) and ICGC (upper right). We measure

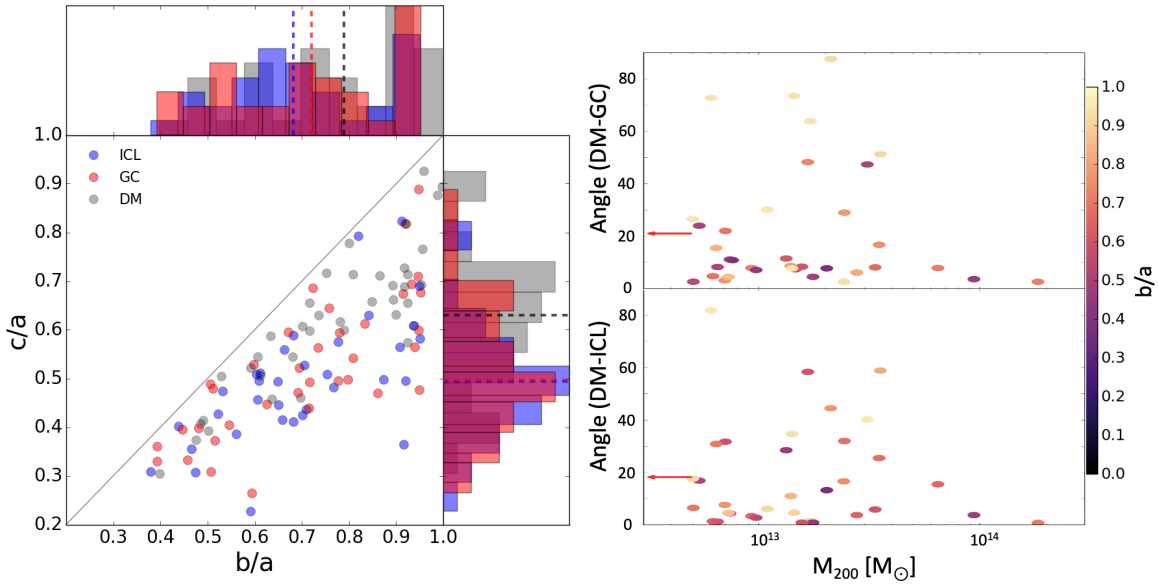

Figure 2.10: Left panel: The b/a vs c/a of the stellar ellipsoid, GC ellipsoid, and DM ellipsoid at the virial radius. Right panels: The misalignment angle between the major axis of the ellipsoids fit to the DM-GC (upper panel), and DM-ICL (lower panel). On average, ICL and GCs serve as reasonably good indicators of the dark matter shape and orientation.

the angle between the major axes of the ellipsoids for each component as a function of the virial mass of the halo. We find that these components are reasonably well aligned at the virial radius, with a median misalignment angle of $\sim 18^{\circ}$ between the ICL and dark matter, and $\sim 21^{\circ}$ between the ICGCs and dark matter (indicated by red arrows on each panel). Some of the systems with large misalignment angles, $> 35^{\circ}$, are found to have more oblate shapes (as indicated by the lighter colors). We know that such cases should be evaluated carefully, as a perfectly oblate system would have an ill-defined direction for a and b, obscuring the interpretation of large misalignment angles. For example, the misalignment angle between dark matter and ICGCs shrinks to 11.3° if only systems with $b/a < 0.7$ are considered. These findings are in good agreement with those reported from the E-MOSAICS simulations (Reina-Campos et al. 2023) for lower mass systems (compared

to the ones considered here). Our results support a scenario where ICGCs may be used as a predictor of the shape of the dark matter up to the outskirts of the halo in groups and clusters.

In comparison to studies exploring the connection between the ICL and the dark matter component, the hydrodynamical simulation by Gonzalez et al. (2021b) shows similar trends, with ICL generally more elongated than dark matter in clusters with $M_{200} > 1.4 \times 10^{14}$ $M_{\odot}$, which are higher mass systems than those in our study. They found that excluding dark matter particles of satellite galaxies results in more spherical dark matter shapes. Note that unlike our study, which excludes dark matter and stellar particles of satellite galaxies to focus on the ICL region, their assessment includes these particles.

Gonzalez et al. (2021b) also compares the misalignment angle between dark matter and ICL, finding a generally good agreement with a median of $\sim 5^{\circ}$, whereas we observe slightly larger values, possibly due to a higher prevalence of oblate shapes in our sample, making it more challenging to precisely determine the direction of the semi-major axis. Our results align better with the study by Kluge et al. (2021), which examined low-redshift clusters with gravitational masses of $\log(M\ [M_{\odot}]) = 14.75 \pm 0.25$, finding alignment angles less than 30° in 80% of cases, consistent with our results where only 8 out of 39 clusters have alignment angles above 30°.

2.8 Conclusions

Using the cosmological hydrodynamical simulation TNG50, we have conducted a comprehensive study of two luminous tracers of dark matter in the outskirts of halos: the

ICL and the GC population. We select all groups and clusters with $M_{200} > 5 \times 10^{12} M_{\odot}$ resulting in a sample of 39 host halos that span the virial mass range $M_{200} = [0.5 - 20] \times 10^{13} M_{\odot}$ and sample a wide range of formation histories. We use the catalog of GCs tagged to the TNG50 groups and clusters presented in Doppel et al. (2023), allowing one of the first explorations of both luminous tracers in high density environments. We focus on the study of possible imprints of these individual accretion histories on observable properties of the ICL and GCs populations. Our findings can be summarized as follows:

- TNG50 predictions for the fraction of light in the ICL, $f_{\rm ICL}$, are in reasonable agreement with current observational constraints for groups and low mass clusters. In addition, $f_{\rm ICL}$ is predicted to increase with virial halo mass, albeit with significant dispersion. We find that this dispersion is well correlated with the assembly history and time of the last major merger for the BCG in our systems. Objects with more recent major mergers tend to show an excess of ICL compared to older or earlier assembled systems of comparable mass.

- There is a good correlation between the radial extent of the ICL (as measured by the radius where the surface brightness profile reaches 28 mag/arcsec^2) and the stellar mass of the central galaxy. This size–mass scaling relation for the ICL seems to agree with the one found observationally for lower mass galaxies as part of the stellar halos in the HERON survey (Rich et al. 2019). The radial extent of the ICL also shows a power-law relation to the virial radius of the halo, offering an observational means with which to constrain r_{200} independent of abundance matching methods.

The typical r.m.s scatter in the relation between ICL-size and virial radius is ~ 0.1 dex.

- The mass of the ICL is deposited by a wide range of progenitors. Some of our systems show sizable contributions from dwarf galaxies with $M* < 10^9 M_\odot$, while others are built up almost entirely by systems as or more massive than the Milky Way. We find that the average metallicity and slope of the metallicity profiles of the ICL retain information on these different assembly histories: halos with a higher contribution from dwarf galaxies generally have shallower metallicity profiles, overall lower average metallicities and also a lower amount of mass/light in the ICL. These findings are different from the common interpretation of flat metallicity profiles as evidence of major mergers (Krick and Bernstein 2007; DeMaio et al. 2015, 2018). In our systems, the incidence of low mass galaxies is the main responsible for flattening up the Z-profiles. A larger role of dwarf galaxies in the build up of the ICL is also manifested by an overall lower metallicity content compared to systems built up by more massive satellite contributors.

- Intra-cluster globular clusters (ICGCs) may also serve as a valuable tool to reconstruct the assembly history of the halos. We find that lower mass dwarfs tend to make more significant contributions to the ICGC population than to the stars in the ICL, a bias that must be taken into account when reconstructing assembly histories based on metallicity of GCs or ICL. This can be understood as a consequence of the single power-law relation of GCs with halo mass, which gives higher weight to the low mass

halos compared to the double-power law expected for the stars in abundance matching relations.

- Finally, our study highlights that the shape and orientation of the ICL and ICGCs show reasonable correlation to those of the dark matter in the outskirts of the halo, highlighting the common origin of these components as well as the potential of these components to be used as luminous tracers for the underlying dark matter. We find, however, small systematic biases. The shape of the dark matter, as measured by the principal-axis ratios b/a and c/a, is typically ~ 0.1 larger compared to the ICL and ICGCs. These components are also well aligned, showing a median of ~ 20 degrees between their major axes.

Several of the trends studied here represent an extension of properties highlighted for the stellar halos of galaxies like the Milky Way, including trends on amount (Pillepich et al. 2014; Elias et al. 2018), metallicity (D'Souza and Bell 2018; Monachesi et al. 2019) and radial extension (Rich et al. 2019) and their link to the assembly history of each halo. Encouragingly, the ICL in groups and clusters is more massive/brighter than in systems like the Milky Way, offering an advantage from the observational point of view to study this diffuse component. The increased sensitivity of upcoming observations with JWST and Euclid VIS Deep survey promise to reach ~ 31 mag/arcsec^2 levels in a few hours integration time. On average, for our simulated systems, this would result in detections for the ICL component all the way out to $\sim 0.7 r_{200}$, opening a new window to explore the predictions of hierarchical assembly expected for galaxies within ΛCDM.

Chapter 3

Star formation beyond galaxies: widespread in-situ formation of intra-cluster stars[1]

3.1 Abstract

We study the fraction of the intra-cluster light (ICL) formed in-situ in the three most massive clusters of the TNG50 simulation, with virial masses $\sim 10^{14}$M$_\odot$. We find that a significant fraction of ICL stars (8%-28%) are born in-situ. This amounts to a total stellar mass comparable to the central galaxy itself. Contrary to simple expectations, only a sub-dominant fraction of these in-situ ICL stars are born in the central regions and later

[1]This chapter contains a draft of an article that is submitted for publication by Open Journal of Astrophysics written by Niusha Ahvazi, Laura V. Sales, Julio F. Navarro, Andrew Benson, Alessandro Boselli, and Richard D'Souza

re-distributed to more energetic orbits during mergers. Instead, many in-situ ICL stars form directly hundreds of kiloparsecs away from the central galaxy, in clouds condensing out of the circum-cluster medium. The simulations predict a present-date diffuse star formation rate of $\sim$1 $M_\odot$/yr, with higher rates at higher redshifts. The diffuse star forming component of the ICL is filamentary in nature, extends for hundreds of kiloparsecs and traces the distribution of neutral gas in the cluster host halo. We discuss briefly how numerical details of the baryonic treatment in the simulation may play a role in this result and conclude that a sensitivity of $1.6 \times 10^{-19} - 2.6 \times 10^{-18}$ erg s^{-1} cm^{-2} arcsec^{-2} in H_α flux (beyond current observational capabilities) would be necessary to detect this diffuse star-forming component in galaxy clusters.

3.2 Introduction

The simplest models of galaxy formation suggest that most stars in a cluster should form in the high-density regions of individual galaxies. These models imply that the majority of stars in the intra-cluster light (ICL) originate from the tidal removal of stars from luminous galaxies with mass similar to the Milky Way (MW) (Puchwein et al. 2010; Cui et al. 2014; Cooper et al. 2015a; Contini et al. 2013, 2018, 2019; Montenegro-Taborda et al. 2023), with relatively small contributions from dwarf mass galaxies, particularly in group environments with halo virial masses $< 10^{13}$ $M_\odot$ (Ahvazi et al. 2023). Nevertheless, observational studies (Barfety et al. 2022; Hlavacek-Larrondo et al. 2020) and some numerical simulations (Puchwein et al. 2010) indicate that a non-negligible fraction of ICL stars are formed in-situ.

In-situ ICL stars could have formed in the brightest cluster galaxy (BCG) galaxy and been later pushed onto highly energetic orbits by mergers. An alternative, more intriguing, possibility is that stars form directly in the intra-cluster medium (ICM), far away from the high density regions of the BCG. This low-density mode of star formation is potentially interesting, as it might occur under very different physical conditions than the normal star formation in galaxies, with consequences for the multi-phase nature of the ICM and its metallicity, as well as for the age distribution of ICL stars, especially if in-situ star formation continues to the present day. From an observational perspective, if a substantial amount of stars form outside galaxies, this would have strong implications for wide-field surveys in the UV or H_α, which are especially sensitive to the presence of young stars.

Several mechanisms have been suggested to explain in-situ ICL star formation. One of the most commonly cited is the compression of gas associated with the ram-pressure trails of infalling galaxies, a phenomenon that has been detected in both observations (Smith et al. 2010; Mihos et al. 2017; Boselli et al. 2018b; Gullieuszik et al. 2020) and some numerical simulations (Kronberger et al. 2008; Kapferer et al. 2009; Tonnesen and Bryan 2012; Lee et al. 2020; Calura et al. 2020; Steyrleithner et al. 2020; Vollmer et al. 2021; Göller et al. 2023, for a detailed discussion see section 5.3.1 in review paper by Boselli et al. 2022). Another possible mechanism is star formation within the tails of stripped material formed during gravitational fly-by encounters of gas-rich systems (see see NGC 4254 in Virgo, Boselli et al. 2018a; VCC 1249, Battaia et al. 2012; IC3418, Hester et al. 2010; Fumagalli et al. 2011; Kenney et al. 2014).

In-situ star formation in the ICM is also predicted to be widespread at high-redshift, where AGN feedback might be less powerful and unable to offset the short timescales for cooling in the dense regions of the ICM (Webb et al. 2015b). In such a scenario, spontaneous run-away cooling in the ICM might lead to an increase of density high enough to trigger violent star-formation events in locations outside galaxies (Hlavacek-Larrondo et al. 2020).

Interestingly, observations of off-center star formation at large distances from the BCG are consistent with this scenario for a few high-z clusters (Webb et al. 2015a; Hlavacek-Larrondo et al. 2020; Barfety et al. 2022), in some cases predicting as much as a MW-worth of stars contributed to the ICM by such cooling events.

Some observations of isolated HII regions in nearby clusters, such as the Virgo cluster, may also hint at a more sustained but lower-level star formation activity taking place directly in the ICM/ICL region (Gerhard et al. 2002; Bellazzini et al. 2018). However, it is not always trivial to disentangle whether these isolated star-forming clouds are ICM-born material or belong to some older ram-pressure or interaction events in the cluster (Junais et al. 2021; Jones et al. 2022).

Numerical simulations therefore emerge as valuable tools to explore this mode of star formation within the realistic framework of the ΛCDM model. For instance, Puchwein et al. (2010) estimate that approximately $\sim 30\%$ of the ICL stars formed in their clusters (with masses between $2 \times 10^{13}\,\mathrm{M}_{\odot}$ and $1.5 \times 10^{15}\,\mathrm{M}_{\odot}$) originated at distances consistent with being ICM-born. The presence of in-situ formed stars in extended stellar halos is also

documented extensively in the literature on the scale of MW-mass halos (Zolotov et al. 2009; Font et al. 2011; Tissera et al. 2012; Cooper et al. 2015b; Pillepich et al. 2015).

Various numerical methods have been employed to study the formation of cold gas in the ICM, which could give rise to star formation outside galaxies. Runaway local production of cold gas in the ICM, as well as thermal instability, have been shown to lead to multi-phase structures in idealized hot haloes (Maller and Bullock 2004; Kaufmann et al. 2006, 2009; McCourt et al. 2012; Sharma et al. 2012).

Given that the cold-phase ICM resulting from such processes is a small-scale phenomenon, it has been studied largely in idealized numerical experiments (Fielding et al. 2020). Previous work by Oppenheimer et al. (2018) demonstrated a relatively significant abundance of cold, low-ionization gas in the circum-galactic medium (CGM) of EAGLE galaxies (for MW and group mass halos), albeit with uncertainties regarding the numerical robustness of the hydrodynamical technique in this regime (see also Ford et al. 2013). Similarly, Butsky et al. (2019) demonstrated evidence for presence of cold gas in the outskirts of the galaxy clusters (in the ICM) using high-resolution hydrodynamical galaxy cluster simulation, RomulusC.

Semi-analytic models have also been developed to explain the unique, possibly drag-induced sub-virial kinematics of cold gas flowing through luminous red galaxy host haloes (Afruni et al. 2019). In the context of IllustrisTNG, Nelson et al. (2018) showed that TNG is consistent with empirical OVI constraints in the CGM of MW and group mass halos.

The cold gas content of galaxies themselves (both neutral HI and molecular H2) has also been favorably compared against data in several regimes, although simplifying assumptions are needed to derive these cold-phase fractions which are not self-consistently followed in typical galaxy-scale simulations. Nelson et al. (2020) also demonstrated that group mass haloes hosting massive galaxies are filled with a hot, virialized plasma at $\sim 10^7$ K, and that they contain a large abundance of cold gas with a characteristic temperature of $\sim 10^4$ K. This cold phase of the ICM takes the form of thousands of small, $\sim$ kpc-sized clouds, which fill the inner halo out to hundreds of kpc (similar to predictions by Maller and Bullock 2004 for MW-mass halos).

There are, however, several important caveats when studying the formation of star-forming clouds in the ICM, mostly connected with limitations of numerical techniques. Approaches such as SPH have been shown to be unable to track the evolution of instabilities, such as the Kelvin-Helmholtz instability, leading to the formation of more dense clouds that are artificially long-lived compared to similar numerical experiments run with grid-base techniques (Agertz et al. 2009; Torrey et al. 2012).

The lack of, or inadequate treatment of other important physics, such as heat conduction, magnetic fields or metal diffusion might also complicate the interpretation of results from simulations (see the discussion in Puchwein et al. 2010). It is clear that, for any numerical technique chosen, high resolution becomes key to study in-situ star formation in low-mass clouds embedded in the hot ICM of clusters, especially considering the low masses of these clouds.

In this context, we present here a study of the in-situ formation of stars and their contribution to the ICL using the three most massive groups/clusters in the TNG50 simulations (Pillepich et al. 2019; Nelson et al. 2019a), one of the highest-resolution cosmological simulations of low-mass clusters with virial mass $\sim 10^{14}$ $M_\odot$ at $z = 0$.

This article is organized as follows: in Section 3.3, we provide a comprehensive overview of the simulation employed, including some definitions crucial for the subsequent sections. Section 3.4 presents our findings, together with an in-depth discussion. Finally, Section 3.5 summarizes the key conclusions drawn from this study.

3.3 Simulation

We use the cosmological hydrodynamical simulation IllustrisTNG (Pillepich et al. 2018a; Springel et al. 2018; Marinacci et al. 2018; Naiman et al. 2018; Nelson et al. 2018, 2019b). The IllustrisTNG project[2] is a suite of state-of-the-art cosmological galaxy formation simulations that come in different physical sizes and mass resolutions. In this work we use the highest resolution baryonic run TNG50-1 (TNG50 for short) (Pillepich et al. 2019; Nelson et al. 2019a), which has a volume of approximately $50^3\,\mathrm{Mpc}^3$. It has 2×2160^3 resolution elements, and the baryon and dark matter particle masses are $8.5 \times 10^4 M_\odot$ and $4.5 \times 10^5 M_\odot$, respectively. The IllustrisTNG cosmological parameters are consistent with ΛCDM model determined by Planck XIII (Collaboration et al. 2016b) to be $\Omega_m = 0.3089$, $\Omega_b = 0.0486$, $\Omega_\Lambda = 0.6911$, $H_0 = 100\,h\mathrm{kms}^{-1}\mathrm{Mpc}^{-1}$ with $h = 0.6774$, $\sigma_8 = 0.8159$, and $n_s = 0.9667$.

[2] https://www.tng-project.org

Gravity and baryons are followed using the Arepo moving mesh code (Springel 2010). The baryonic treatment is based on the code used for its predecessor simulation suite, Illustris (Vogelsberger et al. 2013, 2014b,a; Genel et al. 2014; Nelson et al. 2015), with modifications implemented to better track the formation and evolution of galaxies (as described in Pillepich et al. 2018b; Weinberger et al. 2017).

The updated IllustrisTNG sub-grid models account for star formation, radiative metal cooling, chemical enrichment from SNII, SNIa, and AGB stars, stellar feedback, and super-massive black hole feedback (Weinberger et al. 2017; Pillepich et al. 2018b). The star formation in the Interstellar Medium (ISM) is treated in a sub-resolution fashion following a variation of the Springel and Hernquist (2003) with the adoption of a Chabrier (2003) initial mass function, and model the star-forming dense ISM gas using an effective equation of state where stars form stochastically above a gas density of $\rho_{\rm sfr} = 0.13\ cm^{-3}$ with a star formation time-scale of $t_{\rm sfr} = 2.2$ Gyr (refer to Vogelsberger et al. 2013 for detailed explanations). These models were calibrated to reproduce a set of observational constraints that include the observed $z = 0$ galaxy stellar mass - size (Genel et al. 2018), the color bimodality (Nelson et al. 2018), galaxy clustering (Springel et al. 2018) and stellar mass function (Pillepich et al. 2018b).

Galaxies in the simulations are identified using `SUBFIND` (Springel et al. 2001; Dolag et al. 2009) on Friends-of-Friends (FoF) groups (Davis et al. 1985) identified with a linking length set to 0.2 times the mean interparticle separation. The object at the center of the gravitational potential of each group is called the "central" galaxy, while all other substructures are "satellites". The time evolution of galaxies and halos through

Table 3.1: Quantities related to the 3 most massive groups.

		Group 0	Group 1	Group 2
M_{200}	$[M_\odot]$	1.8×10^{14}	9.4×10^{13}	6.5×10^{13}
R_{200}	[kpc]	1198.91	959.61	846.68
M^*_{BCG}	$[M_\odot]$	3.6×10^{12}	9.7×10^{11}	1.1×10^{12}
r_{h_*}	[kpc]	43.25	11.75	18.79
M^*_{ICL}	$[M_\odot]$	1.8×10^{12}	5.8×10^{11}	5.9×10^{11}
$M^{*,in-situ}_{ICL}$	$[M_\odot]$	1.4×10^{11}	1.6×10^{11}	1.3×10^{11}
f_{ICL}		0.48	0.60	0.56
$F^{in-situ}_{ICL}$		0.08	0.28	0.23

the 99 snapshots of the simulation is followed using the SubLink merger tree algorithm (Rodriguez-Gomez et al. 2015).

3.3.1 Defining ICL and cleaning method

We focus the analysis on the 3 most massive systems included in the TNG50 box, which fulfill $M_{200}/M_\odot > 5 \times 10^{13}$, comparable to nearby systems such as the Fornax and the Virgo clusters. Virial masses for these systems are listed in table 3.1, where virial quantities are defined at the virial radius r_{200}, corresponding to the distance at which the enclosed density is 200 times the critical value.

To define the particles that are considered part of the ICL we proceed as follows. For each of our groups, we remove all stars that `SUBFIND` considers bound to surviving satellite galaxies. The left panel of Fig. 3.1 shows an illustration of this component for

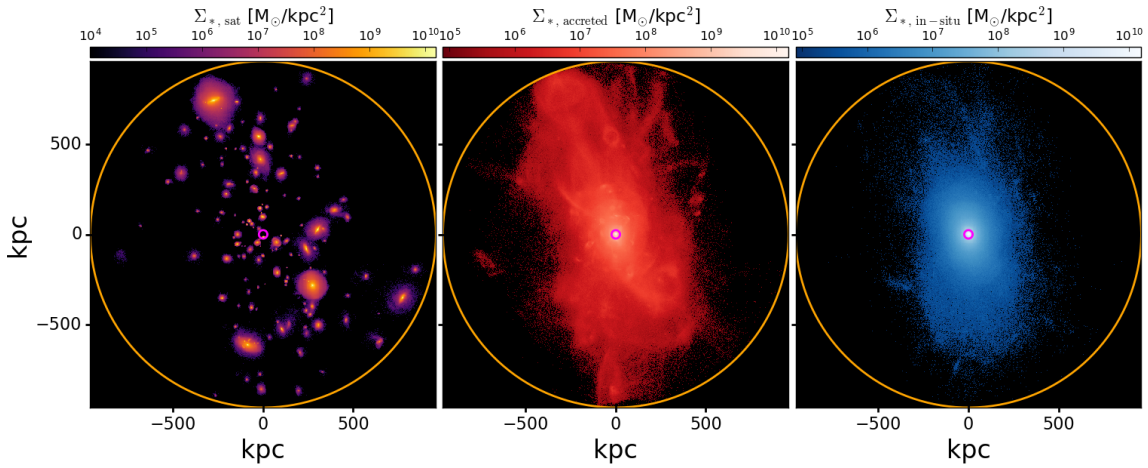

Figure 3.1: Projected density maps for different stellar components in Group 1 at $z = 0$: bound satellites (left), accreted ICL (middle), and in-situ formed ICL (right). The magenta and orange circles indicate twice the stellar half-mass radius of the stars in the central host galaxy ($2\,\mathrm{r_{h_*}}$) and the virial radius ($\mathrm{r_{200}}$), respectively. These are the bounds used to define the ICL component in our study.

our Group 1. Furthermore, to avoid possible contamination by stars in the outskirts of the surviving satellites that are wrongly assigned to the host halo by `SUBFIND`, we further apply a "cleaning" of our ICL: we remove any stellar particle within $4\,\mathrm{r_{h_*}}$ of the center of any subhalo with $M_* > 10^8 \mathrm{M}_\odot$, where $\mathrm{r_{h_*}}$ refers to the stellar half mass radius of the subhalo. This ensures that any stars from satellites and their surrounding stellar halo are not considered part of the ICL.

This leaves us with a sample consisting of all the remaining stellar particles in the FoF group that are beyond $2\,\mathrm{r_{h_*}}$ of the central galaxy and within the virial radius r_{200} of the host cluster, which we call ICL. Stars in the ICL are further divided into those born "in-situ" and those "accreted". Following Rodriguez-Gomez et al. (2016), our algorithm checks if the star is bound to the main progenitor of the central galaxy at the time of birth (or the closest snapshot to it), in which case it is labeled as in-situ, or it is otherwise associated by

SUBFIND to a different substructure in the SubLink merger tree, in which case it is labeled as accreted. The catalogs for in-situ/accreted are provided within the IllustrisTNG database. As an illustration, the middle and right panels of Fig. 3.1 show the accreted and in-situ components of the ICL in Group 1, respectively.

To quantify the mass within the ICL and, specifically, the in-situ stellar component, we introduce the fractions $f_{\rm ICL}$ and $F_{\rm ICL}^{\rm in-situ}$. Various definitions of these fractions exist in the literature, and for the purpose of our study, we adopt the following definitions:

$$f_{\rm ICL} = \frac{M^*_{\rm ICL}}{M^*_{\rm BCG}}, \tag{3.1}$$

and

$$F_{\rm ICL}^{\rm in-situ} = \frac{M^{*,\rm in-situ}_{\rm ICL}}{M^*_{\rm ICL}}, \tag{3.2}$$

where $M^*_{\rm ICL}$ refers to the mass of the stellar component in the ICL, $M^{*,\rm in-situ}_{\rm ICL}$ represents the mass of the in-situ stellar component in the ICL, and $M^*_{\rm BCG}$ is the stellar mass within $2\,{\rm r_{h_*}}$ of the central galaxy. The values for these quantities in the three most massive systems in TNG50 are presented in table 3.1.

3.3.2 H_α predictions

In order to compare results with the recent observations of the ICL in nearby clusters (i.e. Virgo), we use the calibration of Kennicutt and Evans (2012) to convert the star formation rates to H_α luminosities. These calibrations are based on evolutionary population synthesis models, in which the emergent spectral energy distributions (SEDs) are derived for synthetic stellar populations with a prescribed age mix, chemical composition,

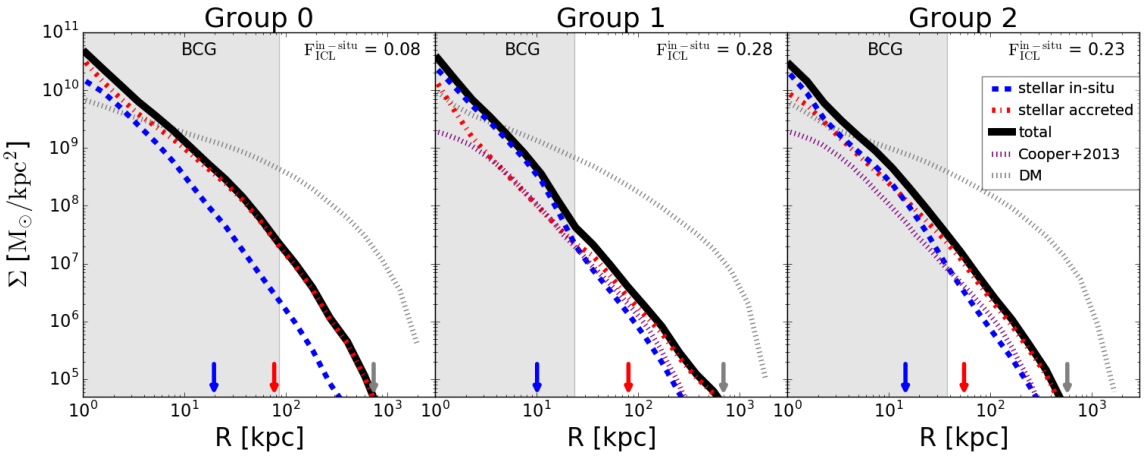

Figure 3.2: Projected density profiles of distinct components within the three most massive groups in TNG50 (including the BCG and ICL region and excluding satellites). The solid black curves represent the total stellar component, while the red curves depict the ex-situ (merged) stellar component, and the blue curves illustrate the in-situ stellar component. Dotted black lines trace the dark matter component, and purple dotted lines represent the median stellar mass surface density profiles from Cooper et al. (2013). The shaded area delineates the region associated with the BCG, defined within $2\,r_{h_*}$ for the central of each group. Arrows in matching colors indicate twice the half-mass radius of each component

and Kroupa (2001) initial mass function (IMF). The resulting relation is

$$\log L_{\rm x} = \log(\dot{M}_*/{\rm M}_\odot\,{\rm yr}^{-1}) + \log C_{\rm x}, \tag{3.3}$$

where $L_{\rm x}$ denotes the H_α luminosity in units of erg s^{-1}, $\dot{M}_*$ represents the star formation rate in units of ${\rm M}_\odot\,{\rm yr}^{-1}$, and $C_{\rm x}$ is the logarithmic SFR calibration constant which we set to be 41.27 (Kennicutt and Evans 2012; Murphy et al. 2011; Hao et al. 2011).

3.4 Results

We begin by characterizing the mass distribution within our groups. Fig. 3.2 illustrates the projected radial distribution of stars (solid thick black line), and dark matter (black dotted line) after projecting each group along the x axis. The stellar component is

predicted to fall off more steeply than the dark matter component. For comparison, the purple dotted line represents the stellar mass surface density profiles from Cooper et al. (2013), averaged for halos with $10^{13.5} < M_{200}/\mathrm{M}_{\odot} < 10^{14}$. These results align closely with our stellar profiles (solid black lines) within the ICL region for the two less massive clusters (as shown in the right and middle panels). However, in the case of our most massive cluster, having a halo mass twice that of the most massive halo in their sample, differences with the predictions in Cooper et al. (2013) are expected (as a result the dashed purple line is removed from this panel). Note that the tagging method in Cooper et al. (2013) does not properly account for the in-situ star formation in the BCG, therefore giving a flatter slope in the inner regions. We further divide the stars according to their origin: in-situ (represented by the thin blue dot-dashed curve) and accreted (depicted by the thin red long-dashed curve). The relatively substantial contribution of the in-situ population to the ICL at hundreds of kpc is intriguing. In our systems, in-situ born stars contribute between 8% and 28% of the stellar mass in the ICL (refer to the top right corner of each panel for the specific percentage of each group).

An inspection of the birth place of the in-situ labelled stars in the ICL shows that the majority of them are formed already at large distances from the BCG (although not associated with substructures) and are not stars from the central galaxy kicked-off by mergers, a common formation path for in-situ stars in the diffuse stellar halos of MW-like galaxies, and as is the case for our most massive cluster (which experienced a recent major merger in its formation history). However, for the remaining groups in our sample, over 60% of the in-situ ICL is formed at $r > 40$ kpc or $r > 2\,\mathrm{r}_{\mathrm{h}_*}$ (where distance is in physical

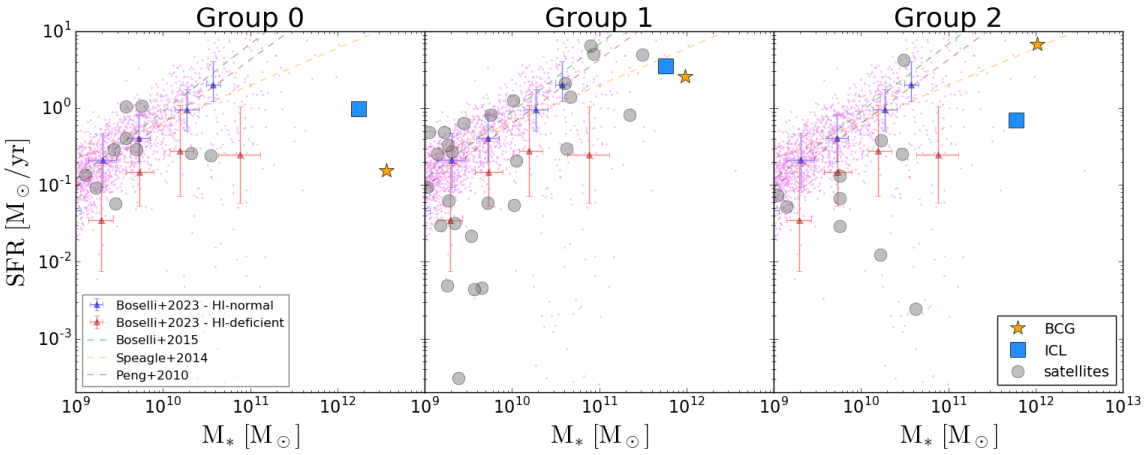

Figure 3.3: Star formation rate (SFR) plotted against stellar mass for various components within each group. Results for the BCGs are represented by orange stars, those for the ICL component by blue squares, and those for satellites within the ICL region by grey circles. Violet points illustrate the SFR distribution for central galaxies in TNG50 within the mass range limit. For comparison the main sequence relation for the galaxies in Virgo cluster from Boselli et al. (2023) are shown by blue and red markers, the extrapolated relations for late-type nearby galaxies are shown by green dashed line (Boselli et al. 2015), the relation for a large sample of SDSS galaxies are shown by brown dashed line (Peng et al. 2010), and work by Speagle et al. (2014) is presented in orange dashed line.

kpc and is measured with respect to the BCG or its main progenitor at the time of birth of the star). This suggests that gas in the ICM must somehow become available for star formation beyond the inner regions dominated by the BCG. This star formation mode is thus happening in unconventionally diffuse conditions, very different from the star formation resulting from the dense interstellar medium of galaxies.

We calculate the total SFR of ICM gas at $z = 0$ for our groups and compare this to the level of star formation ongoing in the central BCG as well as in other galaxies. Fig. 3.3 highlights that, taken as a unit, the ICL (integrated within the virial radius) is forming stars at rates comparable to that of the BCG and other massive galaxies. For this comparison, we assign a stellar mass to the ICL equal to the sum of all in-situ and accreted

stellar particles that lie beyond $2\,r_{h_*}$ and up to the virial radius and that are not associated to any satellite or identified substructure by `SUBFIND`. Similarly, we compute its SFR by summing the star formation rates of all gas cells that are not gravitationally bound to any substructure within the same region. Fig. 3.3 shows that while the ICL lies systematically below the extrapolation of the "main sequence" defined by lower-mass star forming galaxies (magenta points show central galaxies within the TNG50 box), its SFR is comparable to many of the massive satellite galaxies in the group (gray circles) and above the SFR of the central BCG in the case ofGroup 0 and Group 1 (left and middle panels). For comparison, we present the extrapolated "main-sequence" relation derived from the galaxies in the Virgo cluster (see Boselli et al. 2023), for a sample with normal HI gas content (HI-normal) and deficient HI gas content (HI-deficient); the mean values and standard deviations for HI-normal and HI-deficient objects are shown by blue and red markers. We are also presenting results from late-type nearby galaxies in the Herschel Reference Survey by Boselli et al. 2015 (dashed green line), a large statistical sample of SDSS galaxies from Peng et al. 2010 (dashed brown line), and the extrapolated time-dependent main-sequence relation derived by Speagle et al. 2014 (dashed orange line). One should also keep in mind that the fraction of quenched galaxies produced by the TNG model might overestimate the star formation in massive galaxies (e.g., see Fig. 8 in Donnari et al. 2021).

The ongoing star formation in the ICM shows a decreasing trend with distance from the center of the cluster. Fig. 3.4 presents the surface density of star formation rate ($\Sigma_{\rm SFR}$), computed by projecting our groups along the x-axis and integrating star formation within square bins of 2 kpc on each side. Different colors represent different groups,

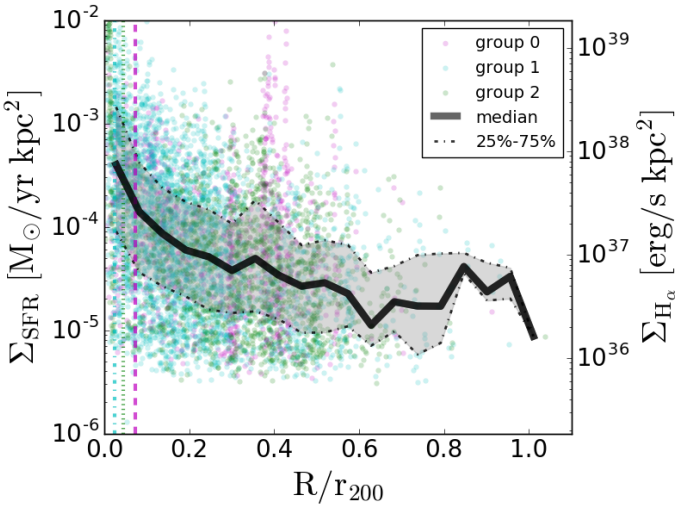

Figure 3.4: Star formation rate surface density profiles for the three most massive groups in TNG50. Different colored points represent different groups, with individual points of the same color illustrating the scatter between various regions at a given clustercentric distance for each group (star formation is measured within square bins of 2×2 [kpc $\times$ kpc] when projecting each group along the x-axis). Vertical lines, color-matched to each group, indicate $2\,\mathrm{r_{h_*}}/\mathrm{r_{200}}$. The black solid line represents the median trend, and the grey shaded region corresponds to the 25-75 percentile dispersion of $\Sigma_{\rm SFR}$ as a function of clustercentric distance for all groups (the median and dispersion are only calculated from regions that have non-zero star formation).

while individual points of the same color depict the scatter between various regions within a given group. Bins with no star formation at all are not shown and not considered for calculating the median and the corresponding dispersion. The thick solid curve corresponds to the median trend (considering all groups collectively) of $\Sigma_{\rm SFR}$ as a function of clustercentric distance, highlighting that the inner regions of the ICM exhibit more prominent star formation compared to the outskirts.

To ease comparison with observations, we convert $\Sigma_{\rm SFR}$ into a surface density of H_α luminosity (right vertical axis) as explained in detail in Sec. 3.3.2 and following Kennicutt and Evans (2012). Typical values in the ICM of our sample span $\Sigma_{\rm H_\alpha} \sim 10^{38} - 10^{36}$ ergs s^{-1} kpc^{-2} with considerable scatter. These values are lower than the average measured $\Sigma_{\rm H_\alpha} \sim 10^{40}$ ergs s^{-1} kpc^{-2} in central regions of disk galaxies, but comparable to the values in the outskirts of MW- and LMC-like objects (Tacchella et al. 2022; Bundy et al. 2015). Beyond clustercentric distances $R > 0.8\,{\rm r_{200}}$ diffuse star formation is rare in all our systems.

Projected maps of our halos in Fig. 3.5 show in more detail where the star formation in the intracluster space is happening. Panels on the first row show the star-forming gas in the region $2\,{\rm r_{h_*}} < {\rm r} < {\rm r_{200}}$ (bounds shown with magenta and orange circles) color coded by SFR (color map on the right). Star formation at $z = 0$ is widespread in these systems and follows filament-like patterns. We highlight that special care was taken to remove any material gravitationally associated with surviving satellites, as described in Sec. 3.3.1, and this star formation is occurring in gas seemingly associated to the central host halo and not to bound substructures. In fact, further inspection of each system revealed that the

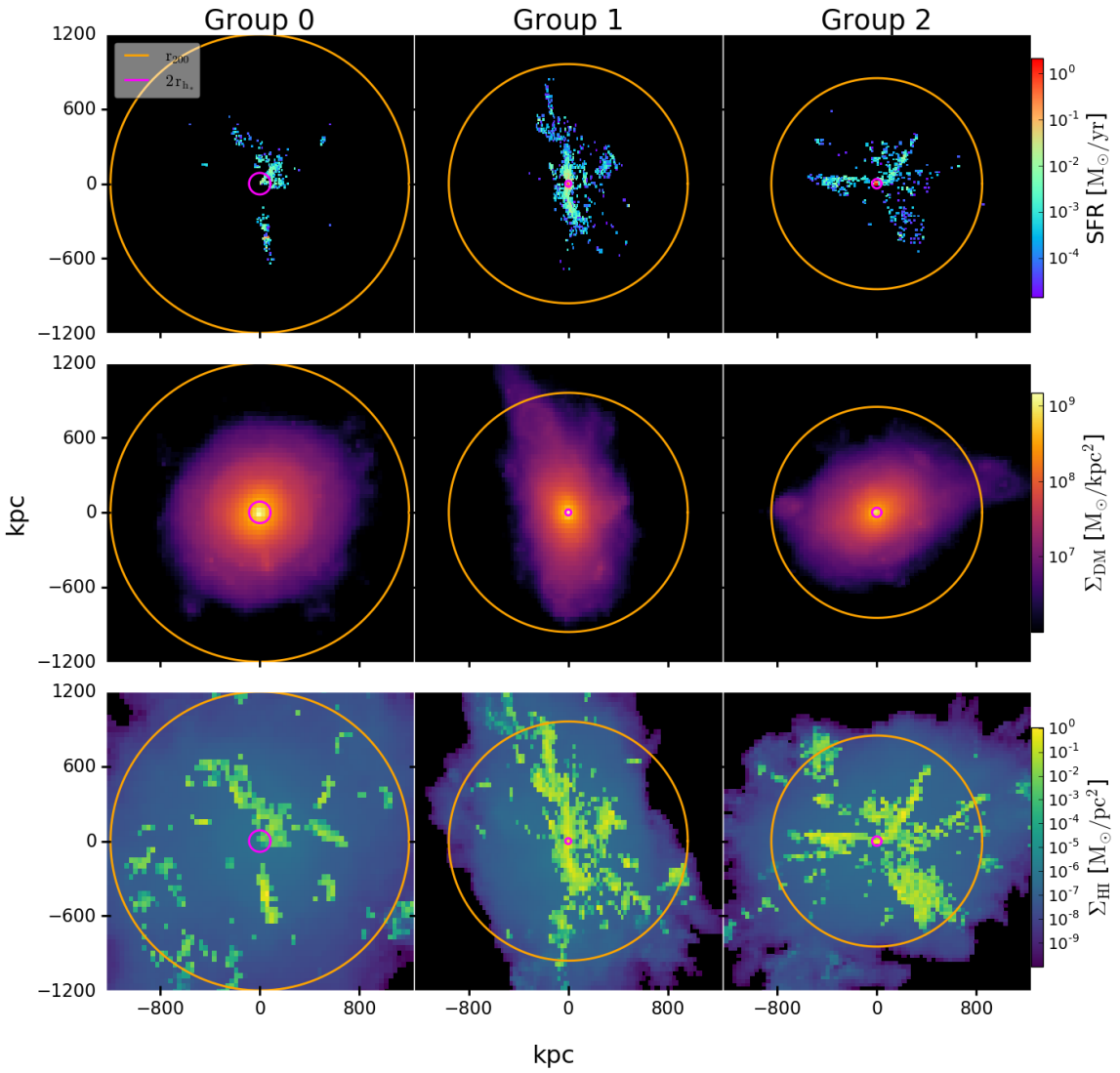

Figure 3.5: Projected maps of star-forming gas, the dark matter component and HI gas in the three most massive groups in TNG50, presented in columns from left to right for groups 0, 1 and 2. Rows from top to bottom show: SFR, dark matter surface density, and HI gas surface density. The colorbar on the right side of each row indicates the respective quantities displayed. The ICL is highlighted by bounds marked with magenta and orange circles, representing $2\,r_{h_*} < r < r_{200}$. These results underscore the widespread nature of star formation, organized in filamentary structures within the halo of our targeted groups.

filamentary nature of the star-forming gas follows the distribution of neutral gas in the main host halo (bottom row), and looks loosely linked to the dark matter distribution (middle row) for at least 2 of the systems (groups 1 and 2).

To gain further insight, we zoom into smaller regions of group 1 in Fig. 3.6. The yellow points show the distribution of the stellar particles in each box and reveal the presence of several galaxies, some with associated stellar streams—most prominently observable in the two innermost regions (red and green panels). The presence of the ICL is apparent in panels as a diffuse yellow stellar background on the end closer to the central region of cluster. We highlight the presence of star forming gas colored in magenta by their estimated H_α flux (refer to the color bar on the side of the main panel). For the zoomed-in panels, the color maps are calculated in $\sim 0.24 \times 0.24$ kpc bins to align with the 3 arcsec spatial resolution of the VESTIGE survey of the Virgo cluster (Boselli et al. 2018b), while the main panel is smoothed to 1 arcmin.

The zoomed-in regions in Fig. 3.6 show that the majority of the star forming gas is mostly unrelated to the distribution of stars or galaxies. Star forming regions are also not obviously associated to ram-pressure tails from gas-rich galaxies note that this is different from what has been observed in cases such as Smith et al. (2010); Mihos et al. (2017); Boselli et al. (2018b); Gullieuszik et al. (2020), where the association of the star-forming region to tails of ram-pressure stripped galaxies is clear upon visual inspection. Instead, stars seem to be forming in cloudlet-like objects with tens-of-pc typical size, which condensate along filamentary structures in the ICM.

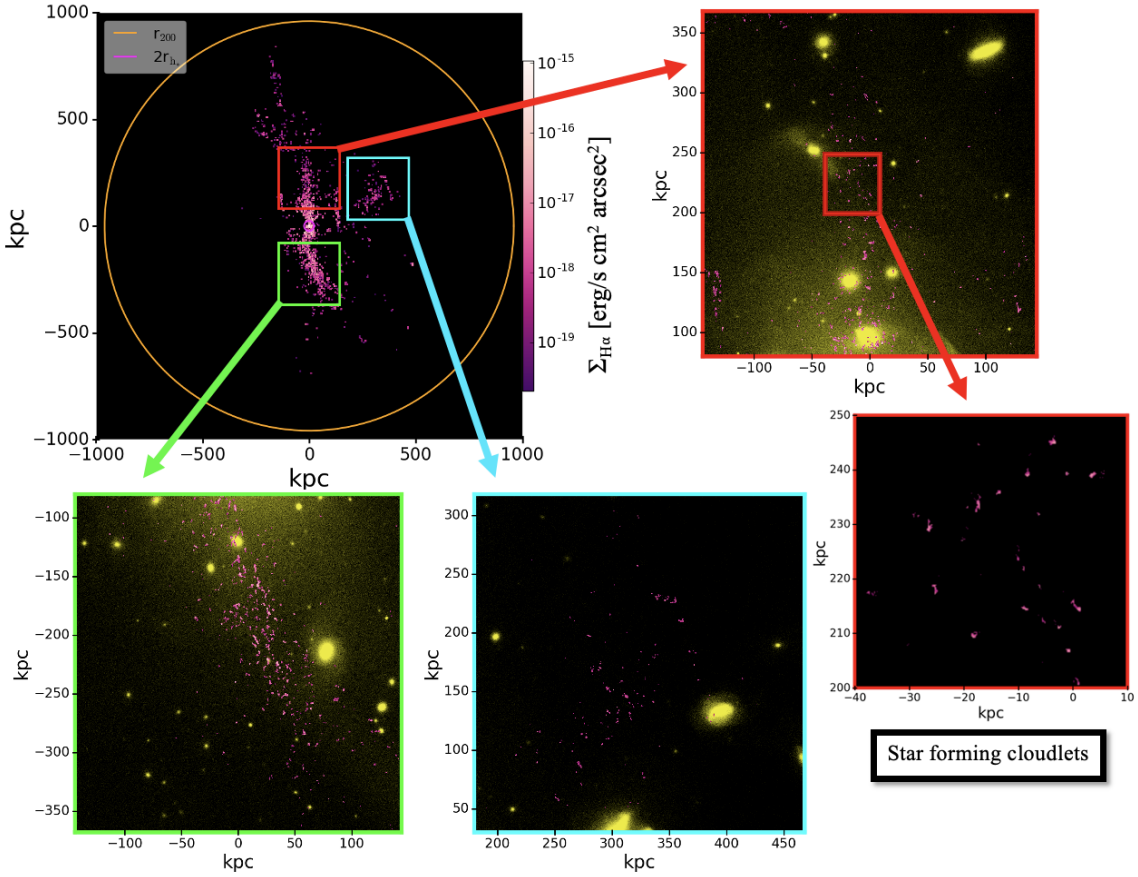

Figure 3.6: Main Panel: x–y projection of star-forming gas in Group 1, color-coded by the flux of H_α and smoothed to 1 arcmin, revealing the filamentary structure of the star-forming gas. Magenta and orange circles represent regions at $2\,r_{h_*}$ and r_{200}. Zoomed-in Panels: H_α flux of star-forming gas (smoothed to 3 arcsec), with yellow points representing stellar particles. These findings suggest that star-forming regions are not necessarily linked to ram-pressure tails from gas-rich galaxies. Instead, stars appear to be forming within cloudlet-like structures, condensing along filamentary structures within the ICM.

This is not the first time that small-scale cold clouds in the ICM have been reported in TNG50. In a detailed analysis of the ICM in $z = 0.5$ halos, Nelson et al. (2020) highlighted this fundamental prediction from the TNG model in combination with the high resolution achieved by TNG50. These small-scale cold clouds seem consistent with being seeded by local inhomogeneities in gas density that later grow due to increased cooling. While the role of magnetic fields in forming these clouds is not clear, the magnetic pressure in these clouds is large and exceeds the thermal pressure, providing support and making these features long-lived, on the scale of several Gyrs. Interestingly, the results in this work show that some of these cold clouds manage to become star-forming and contribute a non-negligible fraction of the stars to the diffuse ICL component.

In agreement with the findings of Nelson et al. (2020), the metallicity of in-situ born ICL stars (with $r_{\rm born} > 2\,{\rm r_{h_*}}$) is relatively high, registering a median value of $[Fe/H] \sim -0.77$ with a substantial scatter of approximately 0.39 dex, comparable to the accreted ICL, the metallicity of dwarf galaxies with $M_* \sim 10^8 {\rm M}_\odot$, and the outskirts of more luminous, MW-like galaxies. This suggests that the gas seeding these density perturbations has galaxy-like abundances and it likely comprises gas that has, a long time ago, been stripped from infalling galaxies. Obvious associations to those satellites do not seem to persist until $z = 0$ in our simulations, suggesting that the timescales for the clouds to form and become star-forming are comparable to the orbital times of the satellites. The similarity between the metallicities for the in-situ and accreted components complicates the chances of observationally distinguishing these two populations.

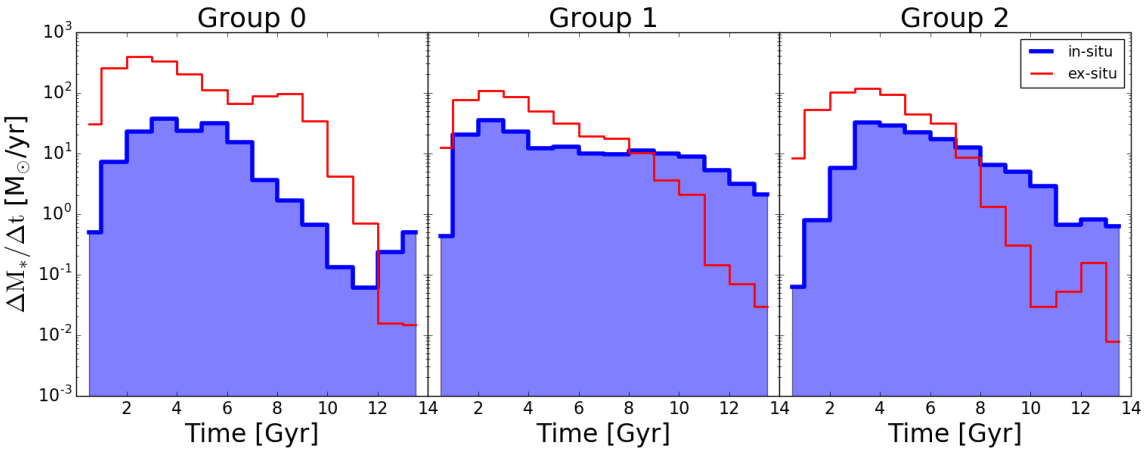

Figure 3.7: Average stellar mass formation rate for the in-situ (blue shaded histogram) and merged (red histogram) components of the ICL. The in-situ intra-cluster star formation is a continuous phenomenon over time, with an average peak intensity around $z \sim 2-3$ (cosmic times $2-4$ Gyr).

The physical conditions for the star-forming clouds seem comparable to those of normal star-forming regions in the ISM of galaxies. The median density of the star-forming cells flagged as part of the ICM is ~ 0.2 cm^{-3}, which is just above the density threshold for star formation in the TNG baryonic treatment $n \approx 0.1$ cm^{-3} Please see Appendix E for a more detailed comparison of density and temperature for star-forming cells in the ICL compared to those in satellite galaxies). Interestingly, the fraction of stellar mass born in-situ in the ICM seems only weakly dependent on numerical resolution, as some of the clusters selected in TNG100 show similar levels of star formation rate in the ICM (see Appendix F). The presence of these in-situ born stars in the ICL is therefore a fundamental consequence (or prediction) of the model in several resolution levels.

It is also important to note that at the current integrated star formation rates shown in the intra-cluster region of our simulated clusters, SFR ~ 1 M$_\odot$/yr (see Fig. 3.3), it would take ~ 100 Gyr to form the total mass of the in-situ ICL stars listed in Table 3.1. This

diffuse mode of star formation must therefore have also been present at earlier times, and with higher intensity. We confirm this by showing the distribution of stellar mass formed in-situ in a given time-bin in Fig. 3.7. This is calculated by adding all the stellar mass of the in situ-labeled stars in the ICL with a given age divided by the size of the time-bin to provide an average star formation rate. The blue shaded histograms indicate that the in-situ intra-cluster star-formation is a rather continuous phenomenon over time and was, on average, stronger around $z \sim$ 2-3 (i.e., cosmic times 2-4 Gyr). As an illustration, we show in Fig. 3.8 the predicted SFR maps for our highest mass group at three different redshifts: $z = 3.7,\ 2.3$ and 0.9. In all cases, extended star forming areas appear out to almost the virial radius of the cluster progenitor.

Have these star-forming regions been detected in observations? In the nearby universe, ongoing star formation in the tails of ram-pressured stripped galaxies has been observed in the past, for example in the Virgo cluster (Mihos et al. 2017; Boselli et al. 2018b). However, the predictions from TNG50 are different in nature from these observations, since the star-forming cloudlets are currently not associated with any satellite. In that sense, they are closer to a recently identified class of young, isolated, and star-forming clouds in Virgo, see Jones et al. (2024); Beccari et al. (2017). We cannot rule out that this gas originated as ram-pressure tails stripped from galaxies in the distant past, where any possible correlation with the galaxy distribution has been long erased. However, if that is the case, the timescale for turning this gas into stars seems too long compared to observations of ram-pressure tails which can still be traced back to their original galaxy. Therefore we consider this a different process than what is observed in ram-pressure tails.

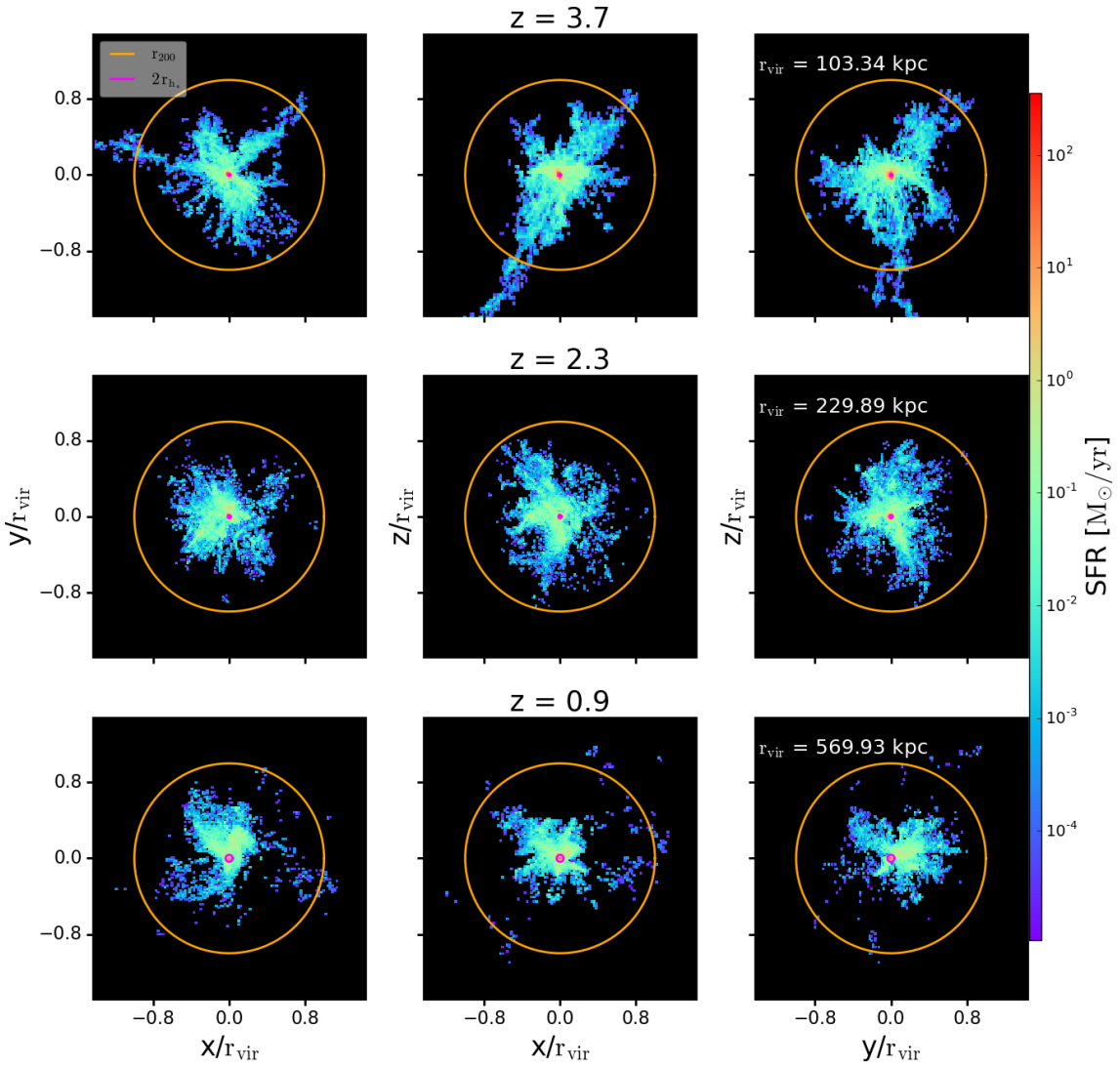

Figure 3.8: Projected maps of star-forming gas at different redshifts for Group 0, arranged in columns from left to right: x-y, x-z, and y-z projections. The projections are normalized by the virial radius of the cluster at each redshift, with the specific value provided in the top left corner of the last panel in each row. Rows from top to bottom correspond to redshifts $z = 3.7$, 2.3, 0.9. The colorbar on the right side indicates the star formation rate (SFR) in each region. The ICL is highlighted by bounds represented by magenta and orange circles, signifying $2\,r_{h*} < r < \mathrm{r}_{200}$. These results emphasize the presence of a diffuse mode of star formation within the ICL of our targeted groups, even at earlier redshifts.

The color coding of the gas in Fig. 3.6 indicates that, at $z = 0$, the expected H_α surface brightness for the intra-cluster gas is rather modest, $\Sigma_{H_\alpha} \sim 1.6 \times 10^{-19}$–$2.6 \times 10^{-18}$ erg s^{-1} cm^{-2} arcsec^{-2}, which could partially explain why this phenomena has so far escaped detection[3]. For comparison, the most extended and deepest surveys available, such as VESTIGE, have a sensitivity $\Sigma_{H_\alpha} \sim 2 \times 10^{-18}$ erg s^{-1} cm^{-2} arcsec^{-2} at 3 arcsec angular resolution (Boselli et al. 2018b)[4]. On the other hand, there are claims of detection of runaway cooling of the hot gas in high-z clusters leading to star formation events with SFR $\sim$ 900 $M_\odot$/yr offset from the main host galaxy by $\sim$ 25 kpc for the coolest gas and $\sim$ 50 kpc for the X-ray peak (Hlavacek-Larrondo et al. 2020) that might be comparable to some of the in-situ formed stars in our simulations.

Finally, we must also consider the possibility that these in-situ formed ICL stars are a numerical effect born out of specific choices made for the baryonic treatment in the simulation. While the multi-phase nature of the gas in the outskirts of groups and clusters have been reported before by several simulation groups (Nelson et al. 2018; Butsky et al. 2019; Oppenheimer et al. 2021), whether warm/cold gas cells in the ICM can turn star-

[3]These quoted values for H_α brightness are derived from Fig. 3.6, where we binned the star-forming gas at similar spatial resolution as VESTIGE (3 arcsec) and measured the H_α flux within each 'pixel". If we analyze the results and compute the median and dispersion, we obtain a median value of 6.8×10^{-19}erg s^{-1} cm^{-2} arcsec^{-2} and a dispersion ranging from 1.6×10^{-19}–2.6×10^{-18} erg s^{-1} cm^{-2} arcsec^{-2}.

[4]The stacking of pixels to increase image sensitivity of the images should be limited to reasonable scales. The 3 arcsec scale (0.24 kpc at the distance of the Virgo cluster) mentioned in the VESTIGE paper is optimized for detecting structures associated with the tails of stripped gas in galaxies. While stacking pixels on 100 kpc scales could theoretically increase sensitivity as $\sqrt{(}N)$ (where N is the number of pixels), this assumes a perfectly flat background, which is rarely the case. Issues such as large-scale structures from flat fielding imperfections and correlated noise due to bright stars and unwanted gradients from non-uniform illumination can affect the results (see Fig. 4 of Boselli et al. (2018b), VESTIGE paper I). Moreover, narrow-band filters centered on the rest-frame H_α line are also sensitive to H_α emission from Galactic cirrus. Hence the contribution of the Galactic cirrus in the direction of the Virgo cluster can complicate measurements (see Fig. 16 of the same VESTIGE I paper). While IFU spectroscopy could help confirm these features, technical limitations exist. For instance, MUSE/VLT can achieve $\Sigma_{H_\alpha} \sim 10^{-18}$ erg s^{-1} cm^{-2} arcsec^{-2} on $\sim$1 arcsec scales in $\sim$1h integration, but its 1 arcmin FoV is insufficient for mapping large areas like the Virgo cluster ($\sim$100 sq.deg), necessitating pre-selection of observation targets.

forming is less robustly predicted by numerical codes. The fact that most star-forming clouds sit near the density threshold for star formation suggests that increasing the value of that parameter might significantly lower the occurrence of stars born in the in-situ ICL component, but more rigorous tests must be performed to quantify this effect. More detailed baryonic prescriptions that explicitly resolve the multiphase structure of the gas in the ISM of galaxies advocate for larger density thresholds for star formation, $n \sim 1$ - 100 cm^{-3}, more in line with the typical densities of molecular clouds with active star formation (refs). Our study points out that baryonic treatments that are able to successfully reproduce many of the properties of galaxy populations, might not be as well attuned to perform well in environments where the typical conditions of the gas differs from that in the ISM of galaxies, for example in the ICM. As shown in Fig. 3.8, the potential limitations of these treatments might worsen at intermediate to high-redshifts, where the associated higher densities translate into larger amounts of gas cells being eligible to become star-forming in prescriptions based on a low density threshold for star formation. As more data become available for low- and high-z groups and clusters, their imaging in wavelengths where young stars are mapped might help understand the applicability of such star formation recipes to these environments.

3.5 Conclusions

We use the cosmological hydrodynamical simulation TNG50 to study the formation of in-situ ICL in Virgo-like systems. We select the 3 most massive clusters in the box with virial masses $M_{200} = 6.5 \times 10^{13}M_\odot$- 1.8×10^{14}M$_\odot$. We find that a significant fraction, $\sim 8\%$-

28% of the present-day mass in the ICL, was formed in-situ. When analyzed in detail, and contrary to what is commonly believed, the majority of these in-situ stars are born directly into the diffuse light component at hundreds of kiloparsecs from the main host and directly from the ICM gas, rather than brought in and dispersed during merger events. This diffuse star-formation proceeds in cloudlets that condense along filamentary-like structures that are aligned with the neutral gas and dark matter distributions and are not clearly associated with ram-pressure stripping of gas in infalling galaxies.

At $z = 0$ the expected H_α surface brightness due to this diffuse mode of star formation reaches $\sim 6.8 \times 10^{-19}$ erg s^{-1} cm^{-2} arcsec^{-2}, just below the detection limits of the ongoing surveys in Virgo when smoothed on scales of 3 arcsec. In the simulated clusters, star formation maps at higher redshift suggest that extended star formation is present throughout the history of the cluster, making it an interesting target for discovery with facilities such as JWST.

One interesting application of our results is that orphan core-collapse supernova events would be expected to occur in relative isolation in the ICL. While such events have not yet been reported, with a predicted average SFR of ~ 1 M$_\odot$/yr, we expect only ~ 1 SN per ~ 200 yr in a Virgo-like system[5], suggesting that a concurrent survey of hundreds of clusters might be needed for detecting such rare events.

If ongoing star formation in the intra-cluster region of observed clusters is really lacking, then this would signal shortcomings in the treatment of star formation in simula-

[5]We have assumed a power-law mass function following Salpeter (1955), for the mass range of 0.1–20 M$_\odot$ with stars more massive than 8 M$_\odot$exploding as SN, which results in $\sim 7.2\%$ of the total stellar mass formed able to generate a SN event. Assuming a mean SN mass 12 M$_\odot$, we anticipate the occurrence of 1 SN in 167 (~ 200) years.

tions like TNG50, especially in low-density regions. The formation of stars in these extended and diffuse structures is possible because of the condensation of denser clouds embedded in the more diffuse ICM, as reported by Nelson et al. (2020). Numerical techniques such as that used in Arepo have been shown to lead to less artificial formation of clouds compared to other techniques such as SPH (Agertz et al. 2009; Torrey et al. 2012), but it is possible that other numerical effects are still at play. We emphasize that further studies of the effect of the star formation threshold in models such as those of TNG would be desirable to determine their role in the formation of stars in such unexpected conditions.

Chapter 4

A comprehensive model for the formation and evolution of the faintest Milky Way dwarf satellites[1]

4.1 Abstract

We modify the semi-analytic model Galacticus in order to accurately reproduce the observed properties of dwarf galaxies in the Milky Way. We find that reproducing observational determinations of the halo occupation fraction and mass-metallicity relation

[1]This chapter contains a draft of an article that has been accepted for publication in March 2024 by Oxford University Press in Monthly Notices of the Royal Astronomical Society written by Niusha Ahvazi, Andrew Benson, Laura V. Sales, Ethan O. Nadler, Sachi Weerasooriya, Xiaolong Du, and Mia Sauda Bovill

for dwarf galaxies requires us to include H_2 cooling, an updated UV background radiation model, and to introduce a model for the metal content of the intergalactic medium. By fine-tuning various model parameters and incorporating empirical constraints, we have tailored the model to match the statistical properties of Milky Way dwarf galaxies, such as their luminosity function and size–mass relation. We have validated our modified semi-analytic framework by undertaking a comparative analysis of the resulting galaxy-halo connection. We predict a total of 300^{+75}_{-99} satellites with an absolute V-band magnitude (M_V) less than 0 within 300 kpc from our Milky Way-analogs. The fraction of subhalos that host a galaxy at least this bright drops to 50% by a halo peak mass of $\sim 8.9 \times 10^7$ $M_\odot$, consistent with the occupation fraction inferred from the latest observations of Milky Way satellite population.

4.2 Introduction

Dwarf galaxies, characterized by their low masses, hold a prominent position in astrophysical research due to their intriguing properties and profound implications for our understanding of galaxy formation and evolution (Simon 2019). From a theoretical perspective, these faint stellar systems offer valuable insights into fundamental aspects of galaxy formation models and cosmological paradigms (Bullock and Boylan-Kolchin 2017; Sales et al. 2022). One key reason for the significant interest in dwarf galaxies is their low mass and shallow gravitational potential wells, which makes them ideal laboratories for testing various feedback mechanisms. Feedback processes, such as stellar winds and supernovae play a crucial role in regulating star formation and shaping the properties of galaxies (Bower et al. 2012; Zolotov et al. 2012; Puchwein and Springel 2013; Madau et al. 2014; Chan

et al. 2015; Read et al. 2016; Tollet et al. 2016; Fitts et al. 2017). Dwarf galaxies, with their shallower gravitational potentials provide an excellent testing ground to investigate the interplay between these feedback processes and the surrounding circumgalactic medium (Lu et al. 2017; Christensen et al. 2018). Their formation predates that of more massive galaxies, allowing us a glimpse of the conditions and processes that prevailed during the early stages of the Universe. For example, the low metallicity exhibited by dwarf galaxies presents an opportunity to probe the mechanisms responsible for chemical enrichment in the early Universe (Bovill and Ricotti 2009, 2011; Wheeler et al. 2015). By studying these ancient systems, we gain valuable insights into the hierarchical assembly of galaxies and the mechanisms responsible for their subsequent evolution.

In addition, the study of dwarf galaxies contributes to our understanding of the nature of dark matter (DM; e.g. Macciò et al. 2019; Nadler et al. 2021; Newton et al. 2021; Dekker et al. 2022). As the most numerous galaxy population in the Universe (Ferguson and Binggeli 1994), their abundance and distribution provide essential constraints for cosmological models, particularly those based on cold dark matter (CDM). By investigating the properties and spatial distribution of dwarf galaxies, we can test the predictions of the CDM model and explore alternative models that may better explain their observed characteristics.

In tandem with theoretical interest, there has been a remarkable growth in the observational landscape of dwarf galaxies over the past two decades—from surveys[2] including the Sloan Digital Sky Survey (SDSS; Ahumada et al. 2020; Abdurro'uf et al. 2022;

[2]We refer the reader to Crnojević and Mutlu-Pakdil (2021) for examples of discovered dwarfs in each survey.

Almeida et al. 2023), Dark Energy Survey (DES; Bechtol et al. 2015; Drlica-Wagner et al. 2015), The DECam Local Volume Exploration Survey (DELVE; Drlica-Wagner et al. 2022), Pan-STARRS (PS1; Chambers et al. 2016), ATLAS (Shanks et al. 2015), and Gaia (Collaboration et al. 2016a). Advancements in survey capabilities and data analysis techniques have led to a significant increase in the number of known Milky Way (MW) dwarfs, enabling a detailed characterization of their properties. Relevant examples that target MW or MW-like environments in the Local Volume include Geha et al. (2017); Mao et al. (2021); Carlsten et al. (2021); Nashimoto et al. (2022); Danieli et al. (2017); Bennet et al. (2020); Doliva-Dolinsky et al. (2023); Smercina et al. (2018). These observations have provided crucial empirical constraints for theoretical models and paved the way for a deeper understanding of the formation and evolution of dwarf galaxies.

The motivation behind this paper is to construct a comprehensive, physical model that accurately reproduces the statistical properties of MW dwarf galaxies. Therefore, by developing this model, we can shed light on the underlying physics and unravel the intricate mechanisms that govern the formation and evolution of these galaxies. Furthermore, our motivation extends beyond the mere reproduction of observed statistical properties. We also seek to investigate how dwarf galaxies respond to changes in the nature of DM. To explore the impact of DM on dwarf galaxies, it is imperative to begin with a model that accurately represents the prevailing cosmological paradigm, specifically the CDM model. By establishing a reliable foundation based on CDM, we can examine how variations in the nature of dark matter affect the properties of dwarf galaxies (specifically, the self-interacting dark mater model, Ahvazi et al. in prep.). This endeavor enables us to probe the sensitivity

of dwarf galaxies to different DM scenarios, providing crucial insights into the nature and fundamental properties of dark matter itself.

In this study, we adopt a systematic approach by modifying the existing Semi-Analytic Model (SAM) known as "Galacticus" (Benson 2012) to accurately reproduce the observed properties of dwarf galaxies in the MW. The SAM framework serves as a powerful tool for establishing the connection between the formation and evolution of galaxies and the underlying dark matter halos in which they reside. One notable advantage of the SAM approach is its computational efficiency, enabling us to explore numerous realizations and, in the future, investigate different dark matter physics rapidly (Benson 2012; Benson et al. 2013). By employing the SAMs, we can effectively resolve dwarfs and ultra-faints within much more massive systems, including clusters, which are typically beyond the reach of hydrodynamic simulations (Pillepich et al. 2019; Nelson et al. 2019a; Tremmel et al. 2019). It should be noted, however, that for MW-like systems, the latest generation of zoom-in hydrodynamical simulations are achieving resolutions sufficient for resolving ultra-faint dwarf galaxies (Buck et al. 2020; Applebaum et al. 2021; Grand et al. 2021; Joshi et al. 2024). It is crucial to recognize that while hydrodynamical simulations, in principle, offer higher accuracy by relying on fewer assumptions, their computational demands are substantially larger than those of SAMs.

Our first objective is to tailor the SAM to match the statistical properties of MW dwarf galaxies, such as their luminosity function and metallicities, by carefully adjusting various model parameters and incorporating empirical constraints. In addition, we include models that we anticipate will play a pivotal role in the evolution of dwarf galaxies. Specif-

ically, we incorporate H_2 cooling and consider the influence of Intergalactic Medium (IGM) metallicity, and UV background radiation. H_2 cooling is particularly significant in low-mass halos, as it affects the ability of gas to condense and form stars. Furthermore, the inclusion of IGM metallicity enables us to account for the metal enrichment of dwarf galaxies more accurately.

To assess the implications of our modifications and refinements, we undertake a comparative analysis of the resulting galaxy–halo connection. This step is crucial as it enables us to investigate the relationship between the observed properties of dwarf galaxies and the underlying dark matter halos. By comparing our results with prior estimates of this connection, we gain insights into the distribution of dark matter within dwarf galaxies and its impact on their observable characteristics. This comparison also serves as a validation of our modified SAM framework and allows us to assess the extent to which our model aligns with existing knowledge and understanding of the galaxy–halo connection in the context of MW dwarf galaxies. Moreover, we leverage our model to make predictions for the mass function of halos across a range of masses, encompassing ultra-faint satellites of Large Magellanic Cloud (LMC)-analogs, satellites of M31-analog systems, as well as dwarfs residing in group and cluster environments.

This paper is organized as follows: In Section 4.3, we provide a detailed description of our methodology, outlining the modifications made to the existing Galacticus model and the incorporation of key physical processes. In Section 4.4, we present our comprehensive results and engage in a discussion of the galaxy–halo connection, in Section 4.4.1. we present our predictions for various quantities associated with dwarf galaxies, in Section 4.4.2,

and we explore the mass functions of halos across different mass scales, in Section 4.4.3. Finally, in Section 4.5, we summarize our significant findings and draw conclusions based on the analysis conducted in this study.

4.3 Methods

We use the Galacticus semi-analytical model (SAM) for galaxy formation and evolution as introduced by Benson (2012).[3] Similar to other SAMs—including the Santa Cruz SAM (Somerville and Primack 1999), GALFORM (Cole et al. 2000), SAG (Cora 2006), MORGANA (Monaco et al. 2007), L-Galaxies (Henriques et al. 2015), SAGE (Croton et al. 2016), and SHARK (Lagos et al. 2018)—Galacticus parameterizes the astrophysical processes that govern galaxy formation and evolution and uses a set of differential equations to model and solve galactic evolution over time. It builds dark matter halo merger trees by employing a modified extended Press-Schechter formalism (Parkinson et al. 2007; Benson 2017) and then simulates the evolution of galaxy populations within this merging hierarchy of halos. At the end of this evolution process, Galacticus provides a comprehensive set of properties for the galaxies, including stellar mass, size, metallicity, morphology, star formation history, and photometric luminosities derived using simple stellar population spectra from the FSPS model[4] (Conroy et al. 2009).

The baryonic physics of the Galacticus model has been constrained by adjusting parameters to match a variety of observational data on massive galaxies (typically L_* and brighter systems) as described in Knebe et al. (2018; Section 2.2), which also summarizes the

[3]The specific version used in this work is publicly available at https://github.com/galacticusorg/galacticus

[4]https://github.com/cconroy20/fsps/releases/tag/v3.2

key baryonic physics in Galacticus. Parameter tuning was performed by manually searching the model parameter space to seek models that closely match observations including the $z = 0$ stellar mass function of galaxies, $z = 0$ luminosity functions, the local Tully-Fisher relation, distributions of galaxy colors and sizes, the black hole–bulge mass relation, and the star formation history of the universe. Knebe et al. (2018) also presents a number of comparisons between the predictions of Galacticus and observations for massive galaxies. These comparisons show that Galacticus performs well in matching observational estimates of the distribution of star formation rates in galaxies, the cosmic star formation history, the distribution of black hole masses, the stellar mass–halo mass relation, and measures of galaxy clustering. However, in other comparisons (e.g. galaxy cold gas content and metallicity), Galacticus fares less well against the observational constraints.

Galacticus is designed to be highly modular, and offers the flexibility to incorporate various models for the complex processes involved in galaxy formation and evolution. Starting from the model presented in Knebe et al. (2018), in this work, we utilize a model similar to that recently proposed by Weerasooriya et al. (2023), but with some differences. In contrast to Weerasooriya et al. (2023), who utilized merger trees extracted from N-body simulations and ran Galacticus on those trees, we employ the merger tree building algorithm of Cole et al. (2000), which is based on the extended Press-Schechter (EPS) formalism, with the modifier function proposed by Parkinson et al. (2007)—recalibrated to improve the match to high-resolution zoom-in simulations of Milky Way mass halos (Sarnaaik et al., in prep.). We combine this with a comprehensive subhalo evolution model in Galacticus. The rationale behind this choice is our aim to generate a large number of realizations of

MW-analogs, while fully-resolving halos hosting the lowest mass galaxies, allowing us to investigate the effects of baryons on galaxy properties. Additionally, in upcoming papers, we plan to explore the implications of different dark matter models and the presence of an LMC-analog.

Given our aim of comprehensively studying the entire MW dwarf population (down to ultra-faints) in this paper, the effects of resolution become particularly important. A key consideration is the impact of resolution on the results obtained by Weerasooriya et al. (2023), as they discussed in Section 3.3.1 of their paper—their merger trees resolved $10^7 M_\odot$ halos with just 100 particles. The resolution of N-body simulations can limit the ability to predict sizes for low-mass dwarfs accurately.

In addition to the resolution difference, other distinctions between these two approaches include the treatment of the effect of reionization and the suppression of gas accretion into low-mass halos. While Weerasooriya et al. (2023) utilized a simple model involving sharp cuts in virial velocity to mimic these effects, we opt for a more realistic model in our work (see Appendix G). Moreover, we adopt different cooling rates, feedback mechanisms, a reionization model, and accretion mode, along with specific angular momentum prescriptions, as explained in detail in Appendix G. Despite employing this more realistic model, we maintain the same level of agreement with observational results and predictions inferred from observational data, ensuring the robustness and reliability of our findings. For a brief comparison with other SAM approaches, the reader is referred to Appendix I.

In our model, we employ a comprehensive treatment for the orbital evolution of subhalos, incorporating essential nonlinear dynamical processes, including dynamical fric-

tion, tidal stripping, and tidal heating. This model was first implemented in GALACTICUS by Pullen et al. (2014, the reader is referred to Yang et al. 2020 for a full explanation and an initial calibration of the model). Subsequently, the tidal heating model was improved by Benson and Du (2022) to include second-order terms in the impulse approximation which is shown to more accurately follow the tidal tracks measured in high-resolution N-body simulations. For a comprehensive and detailed account of the subhalo orbital evolution within our model, please refer to Appendix G.1. In addition to providing a more detailed treatment of the evolution of subhalo density profiles, the primary advantage of this treatment of subhalo orbits for the present work is that it provides orbital radii for all subhalos, allowing us to select satellite galaxies based on their distance from the MW. Furthermore, the central galaxy in our model is evolved self-consistently, following the same baryonic physics (e.g. star formation, feedback, etc) as described for the evolution of subhalos. Importantly, the gravitational potential of the MW is included at all times when modeling our subhalo orbital evolution, providing a more accurate representation of the gravitational interactions between the central galaxy and its satellite subhalos.

In this study, we track the evolution of 100 MW-analogs or host halos with $z = 0$ masses ranging from 7×10^{11} to 1.9×10^{12} $M_\odot$ (Wang et al. 2020; Callingham et al. 2019), and resolving progenitor halos to masses of 10^7 $M_\odot$—sufficient to fully resolve the formation of ultra-faint dwarf galaxies similar to those observed in the vicinity of the MW as we will demonstrate below. To calibrate and test our models of MW-analogs and their subhalo population, we use observational data from Local Group dwarf galaxies, including all Milky Way dwarf galaxies from the DES+PS1 surveys (Drlica-Wagner et al. 2020) and the updated

McConnachie (2012) compilation, along with ultra-faint dwarf population from (Simon 2019, see references therein), and few extra objects such as Pegasus IV (Cerny et al. 2023), Indus I (Koposov et al. 2015), Antlia II (Torrealba et al. 2019), and Centaurus I (Mau et al. 2020).

A primary advantage of using a semi-analytic approach is its computational efficiency, which enables rapid exploration of parameter space and model space. This allows for the study of the effects of various models on the evolution of halos and galaxies. In this paper, we focus on examining the effects of the redshift evolution of the IGM metallicity, the effect of different models of the cosmic UV background radiation, and the contribution of molecular hydrogen, H_2, to the cooling function of CGM gas. We present the implementation details of these models in sections 4.3.1, 4.3.2, and 4.3.3 respectively.

4.3.1 IGM metallicity

The presence of metals in the IGM has been confirmed through observations, indicating their existence at significant levels during the redshifts corresponding to dwarf galaxy formation (Madau and Dickinson 2014; Aguirre et al. 2008; Simcoe et al. 2004; Schaye et al. 2003). In addition, studies of dwarf galaxies have revealed a noticeable plateau in the mass-metallicity relation at lower masses (Simon 2019). Our feedback model, which follows a power law dependence on the gravitational potential of galaxies (and so, for dwarf galaxies, is close to a power law dependence on halo mass), does not inherently produce such a plateau in the mass-metallicity relation —instead it results in an effective yield (and, therefore, a stellar metallicity) that decreases continuously toward lower halo masses (see, for example Cole et al. 2000, §4.2.1 & §4.2.2). Motivated by these facts, we propose that the metallicity of the IGM might play a crucial role in shaping the mass-metallicity relation of

galaxies, and may potentially explain the observed plateau. In light of this hypothesis, we introduce a simple model that incorporates the metallicity of the IGM, aiming to elucidate the underlying mechanisms that govern the observed plateau. By considering the impact of IGM metallicity on the evolution of dwarf galaxies, we can gain valuable insights into the interplay between the metal enrichment of the IGM and the metallicity of inflowing material. It is important to note that the detailed mechanisms responsible for enriching the IGM with metals, including the propagation and mixing of outflows, remain subjects of ongoing theoretical investigation (Mitchell et al. 2020; Muratov et al. 2017; Schneider et al. 2020; see Tumlinson et al. 2017 for a comprehensive review), and we do not attempt to model them here.

Therefore, this study uses a simple polynomial model to describe how the IGM metallicity evolves as a function of redshift. Specifically, we assume that the metallicity is given by

$$\log_{10}(Z_{\rm IGM}/{\rm Z}_{\odot}) = A + B\log_{10}(1+z), \tag{4.1}$$

where $Z_{\rm IGM}$ represents the metallicity of the IGM and z is redshift. This model incorporates two free parameters, A and B that are calibrated to match current observations of the mass-metallicity relation of dwarf galaxies and to satisfy inferences on $Z_{\rm IGM}$ from observations of the Lyα forest in the spectra of distant quasars.

4.3.2 UV background radiation

The cosmic background of UV radiation plays a key role in the evolution of molecular hydrogen in low-mass halos through the process of photodissociation (see §4.3.3 below).

A key factor for our work is the redshift at which reionization of the IGM occurs. After reionization the UV background radiation is able to increase in intensity substantially (as the IGM becomes transparent at these wavelengths), resulting in greatly enhanced photodissociation of molecular hydrogen.

In this work we make use of two models of the cosmic background radiation—with significantly different reionization redshifts—to allow us to explore how our results depend on this choice.

The first model we consider is that of Haardt and Madau (2012) (HM12 hereafter). This model includes a "minimal reionization model" which was shown to produce an optical depth to reionization of $\tau_{\rm es} = 0.084$ in good agreement with the (current at the time of publication of HM12) WMAP 7-year results of $\tau_{\rm es} = 0.088 \pm 0.015$ (Jarosik et al. 2011), and a reionization redshift (the epoch at which the volume filling fraction of HII reaches 50%) of $z \approx 10$.

The second model that we use is that of Faucher-Giguère (2020) (FG20 hereafter) which is calibrated to more recent data (a complete discussion, and comparison to earlier works, is given in the paper). Importantly for our work, the Faucher-Giguère (2020) model produces an optical depth to reionization of $\tau_{\rm es} = 0.054$, matched to that measured by the Planck 2018 analysis, $\tau_{\rm es} = 0.054 \pm 0.007$ (Planck Collaboration et al. 2020), and therefore a lower reionization redshift of $z = 7.8$.

We consider Faucher-Giguère (2020) to be the preferred model for the cosmic background radiation (as it is calibrated to more accurate measures of the optical depth to

reionization), but explore the Haardt and Madau (2012) model also to investigate how the redshift of reionization affects our results.

In both cases, the spectral radiance of the cosmic background radiation is computed by interpolating in tables (as a function of wavelength and redshift) derived from these two models.

4.3.3 Molecular hydrogen cooling

In halos with virial temperatures below the atomic cooling cut off (at around 10^4 K), the primary coolant for gas in the circumgalactic medium of high-redshift halos is molecular hydrogen (H_2; e.g. Abel 1995; Tegmark et al. 1997). Even with our added pre-enrichment in the IGM metallicity (see section 4.3.1), the metallicity of the cooling case remains sufficiently low that the metal line cooling is not substantially enhanced, while H_2 becomes sufficiently abundant at $T < 10^4$ K.[5] The timescales of the reactions which form and destroy H_2 can be long compared to halo assembly timescales, meaning that equilibrium abundances can not be assumed. Therefore, we must solve the rate equations for the production and destruction of H_2 in each halo. This is straightforward as these can simply be added as additional equations passed to Galacticus' differential equation

[5]While this is true for the model presented in this work, we caution readers that the outcomes may be sensitive to the underlying assumptions in computing metal cooling and H_2 formation/destruction in the presence of a radiation field. For instance, a comparison of our cooling efficiencies with Bialy and Sternberg (2019) reveals overall agreement at the typical densities of our halos, although they emphasize the impact of the surrounding radiation field, particularly the susceptibility of H_2 to destruction by the far-UV radiation (see their Fig. 7, top panels), and the strong density dependence in the contribution of H_2 to cooling. The efficiency of H_2 cooling in small, early-forming halos, considering photodissociation through Lyman-Werner radiation in the presence of H_2 self-shielding, remains a debated topic in the literature (see Section 4.3.2 of the review by Klessen and Glover 2023, and references therein). In general, the actual efficiency and relevance of H_2 cooling in small, early-forming halos are subjects of ongoing debate.

solver engine which then integrates them forward in time with adaptive timesteps chosen to achieve a suitable accuracy.

We use the network of chemical reactions described in Abel et al. (1997) to track the abundance of H_2—in particular we follow their recommendation for a "fast" network by assuming that H^- is always present at its equilibrium abundance and ignoring various slow reactions. Therefore, in the circumgalactic medium (CGM) of each halo we track the abundances of H, H^+, H_2, and e^-, and include the following set of reactions:

- $H + e^- \rightarrow H^+ + 2e^-$;
- $H^+ + e^- \rightarrow H + \gamma$;
- $H + H^- \rightarrow H_2 + e^-$;
- $H_2 + e^- \rightarrow 2H + e^-$;
- $H^- + \gamma \rightarrow H + e^-$;
- $H_2 + \gamma \rightarrow H_2^* \rightarrow 2H$;
- $H_2 + \gamma \rightarrow 2H$; and
- $H + \gamma \rightarrow H^+ + e^-$,

utilizing the rate coefficients and cross sections given by Abel et al. (1997) in each case. The temperature of the CGM is assumed to be equal to the virial temperature of the halo for the purposes of computing rate coefficients (and for the purposes of computing cooling functions—see below).

In computing the evolution of the abundances we assume a uniform density CGM, in which the current CGM mass is contained within a sphere of radius $r_{\rm CGM}$ which we take to be the virial radius for halos, and the ram pressure radius for subhalos[6]. However, we account for the fact that the CGM will be denser in the inner regions of the halo via a clumping factor, $f_{\rm c}$, which multiplies the rates of the first three reactions (i.e. those involving two CGM particles). The clumping factor is computed as

$$f_{\rm c} = \frac{\langle \rho_{\rm CGM}^2 \rangle}{\langle \rho_{\rm CGM} \rangle^2} = \frac{4\pi r_{\rm CGM}^3}{3 M_{\rm CGM}^2} \int_0^{r_{\rm CGM}} 4\pi r^2 \rho_{\rm CGM}^2(r) {\rm d}r, \tag{4.2}$$

where $\langle \rangle$ indicates a volume average, and $\rho_{\rm CGM}$ is the density of the CGM, which we model as a β-profile with core radius equal to 30% of the virial radius.

In computing the rate for the reaction $\mathrm{H}_2 + \gamma \rightarrow H_2^* \rightarrow 2\mathrm{H}$ we account for self-shielding of the radiation following the model of Safranek-Shrader et al. (2012; their eqn. 11), estimating the H_2 column density at $N_{\mathrm{H}_2} \approx n_{\mathrm{H}_2} r_{\rm CGM}$, where n_{H_2} is the density of H_2 in the CGM.

Solving the network of reactions to compute the H_2 abundance can be computationally demanding. In particular, in higher mass halos (at higher temperatures) the timescales for the reactions controlling the ionization state of atomic hydrogen can become very short, requiring a large number of small timesteps to solve. However, in such cases the ionization fraction of atomic hydrogen rapidly approaches its equilibrium value and, furthermore, the abundance of H_2 is typically very low in such halos as it is destroyed by collisions at high temperatures, meaning that it makes little contribution to the cooling

[6] Galacticus implements the ram pressure stripping model of Font et al. (2008) as described in Benson et al. (2015). As the mass of the CGM in a subhalo is reduced due to the effects of ram pressure stripping from the CGM of its host halo, we assume that this mass is removed in spherical shells from the subhalo CGM, starting at the outer edge, $r_{\rm CGM}$. In this way, the outer edge, $r_{\rm CGM}$, decreases over time as ram pressure stripping proceeds.

function. Therefore, we choose to switch over to an equilibrium calculation when

$$\tau_{\rm H} < f_{\rm dyn}\tau_{\rm dyn}, \tag{4.3}$$

where $f_{\rm dyn}$ is a parameter, $\tau_{\rm dyn}$ is the dynamical time in the halo[7], and

$$\tau_{\rm H} = \min\left(\tau_\alpha, \tau_\beta, \tau_\Gamma\right), \tag{4.4}$$

where $\tau_\alpha = 1/\alpha n$, $\tau_\beta = 1/\beta n$,$\tau_\Gamma = 1/\Gamma$, n is the number density of hydrogen, and α, β, and Γ are the collisional ionization, radiative recombination, and photoionization rate coefficients for hydrogen respectively.

If the system is judged to be in equilibrium then the neutral fraction of hydrogen is computed as:

$$x_{\rm H} = \frac{\tau_\Gamma^{-1} + \tau_\alpha^{-1} + 2\tau_\beta^{-1} - \sqrt{\tau_\Gamma^{-2} + 2\tau_\alpha^{-1}\tau_\Gamma^{-1} + \tau_\alpha^{-2} + 4\tau_\beta^{-1}\tau_\Gamma^{-1}}}{2\tau_\alpha^{-1} + \tau_\beta^{-1}}. \tag{4.5}$$

The abundances of H, H^+, and e^- are then fixed according to this fraction, and reaction rates for them are set to zero. The reactions controlling the formation/destruction of H_2 are still followed as normal, by directly solving the relevant differential equations (but now using the equilibrium abundances for H, H^+, and e^-).

We use a value of $f_{\rm dyn} = 10^{-3}$, such that this equilibrium approximation is only used when the timescale controlling the ionization state of atomic hydrogen is less than 0.1% of the halo dynamical time. We have checked that the resulting evolution of the H_2 abundance agrees closely with that obtained using a fully non-equilibrium calculation (but is orders of magnitude faster).

[7]Dynamical time here is defined as $\tau_{\rm dyn} = \sqrt{r_{\rm v}^3/{\rm G}M_{\rm v}}$, where $r_{\rm v}$ and $M_{\rm v}$ are virial radius and virial mass of the halo, respectively.

Given the abundance of H_2 we then compute its contribution to the cooling function, $\Lambda(T)$, following the approach of Galli and Palla (1998) using the fitting functions given in that work.

4.4 Results and Discussion

While our semi-analytic model is relatively fast to run, conducting a full likelihood analysis using an approach such as MCMC becomes computationally infeasible due to the large number of parameters involved and the resulting need to make tens of thousands of evaluations of the model. Therefore, we pursued an alternative approach by manually fine-tuning the parameters to accurately replicate the properties of higher-mass galaxies, including the luminosity functions and the mass-metallicity relation. Given that our model already demonstrated reasonably close agreement with higher-mass galaxies, minor adjustments were sufficient to capture the behavior of lower-mass regimes.

However, for the incorporation of the novel aspect of IGM metallicity, we elected to employ a likelihood analysis utilizing a coarse grid search and full likelihood calculations. This decision was motivated by computational tractability since this new aspect introduced only two parameters and was expected to primarily impact the metallicities of ultra-faint dwarfs, with minimal effects on the more massive systems already calibrated. Employing this methodology allowed us to determine the optimal values for the coefficients A and B (as introduced in equation 4.1), yielding A = -1.3 and B = -1.9[8].

[8]The decision to use a coarse grid was primarily due to the computational expense associated with more extensive analyses, such as MCMC, which would be necessary for a comprehensive exploration of all free parameters across all models in this SAM. Given the computational limitations, we focused on finding the optimum values for the free parameters in the IGM metallicity model. However, it is important to acknowl-

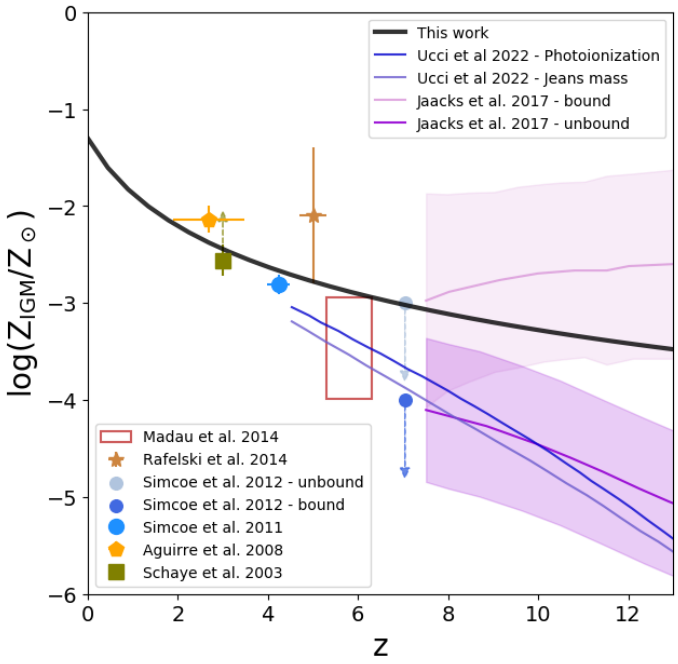

Figure 4.1: Evolution of IGM metallicity as a function of redshift. The black line represents the predicted evolution based on our model. Observational results are depicted by markers of different colors. The green square corresponds to the average [C/H] measurements reported by Schaye et al. (2003). The orange pentagon represents the metallicity of the IGM as probed by O VI absorption in the Lyα forest reported by Aguirre et al. (2008). The blue circles represent results by Simcoe (2011) and Simcoe et al. (2012). Additionally, the brown star marks measurements by Rafelski et al. (2014) and, the red rectangle shows the carbon metallicity in the IGM as calculated by Madau and Dickinson (2014) based on observations from Simcoe (2011) and Becker et al. (2011). We also show results from cosmological hydrodynamical simulations. The simulations of Jaacks et al. (2018, which focus on Pop III modeling) are shown by pink and purple lines, while those of Ucci et al. (2023, which focus on modeling of reionization) are shown by blue and violet lines.

Fig. 4.1 visually presents the variation of IGM metallicity with redshift as predicted by our model, represented by the black line. Additionally, we compared our model predictions with observations of IGM metallicity at higher redshifts. The average [C/H] measurements reported by Schaye et al. (2003) at redshift z = 3 yielded a value of -2.56, considering all their samples at this specific redshift, while not accounting for the effect of overdensity. However, focusing solely on quasars (rather than accounting for both galaxies and quasars in their sample) for determining the spectral shape of the metagalactic UV/X-ray background radiation resulted in measurements showing 0.5 dex higher values. Furthermore, Aguirre et al. (2008) examined the IGM metallicity probed by O VI absorption in the Lyα forest for the redshift range $1.9 < z < 3.6$ (represented by the orange marker). Observations by Rafelski et al. (2014) at $4.7 < z < 5.3$ revealed metallicities ranging from $[-1.4, -2.8]$. The study by Madau and Dickinson (2014) estimated carbon metallicity by probing C IV and C II absorption measurements from Simcoe (2011) and Becker et al. (2011), respectively, over the redshifts $5.3 - 6.4$. Madau and Dickinson (2014) calculated the carbon metallicity assuming a range of [0.1, 1] for the ratio of singly or triply ionized carbon over this redshift range (depicted as the red rectangle on the plot). Simcoe (2011) explored IGM metallicity through C IV absorption in the redshift range $4 - 4.5$, while Simcoe et al. (2012) reported chemical abundances of $< 1/10{,}000$ Solar if the gas is in a gravitationally bound proto-galaxy or $< 1/1{,}000$ Solar if it is diffuse and unbound in a

edge that the coarse grid search resulted in insufficient information to calculate a meaningful theoretical uncertainty for these parameters. Despite this limitation, we have ensured that the optimization process has good coverage of the available parameter space to the best extent possible under the computational constraints.

quasar spectrum at $z = 7.04$, suggesting that gravitationally bound systems could be viable sites for the production of Pop III stars.

Turning to cosmological hydrodynamical simulations, Jaacks et al. (2018) utilized the hydrodynamic and N-body code GIZMO coupled with their sub-grid Pop III model to study the baseline metal enrichment from Pop III star formation at $z > 7$ (results are shown in the figure by pink and purple lines corresponding to bound and unbound systems). Independently, the study by Ucci et al. (2023) discusses the metal enrichment of the IGM at $z > 4.5$ through using a detailed physical model of galaxy chemical enrichment embedded into the ASTRAEUS framework, which couples galaxy formation and reionization in the first billion years. Through their radiative feedback models, they explored a range from a weak, time-delayed (their "Photoionization model") to a strong instantaneous reduction of gas in the galaxy (their "Jeans mass model"), with predictions shown on Fig. 4.1 by blue and violet lines, respectively[9].

While observations appear to narrow down the range of IGM metallicities at lower redshifts, aligning with the expectation of our best model as determined through the likelihood analysis, uncertainties in modeling the metallicity evolution of the universe at higher redshifts prevent precise predictions of the metal content of the IGM. Predictions from our model suggest higher values of IGM metallicity at higher redshifts (the time of formation of ultra-faint galaxies) compared to the examples shown here. Hydrodynamical simulations generally predict IGM metallicities at high redshifts that are lower than those adopted in this work (and which we find are necessary to produce the correct metallicities of ultra-faint

[9]It is essential to treat the IGM metallicity values from Ucci et al. (2023) as a lower limit since their method assumes that ejected metals are homogeneously dispersed into the entire simulation box when calculating $Z_{\rm IGM}$.

dwarf galaxies). However, we note that the simulation of Jaacks et al. (2018) predicts substantially higher metallicities in bound regions. Given that the ultra-faint dwarfs studied in this work are, by definition, forming in a biased environment (the region around the proto-Milky Way), we may expect that they therefore experience a higher metallicity than that of the volume-averaged IGM. As such, while our IGM metallicity model remains empirical and speculative, it is within the bounds of current theory given the environment of interest.

4.4.1 Galaxy–halo connection

In this section, we explore the galaxy-halo connection and its sensitivity to the incorporation of molecular hydrogen cooling and UV background radiation, as introduced in sections 4.3.2 and 4.3.3. By examining the impact of these key physical processes on our sample of MW analogs, we aim to gain deeper insights into the intricate interplay between gas cooling, radiation, and galaxy formation within the context of our simulated galaxy population, particularly the low-mass dwarf satellites of our own MW.

Occupation fraction

The occupation fraction, a crucial measure of the galaxy-halo connection, is defined here to be the fraction of dark matter halos hosting a luminous galaxy with absolute V-band magnitudes less than 0, roughly equivalent to a stellar mass content greater than approximately $100\,\mathrm{M}_\odot$. In Fig. 4.2, we present the occupation fraction as a function of peak halo mass[10]. The dashed line represents the model incorporating only atomic hydro-

[10]In Galacticus halo masses are defined as overdense regions with a mean density equal to that predicted by the spherical collapse model for the adopted cosmology and redshift (Peebles 1980; Lacey and Cole 1993; Eke et al. 1996).

gen cooling, while the dotted-dashed line corresponds to the model including both atomic and molecular hydrogen cooling (but ignoring effects of the UV background radiation). A comparison of these two lines highlights the significant impact of incorporating H_2 cooling, as it brings the model predictions into much closer agreement with occupation fraction estimates inferred from observations (shown by the blue and yellow bands), particularly for dwarf galaxy formation in halos with $M_{halo} < 2–3 \times 10^8$ $M_\odot$, corresponding to virial temperatures of approximately 10^4 K, below which the efficiency of atomic hydrogen cooling rapidly diminishes.

Furthermore, we investigate the effects of incorporating two different background radiation models, HM12 and FG20, as described in section 4.3.2. The inclusion of UV background radiation suppresses the formation of H_2 in low-mass halos and so has an influence on the formation of dwarf galaxies, resulting in a shift of the occupation fraction predictions towards higher masses. The main difference between the two UV background models lies in the chosen redshift of reionization, after which UV background radiation suppresses H_2 formation in low-mass halos. In the case of HM12, characterized by an earlier reionization redshift, we observe an earlier suppression of ultra-faint galaxy formation, thereby elevating the threshold for formation of galaxies in the occupation fraction results. We have confirmed that this result is almost entirely due to the difference in reionization redshifts between the FG20 and HM12 models, rather than, e.g., the spectral distribution of UV radiation. It is worth noting that effects of inhomogeneous reionization have not been explicitly considered in our model. Previous studies have shown that these inhomogeneities may lead to varying

reionization times for low-mass halos in diverse environments (Katz et al. 2020; Ocvirk et al. 2021), potentially introducing scatter in the predictions for occupation fractions.

In order to validate our results and provide a comprehensive comparison, we compare our findings with two independent studies. Firstly, we considered the forward-modeling framework for MW satellites presented by Nadler et al. (2020). Their model extends the abundance-matching framework (Wechsler and Tinker 2018) into the dwarf galaxy regime by parametrizing the galaxy–halo connection—including the faint-end slope of the luminosity function, the galaxy–halo size relation, the scatter in galaxy luminosity and size, and the disruption of subhalos due to baryonic effects (Nadler et al. 2018, 2019)—and constraining these parameters using recent MW satellite observations. In particular, Nadler et al. (2020) focused on MW satellites detected in photometric data from DES and PS1, which together cover a significant portion of the high Galactic latitude sky, including the contribution of satellites originally associated with the LMC. Importantly, they incorporated position-dependent observational selection effects that accurately represented satellite searches in imaging data from surveys such as DES and PS1. In our comparisons, we utilized their posterior on the galaxy occupation fraction, where the dark and light colors in Fig. 4.2 correspond to the 1 and 2 σ confidence intervals, respectively, and the median is represented by the blue curve. We find that our most realistic model which incorporates H_2 cooling and utilizes the UV background radiation prescription from FG20, lies within the 2σ uncertainty of the occupation fraction inferred from observations by Nadler et al. (2020).

Additionally, we examined the results obtained from the regulator-type modeling technique introduced in Kravtsov and Manwadkar (2022) and employed by Manwadkar

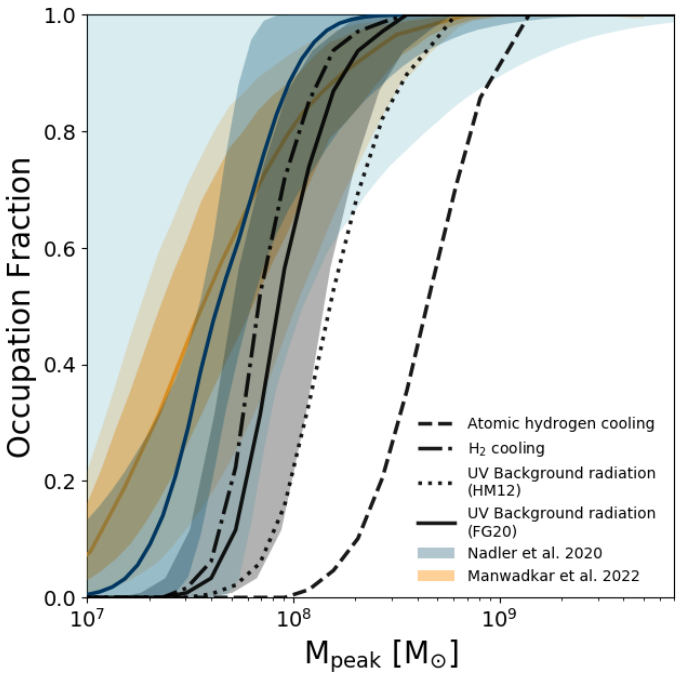

Figure 4.2: Occupation fraction as a function of the peak halo mass. The black curves, with different line styles, correspond to the predictions from our model incorporating various physical processes. Specifically, the dashed line corresponds to the model incorporating only atomic hydrogen cooling, while the dotted-dashed line represents the model incorporating both atomic and molecular hydrogen cooling (but no UV background radiation). The dotted line corresponds to the model including molecular hydrogen cooling and the UV background radiation prescription of HM12. The black curve with a shaded gray region corresponds to the model including molecular hydrogen cooling and the UV background radiation prescription of FG20. The gray shaded region indicates a 40% uncertainty in estimating the peak masses from our simulation. Additionally, the blue curve, along with the dark and light shaded blue regions, corresponds to the predictions by Nadler et al. 2020, while the orange curve, along with the dark and light shaded orange regions, corresponds to the predictions by Manwadkar and Kravtsov 2022.

and Kravtsov (2022) to model the MW satellite population. This approach allowed for an exploration of the luminosity function by forward modeling observations of the population of dwarf galaxies while accounting for observational biases in surveys through their respective selection functions. Furthermore, they incorporated current constraints on the MW halo mass and the presence of the LMC. In our analysis, we utilized the shaded orange region on the plot, where the dark and light colors represent the 1 and 2 σ dispersion, respectively, and the median is indicated by the orange curve.

By comparing our results with these complementary approaches, we find agreement within the 2 σ dispersion range of the respective results. However, based on the median of our findings, we estimated that the peak mass above which 50% of the halos host a luminous component is approximately a factor of 2 higher than the predictions by Nadler et al. (2020) and Manwadkar and Kravtsov (2022).

It is important to highlight that Galacticus does not currently account for any pre-infall mass loss from halos. Nevertheless, N-body simulations demonstrate that peak masses are typically attained before infall, as the effects of tidal stripping begin to diminish the mass to some extent prior to infall (Behroozi et al. 2014). To account for these uncertainties, we include a shaded region representing a 40% uncertainty in the determination of peak masses derived from our SAM prediction. The implementation of this missing physics is currently underway (Du & Benson, in prep.) in Galacticus.

As a result of this caveat, our current model likely overestimates peak masses due to the absence of accounting for pre-infall mass loss. With improved modeling in this regard, we anticipate our estimates to align more closely with these alternative models.

Specifically, our estimate suggest that approximately 50% of the halos with peak masses around $\sim 8.9\times10^7$ $M_\odot$ would host a luminous component, while Nadler et al. (2020) inferred a best-fit value of $\sim 4.2 \times 10^7$ $M_\odot$ and Manwadkar and Kravtsov (2022) predicted a value of $\sim 3.5 \times 10^7$ $M_\odot$.

Comparing these findings against occupation fraction predictions from hydrodynamical simulations targeting similar halo mass ranges reveals that these simulations consistently predict a cutoff in "galaxy formation" at higher halo masses. In particular, many hydrodynamical predictions span a range of 6.5×10^8 to $3.5 \times 10^9 M_\odot$ for the bound mass at which 50% of halos host galaxies, depending on the specific model configurations and reionization redshift assumptions employed (Sawala et al. 2016b; Benitez-Llambay et al. 2017; Benitez-Llambay and Frenk 2020)[11]. Importantly, it should be emphasized that the definition of occupation fraction in these simulations is subject to resolution limitations, and the effects of H_2 cooling must also be considered. These factors notably contribute to the disparities witnessed in the results. Nevertheless, due to the inherent dissimilarities in modeling approaches, a direct comparison between our SAM model and hydrodynamical simulations is not straightforward. For example, the simulation of Agertz et al. (2020) forms a dwarf with $M_\star \approx 3 \times 10^4 M_\odot$ in a halo of mass approximately $8 \times 10^8 M_\odot$, while the simulation of Applebaum et al. (2021) produces several galaxies in halos in the (bound) mass range 10^7–$10^9 M_\odot$. These simulations are therefore consistent with our model (i.e. they imply that the occupation fraction is greater than zero at these halo masses), but do not allow for a detailed characterization of the cut-off in the occupation fraction, precluding

[11]Note that the work by Benitez-Llambay and Frenk (2020) analyze results based on both hydrodynamical and semi-analytical simulations.

a careful comparison with our results. For a more comprehensive understanding of how diverse assumptions and models can influence the predicted occupation fraction, please refer to Appendix H.

Stellar mass – Halo mass relation

Fig. 4.3 showcases the stellar mass–halo mass (SMHM) relation, which provides crucial insights into the connection between the masses of galaxies and their dark matter halos. We present the median values of the SMHM relation obtained from our model, incorporating the various physical processes discussed in section 4.3. Each line style corresponds to a specific combination of physics, as outlined earlier (see section 4.4.1). Our most realistic model, which includes H_2 cooling and the UV background radiation prescription from FG20, is represented by the error bars indicating the 1 and 2 σ dispersion around the median value.

In terms of consistency with previous studies, our estimations for the higher mass end align well with a range of simulations and the abundance matching model by Behroozi et al. (2013) as illustrated by the grey solid line. We show an extrapolation of that relation to lower mass systems in dashed gray, from which our results start to substantially deviate downwards for $M_{\rm halo} < 10^9$ $M_\odot$. Notably, we find overall agreement with recent results from Nadler et al. (2020), whose SMHM relation inferred from MW satellite observations is depicted by the shaded blue region, with darker and lighter shades corresponding to the 1 and 2 σ confidence intervals, respectively.

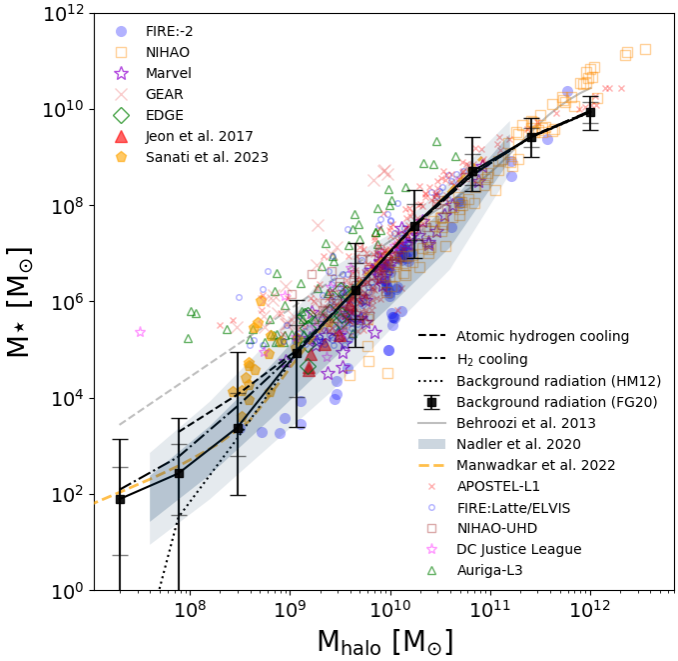

Figure 4.3: Stellar mass–halo mass relation. Our model predictions are represented by black curves with different line styles. We compare our results to the constrained/extrapolated SMHM relation from Behroozi et al. 2013 (depicted by the grey curve/dashed grey curve), the results from Nadler et al. 2020 (illustrated by the shaded blue region), the results from Manwadkar and Kravtsov 2022 (shown by the orange dashed line), and simulations of central/field dwarf galaxies in MW-like environments from various models, as well as simulations that zoom-in on individual dwarf-mass halos (represented by different markers. Please refer to the text or see Figure 2 in Sales et al. 2022 for more details).

Additionally, we compare our results with available simulations of central/field dwarf galaxies in MW-like or Local Group-like environments (with data compiled by Sales et al. 2022)[12]. For these comparisons, different markers are used, as indicated in the lower right part of the plot. The marker guide includes red crosses representing APOSTLE, L1 resolution (Sawala et al. 2016a; Fattahi et al. 2016), blue open circles showing Latte and ELVIS suites (Wetzel et al. 2016; Garrison-Kimmel et al. 2019) of FIRE-2 simulations[13] (Hopkins et al. 2018), brown squares representing NIHAO-UHD (Buck et al. 2019), pink stars showing DC Justice League (Munshi et al. 2021), green triangles representing Auriga, L3 resolution (Grand et al. 2017), while the legend in the upper left corner denotes simulations that zoom-in on individual dwarf-mass halos. These include blue circles showing FIRE-2 (Fitts et al. 2017; Wheeler et al. 2019; Hopkins et al. 2018; Wheeler et al. 2015), orange squares showing NIHAO (Wang et al. 2015), purple stars showing Marvel (Munshi et al. 2021), orange crosses showing GEAR (Revaz and Jablonka 2018), green diamonds showing EDGE (Rey et al. 2019, 2020), red triangles showing work by Jeon et al. (2017), and orange pentagons show results by Sanati et al. (2023).

The agreement observed with various simulations provides strong support for the validity of our modeling approach. Importantly, thanks to the use of SAMs, our predictions extend to fainter regimes, surpassing the capabilities of state-of-the-art hydrodynamical simulations. Overall, our different models comparing the effect of including various physics

[12]It is important to acknowledge that discrepancies might arise when comparing isolated dwarfs from hydrodynamical simulations due to potential variations in the definition of halo mass. Our model specifically focuses on dwarf satellites within MW systems. However, the purpose here is to emphasize the general concurrence between the outcomes of our model and the findings of existing simulations.

[13]The latest version of FIRE simulation (FIRE-3) shows even better agreement with our predictions (see Figure 9 in Hopkins et al. 2023).

remain consistent with each other within the 2 σ dispersion in the SMHM relation. However, some deviations are observed in the ultra-faint regime, where the model incorporating H_2 cooling and UV background radiation from FG20 produces the best results in terms of agreement with previous works. It is worth noting that our model slightly underpredicts the stellar mass content in the central galaxy (MW-analog). Nonetheless, the median value captures the lower end of stellar mass predictions for this halo mass range.

The SMHM relation predicted by Galacticus unveils some intriguing features that align with findings from hydrodynamical simulations, such as the mass-dependent scatter in the SMHM relation, which exhibits an increasing trend around the median in the ultra-faint regime. This behavior seems to be influenced by the impact of formation histories, particularly the duration of star formation prior to reionization, directly affecting the stellar mass content at low redshifts (Rey et al. 2019; Munshi et al. 2021). Another interesting prediction emerges in the ultra-faint regime for $M_{\rm halo} < 10^9$ $M_\odot$ (corresponding to $M_\star < 10^5$ $M_\odot$), where the power-law relation in the SMHM appears to undergo a break. Remarkably, this feature appears to correlate with the dominance of H_2 cooling and is further amplified by the effects of UV background radiation, specifically the time of reionization. These predictions are consistent with the SMHM relation obtained from forward modeling results by Manwadkar and Kravtsov (2022; depicted by the dashed orange line in Fig.4.3), although the position of the break in this study reflects the inefficiency of supernova-driven winds in the smallest galaxies.

Luminosity function

Fig. 4.4 demonstrates our model's predictions for the luminosity function of the MW satellite population. To ensure consistency with conducted observations, we impose two selection criteria: satellites must reside within a distance of 300 kpc from the host halo's center, and they should have a minimum half-light radius of $r_{\rm h} > 10$ pc. The error bars on the plot represent the 1 and 2 σ dispersion due to host-to-host scatter (across a range of halo masses). Our most accurate model predicts a total of 300^{+75}_{-99} (300^{+166}_{-170}) satellites with an absolute V-band magnitude ($\rm M_V$) less than 0, for 1σ (2σ) dispersion.

By examining our models incorporating various physics components (similar line styles as Fig. 4.2 and Fig. 4.3), we discern their impact on the resulting luminosity function. Notably, the inclusion of $\rm H_2$ cooling leads to a considerable increase in the number of predicted ultra-faint satellites, surpassing a factor of > 3, while the incorporation of UV background radiation serves to flatten the luminosity function at the ultra-faint end.

To assess the agreement with observational data, we compare our predictions with the luminosity function of all known MW satellites (light red curve) and the DES+PS1 data (from Drlica-Wagner et al. 2020), corrected for observational incompleteness (maroon line). It is important to note that the light red curve exhibits a more pronounced flattening at the ultra-faint end due to the incompleteness in the observations. In contrast, our results closely capture the rise predicted in the weighted DES+PS1 data (refer to Drlica-Wagner et al. (2020) for details of estimation), with the total number of satellites falling within the 2 σ dispersion.

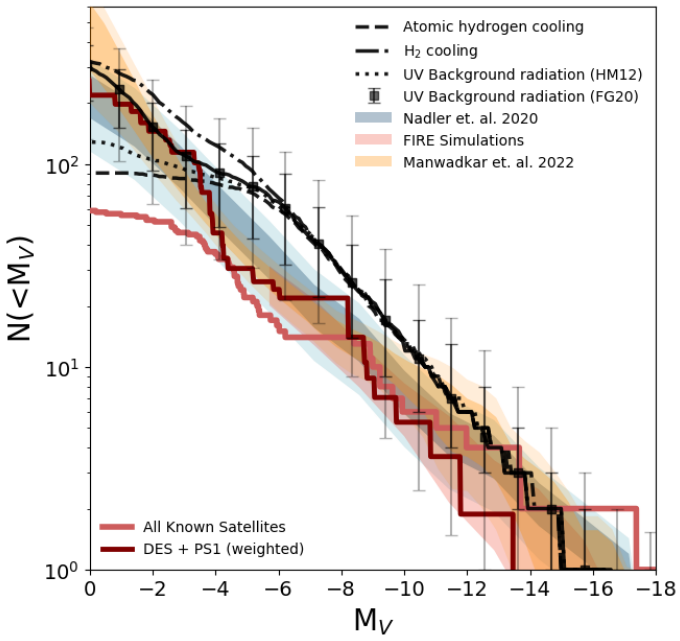

Figure 4.4: The luminosity function of MW satellites satisfying the criteria of $M_V < 0$, $r_{1/2} > 10$ pc, and a maximum distance of 300 kpc from the MW. Our model's predictions, represented by black curves with distinct line styles, are compared to observational data for all known MW satellites (light red curve) and the estimate derived in Drlica-Wagner et al. 2020 (maroon curve), which corrects for observational data incompleteness. Additionally, we present the results from simulations by Nadler et al. 2020 (blue shaded region), Manwadkar and Kravtsov 2022 (orange shaded region), and hydrodynamic simulations of the Local Group using the FIRE feedback prescription (pink shaded region) by Garrison-Kimmel et al. 2019.

Examining the higher end of the luminosity function, we find agreement (within the 2 σ dispersion) between our model and observational results (although we do not constrain our model to produce analogs of the LMC and SMC in all cases). However, it is worth emphasizing that the weighted DES+PS1 results do not encompass the LMC, SMC, and Sagittarius, accounting for the lower values observed compared to the all-known case at the higher end.

Moreover, we juxtapose our results with previous forward modeling methods, including the work by Nadler et al. (2020) (depicted by the blue shaded region) and Manwadkar and Kravtsov (2022) (illustrated by the orange shaded region) (as introduced in section 4.4.1). Additionally, we incorporate the FIRE hydrodynamical simulation by Garrison-Kimmel et al. (2019), extending down to the FIRE resolution limit of ~ -6 mag (represented by the pink shaded region). These systems do not explicitly include analogs of the LMC or SMC. Overall, our results demonstrate strong agreement with previous simulations and forward modelling approaches, albeit with a slight tendency to overpredict the median number of satellites. Notably, in the ultra-faint regime, discrepancies arise between observational data and various simulations; however, the simulations generally converge within the 2 σ limit. Remarkably, our best-performing model closely reproduces the predicted weighted DES+PS1 data at the low-mass end of the luminosity function.

In light of the higher median predicted for the satellite luminosity function in our model compared to other studies, such as Nadler et al. (2020), it is important to consider some underlying differences of the respective models. For instance, variations in the underlying subhalo mass functions predicted by Galacticus and cosmological zoom-in

simulations (e.g., see Fig. 10 of Nadler et al. 2023b) may account for some of the discrepancy. Additionally, the extent to which dark matter subhalos are disrupted by the central galaxy could also influence the resulting luminosity functions. In our model, subhalos are tidally stripped using the Pullen et al. (2014) prescription, including the potential of the central galaxy, while Nadler et al. (2020) apply a random-forest model trained on hydrodynamic simulations to capture this effect (Nadler et al. 2018).[14] Importantly, our main results are robust in the sense that our predictions for the occupation fraction and SMHM relation do not change if we restrict to the subset of merger trees that produce luminosity functions similar to Nadler et al. (2020). We leave direct calibration of our model based on forward-modeling the observed MW satellite population to future work.

4.4.2 Dwarf population

In this study, we utilize the optimal model presented in section 4.3, which incorporates the physics of molecular hydrogen cooling, UV background radiation, and IGM metallicity. Our aim is to predict properties of the dwarf galaxy population and compare these to existing observations[15] and simulations.

[14] We note that Hartwig et al. (2022) predict a total number of MW satellites comparable to our results without incorporating H_2 cooling or accounting for tidal stripping due to the central galaxy.

[15] Observational data are compiled from various resources (mainly from Drlica-Wagner et al. 2020; Simon 2019; McConnachie 2012). When multiple data sources exist for a given galaxy, we use the most precise and/or accurate measurement.

Mass–metallicity relation

The metallicity of a galaxy is commonly quantified by the iron to hydrogen abundance ratio ([Fe/H]). As shown in Fig. 4.5, we present the mean stellar [Fe/H][16] as a function of stellar mass ($M_\star$) for our simulation. The black curve represents the median value, while the black and grey error bars denote the 1 and 2 σ dispersion, respectively. To validate our results, we compare them with observations of dwarf galaxies located within a 300 kpc radius of the MW (illustrated by red markers). The observations indicate the presence of a metallicity plateau around [Fe/H]~ -2.5, which is reproduced well by our simulation incorporating the IGM metallicity model.

Interestingly, the mass-metallicity relation for the very low-mass satellites appears to be strongly influenced by the evolution of IGM metallicity as a function of redshift. This influence becomes apparent when comparing the black curve, which includes IGM metallicity in our model, with the dashed grey curve, where the IGM metallicity is excluded, and which shows a power-law extension to low masses with no plateau[17]. (The inclusion of IGM metallicity significantly affects the predicted metallicities of these satellites—essentially setting a floor in metallicity corresponding to the metallicity of the IGM gas accreted at the time at which the galaxy formed—highlighting the importance of the surrounding cosmic environment in shaping their chemical enrichment history.) When comparing our findings to zoom-in hydrodynamical simulations (such as those conducted by Agertz et al. 2020;

[16]In our present Galacticus model, [Fe/H] is computed using the instantaneous recylcing approximation, and the assumption of Solar abundance ratios.

[17]With no IGM metallicity, the metallicities of our galaxies are determined by our feedback/outflow model, which has a simple power-law dependence on halo mass, and so necessarily leads to a power-law mass-metallicity relation.

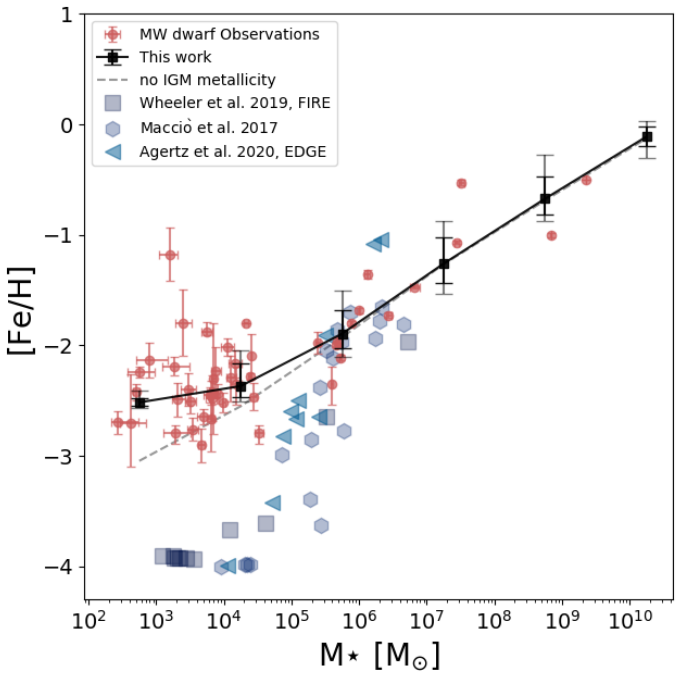

Figure 4.5: Stellar mass–metallicity relation for galaxies. The black curve, along with the black and grey error bars, represents the median value, and the 1 and 2 σ dispersions, respectively, derived from our simulation's predictions. The gray dashed line represent the predictions of our model without the IGM metallicity included. Blue markers indicate results from hydrodynamical simulations (Wheeler et al. 2019: blue squares; Macciò et al. 2017: blue hexagon; and Agertz et al. 2020: by blue triangles). Red markers with error bars depict the observational results for dwarf galaxies located within 300 kpc of the MW, compiled primarily from studies by Drlica-Wagner et al. 2020; Simon 2019; McConnachie 2012.

Wheeler et al. 2019; Macciò et al. 2017), we find that these simulations tend to predict near-primordial abundances for objects with stellar masses below 10^5 $M_\odot$. However, it is important to note that the examples presented in this study do not have a large cosmological environment and thus are not enriched by nearby sources (for a comprehensive comparison with recent simulation predictions refer to Figure 1 in Sanati et al. 2023). The implications of this lack of enrichment (in hydrodynamic simulations) remain uncertain and necessitate further investigation.

Recent studies have considered a few possible self-consistent avenues to populate the plateau in [Fe/H] at the faintest end of the mass–metallicity relation. The study by Prgomet et al. (2022), using the adaptive mesh refinement method, studied the effect of varying the IMF on the evolution of an ultra-faint dwarf. In this framework, at low gas metallicities, the IMF of newborn stellar populations becomes top-heavy, increasing the efficiency of supernova and photoionization feedback in regulating star formation. The increase in the feedback budget is none the less met by increased metal production from more numerous massive stars, leading to nearly constant iron content at $z = 0$ that is consistent with the results achieved from our model (for their case at a stellar mass of $M_\star = 10^3 M_\odot$, the typical metallicity is [Fe/H] ~ -2.5). Additionally, the study by Sanati et al. (2023), running zoom-in chemo-dynamical simulations of multiple halos and including models that account for the first generations of metal-free stars (Pop III), demonstrate an increase in the global metallicity of ultra-faints, although these are insufficient to resolve the tension with observations (see their fig. 6).

Several studies have examined the effect of different feedback processes on shaping the dwarf population (see, for example, Lu et al. 2017; Agertz et al. 2020; Smith et al. 2021). In this context, the work by Lu et al. (2017) using a semi-analytical model provides valuable insights. Their findings shed light on the connection between preventive and ejective feedback mechanisms and the stellar mass function and mass-metallicity relation of Milky Way dwarf galaxies. Where preventive feedback acts to inhibit baryons from accreting onto galaxies, and in the realm of low-mass halos, a commonly employed form of preventive feedback in SAMs is photoionization heating. This mechanism effectively reduces radiative cooling and mass accretion in low-mass halos, thereby influencing the evolution of these galaxies. On the other hand, ejective feedback processes involve the expulsion of baryons from the galaxy into the IGM, often characterized by the presence of outflows. These mechanisms play a significant role in shaping the gas content and subsequent star formation in dwarf galaxies. By incorporating both preventive and ejective feedback in their model, Lu et al. (2017) demonstrate the ability to simultaneously match the observed stellar mass function and the mass-metallicity relation. Moreover, they highlight the importance of considering a redshift dependence for preventive feedback, although the precise nature of this dependence remains largely uncertain.

Building upon the insights from Lu et al. (2017), our results further support the notion that the mass-metallicity relation for low-mass dwarfs is intricately linked to the interplay between feedback processes and the enrichment of the surrounding environment (i.e. enrichment of the IGM). We acknowledge that our approach is not self-consistent, as we do not explicitly account for the metal outflows from our galaxies and their mixing

into the IGM. However, the inclusion of IGM metallicity in our model becomes imperative to achieve consistency with observational data, as demonstrated by our agreement with observations.

Another study, conducted by Pandya et al. (2021), showcases that the mass loading factors for winds in dwarf galaxies can be large (i.e. $\gg 1$; as evident from their Fig. 7), and these winds are responsible for carrying away a significant portion of the produced metals. They also reveal that higher mass galaxies exhibit substantially lower mass loading factors for their winds, along with lower metal-loading factors. This finding suggests that dwarf galaxies may play a substantial role in enriching the IGM. Given these compelling facts, our SAM approach has the potential to allow us to resolve the dwarf galaxies and accurately predict IGM metal enrichment. Simultaneously, our SAM enables us to model the massive halos, which actively accrete gas from the enriched IGM, facilitating a comprehensive understanding of the intricate interplay between galaxies and their surrounding environment.

Size–mass relation

We measure the projected half mass radius ($r_{\rm h}$) for all galaxies in our sample and plot it against the predicted stellar masses. As depicted in Fig. 4.6, the black curve represents the median value, while the black and grey error bars indicate the 1 and 2 σ dispersion, respectively. Our predictions successfully capture the size-mass relation for the majority of observed galaxies (depicted by red markers) within the 2 σ range of our sample. Interestingly, we find that systems resembling Antlia II and Crater II are sometimes predicted by our model, although they lie far away from the median of the relation predicted by the

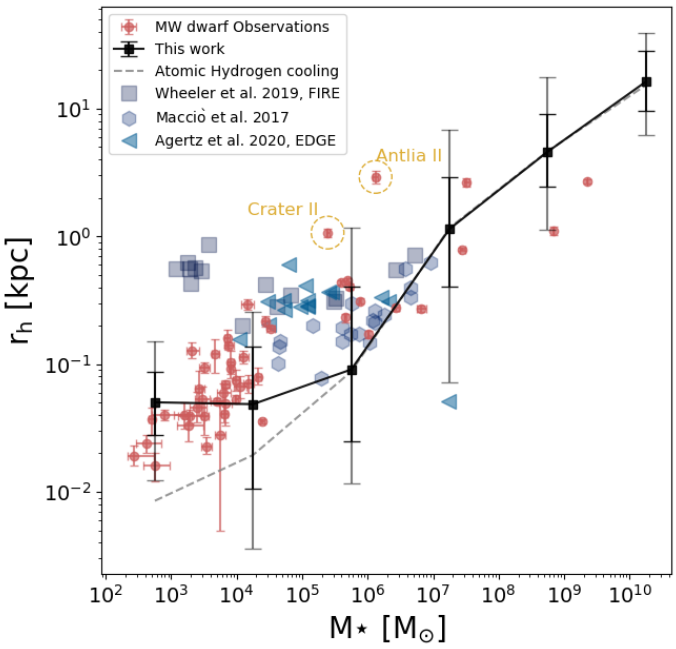

Figure 4.6: The size (projected half stellar mass radius)–stellar mass relation for dwarf galaxies. The black curve, along with the black and grey error bars, represents the median value, and the 1 and 2 σ dispersions, respectively, derived from our simulation's predictions. The gray dashed line represent the predictions of our model only including atomic hydrogen cooling. Blue markers demonstrate results from hydrodynamical simulations (Wheeler et al. 2019: blue squares; Macciò et al. 2017: blue hexagon; and Agertz et al. 2020: blue triangles). Red markers with error bars depict the observational results for dwarf galaxies located within 300 kpc of the MW, compiled primarily from studies by Drlica-Wagner et al. 2020; Simon 2019; McConnachie 2012.

model. Such galaxies correspond to the high angular momentum tail of the distribution of galaxy angular momenta—we will discuss the relation between size and angular momentum in more detail below. When comparing our results to hydrodynamical simulations, we generally agree with their best predictions above the $\sim 10^5$ $M_\odot$ limit, with the exception of a few extreme cases (e.g., the outlier presented by Agertz et al. (2020) where no feedback is included).

In our simulation, sizes are determined by the specific angular momentum content of stars and gas, as described by the equation:

$$j = v_{\rm h} r_{\rm h} = ({\rm G} M_{\rm h}/r_{\rm h})^{1/2} r_{\rm h} = ({\rm G} M_{\rm h} r_{\rm h})^{1/2}, \tag{4.6}$$

where $v_{\rm h}$ is the rotational speed at the half mass radius, $r_{\rm h}$ is the half mass radius, and $M_{\rm h}$ is the total mass content within the half mass radius. Given that intermediate and low-mass dwarfs are predominantly dark matter-dominated, and we have a reasonably accurate SMHM relation and a correctly modeled occupation fraction distribution, it is likely that the dark matter mass estimate is accurate. If we aim to explain the changes of slope in the size–mass relation of galaxies, the most apparent approach would be to look at the changes in the angular momentum content.

The angular momentum is primarily determined by the angular momentum of the gas in the halo during its formation, and subsequently, by the fraction of that angular momentum that is transferred into the galaxy through cooling and gas accretion, as well as the fraction that is expelled by outflows. These factors encompass a certain level of uncertainty. In our current model, we address the inefficiencies of atomic hydrogen cooling by incorporating H_2 cooling. Specifically, for temperatures below 10^4 K, corresponding to halo masses around $10^9 M_\odot$, which host galaxies with stellar mass components ranging from 10^4–$10^5 M_\odot$, the dominant cooling mechanism becomes H_2 cooling. Additionally, we include the UV background radiation model by FG20, which suppresses gas accretion. From Fig. 4.3, we observe that its effects are maximized for dwarfs with stellar masses below $10^5 M_\odot$. The overall effect becomes evident when comparing the black solid line representing

our optimal model to the dashed grey line, where only atomic hydrogen cooling is present and no UV background radiation was used. These results suggest that variations in cooling mechanisms along with gas accretion suppression can account for the observed changes in the slope at these particular mass scales. TAR

Velocity dispersion—mass relation

We measure the 1D line-of-sight velocity dispersions at the half stellar mass radius for all galaxies in our sample and plot them against the predicted stellar masses. In Fig. 4.7, similar to Fig. 4.6, the black curve represents the median value, while the black and grey error bars indicate the 1 and 2 σ dispersion, respectively. Our predictions successfully reproduce the velocity dispersion–mass relation for observed galaxies within the 2 σ limit of our sample (all the observational data are represented by red markers). We compared our results with hydrodynamical simulations by Macciò et al. (2017); Agertz et al. (2020), shown by blue markers, finding general agreement within the 2 σ dispersion limit.

It is worth noting that our model does not fully capture the observed scatter in 1D velocity dispersions at the lower mass end. Several potential reasons may explain this. Firstly, it is possible that our current model does not incorporate all the relevant physical processes that govern the ultra-faint regime. The intricate dynamics and feedback mechanisms specific to these low-mass galaxies could play a significant role in shaping their velocity dispersions. Secondly, observational limitations introduce additional uncertainties in our measurements. Factors such as contamination from foreground stars in the MW

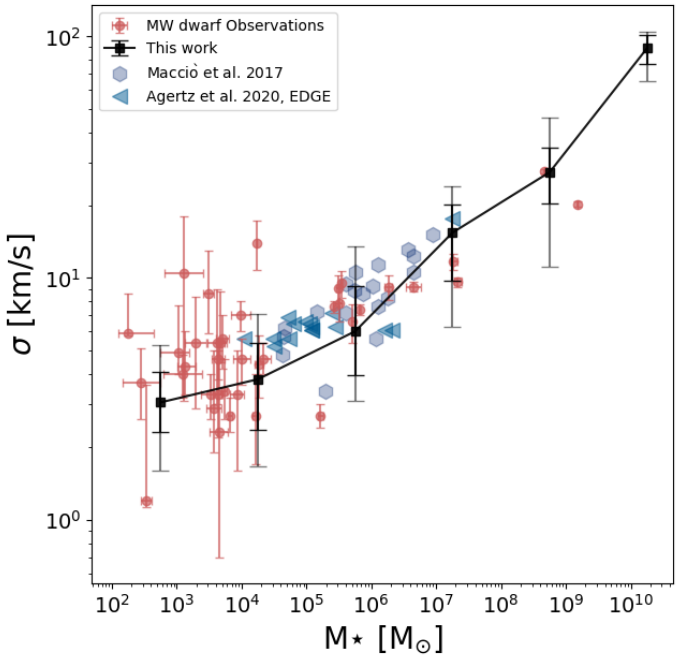

Figure 4.7: The 1D line-of-sight velocity dispersion (measured at the half stellar mass radius)–stellar mass relation. The black curve, along with the black and grey error bars, represents the median value, and the 1 and 2 σ dispersions, respectively, derived from our simulation's predictions. The hydrodynamical simulation results are shown by blue markers, with Macciò et al. 2017 represented by blue hexagons, and Agertz et al. 2020 by blue triangles. The red markers with error bars depict the observational results for dwarf galaxies located within 300 kpc of the MW, compiled primarily from studies by Drlica-Wagner et al. 2020; Simon 2019; McConnachie 2012. Our results demonstrate agreement with the velocity dispersion–mass relation in higher mass galaxies, while indicating lower median predictions for galaxies with stellar masses below 10^5 $M_\odot$.

and the influence of binary stars within the sample of stars from the ultra-faint dwarfs (see Simon 2019 for further details) could contribute to the observed large dispersions.

We would like to highlight that, given the observational uncertainties, our model's predictions align well with the data, providing consistency without necessitating the inclusion of core formation. However, it is crucial to emphasize that these observational uncertainties also mean that we cannot conclusively rule out the possibility of core formation being present. This highlights the need for improved and more precise measurements in order to better understand and constrain the underlying physical processes. Additionally, our model's success in matching the velocity dispersion, combined with accurate predictions of the occupation fraction, suggests that it is effectively free of the too-big-to-fail problem (Boylan-Kolchin et al. 2011).

4.4.3 Mass function predictions for various halo masses

Once calibrated, we can use our model to make predictions on the abundance of satellite galaxies for host systems with varying virial masses. In Fig. 4.8, we depict the cumulative stellar mass functions for subhalos associated with various halos of different masses, specifically showcasing satellites with stellar masses ($M_\star$) greater than $10^2 M_\odot$ and half mass radius ($r_{1/2}$) larger than 10 pc. The dark and light shaded grey regions represent the 1 and 2 σ dispersion, respectively, while the black line shows the median of the results. For comparison, the red curve represents available observational results[18], and the blue

[18]The V-band magnitudes for satellites of the MW, M31, and LMC are sourced from McConnachie (2012)'s revised compilation of Local Group dwarfs. For the Cen A system, values are extracted from Crnojević et al. (2019). Subsequently, the stellar masses are computed by employing relevant mass-to-light ratios derived from Galacticus predictions specific to the respective stellar masses.

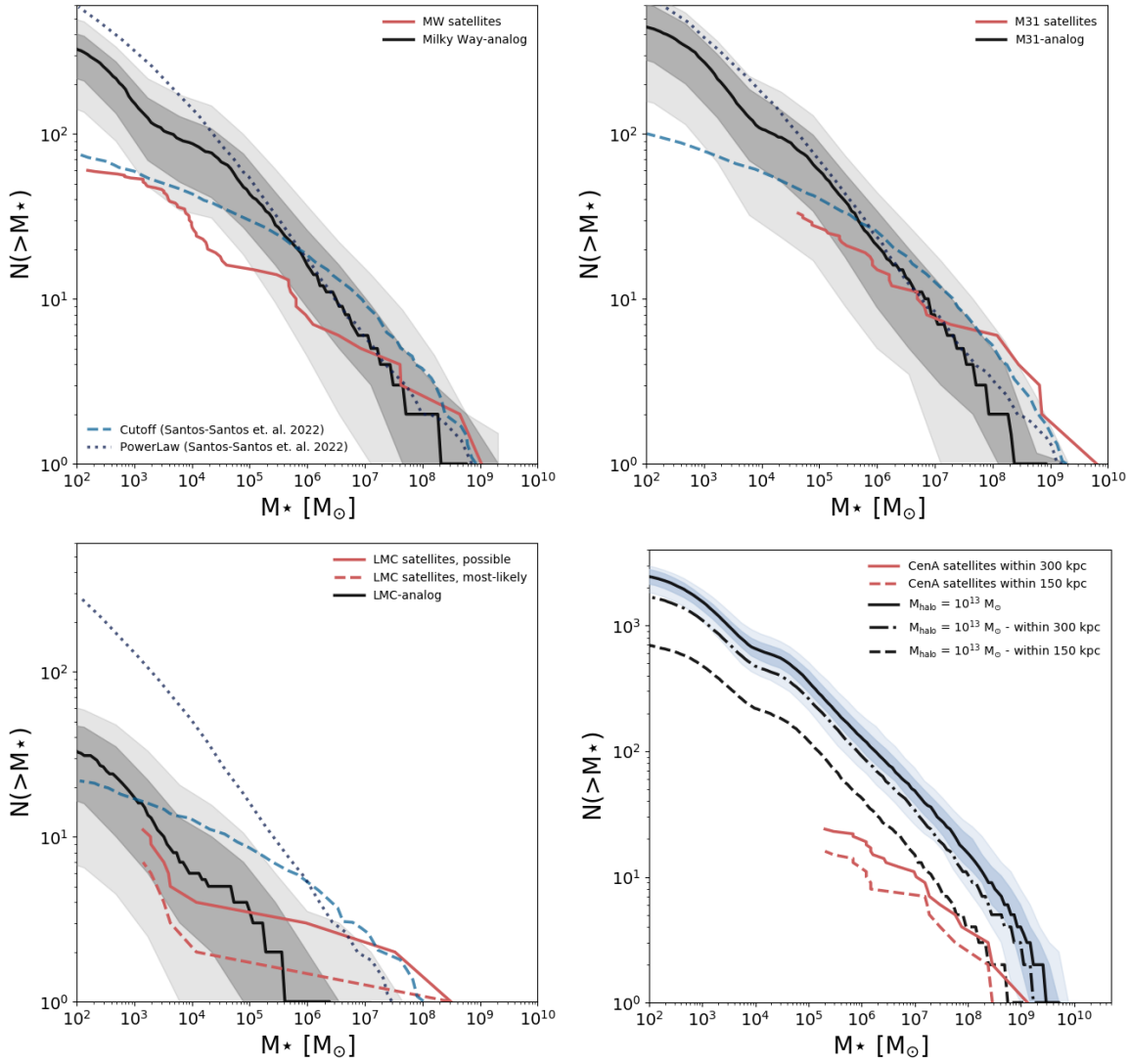

Figure 4.8: Predictions of our model for the cumulative stellar mass function of satellites. The black curve represents the median of our results, while the light and dark shaded regions indicate the 1 and 2 σ dispersions, respectively. Observational constraints, if available, are shown by the red curves. The dashed and dotted blue lines correspond to the "Cutoff" and "PowerLaw" models from Santos-Santos et al. 2022, allowing for a comparison with their results. Each panel displays our results for a different halo mass: the top left panel corresponds to the MW-analog halo, the top right panel to the M31-analog halo, the bottom left panel to the LMC-analog halo, the bottom right panel to a group-size halo with a mass of 10^{13} $M_\odot$.

dashed and dotted curves represent the results from the abundance matching study by Santos-Santos et al. (2022). The blue dotted line corresponds to their "power-law" model, assuming a power law relation for the $M_\star$ – $V_{\rm max}$ relation, while the blue dashed curve corresponds to their "cutoff" model, assuming a cut-off in this relation.

In the top left panel, we present our results for the MW-analog. We ran 100 halos with virial masses ranging from 7×10^{11} to $1.9 \times 10^{12} M_\odot$, in agreement with the current available mass constraints (Wang et al. 2020; Callingham et al. 2019). Our results show a reasonable agreement with the observations for the stellar masses of larger satellites (within 300 kpc from the MW). However, for the lower mass range, the discrepancy between our results and the observations becomes more prominent. This discrepancy could be partially attributed to incompleteness in the observational results, as we discussed in section 4.4.1, where estimations for corrections in the observational data predict much higher values for the number of MW satellites (Tollerud et al. 2008; Drlica-Wagner et al. 2020). Overall, our model suggests that only ∼20% of the MW satellites with $M_V < 0$ have been discovered.

Comparing with the results of Santos-Santos et al. (2022), we find reasonable agreement up to a stellar mass of $10^5 M_\odot$ for the satellites, and our results deviate from their predictions in the ultra-faint regime. Notably, the slope of our results in this regime shows better agreement with their power-law model, although the total predicted number of halos is a factor of ∼2 lower. It is worth mentioning that this slope was only achieved by including the effects of H_2 cooling, as our model with only atomic hydrogen physics shows flatter slopes, in better agreement with their cut-off model (see Fig. 4.4 for comparison of our models).

The top right panel presents our results for the M31-analog. Similar to the MW case, we ran 100 realizations of a halo with a mass of $1.8 \pm 0.5 \times 10^{12} M_{\odot}$, in agreement with M31 mass constraints (from Benisty et al. 2022; Shull 2014; Diaz et al. 2014; Karachentsev and Kudrya 2014). Our results show agreement with the observations within the 2 σ limit (albeit we get lower results for the higher mass end), although the surveyed population in M31 does not extend as deeply as our predictions show. Similar to the MW case, we observe agreement with Santos-Santos et al. (2022)'s results in the higher mass regime, while in the ultra-faint regime, our model predicts results closer to their power-law model. It is worth mentioning that their models assume an occupation fraction of 1 for their halos, whereas we found in section 4.4.1 that only a fraction of our halos with peak masses below $2 \times 10^{8} M_{\odot}$ host a luminous component.

The bottom left panel shows our results for the LMC-analog halo. We present the mass function results for satellite stellar masses based on 100 realizations of hosts with halo masses of $1.88 \pm 0.35 \times 10^{11} M_{\odot}$ (Shipp et al. 2021). Our findings estimate that an isolated LMC-analog is expected to have approximately 33^{+14}_{-12} satellites (for 1 σ dispersion) with stellar masses above $10^{2} M_{\odot}$ and $r_{1/2}$ larger than 10 pc, lying within the halo's virial radius. Most of the realizations indicate that satellites have stellar masses below $4 \times 10^{6} M_{\odot}$, and the likelihood of generating an SMC within the virial radius is relatively low.

We then compare these results with the satellites associated with the LMC based on the kinematic analysis conducted by Santos-Santos et al. (2021). According to their analysis, 11 of the MW satellites appear to have some connection with the LMC ("possible"), and from those, 7 show firm association ("most likely"). Our results seem to under-predict

the number of higher mass subhalos while over-predicting the number of currently observed ultra-faint satellites. Apart from considering the effects of observational incompleteness, other factors may be at play here. Firstly, we do not constrain our LMC-analogs to have any high mass satellites such as the SMC. The occurrence of reproducing such a massive companion for the LMC in our model is probabilistically low, as only 1 such satellite was produced in our 100 realizations of the LMC, and it is located at a distance of approximately 140 kpc from the LMC-analog (beyond the virial radius of this halo/radius of approximately 100 kpc where we measure the associated satellites). Additionally, we are running our LMC-analogs as isolated halos and not in association with a larger halo such as the MW. The presence of a larger gravitational potential can more effectively disrupt the ultra-faint satellites, thereby decreasing the number of predicted satellites associated with the LMC.

Comparing with the results from Nadler et al. (2020), they predict 48 $\pm$ 8 LMC-associated satellites with $M_V < 0$ mag and $r_{1/2} > 10$ pc, approximately consistent with our predictions of 33^{+14}_{-12} for 1σ (33^{+28}_{-26} for 2σ). This is also in reasonable agreement with the $\sim$70 satellites with $-7 < M_V < -1$ predicted by Jethwa et al. (2016) via dynamical modeling of the Magellanic Cloud satellite population. Additionally, our predictions can be compared with the work of Dooley et al. (2017), who explored the satellite population of LMC-like hosts using several abundance-matching models and estimated $\sim$8-15 dwarf satellites with $M_* \geq 10^3 M_\odot$ within a 50 kpc radius of their hosts. Applying similar selection criteria to our model results gives us an estimation of 6^{+6}_{-4}. Furthermore, our results align well with the study by Jahn et al. (2019), where they used five zoom-in simulations of LMC-mass hosts (with halo masses ranging from 1×10^{11} to $3 \times 10^{11} M_\odot$) run with the FIRE galaxy

formation code, predicting $\sim$ 5–10 ultra-faint companions for their LMC-mass systems that have stellar masses above $10^4 M_\odot$ (compared to our estimation of 6^{+5}_{-4} for 1σ dispersion). However, it is worth noting that our stellar mass function is steeper than their results.

The bottom right panel illustrates our model's prediction for the satellite stellar mass function of subhalos within group-sized halos. These results are based on 100 realizations of a host halo with a mass of $10^{13}\,M_\odot$. The shaded region in this plot is depicted in a distinct color as it differs from the other panels. In this case, the dispersion only represents variations resulting from constructing merger trees for the exact same halo mass, while in other panels, we include a range of masses for the halos, leading to a larger halo-to-halo scatter.

Regarding the predicted stellar mass function for the satellites, we find more massive satellites compared to those in the MW and M31, along with a larger number of total subhalos (with $r_{1/2} > 10$ pc) within a radius of 450 kpc from the central galaxy (or the estimated virial radius). This trend is consistent with expectations for a halo with a larger virial mass. As a candidate in the nearby universe, we compare our results to Centaurus A (Cen A for short) with virial mass estimations ranging from $6.4 \times 10^{12} M_\odot$ to $1.8 \times 10^{13} M_\odot$ (Karachentsev et al. 2007; van den Bergh 2000). The V band magnitudes of Cen A's satellites were compiled from Crnojević et al. (2019).

The study by Crnojević et al. (2019) covers approximately half of the virial radius estimated for Cen A and includes satellites down to $M_V = -7.8$ (equivalent to a stellar mass of approximately $10^5 M\odot$). Additionally, Crnojević et al. (2019) provides results from earlier studies of Cen A (Sharina et al. 2008; Karachentsev et al. 2013), which target a

wider region around the central galaxy, albeit with a lower limiting magnitude. Since the observational surveys each cover part of this group, we have adjusted the radius within which we make the comparison accordingly. Our model predictions depicted by the black dashed line, corresponds to satellite mass function within a radius of 150 kpc from the central galaxy. This selection mirrors the observational results with the same cuts, as shown by the red dashed line. Additionally, our results shown by the dashed-dotted line represent the satellite mass function within 300 kpc from the central galaxy, which can be compared to the observational data with similar cuts, as indicated by the red line.

Our results align well with the slope of the observational satellite stellar mass function at the higher mass end, although the exact number of predicted satellites is slightly higher. This can be interpreted as our results favoring a virial mass for Cen A close to the lower end of the current estimates, as number of satellites tend to scale on host halo mass. In any case, if we assume that a $10^{13}M_{\odot}$ halo is a good representation of this system, our results suggest that a factor of ∼5-7 satellites with stellar masses above $10^{5}M_{\odot}$ are waiting to be discovered in this system. Additionally, a forthcoming study by Weerasooriya et al. (in prep.), utilizing the model outlined in Weerasooriya et al. (2023), has also examined the Cen A system. Their prediction for the total count of satellites with M_V magnitudes lower than -7.4 (equivalent to stellar masses around $10^{5}M_{\odot}$) amounts to median number of 50. While the median is slightly lower than their compiled observational data for satellites of Cen A within 150 kpc[19], the predicted distribution of the number of satellites still falls

[19]Their work encompasses a comprehensive compilation of the luminosity function for Cen A, including available observational data from Lauberts and Valentijn (1989); de Vaucouleurs et al. (1991); Karachentsev et al. (2003); James et al. (2004); Doyle et al. (2005); Sharina et al. (2008); Karachentsev et al. (2013); Müller et al. (2015, 2017, 2019); Crnojević et al. (2014, 2016, 2019); Taylor et al. (2016). It is important to note that their dataset includes all dwarf candidates, not exclusively confirmed cases.

within the observed range. These results are marginally lower than our predictions below $M_V \sim$ -10.

4.5 Conclusions

In this study we have modified the Galacticus semi-analytic model to incorporate key physical processes relevant to the formation of dwarf galaxies, and utilized that model to explore predictions for the galaxy-halo connection and the properties of the dwarf galaxy population of the Milky Way. Through the inclusion of essential physical processes such as IGM metallicity, H_2 cooling, and UV background radiation, coupled with the fine-tuning of various parameters, we have achieved significant success in replicating several characteristics observed in the dwarf galaxy population.

First and foremost, we find that our model with updated physics is able to reproduce the inferred SMHM relation while simultaneously reproducing the main physical properties of the dwarf galaxy population. This finding underscores the robustness of our model and its ability to capture the relationship between the stellar content and the underlying dark matter halos. Furthermore, our results demonstrate that the inclusion of H_2 cooling and a UV background radiation (prescribed by FG20), motivated by recent observational constraints, is crucial to achieving an occupation fraction consistent with previous inferences. Our study reveals that the fraction of subhalos hosting galaxies with an absolute V-band magnitude less than 0 drops to 50% at a halo peak mass of $\sim 8.9 \times 10^7$ $M_\odot$. Notably, earlier estimations based on older UV background estimates (HM12) do not yield the same level of agreement.

When examining the statistical properties of the MW dwarf population, we find broad success in reproducing key characteristics. Our predictions for the luminosity function of the MW dwarfs align well with observations once we account for the inherent halo-to-halo scatter. Remarkably, the presence of H_2 cooling is vital for capturing the large number of ultra-faint dwarf galaxies, highlighting its role in driving their formation. Our model predicts a total of 300^{+75}_{-99} satellites with an absolute V-band magnitude less than 0 within 300 kpc from our MW-analogs. This number would drop down to 91^{+42}_{-34} if we were to use our model including only the atomic hydrogen cooling. Our model of H_2 formation/destruction remains quite simplistic. Plausible changes in the underlying assumptions in computing metal cooling and H_2 formation/destruction under a radiation field (e.g. considering radiation from local sources, not just a mean background), could result in changes to the cooling efficiencies in small, early-forming halos. The efficiency and relevance of H_2 cooling in such halos remain subjects of ongoing debate (refer to Section 4.3.2 of the review by Klessen and Glover 2023, and references therein).

Moreover, the inclusion of IGM metallicity enables us to successfully reproduce the mass-metallicity relation without the need for preventive feedback mechanisms. Our model achieves successful agreement with the sizes and velocity dispersions of ultra-faint dwarfs.

Finally, our model successfully predicts the stellar mass function of satellites for both MW and M31 analogs. Additionally, we use our model to make predictions for the two different mass scales: LMC and Cen A analogs. Our results demonstrate a general agreement with the available observational data, emphasizing the robustness of our model

in generating predictions across a broad range of halo masses. The combined functionalities of this model, along with its comprehensive approach to predicting various aspects of the dwarf population, makes it uniquely powerful for investigating the faintest galaxy population across a range of environments/halo masses.

Looking ahead, there are several exciting directions to explore. Investigating how our results are influenced by the inclusion of an LMC-analog in the MW mass halos will provide valuable insights into the impact of satellite galaxies on the MW dwarf population, e.g. following the constrained merger tree methodology presented in Nadler et al. (2023a). Furthermore, exploring alternative non-CDM models, such as self-interacting dark matter, will allow us to gauge the extent to which observations of dwarfs can inform our understanding of the nature of dark matter itself.

Chapter 5

Conclusions

In this dissertation, a comprehensive study was conducted on the formation and evolution of dwarf galaxies, their environments, and corresponding dark matter halos, with a focus on their contributions to the intra-group/intra-cluster light. Advanced cosmological hydrodynamical simulations and semi-analytical models were utilized to address several open questions in the field of galaxy formation and evolution. These include investigating the mechanisms driving the formation of ICL, the role of dwarf galaxies as contributors and building blocks of ICL, and the reliability of ICL and its globular cluster components as tracers of the underlying dark matter and the formation history of halos. The study also explores the relation between dwarf galaxy properties and their corresponding dark matter halos, making predictions about the mass of halos hosting the faintest observed galaxies. Through these simulations, the impact of larger cosmic environments on these faint galaxies and their dark matter halos was examined.

Using the cosmological hydrodynamical simulation TNG50, complemented with a globular cluster catalog, the predicted amount of light, metallicity, and radial distribution of stars and globular clusters in the intra-group/intra-cluster components were explored. It was found that dwarf galaxies have a wide range of relevance as builders of these components. Some systems show negligible contribution from galaxies with $M\star < 10^{10}$ $M_{\odot}$, leaving distinct signatures on the metallicity content of the ICL and resulting in groups with shallower metallicity profiles. These findings have implications for upcoming deep observations, such as those planned by the Euclid and Roman space telescopes. Additionally, intra-cluster globular clusters were identified as valuable tracers of halo assembly histories, especially in cases where observing the ICL proves challenging. Our study highlights that the shape and orientation of the ICL and ICGCs show a reasonable correlation with those of the dark matter in the outskirts of the halo, underscoring the common origin of these components and their potential to be used as luminous tracers for the underlying dark matter.

The ICL component of Virgo-like clusters was investigated by analyzing ICL fractions, density profiles for different components, and star formation rates. Simulation results predict an ICL component comparable to the brightest cluster galaxy in mass and rate of star formation. An in-situ component is always present at any redshift (z) in all Virgo-like clusters, contributing approximately 8–28% of the stellar mass in the ICL (at $z = 0$). It is anticipated that a widespread form of star formation causes the existence of the in-situ stellar component, with filamentary structures extending for hundreds of kiloparsecs and tracing the distribution of neutral gas in the cluster host halo.

Additionally, the semi-analytic model Galacticus was modified to accurately reproduce the observed properties of dwarf galaxies in the Milky Way. This modified semi-analytic framework was validated through a comparative analysis of the resulting galaxy-halo connection. By fine-tuning various model parameters and incorporating empirical constraints, the model was tailored to match the statistical properties of Milky Way dwarf galaxies, such as their luminosity function and size-mass relation. It was found that reproducing observational determinations of the halo occupation fraction (as inferred by Nadler et al. 2020) and the mass-metallicity relation (see Simon 2019) for dwarf galaxies required the inclusion of H_2 cooling, an updated UV background radiation model, and a model for the metal content of the intergalactic medium. Our findings show that, in the model including H_2 cooling and UV background radiation, the fraction of subhalos hosting a galaxy with $M_V < 0$ drops to 50% by a halo peak mass of approximately 8.9×10^7 $M_\odot$, consistent with recent observational estimates from Nadler et al. 2020.

Looking forward, the methodologies and findings of this dissertation pave the way for several promising avenues of research. One example is future studies extending the approach in this work to alternative dark matter models, which might include numerical simulations and also semi-analytical treatments, with the aim to compare their predictions on the formation and evolution of dwarf galaxies to those within the ΛCDM model explored here. Additionally, the integration of observational data from upcoming telescopes will further refine the models and enhance understanding of the role of dwarf galaxies in the broader cosmic structure.

Bibliography

Abdurro'uf, Katherine Accetta, Conny Aerts, Vıctor Silva Aguirre, Romina Ahumada, Nikhil Ajgaonkar, N. Filiz Ak, Shadab Alam, Carlos Allende Prieto, Andrés Almeida, Friedrich Anders, Scott F. Anderson, Brett H. Andrews, Borja Anguiano, Erik Aquino-Ort, Alfonso Aragón-Salamanca, Maria Argudo-Fernández, Metin Ata, Marie Aubert, Vladimir Avila-Reese, Carles Badenes, Rodolfo H. Barbá, Kat Barger, Jorge K. Barrera-Ballesteros, Rachael L. Beaton, Timothy C. Beers, Francesco Belfiore, Chad F. Bender, Mariangela Bernardi, Matthew A. Bershady, Florian Beutler, Christian Moni Bidin, Jonathan C. Bird, Dmitry Bizyaev, Guillermo A. Blanc, Michael R. Blanton, Nicholas Fraser Boardman, Adam S. Bolton, Médéric Boquien, Jura Borissova, Jo Bovy, W. N. Brandt, Jordan Brown, Joel R. Brownstein, Marcella Brusa, Johannes Buchner, Kevin Bundy, Joseph N. Burchett, Martin Bureau, Adam Burgasser, Tuesday K. Cabang, Stephanie Campbell, Michele Cappellari, Joleen K. Carlberg, Fábio Carneiro Wanderley, Ricardo Carrera, Jennifer Cash, Yan-Ping Chen, Wei-Huai Chen, Brian Cherinka, Cristina Chiappini, Peter Doohyun Choi, S. Drew Chojnowski, Haeun Chung, Nicolas Clerc, Roger E. Cohen, Julia M. Comerford, Johan Comparat, Luiz da Costa, Kevin Covey, Jeffrey D. Crane, Irene Cruz-Gonzalez, Connor Culhane, Katia Cunha, Y. Sophia Dai, Guillermo Damke, Jeremy Darling, Jr. Davidson, James W., Roger Davies, Kyle Dawson, Nathan De Lee, Aleksandar M. Diamond-Stanic, Mariana Cano-D´, Helena Dom´úez Sánchez, John Donor, Chris Duckworth, Tom Dwelly, Daniel J. Eisenstein, Yvonne P. Elsworth, Eric Emsellem, Mike Eracleous, Stephanie Escoffier, Xiaohui Fan, Emily Farr, Shuai Feng, José G. Fernández-Trincado, Diane Feuillet, Andreas Filipp, Sean P. Fillingham, Peter M. Frinchaboy, Sebastien Fromenteau, áfael A. Galbany, Llu´sńd Garc´a, D. A. Garc´a-Hńández, Junqiang Ge, Doug Geisler, Joseph Gelfand, Tobias Géron, Benjamin J. Gibson, Julian Goddy, Diego Godoy-Rivera, Kathleen Grabowski, Paul J. Green, Michael Greener, Catherine J. Grier, Emily Griffith, Hong Guo, Julien Guy, Massinissa Hadjara, Paul Harding, Sten Hasselquist, Christian R. Hayes, Fred Hearty, Jesús Hernández, Lewis Hill, David W. Hogg, Jon A. Holtzman, Danny Horta, Bau-Ching Hsieh, Chin-Hao Hsu, Yun-Hsin Hsu, Daniel Huber, Marc Huertas-Company, Brian Hutchinson, Ho Seong Hwang, Héctor J. Ibarra-Medel, Jacob Ider Chitham, Gabriele S. Ilha, Julie Imig, Will Jaekle, Tharindu Jayasinghe, Xihan Ji, Jennifer A. Johnson, Amy Jones, Henrik Jönsson, Ivan Katkov, Dr. Khalatyan, Arman, Karen Kinemuchi, Shobhit Kisku, Johan H. Knapen, Jean-Paul Kneib, Juna A. Kollmeier, Miranda Kong, Marina Kounkel, Kathryn Kreckel, Dhanesh Krishnarao, Ivan Lacerna, Richard R. Lane, Rachel Langgin, Ramon Lavender, David R. Law, Daniel Lazarz, Henry W. Leung, Ho-Hin Leung, Hannah M. Lewis, Cheng Li,

Ran Li, Jianhui Lian, Fu-Heng Liang, Lihwai Lin, Yen-Ting Lin, Sicheng Lin, Chris Lintott, Dan Long, Penélope Longa-Peña, Carlos López-Cobá, Shengdong Lu, Britt F. Lundgren, Yuanze Luo, J. Ted Mackereth, Axel de la Macorra, Suvrath Mahadevan, Steven R. Majewski, Arturo Manchado, Travis Mandeville, Claudia Maraston, Berta Margalef-Bentabol, Thomas Masseron, Karen L. Masters, Savita Mathur, Richard M. McDermid, Myles Mckay, Andrea Merloni, Michael Merrifield, Szabolcs Meszaros, Andrea Miglio, Francesco Di Mille, Dante Minniti, Rebecca Minsley, Antonela Monachesi, Jeongin Moon, Benoit Mosser, John Mulchaey, Demitri Muna, Ricardo R. Muñoz, Adam D. Myers, Natalie Myers, Seshadri Nadathur, Preethi Nair, Kirpal Nandra, Justus Neumann, Jeffrey A. Newman, David L. Nidever, Farnik Nikakhtar, Christian Nitschelm, Julia E. O'Connell, Luis Garma-Oehmichen, Gabriel Luan Souza de Oliveira, Richard Olney, Daniel Oravetz, Mario Ortigoza-Urdaneta, Yeisson Osorio, Justin Otter, Zachary J. Pace, Nelson Padilla, Kaike Pan, Hsi-An Pan, Taniya Parikh, James Parker, Sebastien Peirani, árla Peña Ram´rez, Samantha Penny, Will J. Percival, Ismael Perez-Fournon, Marc Pinsonneault, Frédérick Poidevin, Vijith Jacob Poovelil, Adrian M. Price-Whelan, Anna Bárbara de Andrade Queiroz, M. Jordan Raddick, Amy Ray, Sandro Barboza Rembold, Nicole Riddle, Rogemar A. Riffel, Rogério Riffel, Hans-Walter Rix, Annie C. Robin, Aldo Rodr´guez-ébla, Alexandre Roman-Lopes, Carlos Román-Zúñiga, Benjamin Rose, Ashley J. Ross, Graziano Rossi, Kate H. R. Rubin, Mara Salvato, Sebástian F. Sánchez, José R. Sánchez-Gallego, Robyn Sanderson, Felipe Antonio Santana Rojas, Edgar Sarceno, Regina Sarmiento, Conor Sayres, Elizaveta Sazonova, Adam L. Schaefer, Ricardo Schiavon, David J. Schlegel, Donald P. Schneider, Mathias Schultheis, Axel Schwope, Aldo Serenelli, Javier Serna, Zhengyi Shao, Griffin Shapiro, Anubhav Sharma, Yue Shen, Matthew Shetrone, Yiping Shu, Joshua D. Simon, M. F. Skrutskie, Rebecca Smethurst, Verne Smith, Jennifer Sobeck, Taylor Spoo, Dani Sprague, David V. Stark, Keivan G. Stassun, Matthias Steinmetz, Dennis Stello, Alexander Stone-Martinez, Thaisa Storchi-Bergmann, Guy S. Stringfellow, Amelia Stutz, Yung-Chau Su, Manuchehr Taghizadeh-Popp, Michael S. Talbot, Jamie Tayar, Eduardo Telles, Johanna Teske, Ani Thakar, Christopher Theissen, Andrew Tkachenko, Daniel Thomas, Rita Tojeiro, Hector Hernandez Toledo, Nicholas W. Troup, Jonathan R. Trump, James Trussler, Jacqueline Turner, Sarah Tuttle, Eduardo Unda-Sanzana, José Antonio Vázquez-Mata, Marica Valentini, Octavio Valenzuela, Jaime Vargas-González, Mariana Vargas-Magaña, Pablo Vera Alfaro, Sandro Villanova, Fiorenzo Vincenzo, David Wake, Jack T. Warfield, Jessica Diane Washington, Benjamin Alan Weaver, Anne-Marie Weijmans, David H. Weinberg, Achim Weiss, Kyle B. Westfall, Vivienne Wild, Matthew C. Wilde, John C. Wilson, Robert F. Wilson, Mikayla Wilson, Julien Wolf, W. M. Wood-Vasey, Renbin Yan, Olga Zamora, Gail Zasowski, Kai Zhang, Cheng Zhao, Zheng Zheng, Zheng Zheng, and Kai Zhu. The seventeenth data release of the sloan digital sky surveys: Complete release of manga, mastar, and apogee-2 data. *ApJS*, 259(2):35, April 2022. doi: 10.3847/1538-4365/ac4414.

T. Abel. PhD thesis, -, January 1995.

Tom Abel, Peter Anninos, Yu Zhang, and Michael L. Norman. Modeling primordial gas in numerical cosmology. , 2(3):181–207, August 1997. doi: 10.1016/S1384-1076(97)00010-9.

Andrea Afruni, Filippo Fraternali, and Gabriele Pezzulli. Cool circumgalactic gas of passive galaxies from cosmological inflow. *åp*, 625:A11, May 2019. doi: 10.1051/0004-6361/201835002.

Oscar Agertz, Romain Teyssier, and Ben Moore. Disc formation and the origin of clumpy galaxies at high redshift. *MNRAS*, 397(1):L64–L68, July 2009. doi: 10.1111/j.1745-3933.2009.00685.x.

Oscar Agertz, Andrew Pontzen, Justin I. Read, Martin P. Rey, Matthew Orkney, Joakim Rosdahl, Romain Teyssier, Robbert Verbeke, Michael Kretschmer, and Sarah Nickerson. Edge: the mass-metallicity relation as a critical test of galaxy formation physics. *MNRAS*, 491(2):1656–1672, January 2020. doi: 10.1093/mnras/stz3053.

Anthony Aguirre, Corey Dow-Hygelund, Joop Schaye, and Tom Theuns. Metallicity of the intergalactic medium using pixel statistics. iv. oxygen. *The Astrophysical Journal*, 689: 851–864, 12 2008. ISSN 0004-637X. doi: 10.1086/592554.

Romina Ahumada, Carlos Allende Prieto, Andrés Almeida, Friedrich Anders, Scott F. Anderson, Brett H. Andrews, Borja Anguiano, Riccardo Arcodia, Eric Armengaud, Marie Aubert, Santiago Avila, Vladimir Avila-Reese, Carles Badenes, Christophe Balland, Kat Barger, Jorge K. Barrera-Ballesteros, Sarbani Basu, Julian Bautista, Rachael L. Beaton, Timothy C. Beers, B. Izamar T. Benavides, Chad F. Bender, Mariangela Bernardi, Matthew Bershady, Florian Beutler, Christian Moni Bidin, Jonathan Bird, Dmitry Bizyaev, Guillermo A. Blanc, Michael R. Blanton, Médéric Boquien, Jura Borissova, Jo Bovy, W. N. Brandt, Jonathan Brinkmann, Joel R. Brownstein, Kevin Bundy, Martin Bureau, Adam Burgasser, Etienne Burtin, Mariana Cano-Dıaz, Raffaella Capasso, Michele Cappellari, Ricardo Carrera, Solène Chabanier, William Chaplin, Michael Chapman, Brian Cherinka, Cristina Chiappini, Peter Doohyun Choi, S. Drew Chojnowski, Haeun Chung, Nicolas Clerc, Damien Coffey, Julia M. Comerford, Johan Comparat, Luiz da Costa, Marie-Claude Cousinou, Kevin Covey, Jeffrey D. Crane, Katia Cunha, Gabriele da Silva Ilha, Yu Sophia Dai, Sanna B. Damsted, Jeremy Darling, Jr. Davidson, James W., Roger Davies, Kyle Dawson, Nikhil De, Axel de la Macorra, Nathan De Lee, Anna Bárbara de Andrade Queiroz, Alice Deconto Machado, Sylvain de la Torre, Flavia Dell'Agli, Hélion du Mas des Bourboux, Aleksandar M. Diamond-Stanic, Sean Dillon, John Donor, Niv Drory, Chris Duckworth, Tom Dwelly, Garrett Ebelke, Sarah Eftekharzadeh, Arthur Davis Eigenbrot, Yvonne P. Elsworth, Mike Eracleous, Ghazaleh Erfanianfar, Stephanie Escoffier, Xiaohui Fan, Emily Farr, José G. Fernández-Trincado, Diane Feuillet, Alexis Finoguenov, Patricia Fofie, Amelia Fraser-McKelvie, Peter M. Frinchaboy, Sebastien Fromenteau, Hai Fu, Llu Galbany, Rafael A. Garcia, D. A. Garc´ıa-Hernández, Luis Alberto Garma Oehmichen, Junqiang Ge, Marcio Antonio Geimba Maia, Doug Geisler, Joseph Gelfand, Julian Goddy, Violeta Gonzalez-Perez, Kathleen Grabowski, Paul Green, Catherine J. Grier, Hong Guo, Julien Guy, Paul Harding, Sten Hasselquist, Adam James Hawken, Christian R. Hayes, Fred Hearty, S. Hekker, David W. Hogg, Jon A. Holtzman, Danny Horta, Jiamin Hou, Bau-Ching Hsieh, Daniel Huber, Jason A. S. Hunt, J. Ider Chitham, Julie Imig, Mariana Jaber, Camilo Eduardo Jimenez Angel, Jennifer A. Johnson, Amy M. Jones, Henrik Jönsson,

Eric Jullo, Yerim Kim, Karen Kinemuchi, IV Kirkpatrick, Charles C., George W. Kite, Mark Klaene, Jean-Paul Kneib, Juna A. Kollmeier, Hui Kong, Marina Kounkel, Dhanesh Krishnarao, Ivan Lacerna, Ting-Wen Lan, Richard R. Lane, David R. Law, Jean-Marc Le Goff, Henry W. Leung, Hannah Lewis, Cheng Li, Jianhui Lian, Lihwai Lin, Dan Long, Penélope Longa-Peña, Britt Lundgren, Brad W. Lyke, J. Ted Mackereth, Chelsea L. MacLeod, Steven R. Majewski, Arturo Manchado, Claudia Maraston, Paul Martini, Thomas Masseron, Karen L. Masters, Savita Mathur, Richard M. McDermid, Andrea Merloni, Michael Merrifield, Szabolcs Mészáros, Andrea Miglio, Dante Minniti, Rebecca Minsley, Takamitsu Miyaji, Faizan Gohar Mohammad, Benoit Mosser, Eva-Maria Mueller, Demitri Muna, Andrea Muñoz-Gutiérrez, Adam D. Myers, Seshadri Nadathur, Preethi Nair, Kirpal Nandra, Janaina Correa do Nascimento, Rebecca Jean Nevin, Jeffrey A. Newman, David L. Nidever, Christian Nitschelm, Pasquier Noterdaeme, Julia E. O'Connell, Matthew D. Olmstead, Daniel Oravetz, Audrey Oravetz, Yeisson Osorio, Zachary J. Pace, Nelson Padilla, Nathalie Palanque-Delabrouille, Pedro A. Palicio, Hsi-An Pan, Kaike Pan, James Parker, Romain Paviot, Sebastien Peirani, Karla Peña Ramírez, Samantha Penny, Will J. Percival, Ismael Perez-Fournon, Ignasi Pérez-Ràfols, Patrick Petitjean, Matthew M. Pieri, Marc Pinsonneault, Vijith Jacob Poovelil, Joshua Tyler Povick, Abhishek Prakash, Adrian M. Price-Whelan, M. Jordan Raddick, Anand Raichoor, Amy Ray, Sandro Barboza Rembold, Mehdi Rezaie, Rogemar A. Riffel, Rogério Riffel, Hans-Walter Rix, Annie C. Robin, A. Roman-Lopes, Carlos Román-Zúñiga, Benjamin Rose, Ashley J. Ross, Graziano Rossi, Kate Rowlands, Kate H. R. Rubin, Mara Salvato, Ariel G. Sánchez, Laura Sánchez-Menguiano, José R. Sánchez-Gallego, Conor Sayres, Adam Schaefer, Ricardo P. Schiavon, Jaderson S. Schimoia, Edward Schlafly, David Schlegel, Donald P. Schneider, Mathias Schultheis, Axel Schwope, Hee-Jong Seo, Aldo Serenelli, Arman Shafieloo, Shoaib Jamal Shamsi, Zhengyi Shao, Shiyin Shen, Matthew Shetrone, Raphael Shirley, V´ór Silva Aguirre, Joshua D. Simon, M. F. Skrutskie, Anže Slosar, Rebecca Smethurst, Jennifer Sobeck, Bernardo Cervantes Sodi, Diogo Souto, David V. Stark, Keivan G. Stassun, Matthias Steinmetz, Dennis Stello, Julianna Stermer, Thaisa Storchi-Bergmann, Alina Streblyanska, Guy S. Stringfellow, Amelia Stutz, Genaro Suárez, Jing Sun, Manuchehr Taghizadeh-Popp, Michael S. Talbot, Jamie Tayar, Aniruddha R. Thakar, Riley Theriault, Daniel Thomas, Zak C. Thomas, Jeremy Tinker, Rita Tojeiro, Hector Hernandez Toledo, Christy A. Tremonti, Nicholas W. Troup, Sarah Tuttle, Eduardo Unda-Sanzana, Marica Valentini, Jaime Vargas-González, Mariana Vargas-Magaña, Jose Antonio Vázquez-Mata, M. Vivek, David Wake, Yuting Wang, Benjamin Alan Weaver, Anne-Marie Weijmans, Vivienne Wild, John C. Wilson, Robert F. Wilson, Nathan Wolthuis, W. M. Wood-Vasey, Renbin Yan, Meng Yang, Christophe Yèche, Olga Zamora, Pauline Zarrouk, Gail Zasowski, Kai Zhang, Cheng Zhao, Gongbo Zhao, Zheng Zheng, Zheng Zheng, Guangtun Zhu, and Hu Zou. The 16th data release of the sloan digital sky surveys: First release from the apogee-2 southern survey and full release of eboss spectra. *ApJS*, 249(1):3, July 2020. doi: 10.3847/1538-4365/ab929e.

Niusha Ahvazi, Laura V. Sales, Jessica E. Doppel, Andrew Benson, Richard D'Souza, and Vicente Rodriguez-Gomez. The progenitors of the intra-cluster light and intra-cluster

globular clusters in galaxy groups and clusters. *arXiv e-prints*, art. arXiv:2308.12340, August 2023. doi: 10.48550/arXiv.2308.12340.

Niusha Ahvazi, Laura V. Sales, Julio F. Navarro, Andrew Benson, Alessandro Boselli, and Richard D'Souza. Star formation beyond galaxies: widespread in-situ formation of intracluster stars in tng50. *arXiv e-prints*, art. arXiv:2403.04839, March 2024. doi: 10.48550/arXiv.2403.04839.

K. A. Alamo-Martínez and J. P. Blakeslee. Specific frequencies and luminosity profiles of cluster galaxies and intracluster light in abell 1689. *ApJ*, 849(1):6, November 2017. doi: 10.3847/1538-4357/aa8f44.

Brandon Allgood, Ricardo A. Flores, Joel R. Primack, Andrey V. Kravtsov, Risa H. Wechsler, Andreas Faltenbacher, and James S. Bullock. The shape of dark matter haloes: dependence on mass, redshift, radius and formation. *MNRAS*, 367(4):1781–1796, April 2006. doi: 10.1111/j.1365-2966.2006.10094.x.

Andrés Almeida, Scott F. Anderson, Maria Argudo-Fernández, Carles Badenes, Kat Barger, Jorge K. Barrera-Ballesteros, Chad F. Bender, Erika Benitez, Felipe Besser, Dmitry Bizyaev, Michael R. Blanton, John Bochanski, Jo Bovy, William Nielsen Brandt, Joel R. Brownstein, Johannes Buchner, Esra Bulbul, Joseph N. Burchett, Mariana Cano Dıaz, Joleen K. Carlberg, Andrew R. Casey, Vedant Chandra, Brian Cherinka, Cristina Chiappini, Abigail A. Coker, Johan Comparat, Charlie Conroy, Gabriella Contardo, Arlin Cortes, Kevin Covey, Jeffrey D. Crane, Katia Cunha, Collin Dabbieri, Jr. Davidson, James W., Megan C. Davis, Nathan De Lee, José Eduardo Méndez Delgado, Sebastian Demasi, Francesco Di Mille, John Donor, Peter Dow, Tom Dwelly, Mike Eracleous, Jamey Eriksen, Xiaohui Fan, Emily Farr, Sara Frederick, Logan Fries, Peter Frinchaboy, Boris T. Gaensicke, Junqiang Ge, Consuelo González Ávila, Katie Grabowski, Catherine Grier, Guillaume Guiglion, Pramod Gupta, Patrick Hall, Keith Hawkins, Christian R. Hayes, J. J. Hermes, Lorena Hernández-Garc, David W. Hogg, Jon A. Holtzman, Hector Javier Ibarra-Medel, Alexander Ji, Paula Jofre, Jennifer A. Johnson, Amy M. Jones, Karen Kinemuchi, Matthias Kluge, Anton Koekemoer, Juna A. Kollmeier, Marina Kounkel, Dhanesh Krishnarao, Mirko Krumpe, Ivan Lacerna, Paulo Jakson Assuncao Lago, Chervin Laporte, Ang Liu, Chao Liu, Xin Liu, Alexandre Roman Lopes, Matin Macktoobian, Viktor Malanushenko, Dan Maoz, Thomas Masseron, Karen L. Masters, Gal Matijevic, Aidan McBride, Ilija Medan, Andrea Merloni, Sean Morrison, Natalie Myers, Szabolcs Mészáros, C. Alenka Negrete, David L. Nidever, Christian Nitschelm, Audrey Oravetz, Daniel Oravetz, Kaike Pan, Yingjie Peng, Marc H. Pinsonneault, Rick Pogge, Dan Qiu, Anna Barbara de Andrade Queiroz, Solange V. Ramirez, Hans-Walter Rix, Daniela Fernández Rosso, Jessie Runnoe, Mara Salvato, Sebastian F. Sanchez, Felipe A. Santana, Andrew Saydjari, Conor Sayres, Kevin C. Schlaufman, Donald P. Schneider, Axel Schwope, Javier Serna, Yue Shen, Jennifer Sobeck, Ying-Yi Song, Diogo Souto, Taylor Spoo, Keivan G. Stassun, Matthias Steinmetz, Ilya Straumit, Guy Stringfellow, José Sánchez-Gallego, Manuchehr Taghizadeh-Popp, Jamie Tayar, Ani Thakar, Patricia B. Tissera, Andrew Tkachenko, Hector Hernandez Toledo, Benny Trakhtenbrot, Jose G. Fernandez Trincado, Nicholas Troup, Jonathan R. Trump, Sarah Tuttle, Natalie Ulloa,

Jose Antonio Vazquez-Mata, Pablo Vera Alfaro, Sandro Villanova, Stefanie Wachter, Anne-Marie Weijmans, Adam Wheeler, John Wilson, Leigh Wojno, Julien Wolf, Xiang-Xiang Xue, Jason E. Ybarra, Eleonora Zari, and Gail Zasowski. The eighteenth data release of the sloan digital sky surveys: Targeting and first spectra from sdss-v. *arXiv e-prints*, art. arXiv:2301.07688, January 2023. doi: 10.48550/arXiv.2301.07688.

Isaac Alonso Asensio, Claudio Dalla Vecchia, Yannick M. Bahé, David J. Barnes, and Scott T. Kay. The intracluster light as a tracer of the total matter density distribution: a view from simulations. *MNRAS*, 494(2):1859–1864, May 2020. doi: 10.1093/mnras/staa861.

Elaad Applebaum, Alyson M. Brooks, Charlotte R. Christensen, Ferah Munshi, Thomas R. Quinn, Sijing Shen, and Michael Tremmel. Ultrafaint dwarfs in a milky way context: Introducing the mint condition dc justice league simulations. *ApJ*, 906(2):96, January 2021. doi: 10.3847/1538-4357/abcafa.

Astropy Collaboration, T. P. Robitaille, E. J. Tollerud, P. Greenfield, M. Droettboom, E. Bray, T. Aldcroft, M. Davis, A. Ginsburg, A. M. Price-Whelan, W. E. Kerzendorf, A. Conley, N. Crighton, K. Barbary, D. Muna, H. Ferguson, F. Grollier, M. M. Parikh, P. H. Nair, H. M. Unther, C. Deil, J. Woillez, S. Conseil, R. Kramer, J. E. H. Turner, L. Singer, R. Fox, B. A. Weaver, V. Zabalza, Z. I. Edwards, K. Azalee Bostroem, D. J. Burke, A. R. Casey, S. M. Crawford, N. Dencheva, J. Ely, T. Jenness, K. Labrie, P. L. Lim, F. Pierfederici, A. Pontzen, A. Ptak, B. Refsdal, M. Servillat, and O. Streicher. Astropy: A community Python package for astronomy. *A&A*, 558:A33, October 2013. doi: 10.1051/0004-6361/201322068.

Astropy Collaboration, A. M. Price-Whelan, B. M. Sipőcz, H. M. Günther, P. L. Lim, S. M. Crawford, S. Conseil, D. L. Shupe, M. W. Craig, N. Dencheva, A. Ginsburg, J. T. Vand erPlas, L. D. Bradley, D. Pérez-Suárez, M. de Val-Borro, T. L. Aldcroft, K. L. Cruz, T. P. Robitaille, E. J. Tollerud, C. Ardelean, T. Babej, Y. P. Bach, M. Bachetti, A. V. Bakanov, S. P. Bamford, G. Barentsen, P. Barmby, A. Baumbach, K. L. Berry, F. Biscani, M. Boquien, K. A. Bostroem, L. G. Bouma, G. B. Brammer, E. M. Bray, H. Breytenbach, H. Buddelmeijer, D. J. Burke, G. Calderone, J. L. Cano Rodríguez, M. Cara, J. V. M. Cardoso, S. Cheedella, Y. Copin, L. Corrales, D. Crichton, D. D'Avella, C. Deil, É. Depagne, J. P. Dietrich, A. Donath, M. Droettboom, N. Earl, T. Erben, S. Fabbro, L. A. Ferreira, T. Finethy, R. T. Fox, L. H. Garrison, S. L. J. Gibbons, D. A. Goldstein, R. Gommers, J. P. Greco, P. Greenfield, A. M. Groener, F. Grollier, A. Hagen, P. Hirst, D. Homeier, A. J. Horton, G. Hosseinzadeh, L. Hu, J. S. Hunkeler, Ž. Ivezić, A. Jain, T. Jenness, G. Kanarek, S. Kendrew, N. S. Kern, W. E. Kerzendorf, A. Khvalko, J. King, D. Kirkby, A. M. Kulkarni, A. Kumar, A. Lee, D. Lenz, S. P. Littlefair, Z. Ma, D. M. Macleod, M. Mastropietro, C. McCully, S. Montagnac, B. M. Morris, M. Mueller, S. J. Mumford, D. Muna, N. A. Murphy, S. Nelson, G. H. Nguyen, J. P. Ninan, M. Nöthe, S. Ogaz, S. Oh, J. K. Parejko, N. Parley, S. Pascual, R. Patil, A. A. Patil, A. L. Plunkett, J. X. Prochaska, T. Rastogi, V. Reddy Janga, J. Sabater, P. Sakurikar, M. Seifert, L. E. Sherbert, H. Sherwood-Taylor, A. Y. Shih, J. Sick, M. T. Silbiger, S. Singanamalla, L. P. Singer, P. H. Sladen, K. A. Sooley, S. Sornarajah, O. Streicher, P. Teuben, S. W.

Thomas, G. R. Tremblay, J. E. H. Turner, V. Terrón, M. H. van Kerkwijk, A. de la Vega, L. L. Watkins, B. A. Weaver, J. B. Whitmore, J. Woillez, V. Zabalza, and Astropy Contributors. The Astropy Project: Building an Open-science Project and Status of the v2.0 Core Package. *AJ*, 156(3):123, September 2018. doi: 10.3847/1538-3881/aabc4f.

Astropy Collaboration, Adrian M. Price-Whelan, Pey Lian Lim, Nicholas Earl, Nathaniel Starkman, Larry Bradley, David L. Shupe, Aarya A. Patil, Lia Corrales, C. E. Brasseur, Maximilian N"othe, Axel Donath, Erik Tollerud, Brett M. Morris, Adam Ginsburg, Eero Vaher, Benjamin A. Weaver, James Tocknell, William Jamieson, Marten H. van Kerkwijk, Thomas P. Robitaille, Bruce Merry, Matteo Bachetti, H. Moritz G"unther, Thomas L. Aldcroft, Jaime A. Alvarado-Montes, Anne M. Archibald, Attila B'odi, Shreyas Bapat, Geert Barentsen, Juanjo Baz'an, Manish Biswas, M'ed'eric Boquien, D. J. Burke, Daria Cara, Mihai Cara, Kyle E. Conroy, Simon Conseil, Matthew W. Craig, Robert M. Cross, Kelle L. Cruz, Francesco D'Eugenio, Nadia Dencheva, Hadrien A. R. Devillepoix, J"org P. Dietrich, Arthur Davis Eigenbrot, Thomas Erben, Leonardo Ferreira, Daniel Foreman-Mackey, Ryan Fox, Nabil Freij, Suyog Garg, Robel Geda, Lauren Glattly, Yash Gondhalekar, Karl D. Gordon, David Grant, Perry Greenfield, Austen M. Groener, Steve Guest, Sebastian Gurovich, Rasmus Handberg, Akeem Hart, Zac Hatfield-Dodds, Derek Homeier, Griffin Hosseinzadeh, Tim Jenness, Craig K. Jones, Prajwel Joseph, J. Bryce Kalmbach, Emir Karamehmetoglu, Mikolaj Kaluszy'nski, Michael S. P. Kelley, Nicholas Kern, Wolfgang E. Kerzendorf, Eric W. Koch, Shankar Kulumani, Antony Lee, Chun Ly, Zhiyuan Ma, Conor MacBride, Jakob M. Maljaars, Demitri Muna, N. A. Murphy, Henrik Norman, Richard O'Steen, Kyle A. Oman, Camilla Pacifici, Sergio Pascual, J. Pascual-Granado, Rohit R. Patil, Gabriel I. Perren, Timothy E. Pickering, Tanuj Rastogi, Benjamin R. Roulston, Daniel F. Ryan, Eli S. Rykoff, Jose Sabater, Parikshit Sakurikar, Jes'us Salgado, Aniket Sanghi, Nicholas Saunders, Volodymyr Savchenko, Ludwig Schwardt, Michael Seifert-Eckert, Albert Y. Shih, Anany Shrey Jain, Gyanendra Shukla, Jonathan Sick, Chris Simpson, Sudheesh Singanamalla, Leo P. Singer, Jaladh Singhal, Manodeep Sinha, Brigitta M. SipHocz, Lee R. Spitler, David Stansby, Ole Streicher, Jani Sumak, John D. Swinbank, Dan S. Taranu, Nikita Tewary, Grant R. Tremblay, Miguel de Val-Borro, Samuel J. Van Kooten, Zlatan Vasovi'c, Shresth Verma, Jos'e Vin'icius de Miranda Cardoso, Peter K. G. Williams, Tom J. Wilson, Benjamin Winkel, W. M. Wood-Vasey, Rui Xue, Peter Yoachim, Chen Zhang, Andrea Zonca, and Astropy Project Contributors. The Astropy Project: Sustaining and Growing a Community-oriented Open-source Project and the Latest Major Release (v5.0) of the Core Package. *ApJ*, 935(2):167, August 2022. doi: 10.3847/1538-4357/ac7c74.

Capucine Barfety, Félix-Antoine Valin, Tracy M. A. Webb, Min Yun, Heath Shipley, Kyle Boone, Brian Hayden, Julie Hlavacek-Larrondo, Adam Muzzin, Allison G. Noble, Saul Perlmutter, Carter Rhea, Gillian Wilson, and H. K. C. Yee. An assessment of the in situ growth of the intracluster light in the high-redshift galaxy cluster sparcs1049+56. *ApJ*, 930(1):25, May 2022. doi: 10.3847/1538-4357/ac61dd.

F. Arrigoni Battaia, G. Gavazzi, M. Fumagalli, A. Boselli, S. Boissier, L. Cortese, S. Heinis, L. Ferrarese, P. Côté, J. C. Mihos, J. C. Cuillandre, P.-A. Duc, P. Durrell, S. Gwyn, A. Jordán, C. Liu, E. Peng, and S. Mei. Stripped gas as fuel for newly formed hii regions

in the encounter between vcc1249 and m49: a unified picture from ngvs and guvics. *Astronomy Astrophysics*, 543:A112, 7 2012. ISSN 0004-6361. doi: 10.1051/0004-6361/201218895.

G. Beccari, M. Bellazzini, L. Magrini, L. Coccato, G. Cresci, F. Fraternali, P. T. de Zeeuw, B. Husemann, R. Ibata, G. Battaglia, N. Martin, V. Testa, S. Perina, and M. Correnti. A very dark stellar system lost in virgo: kinematics and metallicity of secco 1 with muse. *MNRAS*, 465(2):2189–2197, February 2017. doi: 10.1093/mnras/stw2874.

K. Bechtol, A. Drlica-Wagner, E. Balbinot, A. Pieres, J. D. Simon, B. Yanny, B. Santiago, R. H. Wechsler, J. Frieman, A. R. Walker, P. Williams, E. Rozo, E. S. Rykoff, A. Queiroz, E. Luque, A. Benoit-Lévy, D. Tucker, I. Sevilla, R. A. Gruendl, L. N. da Costa, A. Fausti Neto, M. A. G. Maia, T. Abbott, S. Allam, R. Armstrong, A. H. Bauer, G. M. Bernstein, R. A. Bernstein, E. Bertin, D. Brooks, E. Buckley-Geer, D. L. Burke, A. Carnero Rosell, F. J. Castander, R. Covarrubias, C. B. D'Andrea, D. L. DePoy, S. Desai, H. T. Diehl, T. F. Eifler, J. Estrada, A. E. Evrard, E. Fernandez, D. A. Finley, B. Flaugher, E. Gaztanaga, D. Gerdes, L. Girardi, M. Gladders, D. Gruen, G. Gutierrez, J. Hao, K. Honscheid, B. Jain, D. James, S. Kent, R. Kron, K. Kuehn, N. Kuropatkin, O. Lahav, T. S. Li, H. Lin, M. Makler, M. March, J. Marshall, P. Martini, K. W. Merritt, C. Miller, R. Miquel, J. Mohr, E. Neilsen, R. Nichol, B. Nord, R. Ogando, J. Peoples, D. Petravick, A. A. Plazas, A. K. Romer, A. Roodman, M. Sako, E. Sanchez, V. Scarpine, M. Schubnell, R. C. Smith, M. Soares-Santos, F. Sobreira, E. Suchyta, M. E. C. Swanson, G. Tarle, J. Thaler, D. Thomas, W. Wester, and J. Zuntz. Eight new milky way companions discovered in first-year dark energy survey data. *The Astrophysical Journal*, 807:50, 6 2015. ISSN 1538-4357. doi: 10.1088/0004-637X/807/1/50.

George D. Becker, Wallace L. W. Sargent, Michael Rauch, and Alexander P. Calverley. High-redshift metals. ii. probing reionization galaxies with low-ionization absorption lines at redshift six. *ApJ*, 735(2):93, July 2011. doi: 10.1088/0004-637X/735/2/93.

Peter S. Behroozi, Danilo Marchesini, Risa H. Wechsler, Adam Muzzin, Casey Papovich, and Mauro Stefanon. Using cumulative number densities to compare galaxies across cosmic time. *The Astrophysical Journal Letters*, 777(1):L10, oct 2013. doi: 10.1088/2041-8205/777/1/L10. URL https://dx.doi.org/10.1088/2041-8205/777/1/L10.

Peter S. Behroozi, Risa H. Wechsler, Yu Lu, Oliver Hahn, Michael T. Busha, Anatoly Klypin, and Joel R. Primack. Mergers and mass accretion for infalling halos both end well outside cluster virial radii. *ApJ*, 787(2):156, June 2014. doi: 10.1088/0004-637X/787/2/156.

M. Bellazzini, L. Armillotta, S. Perina, L. Magrini, G. Cresci, G. Beccari, G. Battaglia, F. Fraternali, P. T. de Zeeuw, N. F. Martin, F. Calura, R. Ibata, L. Coccato, V. Testa, and M. Correnti. Alone on a wide wide sea. The origin of SECCO 1, an isolated star-forming gas cloud in the virgo cluster. *MNRAS*, 476(4):4565–4583, June 2018. doi: 10.1093/mnras/sty467.

David Benisty, Eugene Vasiliev, N. Wyn Evans, Anne-Christine Davis, Odelia V. Hartl, and Louis E. Strigari. The local group mass in the light of gaia. *ApJL*, 928(1):L5, March 2022. doi: 10.3847/2041-8213/ac5c42.

Alejandro Benitez-Llambay and Carlos Frenk. The detailed structure and the onset of galaxy formation in low-mass gaseous dark matter haloes. *MNRAS*, 498(4):4887–4900, November 2020. doi: 10.1093/mnras/staa2698.

Alejandro Benitez-Llambay, Julio F. Navarro, Carlos S. Frenk, Till Sawala, Kyle Oman, Azadeh Fattahi, Matthieu Schaller, Joop Schaye, Robert A. Crain, and Tom Theuns. The properties of 'dark' ΛCDM haloes in the local group. *MNRAS*, 465(4):3913–3926, March 2017. doi: 10.1093/mnras/stw2982.

P. Bennet, D. J. Sand, D. Crnojević, K. Spekkens, A. Karunakaran, D. Zaritsky, and B. Mutlu-Pakdil. The satellite luminosity function of m101 into the ultra-faint dwarf galaxy regime. *ApJL*, 893(1):L9, April 2020. doi: 10.3847/2041-8213/ab80c5.

A. J. Benson, C. S. Frenk, C. G. Lacey, C. M. Baugh, and S. Cole. The effects of photoionization on galaxy formation - ii. satellite galaxies in the local group. *Monthly Notices of the Royal Astronomical Society*, 333:177–190, 6 2002. ISSN 00358711. doi: 10.1046/j.1365-8711.2002.05388.x.

A. J. Benson, N. Sugiyama, A. Nusser, and C. G. Lacey. The epoch of reionization. *Monthly Notices of the Royal Astronomical Society*, 369:1055–1080, 7 2006. ISSN 0035-8711. doi: 10.1111/j.1365-2966.2006.10426.x.

A. J. Benson, E. Toloba, L. Mayer, J. D. Simon, and P. Guhathakurta. Trends in dwarf early-type kinematics with cluster-centric radius driven by tidal stirring. *ApJ*, 799(2): 171, February 2015. doi: 10.1088/0004-637X/799/2/171.

Andrew Benson, Christoph Behrens, and Yu Lu. A random-walk model for dark matter halo spins. *MNRAS*, 496(3):3371–3380, August 2020. doi: 10.1093/mnras/staa1777.

Andrew J. Benson. Galacticus: A semi-analytic model of galaxy formation. *New Astronomy*, 17(2):175–197, 2012. ISSN 1384-1076. doi: https://doi.org/10.1016/j.newast.2011.07.004. URL https://www.sciencedirect.com/science/article/pii/S1384107611000807.

Andrew J. Benson. The mass function of unprocessed dark matter haloes and merger tree branching rates. *MNRAS*, 467(3):3454–3466, May 2017. doi: 10.1093/mnras/stx343.

Andrew J. Benson. The normalization and slope of the dark matter (sub-)halo mass function on sub-galactic scales. *MNRAS*, 493(1):1268–1276, March 2020. doi: 10.1093/mnras/staa341.

Andrew J. Benson and Xiaolong Du. Tidal tracks and artificial disruption of cold dark matter haloes. *MNRAS*, 517(1):1398–1406, November 2022. doi: 10.1093/mnras/stac2750.

Andrew J. Benson, Arya Farahi, Shaun Cole, Leonidas A. Moustakas, Adrian Jenkins, Mark Lovell, Rachel Kennedy, John Helly, and Carlos Frenk. Dark matter halo merger histories beyond cold dark matter - i. methods and application to warm dark matter. *MNRAS*, 428(2):1774–1789, January 2013. doi: 10.1093/mnras/sts159.

Shmuel Bialy and Amiel Sternberg. Thermal phases of the neutral atomic interstellar medium from solar metallicity to primordial gas. *ApJ*, 881(2):160, August 2019. doi: 10.3847/1538-4357/ab2fd1.

Albert Bijaoui and Frédéric Rué. A multiscale vision model adapted to the astronomical images. *Signal Processing*, 46(3):345–362, oct 1995. ISSN 01651684. doi: 10.1016/0165-1684(95)00093-4. URL https://linkinghub.elsevier.com/retrieve/pii/0165168495000934.

James Binney and Scott Tremaine. *Galactic Dynamics: Second Edition*. 2008. ISBN 9780691130262.

A. S. Borlaff, P. Gómez-Alvarez, B. Altieri, P. M. Marcum, R. Vavrek, R. Laureijs, R. Kohley, F. Buitrago, J.-C. Cuillandre, P.-A. Duc, L. M. Gaspar Venancio, A. Amara, S. Andreon, N. Auricchio, R. Azzollini, C. Baccigalupi, A. Balaguera-Antolínez, M. Baldi, S. Bardelli, R. Bender, A. Biviano, C. Bodendorf, D. Bonino, E. Bozzo, E. Branchini, M. Brescia, J. Brinchmann, C. Burigana, R. Cabanac, S. Camera, G. P. Candini, V. Capobianco, A. Cappi, C. Carbone, J. Carretero, C. S. Carvalho, S. Casas, F. J. Castander, M. Castellano, G. Castignani, S. Cavuoti, A. Cimatti, R. Cledassou, C. Colodro-Conde, G. Congedo, C. J. Conselice, L. Conversi, Y. Copin, L. Corcione, J. Coupon, H. M. Courtois, M. Cropper, A. Da Silva, H. Degaudenzi, D. Di Ferdinando, M. Douspis, F. Dubath, C. A. J. Duncan, X. Dupac, S. Dusini, A. Ealet, M. Fabricius, M. Farina, S. Farrens, P. G. Ferreira, S. Ferriol, F. Finelli, P. Flose-Reimberg, P. Fosalba, M. Frailis, E. Franceschi, M. Fumana, S. Galeotta, K. Ganga, B. Garilli, B. Gillis, C. Giocoli, G. Gozaliasl, J. Graciá-Carpio, A. Grazian, F. Grupp, S. V. H. Haugan, W. Holmes, F. Hormuth, K. Jahnke, E. Keihanen, S. Kermiche, A. Kiessling, M. Kilbinger, C. C. Kirkpatrick, T. Kitching, J. H. Knapen, B. Kubik, M. Kümmel, M. Kunz, H. Kurki-Suonio, P. Liebing, S. Ligori, P. B. Lilje, V. Lindholm, I. Lloro, G. Mainetti, D. Maino, O. Mansutti, O. Marggraf, K. Markovic, M. Martinelli, N. Martinet, D. Martínez-Delgado, F. Marulli, R. Massey, M. Maturi, S. Maurogordato, E. Medinaceli, S. Mei, M. Meneghetti, E. Merlin, R. B. Metcalf, G. Meylan, M. Moresco, G. Morgante, L. Moscardini, E. Munari, R. Nakajima, C. Neissner, S. M. Niemi, J. W. Nightingale, A. Nucita, C. Padilla, S. Paltani, F. Pasian, L. Patrizii, K. Pedersen, W. J. Percival, V. Pettorino, S. Pires, M. Poncet, L. Popa, D. Potter, L. Pozzetti, F. Raison, R. Rebolo, A. Renzi, J. Rhodes, G. Riccio, E. Romelli, M. Roncarelli, C. Rosset, E. Rossetti, R. Saglia, A. G. Sánchez, D. Sapone, M. Sauvage, P. Schneider, V. Scottez, A. Secroun, G. Seidel, S. Serrano, C. Sirignano, G. Sirri, J. Skottfelt, L. Stanco, J. L. Starck, F. Sureau, P. Tallada-Crespí, A. N. Taylor, M. Tenti, I. Tereno, R. Teyssier, R. Toledo-Moreo, F. Torradeflot, I. Tutusaus, E. A. Valentijn, L. Valenziano, J. Valiviita, T. Vassallo, M. Viel, Y. Wang, J. Weller, L. Whittaker, A. Zacchei, G. Zamorani, and E. Zucca. ¡i¿euclid¡/i¿ preparation. *Astronomy Astrophysics*, 657:A92, 1 2022. ISSN 0004-6361. doi: 10.1051/0004-6361/202141935.

A. Boselli, M. Fossati, G. Gavazzi, L. Ciesla, V. Buat, S. Boissier, and T. M. Hughes. Hα imaging of the Herschel reference survey. The star formation properties of a volume-limited, k-band-selected sample of nearby late-type galaxies. *åp*, 579:A102, July 2015. doi: 10.1051/0004-6361/201525712.

A. Boselli, M. Fossati, J. C. Cuillandre, S. Boissier, M. Boquien, V. Buat, D. Burgarella, G. Consolandi, L. Cortese, P. Côté, S. Côté, P. Durrell, L. Ferrarese, M. Fumagalli, G. Gavazzi, S. Gwyn, G. Hensler, B. Koribalski, J. Roediger, Y. Roehlly, D. Russeil, M. Sun, E. Toloba, B. Vollmer, and A. Zavagno. A virgo environmental survey tracing ionised gas emission (vestige). iii. star formation in the stripped gas of ngc 4254. *åp*, 615: A114, July 2018a. doi: 10.1051/0004-6361/201732410.

A. Boselli, M. Fossati, L. Ferrarese, S. Boissier, G. Consolandi, A. Longobardi, P. Amram, M. Balogh, P. Barmby, M. Boquien, F. Boulanger, J. Braine, V. Buat, D. Burgarella, F. Combes, T. Contini, L. Cortese, P. Côté, S. Côté, J. C. Cuillandre, L. Drissen, B. Epinat, M. Fumagalli, S. Gallagher, G. Gavazzi, J. Gomez-Lopez, S. Gwyn, W. Harris, G. Hensler, B. Koribalski, M. Marcelin, A. McConnachie, M. A. Miville-Deschenes, J. Navarro, D. Patton, E. W. Peng, H. Plana, N. Prantzos, C. Robert, J. Roediger, Y. Roehlly, D. Russeil, P. Salome, R. Sanchez-Janssen, P. Serra, K. Spekkens, M. Sun, J. Taylor, S. Tonnesen, B. Vollmer, J. Willis, H. Wozniak, T. Burdullis, D. Devost, B. Mahoney, N. Manset, A. Petric, S. Prunet, and K. Withington. A virgo environmental survey tracing ionised gas emission (vestige). i. introduction to the survey. *åp*, 614:A56, June 2018b. doi: 10.1051/0004-6361/201732407.

A. Boselli, M. Fossati, J. Roediger, M. Boquien, M. Fumagalli, M. Balogh, S. Boissier, J. Braine, L. Ciesla, P. Côté, J. C. Cuillandre, L. Ferrarese, G. Gavazzi, S. Gwyn, Junais, G. Hensler, A. Longobardi, and M. Sun. A virgo environmental survey tracing ionised gas emission (vestige). xiv. main-sequence relation in a rich environment down to m$_s tar$ 10^6 m$_{\o dot}$. *åp*, 669:A73, January 2023. doi: 10.1051/0004-6361/202244267.

Alessandro Boselli, Matteo Fossati, and Ming Sun. Ram pressure stripping in high-density environments. *åpr*, 30(1):3, December 2022. doi: 10.1007/s00159-022-00140-3.

Mia S. Bovill and Massimo Ricotti. Pre-reionization fossils, ultra-faint dwarfs, and the missing galactic satellite problem. *ApJ*, 693(2):1859–1870, March 2009. doi: 10.1088/0004-637X/693/2/1859.

Mia S. Bovill and Massimo Ricotti. Where are the fossils of the first galaxies? i. local volume maps and properties of the undetected dwarfs. *ApJ*, 741(1):17, November 2011. doi: 10.1088/0004-637X/741/1/17.

R. G. Bower, A. J. Benson, and Robert A. Crain. What shapes the galaxy mass function? exploring the roles of supernova-driven winds and active galactic nuclei. *Monthly Notices of the Royal Astronomical Society*, 422:2816–2840, 6 2012. ISSN 00358711. doi: 10.1111/j.1365-2966.2012.20516.x.

Michael Boylan-Kolchin, James S. Bullock, and Manoj Kaplinghat. Too big to fail? the puzzling darkness of massive milky way subhaloes. *MNRAS*, 415(1):L40–L44, July 2011. doi: 10.1111/j.1745-3933.2011.01074.x.

Tobias Buck, Andrea V. Macciò, Aaron A. Dutton, Aura Obreja, and Jonas Frings. Nihao xv: the environmental impact of the host galaxy on galactic satellite and field dwarf galaxies. *MNRAS*, 483(1):1314–1341, February 2019. doi: 10.1093/mnras/sty2913.

Tobias Buck, Aura Obreja, Andrea V. Macciò, Ivan Minchev, Aaron A. Dutton, and Jeremiah P. Ostriker. Nihao-uhd: the properties of mw-like stellar discs in high-resolution cosmological simulations. *MNRAS*, 491(3):3461–3478, January 2020. doi: 10.1093/mnras/stz3241.

J. S. Bullock, T. S. Kolatt, Y. Sigad, R. S. Somerville, A. V. Kravtsov, A. A. Klypin, J. R. Primack, and A. Dekel. Profiles of dark haloes: evolution, scatter and environment. *Monthly Notices of the Royal Astronomical Society*, 321(3):559–575, mar 2001. ISSN 0035-8711. doi: 10.1046/j.1365-8711.2001.04068.x. URL https://academic.oup.com/mnras/article-lookup/doi/10.1046/j.1365-8711.2001.04068.x.

James S. Bullock and Michael Boylan-Kolchin. Small-Scale Challenges to the ΛCDM Paradigm. *ARA&A*, 55(1):343–387, August 2017. doi: 10.1146/annurev-astro-091916-055313.

James S. Bullock and Michael Boylan-Kolchin. Small-scale challenges to the cdm paradigm. *Annual Review of Astronomy and Astrophysics*, 55(1):343–387, 2017. doi: 10.1146/annurev-astro-091916-055313. URL https://doi.org/10.1146/annurev-astro-091916-055313.

James S. Bullock and Kathryn V. Johnston. Tracing galaxy formation with stellar halos. i. methods. *ApJ*, 635(2):931–949, December 2005. doi: 10.1086/497422.

Kevin Bundy, Matthew A. Bershady, David R. Law, Renbin Yan, Niv Drory, Nicholas MacDonald, David A. Wake, Brian Cherinka, José R. Sánchez-Gallego, Anne-Marie Weijmans, Daniel Thomas, Christy Tremonti, Karen Masters, Lodovico Coccato, Aleksandar M. Diamond-Stanic, Alfonso Aragón-Salamanca, Vladimir Avila-Reese, Carles Badenes, Jésus Falcón-Barroso, Francesco Belfiore, Dmitry Bizyaev, Guillermo A. Blanc, Joss Bland-Hawthorn, Michael R. Blanton, Joel R. Brownstein, Nell Byler, Michele Cappellari, Charlie Conroy, Aaron A. Dutton, Eric Emsellem, James Etherington, Peter M. Frinchaboy, Hai Fu, James E. Gunn, Paul Harding, Evelyn J. Johnston, Guinevere Kauffmann, Karen Kinemuchi, Mark A. Klaene, Johan H. Knapen, Alexie Leauthaud, Cheng Li, Lihwai Lin, Roberto Maiolino, Viktor Malanushenko, Elena Malanushenko, Shude Mao, Claudia Maraston, Richard M. McDermid, Michael R. Merrifield, Robert C. Nichol, Daniel Oravetz, Kaike Pan, John K. Parejko, Sebastian F. Sanchez, David Schlegel, Audrey Simmons, Oliver Steele, Matthias Steinmetz, Karun Thanjavur, Benjamin A. Thompson, Jeremy L. Tinker, Remco C. E. van den Bosch, Kyle B. Westfall, David Wilkinson, Shelley Wright, Ting Xiao, and Kai Zhang. Overview of the sdss-iv manga survey: Mapping nearby galaxies at apache point observatory. *ApJ*, 798(1):7, January 2015. doi: 10.1088/0004-637X/798/1/7.

Michael T. Busha, Marcelo A. Alvarez, Risa H. Wechsler, Tom Abel, and Louis E. Strigari. The impact of inhomogeneous reionization on the satellite galaxy population of the milky way. *The Astrophysical Journal*, 710:408–420, 2 2010. ISSN 0004-637X. doi: 10.1088/0004-637X/710/1/408.

Iryna S. Butsky, Joseph N. Burchett, Daisuke Nagai, Michael Tremmel, Thomas R. Quinn, and Jessica K. Werk. Ultraviolet signatures of the multiphase intracluster and circumgalactic media in the romulusc simulation. *MNRAS*, 490(3):4292–4306, December 2019. doi: 10.1093/mnras/stz2859.

Thomas M. Callingham, Marius Cautun, Alis J. Deason, Carlos S. Frenk, Wenting Wang, Facundo A. Gómez, Robert J. J. Grand, Federico Marinacci, and Ruediger Pakmor. The mass of the milky way from satellite dynamics. *MNRAS*, 484(4):5453–5467, April 2019. doi: 10.1093/mnras/stz365.

Francesco Calura, Michele Bellazzini, and Annibale D'Ercole. Hydrodynamic simulations of an isolated star-forming gas cloud in the virgo cluster. *MNRAS*, 499(4):5873–5890, December 2020. doi: 10.1093/mnras/staa3133.

Scott G. Carlsten, Jenny E. Greene, Johnny P. Greco, Rachael L. Beaton, and Erin Kado-Fong. Structures of dwarf satellites of milky way-like galaxies: Morphology, scaling relations, and intrinsic shapes. *ApJ*, 922(2):267, December 2021. doi: 10.3847/1538-4357/ac2581.

Arianna Cattapan, Marilena Spavone, Enrichetta Iodice, Roberto Rampazzo, Stefano Ciroi, Emma Ryan-Weber, Pietro Schipani, Massimo Capaccioli, Aniello Grado, Luca Limatola, Paola Mazzei, Enrico V. Held, and Antonietta Marino. Vegas: A vst early-type galaxy survey. iv. ngc 1533, ic 2038, and ic 2039: An interacting triplet in the dorado group. *The Astrophysical Journal*, 874(2):130, apr 2019. ISSN 1538-4357. doi: 10.3847/1538-4357/ab0b44. URL https://iopscience.iop.org/article/10.3847/1538-4357/ab0b44.

Rodrigo Cañas, Claudia del P. Lagos, Pascal J. Elahi, Chris Power, Charlotte Welker, Yohan Dubois, and Christophe Pichon. From stellar haloes to intracluster light: the physics of the intra-halo stellar component in cosmological hydrodynamical simulations. *MNRAS*, 494(3):4314–4333, May 2020. doi: 10.1093/mnras/staa1027.

W. Cerny, J. D. Simon, T. S. Li, A. Drlica-Wagner, A. B. Pace, C. E. Martınez-Vázquez, A. H. Riley, B. Mutlu-Pakdil, S. Mau, P. S. Ferguson, D. Erkal, R. R. Munoz, C. R. Bom, J. L. Carlin, D. Carollo, Y. Choi, A. P. Ji, V. Manwadkar, D. Martez-Delgado, A. E. Miller, N. E. D. Noël, J. D. Sakowska, D. J. Sand, G. S. Stringfellow, E. J. Tollerud, A. K. Vivas, J. A. Carballo-Bello, D. Hernandez-Lang, D. J. James, D. L. Nidever, J. L. Nilo Castellon, K. A. G. Olsen, A. Zenteno, and Delve Collaboration. Pegasus iv: Discovery and spectroscopic confirmation of an ultra-faint dwarf galaxy in the constellation pegasus. *ApJ*, 942(2):111, January 2023. doi: 10.3847/1538-4357/aca1c3.

Gilles Chabrier. The galactic disk mass function: Reconciliation of the hubble space telescope and nearby determinations. *ApJL*, 586(2):L133–L136, April 2003. doi: 10.1086/374879.

K. C. Chambers, E. A. Magnier, N. Metcalfe, H. A. Flewelling, M. E. Huber, C. Z. Waters, L. Denneau, P. W. Draper, D. Farrow, D. P. Finkbeiner, C. Holmberg, J. Koppenhoefer, P. A. Price, A. Rest, R. P. Saglia, E. F. Schlafly, S. J. Smartt, W. Sweeney, R. J. Wainscoat, W. S. Burgett, S. Chastel, T. Grav, J. N. Heasley, K. W. Hodapp, R. Jedicke, N. Kaiser, R. P. Kudritzki, G. A. Luppino, R. H. Lupton, D. G. Monet, J. S. Morgan, P. M. Onaka, B. Shiao, C. W. Stubbs, J. L. Tonry, R. White, E. Bañados, E. F. Bell, R. Bender, E. J. Bernard, M. Boegner, F. Boffi, M. T. Botticella, A. Calamida, S. Casertano, W. P. Chen, X. Chen, S. Cole, N. Deacon, C. Frenk, A. Fitzsimmons, S. Gezari, V. Gibbs, C. Goessl, T. Goggia, R. Gourgue, B. Goldman, P. Grant, E. K. Grebel, N. C. Hambly, G. Hasinger, A. F. Heavens, T. M. Heckman, R. Henderson, T. Henning, M. Holman, U. Hopp, W. H. Ip, S. Isani, M. Jackson, C. D. Keyes, A. M. Koekemoer, R. Kotak, D. Le, D. Liska, K. S. Long, J. R. Lucey, M. Liu, N. F. Martin, G. Masci, B. McLean, E. Mindel, P. Misra, E. Morganson, D. N. A. Murphy, A. Obaika, G. Narayan, M. A. Nieto-Santisteban, P. Norberg, J. A. Peacock, E. A. Pier, M. Postman, N. Primak, C. Rae, A. Rai, A. Riess, A. Riffeser, H. W. Rix, S. Röser, R. Russel, L. Rutz, E. Schilbach, A. S. B. Schultz, D. Scolnic, L. Strolger, A. Szalay, S. Seitz, E. Small, K. W. Smith, D. R. Soderblom, P. Taylor, R. Thomson, A. N. Taylor, A. R. Thakar, J. Thiel, D. Thilker, D. Unger, Y. Urata, J. Valenti, J. Wagner, T. Walder, F. Walter, S. P. Watters, S. Werner, W. M. Wood-Vasey, and R. Wyse. The pan-starrs1 surveys. *arXiv e-prints*, art. arXiv:1612.05560, December 2016. doi: 10.48550/arXiv.1612.05560.

T. K. Chan, D. Kereš, J. Oñorbe, P. F. Hopkins, A. L. Muratov, C. A. Faucher-Giguère, and E. Quataert. The impact of baryonic physics on the structure of dark matter haloes: the view from the fire cosmological simulations. *MNRAS*, 454(3):2981–3001, December 2015. doi: 10.1093/mnras/stv2165.

S. Chandrasekhar. Stochastic problems in physics and astronomy. *Reviews of Modern Physics*, 15:1–89, 1 1943. ISSN 0034-6861. doi: 10.1103/RevModPhys.15.1.

Charlotte R. Christensen, Romeel Davé, Alyson Brooks, Thomas Quinn, and Sijing Shen. Tracing outflowing metals in simulations of dwarf and spiral galaxies. *ApJ*, 867(2):142, November 2018. doi: 10.3847/1538-4357/aae374.

Shaun Cole, Cedric G. Lacey, Carlton M. Baugh, and Carlos S. Frenk. Hierarchical galaxy formation. *MNRAS*, 319(1):168–204, November 2000. doi: 10.1046/j.1365-8711.2000.03879.x.

Gaia Collaboration, A. G. A. Brown, A. Vallenari, T. Prusti, J. H. J. de Bruijne, F. Mignard, R. Drimmel, C. Babusiaux, C. A. L. Bailer-Jones, U. Bastian, M. Biermann, D. W. Evans, L. Eyer, F. Jansen, C. Jordi, D. Katz, S. A. Klioner, U. Lammers, L. Lindegren, X. Luri, W. O'Mullane, C. Panem, D. Pourbaix, S. Randich, P. Sartoretti, H. I. Siddiqui, C. Soubiran, V. Valette, F. van Leeuwen, N. A. Walton, C. Aerts, F. Arenou, M. Cropper, E. Høg, M. G. Lattanzi, E. K. Grebel, A. D. Holland, C. Huc, X. Passot, M. Perryman, L. Bramante, C. Cacciari, J. Castañeda, L. Chaoul, N. Cheek, F. De Angeli, C. Fabricius, R. Guerra, J. Hernández, A. Jean-Antoine-Piccolo, E. Masana, R. Messineo, N. Mowlavi, K. Nienartowicz, D. Ordóñez-Blanco, P. Panuzzo, J. Portell, P. J. Richards,

M. Riello, G. M. Seabroke, P. Tanga, F. Thévenin, J. Torra, S. G. Els, G. Gracia-Abril, G. Comoretto, M. Garcia-Reinaldos, T. Lock, E. Mercier, M. Altmann, R. Andrae, T. L. Astraatmadja, I. Bellas-Velidis, K. Benson, J. Berthier, R. Blomme, G. Busso, B. Carry, A. Cellino, G. Clementini, S. Cowell, O. Creevey, J. Cuypers, M. Davidson, J. De Ridder, A. de Torres, L. Delchambre, A. Dell'Oro, C. Ducourant, Y. Frémat, M. Garcıa-Torres, E. Gosset, J. L. Halbwachs, N. C. Hambly, D. L. Harrison, M. Hauser, D. Hestroffer, S. T. Hodgkin, H. E. Huckle, A. Hutton, G. Jasniewicz, S. Jordan, M. Kontizas, A. J. Korn, A. C. Lanzafame, M. Manteiga, A. Moitinho, K. Muinonen, J. Osinde, E. Pancino, T. Pauwels, J. M. Petit, A. Recio-Blanco, A. C. Robin, L. M. Sarro, C. Siopis, M. Smith, K. W. Smith, A. Sozzetti, W. Thuillot, W. van Reeven, Y. Viala, U. Abbas, A. Abreu Aramburu, S. Accart, J. J. Aguado, P. M. Allan, W. Allasia, G. Altavilla, M. A. Álvarez, J. Alves, R. I. Anderson, A. H. Andrei, E. Anglada Varela, E. Antiche, T. Antoja, S. Antón, B. Arcay, N. Bach, S. G. Baker, L. Balaguer-Núñez, C. Barache, C. Barata, A. Barbier, F. Barblan, D. Barrado y Navascués, M. Barros, M. A. Barstow, U. Becciani, M. Bellazzini, A. Bello Garc, V. Belokurov, P. Bendjoya, A. Berihuete, L. Bianchi, O. Bienaymé, F. Billebaud, N. Blagorodnova, S. Blanco-Cuaresma, T. Boch, A. Bombrun, R. Borrachero, S. Bouquillon, G. Bourda, H. Bouy, A. Bragaglia, M. A. Breddels, N. Brouillet, T. Brüsemeister, B. Bucciarelli, P. Burgess, R. Burgon, A. Burlacu, D. Busonero, R. Buzzi, E. Caffau, J. Cambras, H. Campbell, R. Cancelliere, T. Cantat-Gaudin, T. Carlucci, J. M. Carrasco, M. Castellani, P. Charlot, J. Charnas, A. Chiavassa, M. Clotet, G. Cocozza, R. S. Collins, G. Costigan, F. Crifo, N. J. G. Cross, M. Crosta, C. Crowley, C. Dafonte, Y. Damerdji, A. Dapergolas, P. David, M. David, P. De Cat, F. de Felice, P. de Laverny, F. De Luise, R. De March, D. de Martino, R. de Souza, J. Debosscher, E. del Pozo, M. Delbo, A. Delgado, H. E. Delgado, P. Di Matteo, S. Diakite, E. Distefano, C. Dolding, S. Dos Anjos, P. Drazinos, J. Duran, Y. Dzigan, B. Edvardsson, H. Enke, N. W. Evans, G. Eynard Bontemps, C. Fabre, M. Fabrizio, S. Faigler, A. J. Falcão, M. Farràs Casas, L. Federici, G. Fedorets, J. Fernández-Hernández, P. Fernique, A. Fienga, F. Figueras, F. Filippi, K. Findeisen, A. Fonti, M. Fouesneau, E. Fraile, M. Fraser, J. Fuchs, M. Gai, S. Galleti, L. Galluccio, D. Garabato, F. Garcí́Sedano, A. Garofalo, N. Garralda, P. Gavras, J. Gerssen, R. Geyer, G. Gilmore, S. Girona, G. Giuffrida, M. Gomes, A. González-Marcos, J. González-Núñez, J. J. González-Vidal, M. Granvik, A. Guerrier, P. Guillout, J. Guiraud, A. Gúrpide, R. Gutiérrez-Sánchez, L. P. Guy, R. Haigron, D. Hatzidimitriou, M. Haywood, U. Heiter, A. Helmi, D. Hobbs, W. Hofmann, B. Holl, G. Holland, J. A. S. Hunt, A. Hypki, V. Icardi, M. Irwin, G. Jevardat de Fombelle, P. Jofré, P. G. Jonker, A. Jorissen, F. Julbe, A. Karampelas, A. Kochoska, R. Kohley, K. Kolenberg, E. Kontizas, S. E. Koposov, G. Kordopatis, P. Koubsky, A. Krone-Martins, M. Kudryashova, I. Kull, R. K. Bachchan, F. Lacoste-Seris, A. F. Lanza, J. B. Lavigne, C. Le Poncin-Lafitte, Y. Lebreton, T. Lebzelter, S. Leccia, N. Leclerc, I. Lecoeur-Taibi, V. Lemaitre, H. Lenhardt, F. Leroux, S. Liao, E. Licata, H. E. P. Lindstrøm, T. A. Lister, E. Livanou, A. Lobel, W. Löffler, M. López, D. Lorenz, I. MacDonald, T. Magalhães Fernandes, S. Managau, R. G. Mann, G. Mantelet, O. Marchal, J. M. Marchant, M. Marconi, S. Marinoni, P. M. Marrese, G. Marschalkó, D. J. Marshall, J. M. Mart´Fleitas, M. Martino, N. Mary, G. Matijevič, T. Mazeh, P. J. McMillan, S. Messina, D. Michalik, N. R.

Millar, B. M. H. Miranda, D. Molina, R. Molinaro, M. Molinaro, L. Molnár, M. Moniez, P. Montegriffo, R. Mor, A. Mora, R. Morbidelli, T. Morel, S. Morgenthaler, D. Morris, A. F. Mulone, T. Muraveva, I. Musella, J. Narbonne, G. Nelemans, L. Nicastro, L. Noval, C. Ordénovic, J. Ordieres-Meré, P. Osborne, C. Pagani, I. Pagano, F. Pailler, H. Palacin, L. Palaversa, P. Parsons, M. Pecoraro, R. Pedrosa, H. Pentikäinen, B. Pichon, A. M. Piersimoni, F. X. Pineau, E. Plachy, G. Plum, E. Poujoulet, A. Prša, L. Pulone, S. Ragaini, S. Rago, N. Rambaux, M. Ramos-Lerate, P. Ranalli, G. Rauw, A. Read, S. Regibo, C. Reylé, R. A. Ribeiro, L. Rimoldini, V. Ripepi, A. Riva, G. Rixon, M. Roelens, M. Romero-Gómez, N. Rowell, F. Royer, L. Ruiz-Dern, G. Sadowski, T. Sagristà Sellés, J. Sahlmann, J. Salgado, E. Salguero, M. Sarasso, H. Savietto, M. Schultheis, E. Sciacca, M. Segol, J. C. Segovia, D. Segransan, I. C. Shih, R. Smareglia, R. L. Smart, E. Solano, F. Solitro, R. Sordo, S. Soria Nieto, J. Souchay, A. Spagna, F. Spoto, U. Stampa, I. A. Steele, H. Steidelmüller, C. A. Stephenson, H. Stoev, F. F. Suess, M. Süveges, J. Surdej, L. Szabados, E. Szegedi-Elek, D. Tapiador, F. Taris, G. Tauran, M. B. Taylor, R. Teixeira, D. Terrett, B. Tingley, S. C. Trager, C. Turon, A. Ulla, E. Utrilla, G. Valentini, A. van Elteren, E. Van Hemelryck, M. van Leeuwen, M. Varadi, A. Vecchiato, J. Veljanoski, T. Via, D. Vicente, S. Vogt, H. Voss, V. Votruba, S. Voutsinas, G. Walmsley, M. Weiler, K. Weingrill, T. Wevers, Ł. Wyrzykowski, A. Yoldas, M. Žerjal, S. Zucker, C. Zurbach, T. Zwitter, A. Alecu, M. Allen, C. Allende Prieto, A. Amorim, G. Angladaescudé, V. Arsenijevic, S. Azaz, P. Balm, M. Beck, H. H. Bernstein, L. Bigot, A. Bijaoui, C. Blasco, M. Bonfigli, G. Bono, S. Boudreault, A. Bressan, S. Brown, P. M. Brunet, P. Bunclark, R. Buonanno, A. G. Butkevich, C. Carret, C. Carrion, L. Chemin, F. Chéreau, L. Corcione, E. Darmigny, K. S. de Boer, P. de Teodoro, P. T. de Zeeuw, C. Delle Luche, C. D. Domingues, P. Dubath, F. Fodor, B. Frézouls, A. Fries, D. Fustes, D. Fyfe, E. Gallardo, J. Gallegos, D. Gardiol, M. Gebran, A. Gomboc, A. Gómez, E. Grux, A. Gueguen, A. Heyrovsky, J. Hoar, G. Iannicola, Y. Isasi Parache, A. M. Janotto, E. Joliet, A. Jonckheere, R. Keil, D. W. Kim, P. Klagyivik, J. Klar, J. Knude, O. Kochukhov, I. Kolka, J. Kos, A. Kutka, V. Lainey, D. LeBouquin, C. Liu, D. Loreggia, V. V. Makarov, M. G. Marseille, C. Martayan, O. Martinez-Rubi, B. Massart, F. Meynadier, S. Mignot, U. Munari, A. T. Nguyen, T. Nordlander, P. Ocvirk, K. S. O'Flaherty, A. Olias Sanz, P. Ortiz, J. Osorio, D. Oszkiewicz, A. Ouzounis, M. Palmer, P. Park, E. Pasquato, C. Peltzer, J. Peralta, F. Péturaud, T. Pieniluoma, E. Pigozzi, J. Poels, G. Prat, T. Prod'homme, F. Raison, J. M. Rebordao, D. Risquez, B. Rocca-Volmerange, S. Rosen, M. I. Ruiz-Fuertes, F. Russo, S. Sembay, I. Serraller Vizcaino, A. Short, A. Siebert, H. Silva, D. Sinachopoulos, E. Slezak, M. Soffel, D. Sosnowska, V. Straižys, M. ter Linden, D. Terrell, S. Theil, C. Tiede, L. Troisi, P. Tsalmantza, D. Tur, M. Vaccari, F. Vachier, P. Valles, W. Van Hamme, L. Veltz, J. Virtanen, J. M. Wallut, R. Wichmann, M. I. Wilkinson, H. Ziaeepour, and S. Zschocke. Gaia data release 1. summary of the astrometric, photometric, and survey properties. *åp*, 595:A2, November 2016a. doi: 10.1051/0004-6361/201629512.

Planck Collaboration, P. A. R. Ade, N. Aghanim, M. Arnaud, M. Ashdown, J. Aumont, C. Baccigalupi, A. J. Banday, R. B. Barreiro, J. G. Bartlett, N. Bartolo, E. Battaner, R. Battye, K. Benabed, A. Benoıt, A. Benoit-Lévy, J. P. Bernard, M. Bersanelli, P. Bielewicz, J. J. Bock, A. Bonaldi, L. Bonavera, J. R. Bond, J. Borrill, F. R. Bouchet,

F. Boulanger, M. Bucher, C. Burigana, R. C. Butler, E. Calabrese, J. F. Cardoso, A. Catalano, A. Challinor, A. Chamballu, R. R. Chary, H. C. Chiang, J. Chluba, P. R. Christensen, S. Church, D. L. Clements, S. Colombi, L. P. L. Colombo, C. Combet, A. Coulais, B. P. Crill, A. Curto, F. Cuttaia, L. Danese, R. D. Davies, R. J. Davis, P. de Bernardis, A. de Rosa, G. de Zotti, J. Delabrouille, F. X. Désert, E. Di Valentino, C. Dickinson, J. M. Diego, K. Dolag, H. Dole, S. Donzelli, O. Doré, M. Douspis, A. Ducout, J. Dunkley, X. Dupac, G. Efstathiou, F. Elsner, T. A. Enßlin, H. K. Eriksen, M. Farhang, J. Fergusson, F. Finelli, O. Forni, M. Frailis, A. A. Fraisse, E. Franceschi, A. Frejsel, S. Galeotta, S. Galli, K. Ganga, C. Gauthier, M. Gerbino, T. Ghosh, M. Giard, Y. Giraud-Héraud, E. Giusarma, E. Gjerløw, J. González-Nuevo, K. M. Górski, S. Gratton, A. Gregorio, A. Gruppuso, J. E. Gudmundsson, J. Hamann, F. K. Hansen, D. Hanson, D. L. Harrison, G. Helou, S. Henrot-Versillé, C. Hernández-Monteagudo, D. Herranz, S. R. Hildebrandt, E. Hivon, M. Hobson, W. A. Holmes, A. Hornstrup, W. Hovest, Z. Huang, K. M. Huffenberger, G. Hurier, A. H. Jaffe, T. R. Jaffe, W. C. Jones, M. Juvela, E. Keihänen, R. Keskitalo, T. S. Kisner, R. Kneissl, J. Knoche, L. Knox, M. Kunz, H. Kurki-Suonio, G. Lagache, A. Lähteenmäki, J. M. Lamarre, A. Lasenby, M. Lattanzi, C. R. Lawrence, J. P. Leahy, R. Leonardi, J. Lesgourgues, F. Levrier, A. Lewis, M. Liguori, P. B. Lilje, M. Linden-Vørnle, M. López-Caniego, P. M. Lubin, J. F. Macıas-Pérez, G. Maggio, D. Maino, N. Mandolesi, A. Mangilli, A. Marchini, M. Maris, P. G. Martin, M. Martinelli, E. Martez-González, S. Masi, S. Matarrese, P. McGehee, P. R. Meinhold, A. Melchiorri, J. B. Melin, L. Mendes, A. Mennella, M. Migliaccio, M. Millea, S. Mitra, M. A. Miville-Deschênes, A. Moneti, L. Montier, G. Morgante, D. Mortlock, A. Moss, D. Munshi, J. A. Murphy, P. Naselsky, F. Nati, P. Natoli, C. B. Netterfield, H. U. Nørgaard-Nielsen, F. Noviello, D. Novikov, I. Novikov, C. A. Oxborrow, F. Paci, L. Pagano, F. Pajot, R. Paladini, D. Paoletti, B. Partridge, F. Pasian, G. Patanchon, T. J. Pearson, O. Perdereau, L. Perotto, F. Perrotta, V. Pettorino, F. Piacentini, M. Piat, E. Pierpaoli, D. Pietrobon, S. Plaszczynski, E. Pointecouteau, G. Polenta, L. Popa, G. W. Pratt, G. Prézeau, S. Prunet, J. L. Puget, J. P. Rachen, W. T. Reach, R. Rebolo, M. Reinecke, M. Remazeilles, C. Renault, A. Renzi, I. Ristorcelli, G. Rocha, C. Rosset, M. Rossetti, G. Roudier, B. Rouillé d'Orfeuil, M. Rowan-Robinson, J. A. Rubiño-Martı́, B. Rusholme, N. Said, V. Salvatelli, L. Salvati, M. Sandri, D. Santos, M. Savelainen, G. Savini, D. Scott, M. D. Seiffert, P. Serra, E. P. S. Shellard, L. D. Spencer, M. Spinelli, V. Stolyarov, R. Stompor, R. Sudiwala, R. Sunyaev, D. Sutton, A. S. Suur-Uski, J. F. Sygnet, J. A. Tauber, L. Terenzi, L. Toffolatti, M. Tomasi, M. Tristram, T. Trombetti, M. Tucci, J. Tuovinen, M. Türler, G. Umana, L. Valenziano, J. Valiviita, F. Van Tent, P. Vielva, F. Villa, L. A. Wade, B. D. Wandelt, I. K. Wehus, M. White, S. D. M. White, A. Wilkinson, D. Yvon, A. Zacchei, and A. Zonca. Planck 2015 results. xiii. cosmological parameters. *åp*, 594:A13, September 2016b. doi: 10.1051/0004-6361/201525830.

Charlie Conroy, Risa H. Wechsler, and Andrey V. Kravtsov. The hierarchical build-up of massive galaxies and the intracluster light since z = 1. *The Astrophysical Journal*, 668(2): 826–838, oct 2007. ISSN 0004-637X. doi: 10.1086/521425. URL https://iopscience.iop.org/article/10.1086/521425.

Charlie Conroy, James E. Gunn, and Martin White. The propagation of uncertainties in stellar population synthesis modeling. i. the relevance of uncertain aspects of stellar evolution and the initial mass function to the derived physical properties of galaxies. *ApJ*, 699(1):486–506, July 2009. doi: 10.1088/0004-637X/699/1/486.

E. Contini and Q. Gu. On the mass distribution of the intracluster light in galaxy groups and clusters. *The Astrophysical Journal*, 901(2):128, sep 2020. ISSN 1538-4357. doi: 10.3847/1538-4357/abb1aa. URL https://iopscience.iop.org/article/10.3847/1538-4357/abb1aa.

E. Contini, G. De Lucia, A. Villalobos, and S. Borgani. On the formation and physical properties of the intra-cluster light in hierarchical galaxy formation models. *The Astrophysical Journal*, 699(2):1518–1529, nov 2013. ISSN 0004-637X. doi: 10.1093/mnras/stt2174. URL http://arxiv.org/abs/1311.2076http://dx.doi.org/10.1093/mnras/stt2174.

E Contini, S K Yi, and X Kang. The different growth pathways of brightest cluster galaxies and the intra-cluster light. *Monthly Notices of the Royal Astronomical Society*, 592(3): A7, jun 2018. ISSN 0035-8711. doi: 10.1093/mnras/sty1518. URL https://academic.oup.com/mnras/advance-article/doi/10.1093/mnras/sty1518/5035832.

E. Contini, S. K. Yi, and X. Kang. Theoretical predictions of colors and metallicity of the intracluster light. *ApJ*, 871(1):24, January 2019. doi: 10.3847/1538-4357/aaf41f.

Emanuele Contini. On the origin and evolution of the intra-cluster light: A brief review of the most recent developments. *Galaxies*, 9(3):60, aug 2021. ISSN 2075-4434. doi: 10.3390/galaxies9030060. URL https://www.mdpi.com/2075-4434/9/3/60.

A. P. Cooper, L. Gao, Q. Guo, C. S. Frenk, A. Jenkins, V. Springel, and S. D. M. White. Surface photometry of brightest cluster galaxies and intra-cluster stars in Ł*ambda*cdm. *Monthly Notices of the Royal Astronomical Society*, 451(3):2703–2722, aug 2015a. ISSN 1365-2966. doi: 10.1093/mnras/stv1042. URL http://academic.oup.com/mnras/article/451/3/2703/1180070/Surface-photometry-of-brightest-cluster-galaxies.

Andrew P. Cooper, Richard D'Souza, Guinevere Kauffmann, Jing Wang, Michael Boylan-Kolchin, Qi Guo, Carlos S. Frenk, and Simon D. M. White. Galactic accretion and the outer structure of galaxies in the cdm model. *Monthly Notices of the Royal Astronomical Society*, 434:3348–3367, 10 2013. ISSN 0035-8711. doi: 10.1093/mnras/stt1245.

Andrew P. Cooper, Owen H. Parry, Ben Lowing, Shaun Cole, and Carlos Frenk. Formation of in situ stellar haloes in milky way-mass galaxies. *MNRAS*, 454(3):3185–3199, December 2015b. doi: 10.1093/mnras/stv2057.

Sofia A. Cora. Metal enrichment of the intracluster medium: a three-dimensional picture of chemical and dynamical properties. *MNRAS*, 368(4):1540–1560, June 2006. doi: 10.1111/j.1365-2966.2006.10271.x.

D. Crnojević, D. J. Sand, N. Caldwell, P. Guhathakurta, B. McLeod, A. Seth, J. D. Simon, J. Strader, and E. Toloba. Discovery of a close pair of faint dwarf galaxies in the halo of centaurus a. *ApJL*, 795(2):L35, November 2014. doi: 10.1088/2041-8205/795/2/L35.

D. Crnojević, D. J. Sand, D. Zaritsky, K. Spekkens, B. Willman, and J. R. Hargis. Deep imaging of eridanus ii and its lone star cluster. *The Astrophysical Journal*, 824:L14, 6 2016. ISSN 2041-8213. doi: 10.3847/2041-8205/824/1/L14.

D. Crnojević, D. J. Sand, P. Bennet, S. Pasetto, K. Spekkens, N. Caldwell, P. Guhathakurta, B. McLeod, A. Seth, J. D. Simon, J. Strader, and E. Toloba. The faint end of the centaurus a satellite luminosity function. *ApJ*, 872(1):80, February 2019. doi: 10.3847/1538-4357/aafbe7.

Denija Crnojević and Burçin Mutlu-Pakdil. Dwarf galaxies yesterday, now and tomorrow. *Nature Astronomy*, 5:1191–1194, December 2021. doi: 10.1038/s41550-021-01563-1.

Darren J. Croton, Adam R. H. Stevens, Chiara Tonini, Thibault Garel, Maksym Bernyk, Antonio Bibiano, Luke Hodkinson, Simon J. Mutch, Gregory B. Poole, and Genevieve M. Shattow. Semi-analytic galaxy evolution (sage): Model calibration and basic results. *ApJS*, 222(2):22, February 2016. doi: 10.3847/0067-0049/222/2/22.

Weiguang Cui, G. Murante, P. Monaco, S. Borgani, G. L. Granato, M. Killedar, G. De Lucia, V. Presotto, and Klaus Dolag. Characterizing diffused stellar light in simulated galaxy clusters. *Monthly Notices of the Royal Astronomical Society*, 437(1):816–830, jan 2014. ISSN 0035-8711. doi: 10.1093/mnras/stt1940. URL http://academic.oup.com/mnras/article/437/1/816/1008049/Characterizing-diffused-stellar-light-in-simulated.

C. Da Rocha and C. Mendes de Oliveira. Intragroup diffuse light in compact groups of galaxies: Hcg 79, 88 and 95. *MNRAS*, 364(3):1069–1081, December 2005. doi: 10.1111/j.1365-2966.2005.09641.x.

C. Da Rocha, B. L. Ziegler, and C. Mendes de Oliveira. Intragroup diffuse light in compact groups of galaxies – ii. hcg 15, 35 and 51. *Monthly Notices of the Royal Astronomical Society*, 388(3):1433–1443, 07 2008. ISSN 0035-8711. doi: 10.1111/j.1365-2966.2008.13500.x. URL https://doi.org/10.1111/j.1365-2966.2008.13500.x.

Shany Danieli, Pieter van Dokkum, Allison Merritt, Roberto Abraham, Jielai Zhang, I. D. Karachentsev, and L. N. Makarova. The dragonfly nearby galaxies survey. iii. the luminosity function of the m101 group. *ApJ*, 837(2):136, March 2017. doi: 10.3847/1538-4357/aa615b.

M. Davis, G. Efstathiou, C. S. Frenk, and S. D. M. White. The evolution of large-scale structure in a universe dominated by cold dark matter. *ApJ*, 292:371–394, May 1985. doi: 10.1086/163168.

Gabriella De Lucia and Jérémy Blaizot. The hierarchical formation of the brightest cluster galaxies. *MNRAS*, 375(1):2–14, February 2007. doi: 10.1111/j.1365-2966.2006.11287.x.

Nıcolas O. L. de Oliveira, Yolanda Jiménez-Teja, and Renato Dupke. The intracluster light on frontier fields clusters abell 370 and abell s1063. *MNRAS*, 512(2):1916–1923, May 2022. doi: 10.1093/mnras/stac407.

Gerard de Vaucouleurs, Antoinette de Vaucouleurs, Jr. Corwin, Herold G., Ronald J. Buta, Georges Paturel, and Pascal Fouque. *Third Reference Catalogue of Bright Galaxies*. 1991.

Alis J. Deason, Yao-Yuan Mao, and Risa H. Wechsler. The eating habits of milky way-mass halos: Destroyed dwarf satellites and the metallicity distribution of accreted stars. *ApJ*, 821(1):5, April 2016. doi: 10.3847/0004-637X/821/1/5.

Alis J Deason, Kyle A Oman, Azadeh Fattahi, Matthieu Schaller, Mathilde Jauzac, Yuanyuan Zhang, Mireia Montes, Yannick M Bahé, Claudio Dalla Vecchia, Scott T Kay, and Tilly A Evans. Stellar splashback: the edge of the intracluster light. *Monthly Notices of the Royal Astronomical Society*, 500(3):4181–4192, dec 2020. ISSN 0035-8711. doi: 10.1093/mnras/staa3590. URL https://academic.oup.com/mnras/article/500/3/4181/5992341.

Ariane Dekker, Shin'ichiro Ando, Camila A. Correa, and Kenny C. Y. Ng. Warm dark matter constraints using milky way satellite observations and subhalo evolution modeling. *PhRvD*, 106(12):123026, December 2022. doi: 10.1103/PhysRevD.106.123026.

Tahlia DeMaio, Anthony H. Gonzalez, Ann Zabludoff, Dennis Zaritsky, and Maruša Bradač. On the origin of the intracluster light in massive galaxy clusters. *Monthly Notices of the Royal Astronomical Society*, 448(2):1162–1177, apr 2015. ISSN 1365-2966. doi: 10.1093/mnras/stv033. URL http://academic.oup.com/mnras/article/448/2/1162/1051011/On-the-origin-of-the-intracluster-light-in-massive.

Tahlia DeMaio, Anthony H Gonzalez, Ann Zabludoff, Dennis Zaritsky, Thomas Connor, Megan Donahue, and John S Mulchaey. Lost but not forgotten: intracluster light in galaxy groups and clusters. *Monthly Notices of the Royal Astronomical Society*, 474 (3):3009–3031, mar 2018. ISSN 0035-8711. doi: 10.1093/mnras/stx2946. URL http://academic.oup.com/mnras/article/474/3/3009/4636556.

J. D. Diaz, S. E. Koposov, M. Irwin, V. Belokurov, and N. W. Evans. Balancing mass and momentum in the local group. *Monthly Notices of the Royal Astronomical Society*, 443: 1688–1703, 9 2014. ISSN 1365-2966. doi: 10.1093/mnras/stu1210.

K. Dolag, S. Borgani, G. Murante, and V. Springel. Substructures in hydrodynamical cluster simulations. *MNRAS*, 399(2):497–514, October 2009. doi: 10.1111/j.1365-2966.2009.15034.x.

Amandine Doliva-Dolinsky, Nicolas F. Martin, Zhen Yuan, Alessandro Savino, Daniel R. Weisz, Annette M. N. Ferguson, Rodrigo A. Ibata, Stacy Y. Kim, Geraint F. Lewis, Alan W. McConnachie, and Guillaume F. Thomas. The pandas view of the andromeda satellite system. iv. global properties. *ApJ*, 952(1):72, July 2023. doi: 10.3847/1538-4357/acdcf6.

Martina Donnari, Annalisa Pillepich, Dylan Nelson, Federico Marinacci, Mark Vogelsberger, and Lars Hernquist. Quenched fractions in the illustristng simulations: comparison with observations and other theoretical models. *MNRAS*, 506(4):4760–4780, October 2021. doi: 10.1093/mnras/stab1950.

Gregory A. Dooley, Annika H.G. Peter, Jeffrey L. Carlin, Anna Frebel, Keith Bechtol, and Beth Willman. The predicted luminous satellite populations around smc- and lmc-mass galaxies – a missing satellite problem around the lmc? *Monthly Notices of the Royal Astronomical Society*, 472:1060–1073, 11 2017. ISSN 0035-8711. doi: 10.1093/mnras/stx2001.

Jessica E. Doppel, Laura V. Sales, Dylan Nelson, Annalisa Pillepich, Mario G. Abadi, Eric W. Peng, Federico Marinacci, Jill Naiman, Paul Torrey, Mark Vogelsberger, Rainer Weinberger, and Lars Hernquist. Modelling globular clusters in the tng50 simulation: predictions from dwarfs to giant galaxies. *MNRAS*, 518(2):2453–2470, January 2023. doi: 10.1093/mnras/stac2818.

M. T. Doyle, M. J. Drinkwater, D. J. Rohde, K. A. Pimbblet, M. Read, M. J. Meyer, M. A. Zwaan, E. Ryan-Weber, J. Stevens, B. S. Koribalski, R. L. Webster, L. Staveley-Smith, D. G. Barnes, M. Howlett, V. A. Kilborn, M. Waugh, M. J. Pierce, R. Bhathal, W. J. G. de Blok, M. J. Disney, R. D. Ekers, K. C. Freeman, D. A. Garcia, B. K. Gibson, J. Harnett, P. A. Henning, H. Jerjen, M. J. Kesteven, P. M. Knezek, S. Mader, M. Marquarding, R. F. Minchin, J. O'Brien, T. Oosterloo, R. M. Price, M. E. Putman, S. D. Ryder, E. M. Sadler, I. M. Stewart, F. Stootman, and A. E. Wright. The hipass catalogue - iii. optical counterparts and isolated dark galaxies. *MNRAS*, 361(1):34–44, July 2005. doi: 10.1111/j.1365-2966.2005.09159.x.

A. Drlica-Wagner, K. Bechtol, E. S. Rykoff, E. Luque, A. Queiroz, Y.-Y. Mao, R. H. Wechsler, J. D. Simon, B. Santiago, B. Yanny, E. Balbinot, S. Dodelson, A. Fausti Neto, D. J. James, T. S. Li, M. A. G. Maia, J. L. Marshall, A. Pieres, K. Stringer, A. R. Walker, T. M. C. Abbott, F. B. Abdalla, S. Allam, A. Benoit-Lévy, G. M. Bernstein, E. Bertin, D. Brooks, E. Buckley-Geer, D. L. Burke, A. Carnero Rosell, M. Carrasco Kind, J. Carretero, M. Crocce, L. N. da Costa, S. Desai, H. T. Diehl, J. P. Dietrich, P. Doel, T. F. Eifler, A. E. Evrard, D. A. Finley, B. Flaugher, P. Fosalba, J. Frieman, E. Gaztanaga, D. W. Gerdes, D. Gruen, R. A. Gruendl, G. Gutierrez, K. Honscheid, K. Kuehn, N. Kuropatkin, O. Lahav, P. Martini, R. Miquel, B. Nord, R. Ogando, A. A. Plazas, K. Reil, A. Roodman, M. Sako, E. Sanchez, V. Scarpine, M. Schubnell, I. Sevilla-Noarbe, R. C. Smith, M. Soares-Santos, F. Sobreira, E. Suchyta, M. E. C. Swanson, G. Tarle, D. Tucker, V. Vikram, W. Wester, Y. Zhang, and J. Zuntz. Eight ultra-faint galaxy candidates discovered in year two of the dark energy survey. *The Astrophysical Journal*, 813:109, 11 2015. ISSN 1538-4357. doi: 10.1088/0004-637X/813/2/109.

A. Drlica-Wagner, K. Bechtol, S. Mau, M. McNanna, E. O. Nadler, A. B. Pace, T. S. Li, A. Pieres, E. Rozo, J. D. Simon, A. R. Walker, R. H. Wechsler, T. M. C. Abbott, S. Allam, J. Annis, E. Bertin, D. Brooks, D. L. Burke, A. Carnero Rosell, M. Carrasco Kind, J. Carretero, M. Costanzi, L. N. da Costa, J. De Vicente, S. Desai, H. T. Diehl, P. Doel, T. F. Eifler, S. Everett, B. Flaugher, J. Frieman, J. Garcıa-Bellido, E. Gaztanaga, D. Gruen, R. A.

Gruendl, J. Gschwend, G. Gutierrez, K. Honscheid, D. J. James, E. Krause, K. Kuehn, N. Kuropatkin, O. Lahav, M. A. G. Maia, J. L. Marshall, P. Melchior, F. Menanteau, R. Miquel, A. Palmese, A. A. Plazas, E. Sanchez, V. Scarpine, M. Schubnell, S. Serrano, I. Sevilla-Noarbe, M. Smith, E. Suchyta, G. Tarle, and DES Collaboration. Milky way satellite census. i. the observational selection function for milky way satellites in des y3 and pan-starrs dr1. *ApJ*, 893(1):47, April 2020. doi: 10.3847/1538-4357/ab7eb9.

A. Drlica-Wagner, P. S. Ferguson, M. Adamów, M. Aguena, S. Allam, F. Andrade-Oliveira, D. Bacon, K. Bechtol, E. F. Bell, E. Bertin, P. Bilaji, S. Bocquet, C. R. Bom, D. Brooks, D. L. Burke, J. A. Carballo-Bello, J. L. Carlin, A. Carnero Rosell, M. Carrasco Kind, J. Carretero, F. J. Castander, W. Cerny, C. Chang, Y. Choi, C. Conselice, M. Costanzi, D. Crnojević, L. N. da Costa, J. de Vicente, S. Desai, J. Esteves, S. Everett, I. Ferrero, M. Fitzpatrick, B. Flaugher, D. Friedel, J. Frieman, J. Garc-Bellido, M. Gatti, E. Gaztanaga, D. W. Gerdes, D. Gruen, R. A. Gruendl, J. Gschwend, W. G. Hartley, D. Hernandez-Lang, S. R. Hinton, D. L. Hollowood, K. Honscheid, A. K. Hughes, A. Jacques, D. J. James, M. D. Johnson, K. Kuehn, N. Kuropatkin, O. Lahav, T. S. Li, C. Lidman, H. Lin, M. March, J. L. Marshall, D. Mart´z-Delgado, C. E. Mart´ź-Vázquez, P. Massana, S. Mau, M. McNanna, P. Melchior, F. Menanteau, A. E. Miller, R. Miquel, J. J. Mohr, R. Morgan, B. Mutlu-Pakdil, R. R. Muñoz, E. H. Neilsen, D. L. Nidever, R. Nikutta, J. L. Nilo Castellon, N. E. D. Noël, R. L. C. Ogando, K. A. G. Olsen, A. B. Pace, A. Palmese, F. Paz-Chinchón, M. E. S. Pereira, A. Pieres, A. A. Plazas Malagón, J. Prat, A. H. Riley, M. Rodriguez-Monroy, A. K. Romer, A. Roodman, M. Sako, J. D. Sakowska, E. Sanchez, F. J. Sánchez, D. J. Sand, L. Santana-Silva, B. Santiago, M. Schubnell, S. Serrano, I. Sevilla-Noarbe, J. D. Simon, M. Smith, M. Soares-Santos, G. S. Stringfellow, E. Suchyta, D. J. Suson, C. Y. Tan, G. Tarle, K. Tavangar, D. Thomas, C. To, E. J. Tollerud, M. A. Troxel, D. L. Tucker, T. N. Varga, A. K. Vivas, A. R. Walker, J. Weller, R. D. Wilkinson, J. F. Wu, B. Yanny, E. Zaborowski, A. Zenteno, Delve Collaboration, Des Collaboration, and Astro Data Lab. The decam local volume exploration survey data release 2. *ApJS*, 261(2):38, August 2022. doi: 10.3847/1538-4365/ac78eb.

Richard D'Souza and Eric F. Bell. The andromeda galaxy's most important merger about 2 billion years ago as m32's likely progenitor. *Nature Astronomy*, 2:737–743, July 2018. doi: 10.1038/s41550-018-0533-x.

Renato A. Dupke, Yolanda Jimenez-Teja, Yuanyuan Su, Eleazar R. Carrasco, Anton M. Koekemoer, Rebeca M. Batalha, Lucas Johnson, Jimmy Irwin, Eric MIller, Paola Dimauro, Nıcolas O. L. de Oliveira, and Jose Vilchez. Independent evidence for earlier formation epochs of fossil groups of galaxies through the intracluster light: The case for rx j100742.53+380046.6. *ApJ*, 936(1):59, September 2022. doi: 10.3847/1538-4357/ac7f3f.

Patrick R. Durrell, Patrick Côté, Eric W. Peng, John P. Blakeslee, Laura Ferrarese, J. Christopher Mihos, Thomas H. Puzia, Ariane Lançon, Chengze Liu, Hongxin Zhang, Jean-Charles Cuillandre, Alan McConnachie, Andrés Jordán, Katharine Accetta, Samuel Boissier, Alessandro Boselli, Stéphane Courteau, Pierre-Alain Duc, Eric Emsellem, Stephen Gwyn, Simona Mei, and James E. Taylor. The next generation virgo cluster

survey. viii. the spatial distribution of globular clusters in the virgo cluster. *ApJ*, 794(2): 103, October 2014. doi: 10.1088/0004-637X/794/2/103.

Vincent R. Eke, Shaun Cole, and Carlos S. Frenk. Cluster evolution as a diagnostic for omega. *MNRAS*, 282:263–280, September 1996. doi: 10.1093/mnras/282.1.263.

Lydia M. Elias, Laura V. Sales, Peter Creasey, Michael C. Cooper, James S. Bullock, R. Michael Rich, and Lars Hernquist. Stellar halos in illustris: probing the histories of milky way-mass galaxies. *MNRAS*, 479(3):4004–4016, September 2018. doi: 10.1093/mnras/sty1718.

A. Ellien, E. Slezak, N. Martinet, F. Durret, C. Adami, R. Gavazzi, C. R. Rabaça, C. Da Rocha, and D. N. Epitácio Pereira. Dawis: a detection algorithm with wavelets for intracluster light studies. *åp*, 649:A38, May 2021. doi: 10.1051/0004-6361/202038419.

Christoph Engler, Annalisa Pillepich, Anna Pasquali, Dylan Nelson, Vicente Rodriguez-Gomez, Kun Ting Eddie Chua, Eva K. Grebel, Volker Springel, Federico Marinacci, Rainer Weinberger, Mark Vogelsberger, and Lars Hernquist. The abundance of satellites around milky way- and m31-like galaxies with the tng50 simulation: a matter of diversity. *MNRAS*, 507(3):4211–4240, November 2021. doi: 10.1093/mnras/stab2437.

Azadeh Fattahi, Julio F. Navarro, Till Sawala, Carlos S. Frenk, Kyle A. Oman, Robert A. Crain, Michelle Furlong, Matthieu Schaller, Joop Schaye, Tom Theuns, and Adrian Jenkins. The apostle project: Local group kinematic mass constraints and simulation candidate selection. *MNRAS*, 457(1):844–856, March 2016. doi: 10.1093/mnras/stv2970.

Claude-André Faucher-Giguère. A cosmic uv/x-ray background model update. *MNRAS*, 493(2):1614–1632, April 2020. doi: 10.1093/mnras/staa302.

Henry C. Ferguson and Bruno Binggeli. Dwarf elliptical galaxies. *The Astronomy and Astrophysics Review*, 6:67–122, 3 1994. ISSN 0935-4956. doi: 10.1007/BF01208252.

Drummond B. Fielding, Eve C. Ostriker, Greg L. Bryan, and Adam S. Jermyn. Multiphase gas and the fractal nature of radiative turbulent mixing layers. *ApJL*, 894(2):L24, May 2020. doi: 10.3847/2041-8213/ab8d2c.

Alex Fitts, Michael Boylan-Kolchin, Oliver D. Elbert, James S. Bullock, Philip F. Hopkins, Jose Oñorbe, Andrew Wetzel, Coral Wheeler, Claude-André Faucher-Giguère, Dušan Kereš, Evan D. Skillman, and Daniel R. Weisz. fire in the field: simulating the threshold of galaxy formation. *MNRAS*, 471(3):3547–3562, November 2017. doi: 10.1093/mnras/stx1757.

Ricardo A. Flores and Joel R. Primack. Observational and Theoretical Constraints on Singular Dark Matter Halos. *ApJL*, 427:L1, May 1994. doi: 10.1086/187350.

A. S. Font, R. G. Bower, I. G. McCarthy, A. J. Benson, C. S. Frenk, J. C. Helly, C. G. Lacey, C. M. Baugh, and S. Cole. The colours of satellite galaxies in groups and clusters. *MNRAS*, 389(4):1619–1629, October 2008. doi: 10.1111/j.1365-2966.2008.13698.x.

A. S. Font, A. J. Benson, R. G. Bower, C. S. Frenk, A. Cooper, G. DeLucia, J. C. Helly, A. Helmi, Y.-S. Li, I. G. McCarthy, J. F. Navarro, V. Springel, E. Starkenburg, J. Wang, and S. D. M. White. The population of milky way satellites in the cold dark matter cosmology. *Monthly Notices of the Royal Astronomical Society*, 417:1260–1279, 10 2011. ISSN 00358711. doi: 10.1111/j.1365-2966.2011.19339.x.

Amanda Brady Ford, Benjamin D. Oppenheimer, Romeel Davé, Neal Katz, Juna A. Kollmeier, and David H. Weinberg. Hydrogen and metal line absorption around low-redshift galaxies in cosmological hydrodynamic simulations. *MNRAS*, 432(1):89–112, June 2013. doi: 10.1093/mnras/stt393.

Mattia Fumagalli, G. Gavazzi, R. Scaramella, and P. Franzetti. Constraining the ages of the fireballs in the wake of the dirr galaxy vcc 1217/ic 3418. *åp*, 528:A46, April 2011. doi: 10.1051/0004-6361/201015463.

Daniele Galli and Francesco Palla. The chemistry of the early universe. *åp*, 335:403–420, July 1998. doi: 10.48550/arXiv.astro-ph/9803315.

Shea Garrison-Kimmel, Philip F. Hopkins, Andrew Wetzel, James S. Bullock, Michael Boylan-Kolchin, Dušan Kereš, Claude-André Faucher-Giguère, Kareem El-Badry, Astrid Lamberts, Eliot Quataert, and Robyn Sanderson. The local group on fire: dwarf galaxy populations across a suite of hydrodynamic simulations. *MNRAS*, 487(1):1380–1399, July 2019. doi: 10.1093/mnras/stz1317.

Marla Geha, Risa H. Wechsler, Yao-Yuan Mao, Erik J. Tollerud, Benjamin Weiner, Rebecca Bernstein, Ben Hoyle, Sebastian Marchi, Phil J. Marshall, Ricardo Muñoz, and Yu Lu. The saga survey. i. satellite galaxy populations around eight milky way analogs. *ApJ*, 847(1):4, September 2017. doi: 10.3847/1538-4357/aa8626.

Shy Genel, Mark Vogelsberger, Volker Springel, Debora Sijacki, Dylan Nelson, Greg Snyder, Vicente Rodriguez-Gomez, Paul Torrey, and Lars Hernquist. Introducing the illustris project: the evolution of galaxy populations across cosmic time. *MNRAS*, 445(1):175–200, November 2014. doi: 10.1093/mnras/stu1654.

Shy Genel, Dylan Nelson, Annalisa Pillepich, Volker Springel, Rüdiger Pakmor, Rainer Weinberger, Lars Hernquist, Jill Naiman, Mark Vogelsberger, Federico Marinacci, and Paul Torrey. The size evolution of star-forming and quenched galaxies in the illustristng simulation. *MNRAS*, 474(3):3976–3996, March 2018. doi: 10.1093/mnras/stx3078.

Ortwin Gerhard, Magda Arnaboldi, Kenneth C. Freeman, and Sadanori Okamura. Isolated star formation: A compact h ii region in the virgo cluster. *ApJL*, 580(2):L121–L124, December 2002. doi: 10.1086/345657.

Nickolay Y. Gnedin. Effect of reionization on structure formation in the universe. *ApJ*, 542 (2):535–541, October 2000. doi: 10.1086/317042.

Oleg Y. Gnedin and Jeremiah P. Ostriker. On the self-consistent response of stellar systems to gravitational shocks. *The Astrophysical Journal*, 513:626–637, 3 1999. ISSN 0004-637X. doi: 10.1086/306864.

Anthony H Gonzalez, Tyler George, Thomas Connor, Alis Deason, Megan Donahue, Mireia Montes, Ann I Zabludoff, and Dennis Zaritsky. Discovery of a possible splashback feature in the intracluster light of macs j1149.5+2223. *Monthly Notices of the Royal Astronomical Society*, 507(1):963–970, aug 2021a. ISSN 0035-8711. doi: 10.1093/mnras/stab2117. URL https://academic.oup.com/mnras/article/507/1/963/6338115.

Elizabeth J. Gonzalez, Cinthia Ragone-Figueroa, Carlos J. Donzelli, Martın Makler, Diego Garc Lambas, and Gian Luigi Granato. Halo cluster shapes: insights from simulated galaxies and icl with prospects for weak lensing applications. *MNRAS*, 508(1):1280–1295, November 2021b. doi: 10.1093/mnras/stab2585.

Robert J. J. Grand, Facundo A. Gómez, Federico Marinacci, Rüdiger Pakmor, Volker Springel, David J. R. Campbell, Carlos S. Frenk, Adrian Jenkins, and Simon D. M. White. The auriga project: the properties and formation mechanisms of disc galaxies across cosmic time. *MNRAS*, 467(1):179–207, May 2017. doi: 10.1093/mnras/stx071.

Robert J. J. Grand, Federico Marinacci, Rüdiger Pakmor, Christine M. Simpson, Ashley J. Kelly, Facundo A. Gómez, Adrian Jenkins, Volker Springel, Carlos S. Frenk, and Simon D. M. White. Determining the full satellite population of a milky way-mass halo in a highly resolved cosmological hydrodynamic simulation. *MNRAS*, 507(4):4953–4967, November 2021. doi: 10.1093/mnras/stab2492.

Raffaele Gratton, Angela Bragaglia, Eugenio Carretta, Valentina D'Orazi, Sara Lucatello, and Antonio Sollima. What is a globular cluster? an observational perspective. *The Astronomy and Astrophysics Review*, 27(1), nov 2019. doi: 10.1007/s00159-019-0119-3. URL https://doi.org/10.1007%2Fs00159-019-0119-3.

Meng Gu, Charlie Conroy, David Law, Pieter van Dokkum, Renbin Yan, David Wake, Kevin Bundy, Alexa Villaume, Roberto Abraham, Allison Merritt, Jielai Zhang, Matthew Bershady, Dmitry Bizyaev, Niv Drory, Kaike Pan, Daniel Thomas, and Anne-Marie Weijmans. Spectroscopic constraints on the buildup of intracluster light in the coma cluster. *ApJ*, 894(1):32, May 2020. doi: 10.3847/1538-4357/ab845c.

Marco Gullieuszik, Bianca M. Poggianti, Sean L. McGee, Alessia Moretti, Benedetta Vulcani, Stephanie Tonnesen, Elke Roediger, Yara L. Jaffé, Jacopo Fritz, Andrea Franchetto, Alessandro Omizzolo, Daniela Bettoni, Mario Radovich, and Anna Wolter. Gasp. xxi. star formation rates in the tails of galaxies undergoing ram pressure stripping. *ApJ*, 899 (1):13, August 2020. doi: 10.3847/1538-4357/aba3cb.

Junia Göller, Gandhali D. Joshi, Eric Rohr, Elad Zinger, and Annalisa Pillepich. Jellyfish galaxies with the illustristng simulations - no enhanced population-wide star formation according to tng50. *MNRAS*, 525(3):3551–3570, November 2023. doi: 10.1093/mnras/stad2551.

F. Haardt and P. Madau. Modelling the uv/x-ray cosmic background with cuba. In D. M. Neumann and J. T. V. Tran, editors, *Clusters of Galaxies and the High Redshift Universe Observed in X-rays*, page 64, January 2001. doi: 10.48550/arXiv.astro-ph/0106018.

Francesco Haardt and Piero Madau. Radiative transfer in a clumpy universe. iv. new synthesis models of the cosmic uv/x-ray background. *ApJ*, 746(2):125, February 2012. doi: 10.1088/0004-637X/746/2/125.

Cai-Na Hao, Robert C. Kennicutt, Benjamin D. Johnson, Daniela Calzetti, Daniel A. Dale, and John Moustakas. Dust-corrected star formation rates of galaxies. ii. combinations of ultraviolet and infrared tracers. *ApJ*, 741(2):124, November 2011. doi: 10.1088/0004-637X/741/2/124.

Charles R Harris, K Jarrod Millman, Stéfan J van der Walt, Ralf Gommers, Pauli Virtanen, David Cournapeau, Eric Wieser, Julian Taylor, Sebastian Berg, Nathaniel J Smith, Robert Kern, Matti Picus, Stephan Hoyer, Marten H van Kerkwijk, Matthew Brett, Allan Haldane, Jaime Fernández del Río, Mark Wiebe, Pearu Peterson, Pierre Gérard-Marchant, Kevin Sheppard, Tyler Reddy, Warren Weckesser, Hameer Abbasi, Christoph Gohlke, and Travis E Oliphant. Array programming with NumPy. *Nature*, 585(7825):357–362, 2020a. ISSN 1476-4687. doi: 10.1038/s41586-020-2649-2. URL https://doi.org/10.1038/s41586-020-2649-2.

William E. Harris and Marta Reina-Campos. Jwst photometry of globular cluster populations in abell 2744 at z = 0.3. *MNRAS*, 526(2):2696–2708, December 2023. doi: 10.1093/mnras/stad2903.

William E. Harris, Gretchen L. H. Harris, and Matthew Alessi. A catalog of globular cluster systems: What determines the size of a galaxy's globular cluster population? *The Astrophysical Journal*, 772(2):82, jul 2013. ISSN 0004-637X. doi: 10.1088/0004-637X/772/2/82. URL https://iopscience.iop.org/article/10.1088/2041-8205/787/1/L5https://iopscience.iop.org/article/10.1088/0004-637X/772/2/82.

William E. Harris, Gretchen L. Harris, and Michael J. Hudson. Dark matter halos in galaxies and globular cluster populations. ii. metallicity and morphology. *The Astrophysical Journal*, 806(1):36, jun 2015. ISSN 1538-4357. doi: 10.1088/0004-637X/806/1/36. URL https://iopscience.iop.org/article/10.1088/0004-637X/806/1/36.

William E. Harris, Rachel A. Brown, Patrick R. Durrell, Aaron J. Romanowsky, John Blakeslee, Jean Brodie, Steven Janssens, Thorsten Lisker, Sakurako Okamoto, and Carolin Wittmann. The piper survey. i. an initial look at the intergalactic globular cluster population in the perseus cluster. *ApJ*, 890(2):105, February 2020b. doi: 10.3847/1538-4357/ab6992.

Tilman Hartwig, Mattis Magg, Li-Hsin Chen, Yuta Tarumi, Volker Bromm, Simon C. O. Glover, Alexander P. Ji, Ralf S. Klessen, Muhammad A. Latif, Marta Volonteri, and Naoki Yoshida. Public release of a-sloth: Ancient stars and local observables by tracing halos. *ApJ*, 936(1):45, September 2022. doi: 10.3847/1538-4357/ac7150.

Bruno M. B. Henriques, Simon D. M. White, Peter A. Thomas, Raul Angulo, Qi Guo, Gerard Lemson, Volker Springel, and Roderik Overzier. Galaxy formation in the planck cosmology - i. matching the observed evolution of star formation rates, colours and stellar masses. *MNRAS*, 451(3):2663–2680, August 2015. doi: 10.1093/mnras/stv705.

Lars Hernquist. An analytical model for spherical galaxies and bulges. *ApJ*, 356:359, June 1990. doi: 10.1086/168845.

J. A. Hester. Ram Pressure Stripping in Clusters and Groups. *ApJ*, 647(2):910–921, August 2006. doi: 10.1086/505614.

Janice A. Hester, Mark Seibert, James D. Neill, Ted K. Wyder, Armando Gil de Paz, Barry F. Madore, D. Christopher Martin, David Schiminovich, and R. Michael Rich. Ic 3418: Star formation in a turbulent wake. *ApJL*, 716(1):L14–L18, June 2010. doi: 10.1088/2041-8205/716/1/L14.

G. Hinshaw, D. Larson, E. Komatsu, D. N. Spergel, C. L. Bennett, J. Dunkley, M. R. Nolta, M. Halpern, R. S. Hill, N. Odegard, L. Page, K. M. Smith, J. L. Weiland, B. Gold, N. Jarosik, A. Kogut, M. Limon, S. S. Meyer, G. S. Tucker, E. Wollack, and E. L. Wright. Nine-year wilkinson microwave anisotropy probe (wmap) observations: Cosmological parameter results. *ApJS*, 208(2):19, October 2013. doi: 10.1088/0067-0049/208/2/19.

J. Hlavacek-Larrondo, C. L. Rhea, T. Webb, M. McDonald, A. Muzzin, G. Wilson, K. Finner, F. Valin, N. Bonaventura, M. Cooper, A. C. Fabian, M. L. Gendron-Marsolais, M. J. Jee, C. Lidman, M. Mezcua, A. Noble, H. R. Russell, J. Surace, A. Trudeau, and H. K. C. Yee. Evidence of runaway gas cooling in the absence of supermassive black hole feedback at the epoch of cluster formation. *ApJL*, 898(2):L50, August 2020. doi: 10.3847/2041-8213/ab9ca5.

Philip F. Hopkins, Andrew Wetzel, Dušan Kereš, Claude-André Faucher-Giguère, Eliot Quataert, Michael Boylan-Kolchin, Norman Murray, Christopher C. Hayward, Shea Garrison-Kimmel, Cameron Hummels, Robert Feldmann, Paul Torrey, Xiangcheng Ma, Daniel Anglés-Alcázar, Kung-Yi Su, Matthew Orr, Denise Schmitz, Ivanna Escala, Robyn Sanderson, Michael Y. Grudić, Zachary Hafen, Ji-Hoon Kim, Alex Fitts, James S. Bullock, Coral Wheeler, T. K. Chan, Oliver D. Elbert, and Desika Narayanan. Fire-2 simulations: physics versus numerics in galaxy formation. *MNRAS*, 480(1):800–863, October 2018. doi: 10.1093/mnras/sty1690.

Philip F. Hopkins, Andrew Wetzel, Coral Wheeler, Robyn Sanderson, Michael Y. Grudić, Omid Sameie, Michael Boylan-Kolchin, Matthew Orr, Xiangcheng Ma, Claude-André Faucher-Giguère, Dušan Kereš, Eliot Quataert, Kung-Yi Su, Jorge Moreno, Robert Feldmann, James S. Bullock, Sarah R. Loebman, Daniel Anglés-Alcázar, Jonathan Stern, Lina Necib, Caleb R. Choban, and Christopher C. Hayward. Fire-3: updated stellar evolution models, yields, and microphysics and fitting functions for applications in galaxy simulations. *MNRAS*, 519(2):3154–3181, February 2023. doi: 10.1093/mnras/stac3489.

Michael J. Hudson, Gretchen L. Harris, and William E. Harris. Dark matter halos in galaxies and globular cluster populations. *The Astrophysical Journal*, 787(1):L5, apr 2014. ISSN 2041-8205. doi: 10.1088/2041-8205/787/1/L5. URL https://iopscience.iop.org/article/10.1088/2041-8205/787/1/L5.

Michael J. Hudson, Bryan R. Gillis, Jean Coupon, Hendrik Hildebrandt, Thomas Erben, Catherine Heymans, Henk Hoekstra, Thomas D. Kitching, Yannick Mellier, Lance

Miller, Ludovic Van Waerbeke, Christopher Bonnett, Liping Fu, Konrad Kuijken, Barnaby Rowe, Tim Schrabback, Elisabetta Semboloni, Edo van Uitert, and Malin Velander. Cfhtlens: co-evolution of galaxies and their dark matter haloes. *Monthly Notices of the Royal Astronomical Society*, 447(1):298–314, feb 2015. ISSN 1365-2966. doi: 10.1093/mnras/stu2367. URL http://academic.oup.com/mnras/article/447/1/298/987958/CFHTLenS-coevolution-of-galaxies-and-their-dark.

John D. Hunter. Matplotlib: A 2d graphics environment. *Computing in Science Engineering*, 9(3):90–95, 2007. doi: 10.1109/MCSE.2007.55.

Enrichetta Iodice, Marilena Spavone, Arianna Cattapan, Elena Bannikova, Duncan A. Forbes, Roberto Rampazzo, Stefano Ciroi, Enrico Maria Corsini, Giuseppe D'Ago, Tom Oosterloo, Pietro Schipani, and Massimo Capaccioli. Vegas: a vst early-type galaxy survey. v. ic 1459 group: Mass assembly history in low-density environments. *åp*, 635:A3, March 2020. doi: 10.1051/0004-6361/201936435.

Jason Jaacks, Robert Thompson, Steven L. Finkelstein, and Volker Bromm. Baseline metal enrichment from population iii star formation in cosmological volume simulations. *MNRAS*, 475(4):4396–4410, April 2018. doi: 10.1093/mnras/sty062.

Ethan D. Jahn, Laura V. Sales, Andrew Wetzel, Michael Boylan-Kolchin, T. K. Chan, Kareem El-Badry, Alexandres Lazar, and James S. Bullock. Dark and luminous satellites of lmc-mass galaxies in the fire simulations. *MNRAS*, 489(4):5348–5364, November 2019. doi: 10.1093/mnras/stz2457.

P. A. James, N. S. Shane, J. E. Beckman, A. Cardwell, C. A. Collins, J. Etherton, R. S. de Jong, K. Fathi, J. H. Knapen, R. F. Peletier, S. M. Percival, D. L. Pollacco, M. S. Seigar, S. Stedman, and I. A. Steele. The Hα galaxy survey. i. the galaxy sample, Hα narrow-band observations and star formation parameters for 334 galaxies. *åp*, 414:23–43, January 2004. doi: 10.1051/0004-6361:20031568.

N. Jarosik, C. L. Bennett, J. Dunkley, B. Gold, M. R. Greason, M. Halpern, R. S. Hill, G. Hinshaw, A. Kogut, E. Komatsu, D. Larson, M. Limon, S. S. Meyer, M. R. Nolta, N. Odegard, L. Page, K. M. Smith, D. N. Spergel, G. S. Tucker, J. L. Weiland, E. Wollack, and E. L. Wright. Seven-year wilkinson microwave anisotropy probe (wmap) observations: Sky maps, systematic errors, and basic results. *ApJS*, 192(2):14, February 2011. doi: 10.1088/0067-0049/192/2/14.

Myoungwon Jeon, Gurtina Besla, and Volker Bromm. Connecting the first galaxies with ultrafaint dwarfs in the local group: Chemical signatures of population iii stars. *ApJ*, 848 (2):85, October 2017. doi: 10.3847/1538-4357/aa8c80.

P. Jethwa, D. Erkal, and V. Belokurov. A magellanic origin of the des dwarfs. *MNRAS*, 461(2):2212–2233, September 2016. doi: 10.1093/mnras/stw1343.

Lilian Jiang, Shaun Cole, Till Sawala, and Carlos S. Frenk. Orbital parameters of infalling satellite haloes in the hierarchical ΛCDM model. *MNRAS*, 448(2):1674–1686, April 2015. doi: 10.1093/mnras/stv053.

Y. Jiménez-Teja and R. Dupke. Disentangling the icl with the chefs: Abell 2744 as a case study. *ApJ*, 820(1):49, March 2016. doi: 10.3847/0004-637X/820/1/49.

Y. Jiménez-Teja, R. A. Dupke, R. Lopes de Oliveira, H. S. Xavier, P. R. T. Coelho, A. L. Chies-Santos, C. López-Sanjuan, A. Alvarez-Candal, M. V. Costa-Duarte, E. Telles, J. A. Hernandez-Jimenez, N. Benıtez, J. Alcaniz, J. Cenarro, D. Cristóbal-Hornillos, A. Ederoclite, A. Mar-Franch, C. Mendes de Oliveira, M. Moles, L. Sodré, J. Varela, and H. Vázquez Ramió. J-plus: Analysis of the intracluster light in the coma cluster. *åp*, 622: A183, February 2019. doi: 10.1051/0004-6361/201833547.

Yolanda Jiménez-Teja, Renato Dupke, Narciso Benıtez, Anton M. Koekemoer, Adi Zitrin, Keiichi Umetsu, Bodo L. Ziegler, Brenda L. Frye, Holland Ford, Rychard J. Bouwens, Larry D. Bradley, Thomas Broadhurst, Dan Coe, Megan Donahue, Genevieve J. Graves, Claudio Grillo, Leopoldo Infante, Stephanie Jouvel, Daniel D. Kelson, Ofer Lahav, Ruth Lazkoz, Dorom Lemze, Dan Maoz, Elinor Medezinski, Peter Melchior, Massimo Meneghetti, Amata Mercurio, Julian Merten, Alberto Molino, Leonidas A. Moustakas, Mario Nonino, Sara Ogaz, Adam G. Riess, Piero Rosati, Jack Sayers, Stella Seitz, and Wei Zheng. Unveiling the dynamical state of massive clusters through the icl fraction. *ApJ*, 857(2):79, April 2018. doi: 10.3847/1538-4357/aab70f.

Yolanda Jiménez-Teja, Jose M. Vılchez, Renato A. Dupke, Paulo A. A. Lopes, Ņolas O. L. de Oliveira, and Dan Coe. Relics: Icl analysis of the z = 0.566 merging cluster whl j013719.8-08284. *ApJ*, 922(2):268, December 2021. doi: 10.3847/1538-4357/ac24a3.

Michael G. Jones, David J. Sand, Michele Bellazzini, Kristine Spekkens, Ananthan Karunakaran, Elizabeth A. K. Adams, Giuseppina Battaglia, Giacomo Beccari, Paul Bennet, John M. Cannon, Giovanni Cresci, Denija Crnojević, Nelson Caldwell, Jackson Fuson, Puragra Guhathakurta, Martha P. Haynes, John L. Inoue, Laura Magrini, Ricardo R. Muñoz, Burçin Mutlu-Pakdil, Anil Seth, Jay Strader, Elisa Toloba, and Dennis Zaritsky. Young, blue, and isolated stellar systems in the virgo cluster. ii. a new class of stellar system. *ApJ*, 935(1):51, August 2022. doi: 10.3847/1538-4357/ac7c6c.

Michael G. Jones, Steven Janowiecki, Swapnaneel Dey, David J. Sand, Paul Bennet, Denija Crnojević, Catherine E. Fielder, Ananthan Karunakaran, Brian R. Kent, Nicolas Mazziotti, Burçin Mutlu-Pakdil, and Kristine Spekkens. Dark no more: The low-luminosity stellar counterpart of a dark cloud in the virgo cluster. *ApJL*, 966(1):L15, May 2024. doi: 10.3847/2041-8213/ad3ef5.

Andres Jordan, Dean E. McLaughlin, Patrick Cote, Laura Ferrarese, Eric W. Peng, Simona Mei, Daniela Villegas, David Merritt, John L. Tonry, and Michael J. West. The acs virgo cluster survey. xii. the luminosity function of globular clusters in early-type galaxies. *The Astrophysical Journal Supplement Series*, 171(1):101–145, jul 2007. ISSN 0067-0049. doi: 10.1086/516840. URL https://iopscience.iop.org/article/10.1086/516840.

Gandhali D. Joshi, Andrew Pontzen, Oscar Agertz, Martin P. Rey, Justin Read, and Florent Renaud. Vintergatan-gm: How do mergers affect the satellite populations of mw-like galaxies? *MNRAS*, 528(2):2346–2357, February 2024. doi: 10.1093/mnras/stae129.

Junais, S. Boissier, A. Boselli, M. Boquien, A. Longobardi, Y. Roehlly, P. Amram, M. Fossati, J. C. Cuillandre, S. Gwyn, L. Ferrarese, P. Côté, J. Roediger, S. Lim, E. W. Peng, G. Hensler, G. Trinchieri, J. Koda, and N. Prantzos. A virgo environmental survey tracing ionised gas emission (vestige). x. formation of a red ultra-diffuse galaxy and an almost dark galaxy during a ram-pressure stripping event. *åp*, 650:A99, June 2021. doi: 10.1051/0004-6361/202040185.

X. Kang. Modeling the milky-way satellite galaxies. *arXiv e-prints*, art. arXiv:0806.3279, December 2008. doi: 10.48550/arXiv.0806.3279.

W. Kapferer, C. Sluka, S. Schindler, C. Ferrari, and B. Ziegler. The effect of ram pressure on the star formation, mass distribution and morphology of galaxies. *åp*, 499(1):87–102, May 2009. doi: 10.1051/0004-6361/200811551.

I. D. Karachentsev, D. I. Makarov, M. E. Sharina, A. E. Dolphin, E. K. Grebel, D. Geisler, P. Guhathakurta, P. W. Hodge, V. E. Karachentseva, A. Sarajedini, and P. Seitzer. Local galaxy flows within 5 mpc. *åp*, 398:479–491, February 2003. doi: 10.1051/0004-6361:20021566.

Igor D. Karachentsev and Yuri N. Kudrya. Orbital masses of nearby luminous galaxies. *The Astronomical Journal*, 148:50, 8 2014. ISSN 0004-6256. doi: 10.1088/0004-6256/148/3/50.

Igor D. Karachentsev, R. Brent Tully, Andrew Dolphin, Margarita Sharina, Lidia Makarova, Dmitry Makarov, Shoko Sakai, Edward J. Shaya, Olga G. Kashibadze, Valentina Karachentseva, and Luca Rizzi. The hubble flow around the centaurus a/m83 galaxy complex. *The Astronomical Journal*, 133:504–517, 2 2007. ISSN 0004-6256. doi: 10.1086/510125.

Igor D. Karachentsev, Dmitry I. Makarov, and Elena I. Kaisina. Updated nearby galaxy catalog. *AJ*, 145(4):101, April 2013. doi: 10.1088/0004-6256/145/4/101.

Harley Katz, Marius Ramsoy, Joakim Rosdahl, Taysun Kimm, Jérémy Blaizot, Martin G. Haehnelt, Léo Michel-Dansac, Thibault Garel, Clotilde Laigle, Julien Devriendt, and Adrianne Slyz. How to quench a dwarf galaxy: The impact of inhomogeneous reionization on dwarf galaxies and cosmic filaments. *MNRAS*, 494(2):2200–2220, May 2020. doi: 10.1093/mnras/staa639.

Tobias Kaufmann, Lucio Mayer, James Wadsley, Joachim Stadel, and Ben Moore. Cooling flows within galactic haloes: the kinematics and properties of infalling multiphase gas. *MNRAS*, 370(4):1612–1622, August 2006. doi: 10.1111/j.1365-2966.2006.10599.x.

Tobias Kaufmann, James S. Bullock, Ariyeh H. Maller, Taotao Fang, and James Wadsley. Redistributing hot gas around galaxies: do cool clouds signal a solution to the overcooling problem? *MNRAS*, 396(1):191–202, June 2009. doi: 10.1111/j.1365-2966.2009.14744.x.

Jeffrey D. P. Kenney, Marla Geha, Pavel Jáchym, Hugh H. Crowl, William Dague, Aeree Chung, Jacqueline van Gorkom, and Bernd Vollmer. Transformation of a virgo cluster

dwarf irregular galaxy by ram pressure stripping: Ic3418 and its fireballs. *ApJ*, 780(2): 119, January 2014. doi: 10.1088/0004-637X/780/2/119.

Robert C. Kennicutt and Neal J. Evans. Star formation in the milky way and nearby galaxies. *Annual Review of Astronomy and Astrophysics*, 50(1):531–608, Sep 2012. ISSN 1545-4282. doi: 10.1146/annurev-astro-081811-125610. URL http://dx.doi.org/10.1146/annurev-astro-081811-125610.

Ivan King. The structure of star clusters. i. an empirical density law. *AJ*, 67:471, October 1962. doi: 10.1086/108756.

Ralf S. Klessen and Simon C. O. Glover. The first stars: Formation, properties, and impact. *ARA&A*, 61:65–130, August 2023. doi: 10.1146/annurev-astro-071221-053453.

M. Kluge, R. Bender, A. Riffeser, C. Goessl, U. Hopp, M. Schmidt, and C. Ries. Photometric dissection of intracluster light and its correlations with host cluster properties. *ApJS*, 252 (2):27, February 2021. doi: 10.3847/1538-4365/abcda6.

M. Kluge, N. A. Hatch, M. Montes, J. B. Golden-Marx, A. H. Gonzalez, J. C. Cuillandre, M. Bolzonella, A. Lançon, R. Laureijs, T. Saifollahi, M. Schirmer, C. Stone, A. Boselli, M. Cantiello, J. G. Sorce, F. R. Marleau, P. A. Duc, E. Sola, M. Urbano, S. L. Ahad, Y. M. Bahé, S. P. Bamford, C. Bellhouse, F. Buitrago, P. Dimauro, F. Durret, A. Ellien, Y. Jimenez-Teja, E. Slezak, N. Aghanim, B. Altieri, S. Andreon, N. Auricchio, M. Baldi, A. Balestra, S. Bardelli, R. Bender, D. Bonino, E. Branchini, M. Brescia, J. Brinchmann, S. Camera, G. P. Candini, V. Capobianco, C. Carbone, J. Carretero, S. Casas, M. Castellano, S. Cavuoti, A. Cimatti, G. Congedo, C. J. Conselice, L. Conversi, Y. Copin, F. Courbin, H. M. Courtois, M. Cropper, A. Da Silva, H. Degaudenzi, J. Dinis, C. A. J. Duncan, X. Dupac, S. Dusini, M. Farina, S. Farrens, S. Ferriol, P. Fosalba, M. Frailis, E. Franceschi, M. Fumana, S. Galeotta, B. Garilli, W. Gillard, B. Gillis, C. Giocoli, P. Gómez-Alvarez, B. R. Granett, A. Grazian, F. Grupp, L. Guzzo, S. V. H. Haugan, J. Hoar, H. Hoekstra, W. Holmes, I. Hook, F. Hormuth, A. Hornstrup, P. Hudelot, K. Jahnke, E. Keihänen, S. Kermiche, A. Kiessling, T. Kitching, R. Kohley, B. Kubik, M. Kümmel, M. Kunz, H. Kurki-Suonio, O. Lahav, S. Ligori, P. B. Lilje, V. Lindholm, I. Lloro, E. Maiorano, O. Mansutti, O. Marggraf, K. Markovic, N. Martinet, F. Marulli, R. Massey, S. Maurogordato, H. J. McCracken, E. Medinaceli, S. Mei, M. Melchior, Y. Mellier, M. Meneghetti, E. Merlin, G. Meylan, M. Moresco, L. Moscardini, E. Munari, R. C. Nichol, S. M. Niemi, J. W. Nightingale, C. Padilla, S. Paltani, F. Pasian, K. Pedersen, W. J. Percival, V. Pettorino, S. Pires, G. Polenta, M. Poncet, L. A. Popa, L. Pozzetti, G. D. Racca, F. Raison, R. Rebolo, A. Renzi, J. Rhodes, G. Riccio, H. W. Rix, E. Romelli, M. Roncarelli, E. Rossetti, R. Saglia, D. Sapone, B. Sartoris, M. Sauvage, R. Scaramella, P. Schneider, T. Schrabback, A. Secroun, G. Seidel, M. Seiffert, S. Serrano, C. Sirignano, G. Sirri, J. Skottfelt, L. Stanco, P. Tallada-Crespí, A. N. Taylor, H. I. Teplitz, I. Tereno, R. Toledo-Moreo, F. Torradeflot, I. Tutusaus, E. A. Valentijn, L. Valenziano, T. Vassallo, G. Verdoes Kleijn, A. Veropalumbo, Y. Wang, J. Weller, O. R. Williams, G. Zamorani, E. Zucca, A. Biviano, C. Burigana, G. De Lucia, K. George, V. Scottez, P. Simon, A. Mora, J. Martín-Fleitas, F. Ruppin, and D. Scott. Euclid: Early Release Observations

– The intracluster light and intracluster globular clusters of the Perseus cluster. *arXiv e-prints*, art. arXiv:2405.13503, May 2024. doi: 10.48550/arXiv.2405.13503.

Anatoly Klypin, Gustavo Yepes, Stefan Gottlöber, Francisco Prada, and Steffen Heß. Multidark simulations: the story of dark matter halo concentrations and density profiles. *MNRAS*, 457(4):4340–4359, April 2016. doi: 10.1093/mnras/stw248.

Alexander Knebe, Doris Stoppacher, Francisco Prada, Christoph Behrens, Andrew Benson, Sofia A. Cora, Darren J. Croton, Nelson D. Padilla, Andrés N. Ruiz, Manodeep Sinha, Adam R. H. Stevens, Cristian A. Vega-Martınez, Peter Behroozi, Violeta Gonzalez-Perez, Stefan Gottlöber, Anatoly A. Klypin, Gustavo Yepes, Harry Enke, Noam I. Libeskind, Kristin Riebe, and Matthias Steinmetz. Multidark-galaxies: data release and first results. *MNRAS*, 474(4):5206–5231, March 2018. doi: 10.1093/mnras/stx2662.

Youkyung Ko, Ho Seong Hwang, Myung Gyoon Lee, Hong Soo Park, Sungsoon Lim, Jubee Sohn, In Sung Jang, Narae Hwang, and Byeong-Gon Park. To the edge of m87 and beyond: Spectroscopy of intracluster globular clusters and ultracompact dwarfs in the virgo cluster. *ApJ*, 835(2):212, February 2017. doi: 10.3847/1538-4357/835/2/212.

Sergey E. Koposov, Vasily Belokurov, Gabriel Torrealba, and N. Wyn Evans. Beasts of the southern wild: Discovery of nine ultra faint satellites in the vicinity of the magellanic clouds. *ApJ*, 805(2):130, June 2015. doi: 10.1088/0004-637X/805/2/130.

Andrey Kravtsov and Viraj Manwadkar. Grumpy: a simple framework for realistic forward modelling of dwarf galaxies. *MNRAS*, 514(2):2667–2691, August 2022. doi: 10.1093/mnras/stac1439.

Andrey V. Kravtsov, Oleg Y. Gnedin, and Anatoly A. Klypin. The tumultuous lives of galactic dwarfs and the missing satellites problem. *The Astrophysical Journal*, 609:482–497, 7 2004. ISSN 0004-637X. doi: 10.1086/421322.

J. E. Krick and R. A. Bernstein. Diffuse optical light in galaxy clusters. ii. correlations with cluster properties. *AJ*, 134(2):466–493, August 2007. doi: 10.1086/518787.

T. Kronberger, W. Kapferer, S. Unterguggenberger, S. Schindler, and B. L. Ziegler. The effects of ram-pressure stripping on the internal kinematics of simulated spiral galaxies. *åp*, 483(3):783–791, June 2008. doi: 10.1051/0004-6361:200809387.

Pavel Kroupa. On the variation of the initial mass function. *MNRAS*, 322(2):231–246, April 2001. doi: 10.1046/j.1365-8711.2001.04022.x.

Cedric Lacey and Shaun Cole. Merger rates in hierarchical models of galaxy formation. *MNRAS*, 262(3):627–649, June 1993. doi: 10.1093/mnras/262.3.627.

Claudia del P. Lagos, Rodrigo J. Tobar, Aaron S. G. Robotham, Danail Obreschkow, Peter D. Mitchell, Chris Power, and Pascal J. Elahi. Shark: introducing an open source, free, and flexible semi-analytic model of galaxy formation. *MNRAS*, 481(3):3573–3603, December 2018. doi: 10.1093/mnras/sty2440.

Andris Lauberts and Edwin A. Valentijn. *The surface photometry catalogue of the ESO-Uppsala galaxies*. 1989.

Jaehyun Lee, Taysun Kimm, Harley Katz, Joakim Rosdahl, Julien Devriendt, and Adrianne Slyz. Dual effects of ram pressure on star formation in multiphase disk galaxies with strong stellar feedback. *ApJ*, 905(1):31, December 2020. doi: 10.3847/1538-4357/abc3b8.

Myung Gyoon Lee, Hong Soo Park, and Ho Seong Hwang. Detection of a large-scale structure of intracluster globular clusters in the virgo cluster. *Science*, 328(5976):334–336, apr 2010. ISSN 0036-8075. doi: 10.1126/science.1186496. URL https://www.science.org/doi/10.1126/science.1186496.

Yang-Shyang Li, Gabriella De Lucia, and Amina Helmi. On the nature of the milky way satellites. *Monthly Notices of the Royal Astronomical Society*, 401:2036–2052, 1 2010. ISSN 00358711. doi: 10.1111/j.1365-2966.2009.15803.x.

E. L. Lokas and G. A. Mamon. Properties of spherical galaxies and clusters with an nfw density profile. *Monthly Notices of the Royal Astronomical Society*, 321(1):155–166, feb 2001. ISSN 0035-8711. doi: 10.1046/j.1365-8711.2001.04007.x. URL https://academic.oup.com/mnras/article-lookup/doi/10.1046/j.1365-8711.2001.04007.x.

Alessia Longobardi, Eric W. Peng, Patrick Côté, J. Christopher Mihos, Laura Ferrarese, Thomas H. Puzia, Ariane Lançon, Hong-Xin Zhang, Roberto P. Muñoz, John P. Blakeslee, Puragra Guhathakurta, Patrick R. Durrell, Rúben Sánchez-Janssen, Elisa Toloba, Andrés Jordán, Susana Eyheramendy, Jean-Charles Cuillandre, Stephen D. J. Gwyn, Alessandro Boselli, Pierre-Alain Duc, Chengze Liu, Karla Alamo-Martınez, Mathieu Powalka, and Sungsoon Lim. The next generation virgo cluster survey (ngvs). xxxi. the kinematics of intracluster globular clusters in the core of the virgo cluster. *ApJ*, 864(1):36, September 2018. doi: 10.3847/1538-4357/aad3d2.

Yu Lu, Andrew Benson, Andrew Wetzel, Yao-Yuan Mao, Stephanie Tonnesen, Annika H. G. Peter, Michael Boylan-Kolchin, and Risa H. Wechsler. The importance of preventive feedback: Inference from observations of the stellar masses and metallicities of milky way dwarf galaxies. *The Astrophysical Journal*, 846(1):66, aug 2017. doi: 10.3847/1538-4357/aa845e. URL https://doi.org/10.3847%2F1538-4357%2Faa845e.

Andrea V. Macciò, Xi Kang, Fabio Fontanot, Rachel S. Somerville, Sergey Koposov, and Pierluigi Monaco. Luminosity function and radial distribution of milky way satellites in a ΛCDM universe. *MNRAS*, 402(3):1995–2008, March 2010. doi: 10.1111/j.1365-2966.2009.16031.x.

Andrea V. Macciò, Jonas Frings, Tobias Buck, Camilla Penzo, Aaron A. Dutton, Marvin Blank, and Aura Obreja. The edge of galaxy formation - i. formation and evolution of mw-satellite analogues before accretion. *MNRAS*, 472(2):2356–2366, December 2017. doi: 10.1093/mnras/stx2048.

Andrea V. Macciò, Jonas Frings, Tobias Buck, Aaron A. Dutton, Marvin Blank, Aura Obreja, and Keri L. Dixon. The edge of galaxy formation iii: the effects of warm dark

matter on milky way satellites and field dwarfs. *MNRAS*, 484(4):5400–5408, April 2019. doi: 10.1093/mnras/stz327.

Piero Madau and Mark Dickinson. Cosmic star-formation history. *Annual Review of Astronomy and Astrophysics*, 52:415–486, 8 2014. ISSN 0066-4146. doi: 10.1146/annurev-astro-081811-125615.

Piero Madau, Sijing Shen, and Fabio Governato. Dark matter heating and early core formation in dwarf galaxies. *ApJL*, 789(1):L17, July 2014. doi: 10.1088/2041-8205/789/1/L17.

Juan P. Madrid, Conor R. O'Neill, Alexander T. Gagliano, and Joshua R. Marvil. A wide-field map of intracluster globular clusters in coma. *ApJ*, 867(2):144, November 2018. doi: 10.3847/1538-4357/aae206.

Ariyeh H. Maller and James S. Bullock. Multiphase galaxy formation: high-velocity clouds and the missing baryon problem. *MNRAS*, 355(3):694–712, December 2004. doi: 10.1111/j.1365-2966.2004.08349.x.

Viraj Manwadkar and Andrey V Kravtsov. Forward-modelling the luminosity, distance, and size distributions of the milky way satellites. *Monthly Notices of the Royal Astronomical Society*, 516:3944–3971, 9 2022. ISSN 0035-8711. doi: 10.1093/mnras/stac2452.

Yao-Yuan Mao, Marla Geha, Risa H. Wechsler, Benjamin Weiner, Erik J. Tollerud, Ethan O. Nadler, and Nitya Kallivayalil. The saga survey. ii. building a statistical sample of satellite systems around milky way-like galaxies. *ApJ*, 907(2):85, February 2021. doi: 10.3847/1538-4357/abce58.

Federico Marinacci, Mark Vogelsberger, Rüdiger Pakmor, Paul Torrey, Volker Springel, Lars Hernquist, Dylan Nelson, Rainer Weinberger, Annalisa Pillepich, Jill Naiman, and Shy Genel. First results from the illustristng simulations: radio haloes and magnetic fields. *MNRAS*, 480(4):5113–5139, November 2018. doi: 10.1093/mnras/sty2206.

S. Mau, W. Cerny, A. B. Pace, Y. Choi, A. Drlica-Wagner, L. Santana-Silva, A. H. Riley, D. Erkal, G. S. Stringfellow, M. Adamów, J. L. Carlin, R. A. Gruendl, D. Hernandez-Lang, N. Kuropatkin, T. S. Li, C. E. Martınez-Vázquez, E. Morganson, B. Mutlu-Pakdil, E. H. Neilsen, D. L. Nidever, K. A. G. Olsen, D. J. Sand, E. J. Tollerud, D. L. Tucker, B. Yanny, A. Zenteno, S. Allam, W. A. Barkhouse, K. Bechtol, E. F. Bell, P. Balaji, D. Crnojevi J. Esteves, P. S. Ferguson, C. Gallart, A. K. Hughes, D. J. James, P. Jethwa, L. C. Johnson, K. Kuehn, S. Majewski, Y. Y. Mao, P. Massana, M. McNanna, A. Monachesi, E. O. Nadler, N. E. D. Noël, A. Palmese, F. Paz-Chinchon, A. Pieres, J. Sanchez, N. Shipp, J. D. Simon, M. Soares-Santos, K. Tavangar, R. P. van der Marel, A. K. Vivas, A. R. Walker, and R. H. Wechsler. Two ultra-faint milky way stellar systems discovered in early data from the decam local volume exploration survey. *ApJ*, 890(2):136, February 2020. doi: 10.3847/1538-4357/ab6c67.

Alan W. McConnachie. The observed properties of dwarf galaxies in and around the local group. *The Astronomical Journal*, 144:4, 7 2012. ISSN 0004-6256. doi: 10.1088/0004-6256/144/1/4.

Michael McCourt, Prateek Sharma, Eliot Quataert, and Ian J. Parrish. Thermal instability in gravitationally stratified plasmas: implications for multiphase structure in clusters and galaxy haloes. *MNRAS*, 419(4):3319–3337, February 2012. doi: 10.1111/j.1365-2966.2011.19972.x.

Sean L. McGee and Michael L. Balogh. Constraints on intragroup stellar mass from hostless type ia supernovae. *Monthly Notices of the Royal Astronomical Society: Letters*, 403(1):L79–L83, mar 2010. ISSN 17453925. doi: 10.1111/j.1745-3933.2010.00819.x. URL https://academic.oup.com/mnrasl/article-lookup/doi/10.1111/j.1745-3933.2010.00819.x.

J. Melnick, E. Giraud, I. Toledo, F. Selman, and H. Quintana. Intergalactic stellar populations in intermediate redshift clusters. *MNRAS*, 427(1):850–858, November 2012. doi: 10.1111/j.1365-2966.2012.21924.x.

Allison Merritt, Pieter van Dokkum, Roberto Abraham, and Jielai Zhang. The dragonfly nearby galaxies survey. i. substantial variation in the diffuse stellar halos around spiral galaxies. *ApJ*, 830(2):62, October 2016. doi: 10.3847/0004-637X/830/2/62.

J. Christopher Mihos, Paul Harding, John Feldmeier, and Heather Morrison. Diffuse light in the virgo cluster. *ApJL*, 631(1):L41–L44, September 2005. doi: 10.1086/497030.

J. Christopher Mihos, Paul Harding, John J. Feldmeier, Craig Rudick, Steven Janowiecki, Heather Morrison, Colin Slater, and Aaron Watkins. The burrell schmidt deep virgo survey: Tidal debris, galaxy halos, and diffuse intracluster light in the virgo cluster. *ApJ*, 834(1):16, January 2017. doi: 10.3847/1538-4357/834/1/16.

Peter D. Mitchell, Joop Schaye, Richard G. Bower, and Robert A. Crain. Galactic outflow rates in the eagle simulations. *MNRAS*, 494(3):3971–3997, May 2020. doi: 10.1093/mnras/staa938.

Antonela Monachesi, Facundo A Gómez, Robert J J Grand, Christine M Simpson, Guinevere Kauffmann, Sebastián Bustamante, Federico Marinacci, Rüdiger Pakmor, Volker Springel, Carlos S Frenk, Simon D M White, and Patricia B Tissera. The auriga stellar haloes: connecting stellar population properties with accretion and merging history. *Monthly Notices of the Royal Astronomical Society*, 485:2589–2616, 5 2019. ISSN 0035-8711. doi: 10.1093/mnras/stz538.

Pierluigi Monaco, Fabio Fontanot, and Giuliano Taffoni. The morgana model for the rise of galaxies and active nuclei. *MNRAS*, 375(4):1189–1219, March 2007. doi: 10.1111/j.1365-2966.2006.11253.x.

Daniel Montenegro-Taborda, Vicente Rodriguez-Gomez, Annalisa Pillepich, Vladimir Avila-Reese, Laura V. Sales, Aldo Rodrıguez-Puebla, and Lars Hernquist. The growth of brightest cluster galaxies in the tng300 simulation: dissecting the contributions from mergers and in situ star formation. *MNRAS*, 521(1):800–817, May 2023. doi: 10.1093/mnras/stad586.

Mireia Montes. The faint light in groups and clusters of galaxies. *Nature Astronomy*, 6: 308–316, March 2022. doi: 10.1038/s41550-022-01616-z.

Mireia Montes and Ignacio Trujillo. Intracluster light at the frontier: A2744. *The Astrophysical Journal*, 794(2):137, oct 2014. ISSN 1538-4357. doi: 10.1088/0004-637X/794/2/137. URL https://iopscience.iop.org/article/10.1088/0004-637X/794/2/137.

Mireia Montes and Ignacio Trujillo. Intracluster light at the frontier - ii. the frontier fields clusters. *MNRAS*, 474(1):917–932, February 2018. doi: 10.1093/mnras/stx2847.

Mireia Montes and Ignacio Trujillo. Intracluster light: a luminous tracer for dark matter in clusters of galaxies. *MNRAS*, 482(2):2838–2851, January 2019. doi: 10.1093/mnras/sty2858.

Mireia Montes and Ignacio Trujillo. A new era of intracluster light studies with jwst. *ApJL*, 940(2):L51, December 2022. doi: 10.3847/2041-8213/ac98c5.

Mireia Montes, Sarah Brough, Matt S. Owers, and Giulia Santucci. The buildup of the intracluster light of a85 as seen by subaru's hyper suprime-cam. *ApJ*, 910(1):45, March 2021. doi: 10.3847/1538-4357/abddb6.

Ben Moore. Evidence against dissipation-less dark matter from observations of galaxy haloes. *Nature*, 370(6491):629–631, August 1994. doi: 10.1038/370629a0.

Takahiro Morishita, Louis E. Abramson, Tommaso Treu, Kasper B. Schmidt, Benedetta Vulcani, and Xin Wang. Characterizing intracluster light in the hubble frontier fields. *The Astrophysical Journal*, 846(2):139, sep 2017. ISSN 1538-4357. doi: 10.3847/1538-4357/aa8403. URL https://iopscience.iop.org/article/10.3847/1538-4357/aa8403.

Ferah Munshi, Alyson M. Brooks, Elaad Applebaum, Charlotte R. Christensen, T. Quinn, and Serena Sligh. Quantifying scatter in galaxy formation at the lowest masses. *ApJ*, 923(1):35, December 2021. doi: 10.3847/1538-4357/ac0db6.

G. Murante, M. Giovalli, O. Gerhard, M. Arnaboldi, S. Borgani, and K. Dolag. The importance of mergers for the origin of intracluster stars in cosmological simulations of galaxy clusters. *Monthly Notices of the Royal Astronomical Society*, 377(1):2–16, may 2007. ISSN 0035-8711. doi: 10.1111/j.1365-2966.2007.11568.x. URL https://academic.oup.com/mnras/article-lookup/doi/10.1111/j.1365-2966.2007.11568.x.

Alexander L. Muratov, Dušan Kereš, Claude-André Faucher-Giguère, Philip F. Hopkins, Xiangcheng Ma, Daniel Anglés-Alcázar, T. K. Chan, Paul Torrey, Zachary H. Hafen, Eliot Quataert, and Norman Murray. Metal flows of the circumgalactic medium, and the metal budget in galactic haloes. *MNRAS*, 468(4):4170–4188, July 2017. doi: 10.1093/mnras/stx667.

E. J. Murphy, J. J. Condon, E. Schinnerer, R. C. Kennicutt, D. Calzetti, L. Armus, G. Helou, J. L. Turner, G. Aniano, P. Beirão, A. D. Bolatto, B. R. Brandl, K. V. Croxall, D. A. Dale, J. L. Donovan Meyer, B. T. Draine, C. Engelbracht, L. K. Hunt, C.-N. Hao, J. Koda,

H. Roussel, R. Skibba, and J.-D. T. Smith. Calibrating extinction-free star formation rate diagnostics with 33 ghz free-free emission in ngc 6946. *The Astrophysical Journal*, 737(2):67, Aug 2011. ISSN 1538-4357. doi: 10.1088/0004-637x/737/2/67. URL http://dx.doi.org/10.1088/0004-637X/737/2/67.

Joseph A. Muñoz, Piero Madau, Abraham Loeb, and Jürg Diemand. Probing the epoch of reionization with milky way satellites. *Monthly Notices of the Royal Astronomical Society*, 400:1593–1602, 12 2009. ISSN 00358711. doi: 10.1111/j.1365-2966.2009.15562.x.

Juan Carlos Muñoz-Mateos, Kartik Sheth, Michael Regan, Taehyun Kim, Jarkko Laine, Santiago Erroz Ferrer, Armando Gil de Paz, Sebastien Comeron, Joannah Hinz, Eija Laurikainen, Heikki Salo, E. Athanassoula, Albert Bosma, Alexandre Y. K. Bouquin, Eva Schinnerer, Luis Ho, Dennis Zaritsky, Dimitri A. Gadotti, Barry Madore, Benne Holwerda, Karín Menéndez-Delmestre, Johan H. Knapen, Sharon Meidt, Miguel Querejeta, Trisha Mizusawa, Mark Seibert, Seppo Laine, and Helene Courtois. The spitzer survey of stellar structure in galaxies (s 4 g): Stellar masses, sizes, and radial profiles for 2352 nearby galaxies. *The Astrophysical Journal Supplement Series*, 219(1):3, jul 2015. ISSN 1538-4365. doi: 10.1088/0067-0049/219/1/3. URL https://iopscience.iop.org/article/10.1088/0067-0049/219/1/3.

Oliver Müller, Helmut Jerjen, and Bruno Binggeli. New dwarf galaxy candidates in the centaurus group. *åp*, 583:A79, November 2015. doi: 10.1051/0004-6361/201526748.

Oliver Müller, Helmut Jerjen, and Bruno Binggeli. New low surface brightness dwarf galaxies in the centaurus group. *åp*, 597:A7, January 2017. doi: 10.1051/0004-6361/201628921.

Oliver Müller, Marina Rejkuba, Marcel S. Pawlowski, Rodrigo Ibata, Federico Lelli, Michael Hilker, and Helmut Jerjen. The dwarf galaxy satellite system of centaurus a. *åp*, 629: A18, September 2019. doi: 10.1051/0004-6361/201935807.

E. O. Nadler, R. H. Wechsler, K. Bechtol, Y.-Y. Mao, G. Green, A. Drlica-Wagner, M. McNanna, S. Mau, A. B. Pace, J. D. Simon, A. Kravtsov, S. Dodelson, T. S. Li, A. H. Riley, M. Y. Wang, T. M. C. Abbott, M. Aguena, S. Allam, J. Annis, S. Avila, G. M. Bernstein, E. Bertin, D. Brooks, D. L. Burke, A. Carnero Rosell, M. Carrasco Kind, J. Carretero, M. Costanzi, L. N. da Costa, J. De Vicente, S. Desai, A. E. Evrard, B. Flaugher, P. Fosalba, J. Frieman, J. García-Bellido, E. Gaztanaga, D. W. Gerdes, D. Gruen, J. Gschwend, G. Gutierrez, W. G. Hartley, S. R. Hinton, K. Honscheid, E. Krause, K. Kuehn, N. Kuropatkin, O. Lahav, M. A. G. Maia, J. L. Marshall, F. Menanteau, R. Miquel, A. Palmese, F. Paz-Chinchón, A. A. Plazas, A. K. Romer, E. Sanchez, B. Santiago, V. Scarpine, S. Serrano, M. Smith, M. Soares-Santos, E. Suchyta, G. Tarle, D. Thomas, T. N. Varga, and A. R. Walker. Milky way satellite census. ii. galaxy–halo connection constraints including the impact of the large magellanic cloud. *The Astrophysical Journal*, 893:48, 4 2020. ISSN 1538-4357. doi: 10.3847/1538-4357/ab846a.

E. O. Nadler, A. Drlica-Wagner, K. Bechtol, S. Mau, R. H. Wechsler, V. Gluscevic, K. Boddy, A. B. Pace, T. S. Li, M. McNanna, A. H. Riley, J. Garcıa-Bellido, Y. Y. Mao,

G. Green, D. L. Burke, A. Peter, B. Jain, T. M. C. Abbott, M. Aguena, S. Allam, J. Annis, S. Avila, D. Brooks, M. Carrasco Kind, J. Carretero, M. Costanzi, L. N. da Costa, J. De Vicente, S. Desai, H. T. Diehl, P. Doel, S. Everett, A. E. Evrard, B. Flaugher, J. Frieman, D. W. Gerdes, D. Gruen, R. A. Gruendl, J. Gschwend, G. Gutierrez, S. R. Hinton, K. Honscheid, D. Huterer, D. J. James, E. Krause, K. Kuehn, N. Kuropatkin, O. Lahav, M. A. G. Maia, J. L. Marshall, F. Menanteau, R. Miquel, A. Palmese, F. Paz-Chinchón, A. A. Plazas, A. K. Romer, E. Sanchez, V. Scarpine, S. Serrano, I. Sevilla-Noarbe, M. Smith, M. Soares-Santos, E. Suchyta, M. E. C. Swanson, G. Tarle, D. L. Tucker, A. R. Walker, W. Wester, and DES Collaboration. Constraints on dark matter properties from observations of milky way satellite galaxies. , 126(9):091101, March 2021. doi: 10.1103/PhysRevLett.126.091101.

Ethan O. Nadler, Yao-Yuan Mao, Risa H. Wechsler, Shea Garrison-Kimmel, and Andrew Wetzel. Modeling the impact of baryons on subhalo populations with machine learning. *ApJ*, 859(2):129, June 2018. doi: 10.3847/1538-4357/aac266.

Ethan O. Nadler, Yao-Yuan Mao, Gregory M. Green, and Risa H. Wechsler. Modeling the connection between subhalos and satellites in milky way-like systems. *ApJ*, 873(1):34, March 2019. doi: 10.3847/1538-4357/ab040e.

Ethan O. Nadler, Andrew Benson, Trey Driskell, Xiaolong Du, and Vera Gluscevic. Growing the first galaxies' merger trees. *MNRAS*, 521(3):3201–3220, May 2023a. doi: 10.1093/mnras/stad666.

Ethan O. Nadler, Philip Mansfield, Yunchong Wang, Xiaolong Du, Susmita Adhikari, Arka Banerjee, Andrew Benson, Elise Darragh-Ford, Yao-Yuan Mao, Sebastian Wagner-Carena, Risa H. Wechsler, and Hao-Yi Wu. Symphony: Cosmological zoom-in simulation suites over four decades of host halo mass. *ApJ*, 945(2):159, March 2023b. doi: 10.3847/1538-4357/acb68c.

Jill P. Naiman, Annalisa Pillepich, Volker Springel, Enrico Ramirez-Ruiz, Paul Torrey, Mark Vogelsberger, Rüdiger Pakmor, Dylan Nelson, Federico Marinacci, Lars Hernquist, Rainer Weinberger, and Shy Genel. First results from the illustristng simulations: a tale of two elements - chemical evolution of magnesium and europium. *MNRAS*, 477(1):1206–1224, June 2018. doi: 10.1093/mnras/sty618.

S. Naoz and R. Barkana. The formation and gas content of high-redshift galaxies and minihaloes. *MNRAS*, 377(2):667–676, May 2007. doi: 10.1111/j.1365-2966.2007.11636.x.

Masashi Nashimoto, Masayuki Tanaka, Masashi Chiba, Kohei Hayashi, Yutaka Komiyama, and Takashi Okamoto. The missing satellite problem outside of the local group. ii. statistical properties of satellites of milky way-like galaxies. *ApJ*, 936(1):38, September 2022. doi: 10.3847/1538-4357/ac83a4.

Julio F. Navarro, Carlos S. Frenk, and Simon D. M. White. The structure of cold dark matter halos. *ApJ*, 462:563, May 1996. doi: 10.1086/177173.

D. Nelson, A. Pillepich, S. Genel, M. Vogelsberger, V. Springel, P. Torrey, V. Rodriguez-Gomez, D. Sijacki, G. F. Snyder, B. Griffen, F. Marinacci, L. Blecha, L. Sales, D. Xu, and L. Hernquist. The illustris simulation: Public data release. *Astronomy and Computing*, 13:12–37, November 2015. doi: 10.1016/j.ascom.2015.09.003.

Dylan Nelson, Annalisa Pillepich, Volker Springel, Rainer Weinberger, Lars Hernquist, Rüdiger Pakmor, Shy Genel, Paul Torrey, Mark Vogelsberger, Guinevere Kauffmann, Federico Marinacci, and Jill Naiman. First results from the illustristng simulations: the galaxy colour bimodality. *Monthly Notices of the Royal Astronomical Society*, 475:624–647, 3 2018. ISSN 0035-8711. doi: 10.1093/mnras/stx3040.

Dylan Nelson, Annalisa Pillepich, Volker Springel, Rüdiger Pakmor, Rainer Weinberger, Shy Genel, Paul Torrey, Mark Vogelsberger, Federico Marinacci, and Lars Hernquist. First results from the tng50 simulation: galactic outflows driven by supernovae and black hole feedback. *MNRAS*, 490(3):3234–3261, December 2019a. doi: 10.1093/mnras/stz2306.

Dylan Nelson, Volker Springel, Annalisa Pillepich, Vicente Rodriguez-Gomez, Paul Torrey, Shy Genel, Mark Vogelsberger, Ruediger Pakmor, Federico Marinacci, Rainer Weinberger, Luke Kelley, Mark Lovell, Benedikt Diemer, and Lars Hernquist. The illustristng simulations: public data release. *Computational Astrophysics and Cosmology*, 6(1):2, May 2019b. doi: 10.1186/s40668-019-0028-x.

Dylan Nelson, Prateek Sharma, Annalisa Pillepich, Volker Springel, Rüdiger Pakmor, Rainer Weinberger, Mark Vogelsberger, Federico Marinacci, and Lars Hernquist. Resolving small-scale cold circumgalactic gas in tng50. *MNRAS*, 498(2):2391–2414, October 2020. doi: 10.1093/mnras/staa2419.

Oliver Newton, Matteo Leo, Marius Cautun, Adrian Jenkins, Carlos S. Frenk, Mark R. Lovell, John C. Helly, Andrew J. Benson, and Shaun Cole. Constraints on the properties of warm dark matter using the satellite galaxies of the milky way. , 2021(8):062, August 2021. doi: 10.1088/1475-7516/2021/08/062.

Pierre Ocvirk, Joseph S. W. Lewis, Nicolas Gillet, Jonathan Chardin, Dominique Aubert, Nicolas Deparis, and Émilie Thélie. Lyman-alpha opacities at z = 4-6 require low mass, radiatively-suppressed galaxies to drive cosmic reionization. *MNRAS*, 507(4):6108–6117, November 2021. doi: 10.1093/mnras/stab2502.

Benjamin D. Oppenheimer, Joop Schaye, Robert A. Crain, Jessica K. Werk, and Alexander J. Richings. The multiphase circumgalactic medium traced by low metal ions in eagle zoom simulations. *MNRAS*, 481(1):835–859, November 2018. doi: 10.1093/mnras/sty2281.

Benjamin D. Oppenheimer, Arif Babul, Yannick Bahé, Iryna S. Butsky, and Ian G. McCarthy. Simulating groups and the intragroup medium: The surprisingly complex and rich middle ground between clusters and galaxies. *Universe*, 7(7):209, June 2021. doi: 10.3390/universe7070209.

Viraj Pandya, Drummond B. Fielding, Daniel Anglés-Alcázar, Rachel S. Somerville, Greg L. Bryan, Christopher C. Hayward, Jonathan Stern, Chang-Goo Kim, Eliot Quataert, John C. Forbes, Claude-André Faucher-Giguère, Robert Feldmann, Zachary Hafen, Philip F. Hopkins, Dušan Kereš, Norman Murray, and Andrew Wetzel. Characterizing mass, momentum, energy, and metal outflow rates of multiphase galactic winds in the fire-2 cosmological simulations. *MNRAS*, 508(2):2979–3008, December 2021. doi: 10.1093/mnras/stab2714.

Hannah Parkinson, Shaun Cole, and John Helly. Generating dark matter halo merger trees. *Monthly Notices of the Royal Astronomical Society*, 383(2):557–564, 12 2007. ISSN 0035-8711. doi: 10.1111/j.1365-2966.2007.12517.x. URL https://doi.org/10.1111/j.1365-2966.2007.12517.x.

P. J. E. Peebles. *The large-scale structure of the universe*. 1980.

J. Penarrubia and A. J. Benson. Effects of dynamical evolution on the distribution of substructures. *Monthly Notices of the Royal Astronomical Society*, 364:977–989, 12 2005. ISSN 0035-8711. doi: 10.1111/j.1365-2966.2005.09633.x.

Ying-jie Peng, Simon J. Lilly, Katarina Kovač, Micol Bolzonella, Lucia Pozzetti, Alvio Renzini, Gianni Zamorani, Olivier Ilbert, Christian Knobel, Angela Iovino, Christian Maier, Olga Cucciati, Lidia Tasca, C. Marcella Carollo, John Silverman, Pawel Kampczyk, Loic de Ravel, David Sanders, Nicholas Scoville, Thierry Contini, Vincenzo Mainieri, Marco Scodeggio, Jean-Paul Kneib, Olivier Le Fèvre, Sandro Bardelli, Angela Bongiorno, Karina Caputi, Graziano Coppa, Sylvain de la Torre, Paolo Franzetti, Bianca Garilli, Fabrice Lamareille, Jean-Francois Le Borgne, Vincent Le Brun, Marco Mignoli, Enrique Perez Montero, Roser Pello, Elena Ricciardelli, Masayuki Tanaka, Laurence Tresse, Daniela Vergani, Niraj Welikala, Elena Zucca, Pascal Oesch, Ummi Abbas, Luke Barnes, Rongmon Bordoloi, Dario Bottini, Alberto Cappi, Paolo Cassata, Andrea Cimatti, Marco Fumana, Gunther Hasinger, Anton Koekemoer, Alexei Leauthaud, Dario Maccagni, Christian Marinoni, Henry McCracken, Pierdomenico Memeo, Baptiste Meneux, Preethi Nair, Cristiano Porciani, Valentina Presotto, and Roberto Scaramella. Mass and environment as drivers of galaxy evolution in sdss and zcosmos and the origin of the schechter function. *ApJ*, 721(1):193–221, September 2010. doi: 10.1088/0004-637X/721/1/193.

Annalisa Pillepich, Mark Vogelsberger, Alis Deason, Vicente Rodriguez-Gomez, Shy Genel, Dylan Nelson, Paul Torrey, Laura V. Sales, Federico Marinacci, Volker Springel, Debora Sijacki, and Lars Hernquist. Halo mass and assembly history exposed in the faint outskirts: the stellar and dark matter haloes of illustris galaxies. *MNRAS*, 444(1):237–249, October 2014. doi: 10.1093/mnras/stu1408.

Annalisa Pillepich, Piero Madau, and Lucio Mayer. Building late-type spiral galaxies by in-situ and ex-situ star formation. *ApJ*, 799(2):184, February 2015. doi: 10.1088/0004-637X/799/2/184.

Annalisa Pillepich, Dylan Nelson, Lars Hernquist, Volker Springel, Rüdiger Pakmor, Paul Torrey, Rainer Weinberger, Shy Genel, Jill P. Naiman, Federico Marinacci, and Mark

Vogelsberger. First results from the illustristng simulations: the stellar mass content of groups and clusters of galaxies. *MNRAS*, 475(1):648–675, March 2018a. doi: 10.1093/mnras/stx3112.

Annalisa Pillepich, Volker Springel, Dylan Nelson, Shy Genel, Jill Naiman, Rüdiger Pakmor, Lars Hernquist, Paul Torrey, Mark Vogelsberger, Rainer Weinberger, and Federico Marinacci. Simulating galaxy formation with the illustristng model. *MNRAS*, 473(3): 4077–4106, January 2018b. doi: 10.1093/mnras/stx2656.

Annalisa Pillepich, Dylan Nelson, Volker Springel, Rüdiger Pakmor, Paul Torrey, Rainer Weinberger, Mark Vogelsberger, Federico Marinacci, Shy Genel, Arjen van der Wel, and Lars Hernquist. First results from the tng50 simulation: the evolution of stellar and gaseous discs across cosmic time. *MNRAS*, 490(3):3196–3233, December 2019. doi: 10.1093/mnras/stz2338.

Planck Collaboration, N. Aghanim, Y. Akrami, M. Ashdown, J. Aumont, C. Baccigalupi, M. Ballardini, A. J. Banday, R. B. Barreiro, N. Bartolo, S. Basak, R. Battye, K. Benabed, J. P. Bernard, M. Bersanelli, P. Bielewicz, J. J. Bock, J. R. Bond, J. Borrill, F. R. Bouchet, F. Boulanger, M. Bucher, C. Burigana, R. C. Butler, E. Calabrese, J. F. Cardoso, J. Carron, A. Challinor, H. C. Chiang, J. Chluba, L. P. L. Colombo, C. Combet, D. Contreras, B. P. Crill, F. Cuttaia, P. de Bernardis, G. de Zotti, J. Delabrouille, J. M. Delouis, E. Di Valentino, J. M. Diego, O. Doré, M. Douspis, A. Ducout, X. Dupac, S. Dusini, G. Efstathiou, F. Elsner, T. A. Enßlin, H. K. Eriksen, Y. Fantaye, M. Farhang, J. Fergusson, R. Fernandez-Cobos, F. Finelli, F. Forastieri, M. Frailis, A. A. Fraisse, E. Franceschi, A. Frolov, S. Galeotta, S. Galli, K. Ganga, R. T. Génova-Santos, M. Gerbino, T. Ghosh, J. González-Nuevo, K. M. Górski, S. Gratton, A. Gruppuso, J. E. Gudmundsson, J. Hamann, W. Handley, F. K. Hansen, D. Herranz, S. R. Hildebrandt, E. Hivon, Z. Huang, A. H. Jaffe, W. C. Jones, A. Karakci, E. Keihänen, R. Keskitalo, K. Kiiveri, J. Kim, T. S. Kisner, L. Knox, N. Krachmalnicoff, M. Kunz, H. Kurki-Suonio, G. Lagache, J. M. Lamarre, A. Lasenby, M. Lattanzi, C. R. Lawrence, M. Le Jeune, P. Lemos, J. Lesgourgues, F. Levrier, A. Lewis, M. Liguori, P. B. Lilje, M. Lilley, V. Lindholm, M. López-Caniego, P. M. Lubin, Y. Z. Ma, J. F. Macıas-Pérez, G. Maggio, D. Maino, N. Mandolesi, A. Mangilli, A. Marcos-Caballero, M. Maris, P. G. Martin, M. Martinelli, E. Martez-González, S. Matarrese, N. Mauri, J. D. McEwen, P. R. Meinhold, A. Melchiorri, A. Mennella, M. Migliaccio, M. Millea, S. Mitra, M. A. Miville-Deschênes, D. Molinari, L. Montier, G. Morgante, A. Moss, P. Natoli, H. U. Nørgaard-Nielsen, L. Pagano, D. Paoletti, B. Partridge, G. Patanchon, H. V. Peiris, F. Perrotta, V. Pettorino, F. Piacentini, L. Polastri, G. Polenta, J. L. Puget, J. P. Rachen, M. Reinecke, M. Remazeilles, A. Renzi, G. Rocha, C. Rosset, G. Roudier, J. A. Rubiño-Mart; B. Ruiz-Granados, L. Salvati, M. Sandri, M. Savelainen, D. Scott, E. P. S. Shellard, C. Sirignano, G. Sirri, L. D. Spencer, R. Sunyaev, A. S. Suur-Uski, J. A. Tauber, D. Tavagnacco, M. Tenti, L. Toffolatti, M. Tomasi, T. Trombetti, L. Valenziano, J. Valiviita, B. Van Tent, L. Vibert, P. Vielva, F. Villa, N. Vittorio, B. D. Wandelt, I. K. Wehus, M. White, S. D. M. White, A. Zacchei, and A. Zonca. Planck 2018 results. vi. cosmological parameters. *åp*, 641:A6, September 2020. doi: 10.1051/0004-6361/201833910.

Denis Poliakov, Aleksandr V. Mosenkov, Noah Brosch, Shuki Koriski, and R. Michael Rich. Quantified diffuse light in compact groups of galaxies. *MNRAS*, 503(4):6059–6077, June 2021. doi: 10.1093/mnras/stab853.

Mateo Prgomet, Martin P. Rey, Eric P. Andersson, Alvaro Segovia Otero, Oscar Agertz, Florent Renaud, Andrew Pontzen, and Justin I. Read. Edge: The sensitivity of ultra-faint dwarfs to a metallicity-dependent initial mass function. *MNRAS*, 513(2):2326–2334, June 2022. doi: 10.1093/mnras/stac1074.

Ewald Puchwein and Volker Springel. Shaping the galaxy stellar mass function with supernova- and agn-driven winds. *MNRAS*, 428(4):2966–2979, February 2013. doi: 10.1093/mnras/sts243.

Ewald Puchwein, Volker Springel, Debora Sijacki, and Klaus Dolag. Intracluster stars in simulations with active galactic nucleus feedback. *Monthly Notices of the Royal Astronomical Society*, 447(1):no–no, may 2010. ISSN 00358711. doi: 10.1111/j.1365-2966.2010.16786.x. URL https://academic.oup.com/mnras/article-lookup/doi/10.1111/j.1365-2966.2010.16786.x.

Anthony R. Pullen, Andrew J. Benson, and Leonidas A. Moustakas. Nonlinear evolution of dark matter subhalos and applications to warm dark matter. *The Astrophysical Journal*, 792:24, 8 2014. ISSN 1538-4357. doi: 10.1088/0004-637X/792/1/24.

Chris W. Purcell, James S. Bullock, and Andrew R. Zentner. Shredded galaxies as the source of diffuse intrahalo light on varying scales. *ApJ*, 666(1):20–33, September 2007. doi: 10.1086/519787.

Marc Rafelski, Marcel Neeleman, Michele Fumagalli, Arthur M. Wolfe, and J. Xavier Prochaska. The rapid decline in metallicity of damped Lyα systems at z $\sim$ 5. *ApJL*, 782(2):L29, February 2014. doi: 10.1088/2041-8205/782/2/L29.

R. Ragusa, E. Iodice, M. Spavone, M. Montes, D. A. Forbes, S. Brough, M. Mirabile, M. Cantiello, M. Paolillo, and P. Schipani. Does the virial mass drive the intra-cluster light? Relationship between the ICL and M_{vir} from VEGAS. *åp*, 670:L20, February 2023. doi: 10.1051/0004-6361/202245530.

Rossella Ragusa, Marilena Spavone, Enrichetta Iodice, Sarah Brough, Maria Angela Raj, Maurizio Paolillo, Michele Cantiello, Duncan A. Forbes, Antonio La Marca, Giuseppe D'Ago, Roberto Rampazzo, and Pietro Schipani. VEGAS: A VST Early-type GAlaxy Survey. vi. diffuse light in HCG 86 as seen from the ultra-deep VEGAS images. *åp*, 651: A39, July 2021. doi: 10.1051/0004-6361/202039921.

Felipe Ramos-Almendares, Laura V. Sales, Mario G. Abadi, Jessica E. Doppel, Hernan Muriel, and Eric W. Peng. Simulating the spatial distribution and kinematics of globular clusters within galaxy clusters in illustris. *MNRAS*, 493(4):5357–5368, April 2020. doi: 10.1093/mnras/staa551.

J. I. Read, O. Agertz, and M. L. M. Collins. Dark matter cores all the way down. *MNRAS*, 459(3):2573–2590, July 2016. doi: 10.1093/mnras/stw713.

Marta Reina-Campos, Sebastian Trujillo-Gomez, Joel L Pfeffer, Alison Sills, Alis J Deason, Robert A Crain, and J M Diederik Kruijssen. Constraining the shape of dark matter haloes with globular clusters and diffuse stellar light in the e-mosaics simulations. *Monthly Notices of the Royal Astronomical Society*, 521:6368–6382, 3 2023. ISSN 0035-8711. doi: 10.1093/mnras/stad920.

Yves Revaz and Pascale Jablonka. Pushing back the limits: detailed properties of dwarf galaxies in a ΛCDM universe. *åp*, 616:A96, August 2018. doi: 10.1051/0004-6361/201832669.

Martin P. Rey, Andrew Pontzen, Oscar Agertz, Matthew D. A. Orkney, Justin I. Read, Amélie Saintonge, and Christian Pedersen. Edge: The origin of scatter in ultra-faint dwarf stellar masses and surface brightnesses. *ApJL*, 886(1):L3, November 2019. doi: 10.3847/2041-8213/ab53dd.

Martin P. Rey, Andrew Pontzen, Oscar Agertz, Matthew D. A. Orkney, Justin I. Read, and Joakim Rosdahl. Edge: from quiescent to gas-rich to star-forming low-mass dwarf galaxies. *MNRAS*, 497(2):1508–1520, September 2020. doi: 10.1093/mnras/staa1640.

R. Michael Rich, Aleksandr Mosenkov, Henry Lee-Saunders, Andreas Koch, John Kormendy, Julia Kennefick, Noah Brosch, Laura Sales, James Bullock, Andreas Burkert, Michelle Collins, Michael Cooper, Michael Fusco, David Reitzel, David Thilker, Dave G. Milewski, Lydia Elias, M. L. Saade, and Laura De Groot. The haloes and environments of nearby galaxies (heron) - i. imaging, sample characteristics, and envelope diameters. *MNRAS*, 490(2):1539–1569, December 2019. doi: 10.1093/mnras/stz2106.

Vicente Rodriguez-Gomez, Shy Genel, Mark Vogelsberger, Debora Sijacki, Annalisa Pillepich, Laura V. Sales, Paul Torrey, Greg Snyder, Dylan Nelson, Volker Springel, Chung-Pei Ma, and Lars Hernquist. The merger rate of galaxies in the illustris simulation: a comparison with observations and semi-empirical models. *MNRAS*, 449(1):49–64, May 2015. doi: 10.1093/mnras/stv264.

Vicente Rodriguez-Gomez, Annalisa Pillepich, Laura V. Sales, Shy Genel, Mark Vogelsberger, Qirong Zhu, Sarah Wellons, Dylan Nelson, Paul Torrey, Volker Springel, Chung-Pei Ma, and Lars Hernquist. The stellar mass assembly of galaxies in the illustris simulation: growth by mergers and the spatial distribution of accreted stars. *MNRAS*, 458 (3):2371–2390, May 2016. doi: 10.1093/mnras/stw456.

Craig S. Rudick, J. Christopher Mihos, and Cameron McBride. The formation and evolution of intracluster light. *The Astrophysical Journal*, 648(2):936–946, sep 2006. ISSN 0004-637X. doi: 10.1086/506176. URL https://iopscience.iop.org/article/10.1086/506176.

Craig S. Rudick, J. Christopher Mihos, Lucille H. Frey, and Cameron K. McBride. Tidal streams of intracluster light. *The Astrophysical Journal*, 699(2):1518–1529, jul 2009. ISSN 0004-637X. doi: 10.1088/0004-637X/699/2/1518. URL https://iopscience.iop.org/article/10.1088/0004-637X/699/2/1518.

Craig S. Rudick, J. Christopher Mihos, and Cameron K. McBride. The quantity of intracluster light: Comparing theoretical and observational measurement techniques using simulated clusters. *ApJ*, 732(1):48, May 2011. doi: 10.1088/0004-637X/732/1/48.

Chalence Safranek-Shrader, Meghann Agarwal, Christoph Federrath, Anshu Dubey, Miloš Milosavljević, and Volker Bromm. Star formation in the first galaxies - i. collapse delayed by lyman-werner radiation. *MNRAS*, 426(2):1159–1177, October 2012. doi: 10.1111/j.1365-2966.2012.21852.x.

Laura V. Sales, Andrew Wetzel, and Azadeh Fattahi. Baryonic solutions and challenges for cosmological models of dwarf galaxies. *Nature Astronomy*, 6:897–910, June 2022. doi: 10.1038/s41550-022-01689-w.

Edwin E. Salpeter. The luminosity function and stellar evolution. *ApJ*, 121:161, January 1955. doi: 10.1086/145971.

Mahsa Sanati, Fabien Jeanquartier, Yves Revaz, and Pascale Jablonka. How much metal did the first stars provide to the ultra-faint dwarfs? *åp*, 669:A94, January 2023. doi: 10.1051/0004-6361/202244309.

Isabel M. Santos-Santos, Arianna Di Cintio, Chris B. Brook, Andrea Macciò, Aaron Dutton, and Rosa Domínguez-Tenreiro. NIHAO - XIV. Reproducing the observed diversity of dwarf galaxy rotation curve shapes in ΛCDM. *MNRAS*, 473(4):4392–4403, February 2018. doi: 10.1093/mnras/stx2660.

Isabel M. E. Santos-Santos, Julio F. Navarro, Andrew Robertson, Alejandro Benítez-Llambay, Kyle A. Oman, Mark R. Lovell, Carlos S. Frenk, Aaron D. Ludlow, Azadeh Fattahi, and Adam Ritz. Baryonic clues to the puzzling diversity of dwarf galaxy rotation curves. *MNRAS*, 495(1):58–77, June 2020. doi: 10.1093/mnras/staa1072.

Isabel M E Santos-Santos, Azadeh Fattahi, Laura V Sales, and Julio F Navarro. Magellanic satellites in cdm cosmological hydrodynamical simulations of the local group. *Monthly Notices of the Royal Astronomical Society*, 504:4551–4567, 5 2021. ISSN 0035-8711. doi: 10.1093/mnras/stab1020.

Isabel M E Santos-Santos, Laura V Sales, Azadeh Fattahi, and Julio F Navarro. Satellite mass functions and the faint end of the galaxy mass–halo mass relation in lcdm. *Monthly Notices of the Royal Astronomical Society*, 515:3685–3697, 8 2022. ISSN 0035-8711. doi: 10.1093/mnras/stac2057.

Till Sawala, Carlos S. Frenk, Azadeh Fattahi, Julio F. Navarro, Richard G. Bower, Robert A. Crain, Claudio Dalla Vecchia, Michelle Furlong, John. C. Helly, Adrian Jenkins, Kyle A. Oman, Matthieu Schaller, Joop Schaye, Tom Theuns, James Trayford, and Simon D. M. White. The apostle simulations: solutions to the local group's cosmic puzzles. *MNRAS*, 457(2):1931–1943, April 2016a. doi: 10.1093/mnras/stw145.

Till Sawala, Carlos S. Frenk, Azadeh Fattahi, Julio F. Navarro, Tom Theuns, Richard G. Bower, Robert A. Crain, Michelle Furlong, Adrian Jenkins, Matthieu Schaller, and Joop

Schaye. The chosen few: the low-mass haloes that host faint galaxies. *MNRAS*, 456(1): 85–97, February 2016b. doi: 10.1093/mnras/stv2597.

Anna T. P. Schauer, Volker Bromm, Michael Boylan-Kolchin, Simon C. O. Glover, and Ralf S. Klessen. Globular clusters and streaming velocities: Testing the new formation channel in high-resolution cosmological simulations. *ApJ*, 922(2):193, December 2021. doi: 10.3847/1538-4357/ac27aa.

Joop Schaye, Anthony Aguirre, Tae-Sun Kim, Tom Theuns, Michael Rauch, and Wallace L. W. Sargent. Metallicity of the intergalactic medium using pixel statistics. ii. the distribution of metals as traced by c iv. *ApJ*, 596(2):768–796, October 2003. doi: 10.1086/378044.

Evan E. Schneider, Eve C. Ostriker, Brant E. Robertson, and Todd A. Thompson. The physical nature of starburst-driven galactic outflows. *ApJ*, 895(1):43, May 2020. doi: 10.3847/1538-4357/ab8ae8.

Y. Schuberth, T. Richtler, L. Bassino, and M. Hilker. Intra-cluster globular clusters around ngc 1399 in fornax? *Astronomy Astrophysics*, 477(2):L9–L12, jan 2008. ISSN 0004-6361. doi: 10.1051/0004-6361:20078668. URL http://www.aanda.org/10.1051/0004-6361:20078668.

T. Shanks, N. Metcalfe, B. Chehade, J. R. Findlay, M. J. Irwin, E. Gonzalez-Solares, J. R. Lewis, A. Kupcu Yoldas, R. G. Mann, M. A. Read, E. T. W. Sutorius, and S. Voutsinas. The vlt survey telescope atlas. *MNRAS*, 451(4):4238–4252, August 2015. doi: 10.1093/mnras/stv1130.

M. E. Sharina, I. D. Karachentsev, A. E. Dolphin, V. E. Karachentseva, R. Brent Tully, G. M. Karataeva, D. I. Makarov, L. N. Makarova, S. Sakai, E. J. Shaya, E. Yu. Nikolaev, and A. N. Kuznetsov. Photometric properties of the local volume dwarf galaxies. *Monthly Notices of the Royal Astronomical Society*, 384:1544–1562, 3 2008. ISSN 1365-2966. doi: 10.1111/j.1365-2966.2007.12814.x.

Prateek Sharma, Michael McCourt, Eliot Quataert, and Ian J. Parrish. Thermal instability and the feedback regulation of hot haloes in clusters, groups and galaxies. *MNRAS*, 420 (4):3174–3194, March 2012. doi: 10.1111/j.1365-2966.2011.20246.x.

Nora Shipp, Denis Erkal, Alex Drlica-Wagner, Ting S. Li, Andrew B. Pace, Sergey E. Koposov, Lara R. Cullinane, Gary S. Da Costa, Alexander P. Ji, Kyler Kuehn, Geraint F. Lewis, Dougal Mackey, Jeffrey D. Simpson, Zhen Wan, Daniel B. Zucker, Joss Bland-Hawthorn, Peter S. Ferguson, Sophia Lilleengen, and Sophia Lilleengen. Measuring the mass of the large magellanic cloud with stellar streams observed by s [5]. *ApJ*, 923(2):149, December 2021. doi: 10.3847/1538-4357/ac2e93.

J. Michael Shull. Where do galaxies end? *The Astrophysical Journal*, 784:142, 3 2014. ISSN 0004-637X. doi: 10.1088/0004-637X/784/2/142.

Robert A. Simcoe. The carbon content of intergalactic gas at z = 4.25 and its evolution toward z = 2.4. *The Astrophysical Journal*, 738:159, 9 2011. ISSN 0004-637X. doi: 10.1088/0004-637X/738/2/159.

Robert A. Simcoe, Wallace L. W. Sargent, and Michael Rauch. The distribution of metallicity in the intergalactic medium at z $\sim$ 2.5: O VI and C IV absorption in the spectra of seven QSOs. *The Astrophysical Journal*, 606:92–115, 5 2004. ISSN 0004-637X. doi: 10.1086/382777.

Robert A. Simcoe, Peter W. Sullivan, Kathy L. Cooksey, Melodie M. Kao, Michael S. Matejek, and Adam J. Burgasser. Extremely metal-poor gas at a redshift of 7. *Nature*, 492(7427):79–82, December 2012. doi: 10.1038/nature11612.

Joshua D. Simon. The faintest dwarf galaxies. *ARA&A*, 57:375–415, August 2019. doi: 10.1146/annurev-astro-091918-104453.

Adam Smercina, Eric F. Bell, Paul A. Price, Richard D'Souza, Colin T. Slater, Jeremy Bailin, Antonela Monachesi, and David Nidever. A lonely giant: The sparse satellite population of m94 challenges galaxy formation. *ApJ*, 863(2):152, August 2018. doi: 10.3847/1538-4357/aad2d6.

Matthew C. Smith, Greg L. Bryan, Rachel S. Somerville, Chia-Yu Hu, Romain Teyssier, Blakesley Burkhart, and Lars Hernquist. Efficient early stellar feedback can suppress galactic outflows by reducing supernova clustering. *MNRAS*, 506(3):3882–3915, September 2021. doi: 10.1093/mnras/stab1896.

Russell J. Smith, John R. Lucey, Derek Hammer, Ann E. Hornschemeier, David Carter, Michael J. Hudson, Ronald O. Marzke, Mustapha Mouhcine, Sareh Eftekharzadeh, Phil James, Habib Khosroshahi, Ehsan Kourkchi, and Arna Karick. Ultraviolet tails and trails in cluster galaxies: a sample of candidate gaseous stripping events in coma. *MNRAS*, 408 (3):1417–1432, November 2010. doi: 10.1111/j.1365-2966.2010.17253.x.

Rachel S. Somerville. Can photoionization squelching resolve the substructure crisis? *The Astrophysical Journal*, 572:L23–L26, 6 2002. ISSN 0004637X. doi: 10.1086/341444.

Rachel S. Somerville and Joel R. Primack. Semi-analytic modelling of galaxy formation: the local universe. *MNRAS*, 310(4):1087–1110, December 1999. doi: 10.1046/j.1365-8711.1999.03032.x.

Rachel S. Somerville, Philip F. Hopkins, Thomas J. Cox, Brant E. Robertson, and Lars Hernquist. A semi-analytic model for the co-evolution of galaxies, black holes and active galactic nuclei. *MNRAS*, 391(2):481–506, December 2008. doi: 10.1111/j.1365-2966.2008.13805.x.

M. Spavone, E. Iodice, G. van de Ven, J. Falcón-Barroso, M. A. Raj, M. Hilker, R. P. Peletier, M. Capaccioli, S. Mieske, A. Venhola, N. R. Napolitano, M. Cantiello, M. Paolillo, and P. Schipani. The fornax deep survey with vst. viii. connecting the accretion history with the cluster density. *åp*, 639:A14, July 2020. doi: 10.1051/0004-6361/202038015.

Marilena Spavone, Enrichetta Iodice, Massimo Capaccioli, Daniela Bettoni, Roberto Rampazzo, Noah Brosch, Michele Cantiello, Nicola R. Napolitano, Luca Limatola, Aniello Grado, and Pietro Schipani. Vegas: A vst early-type galaxy survey. iii. mapping the galaxy structure, interactions, and intragroup light in the ngc 5018 group. *ApJ*, 864(2): 149, September 2018. doi: 10.3847/1538-4357/aad6e9.

J. S. Speagle, C. L. Steinhardt, P. L. Capak, and J. D. Silverman. A highly consistent framework for the evolution of the star-forming "main sequence" from z åisebox-0.5ex 0-6. *ApJS*, 214(2):15, October 2014. doi: 10.1088/0067-0049/214/2/15.

L. R. Spitler and D. A. Forbes. A new method for estimating dark matter halo masses using globular cluster systems. *MNRAS*, 392(1):L1–L5, January 2009. doi: 10.1111/j.1745-3933.2008.00567.x.

Volker Springel. E pur si muove: Galilean-invariant cosmological hydrodynamical simulations on a moving mesh. *MNRAS*, 401(2):791–851, January 2010. doi: 10.1111/j.1365-2966.2009.15715.x.

Volker Springel and Lars Hernquist. Cosmological smoothed particle hydrodynamics simulations: a hybrid multiphase model for star formation. *MNRAS*, 339(2):289–311, February 2003. doi: 10.1046/j.1365-8711.2003.06206.x.

Volker Springel, Simon D. M. White, Giuseppe Tormen, and Guinevere Kauffmann. Populating a cluster of galaxies - i. Results at z=0. *MNRAS*, 328(3):726–750, December 2001. doi: 10.1046/j.1365-8711.2001.04912.x.

Volker Springel, Rüdiger Pakmor, Annalisa Pillepich, Rainer Weinberger, Dylan Nelson, Lars Hernquist, Mark Vogelsberger, Shy Genel, Paul Torrey, Federico Marinacci, and Jill Naiman. First results from the illustristng simulations: matter and galaxy clustering. *MNRAS*, 475(1):676–698, March 2018. doi: 10.1093/mnras/stx3304.

P. Steyrleithner, G. Hensler, and A. Boselli. The effect of ram-pressure stripping on dwarf galaxies. *MNRAS*, 494(1):1114–1127, May 2020. doi: 10.1093/mnras/staa775.

Sandro Tacchella, Aaron Smith, Rahul Kannan, Federico Marinacci, Lars Hernquist, Mark Vogelsberger, Paul Torrey, Laura Sales, and Hui Li. Hα emission in local galaxies: star formation, time variability, and the diffuse ionized gas. *MNRAS*, 513(2):2904–2929, June 2022. doi: 10.1093/mnras/stac818.

Matthew A. Taylor, Roberto P. Muñoz, Thomas H. Puzia, Steffen Mieske, Paul Eigenthaler, and Mia Sauda Bovill. The Survey of Centaurus A's Baryonic Structures (SCABS). i. survey description and initial source catalogues. *arXiv e-prints*, art. arXiv:1608.07285, August 2016. doi: 10.48550/arXiv.1608.07285.

Matthew A. Taylor, Thomas H. Puzia, Roberto P. Muñoz, Steffen Mieske, Ariane Lançon, Hongxin Zhang, Paul Eigenthaler, and Mia Sauda Bovill. The Survey of Centaurus A's Baryonic Structures (SCABS) – ii. the extended globular cluster system of NGC 5128 and its nearby environment. *Monthly Notices of the Royal Astronomical Society*, 469

(3):3444–3467, 04 2017. ISSN 0035-8711. doi: 10.1093/mnras/stx1021. URL https://doi.org/10.1093/mnras/stx1021.

Max Tegmark, Joseph Silk, Martin J. Rees, Alain Blanchard, Tom Abel, and Francesco Palla. How small were the first cosmological objects? *ApJ*, 474:1, January 1997. doi: 10.1086/303434.

Patricia B. Tissera, Simon D. M. White, and Cecilia Scannapieco. Chemical signatures of formation processes in the stellar populations of simulated galaxies. *MNRAS*, 420(1): 255–270, February 2012. doi: 10.1111/j.1365-2966.2011.20028.x.

Erik J. Tollerud, James S. Bullock, Louis E. Strigari, and Beth Willman. Hundreds of milky way satellites? luminosity bias in the satellite luminosity function. *ApJ*, 688(1):277–289, November 2008. doi: 10.1086/592102.

Edouard Tollet, Andrea V. Macciò, Aaron A. Dutton, Greg S. Stinson, Liang Wang, Camilla Penzo, Thales A. Gutcke, Tobias Buck, Xi Kang, Chris Brook, Arianna Di Cintio, Ben W. Keller, and James Wadsley. NIHAO - iv: core creation and destruction in dark matter density profiles across cosmic time. *MNRAS*, 456(4):3542–3552, March 2016. doi: 10.1093/mnras/stv2856.

Stephanie Tonnesen and Greg L. Bryan. Star formation in ram pressure stripped galactic tails. *MNRAS*, 422(2):1609–1624, May 2012. doi: 10.1111/j.1365-2966.2012.20737.x.

G. Torrealba, V. Belokurov, S. E. Koposov, T. S. Li, M. G. Walker, J. L. Sanders, A. Geringer-Sameth, D. B. Zucker, K. Kuehn, N. W. Evans, and W. Dehnen. The hidden giant: discovery of an enormous galactic dwarf satellite in Gaia DR2. *MNRAS*, 488(2):2743–2766, September 2019. doi: 10.1093/mnras/stz1624.

Paul Torrey, Mark Vogelsberger, Debora Sijacki, Volker Springel, and Lars Hernquist. Moving-mesh cosmology: properties of gas discs. *MNRAS*, 427(3):2224–2238, December 2012. doi: 10.1111/j.1365-2966.2012.22082.x.

M Tremmel, T R Quinn, A Ricarte, A Babul, U Chadayammuri, P Natarajan, D Nagai, A Pontzen, and M Volonteri. Introducing *romulusc*: a cosmological simulation of a galaxy cluster with an unprecedented resolution. *Monthly Notices of the Royal Astronomical Society*, 483:3336–3362, 3 2019. ISSN 0035-8711. doi: 10.1093/mnras/sty3336.

Jason Tumlinson, Molly S. Peeples, and Jessica K. Werk. The circumgalactic medium. *ARA&A*, 55(1):389–432, August 2017. doi: 10.1146/annurev-astro-091916-055240.

Graziano Ucci, Pratika Dayal, Anne Hutter, Chiaki Kobayashi, Stefan Gottlöber, Gustavo Yepes, Leslie Hunt, Laurent Legrand, and Crescenzo Tortora. Astraeus v: the emergence and evolution of metallicity scaling relations during the epoch of reionization. *MNRAS*, 518(3):3557–3575, January 2023. doi: 10.1093/mnras/stac2654.

Sidney van den Bergh. The mass of the centaurus a group of galaxies. *The Astronomical Journal*, 119:609–611, 2 2000. ISSN 00046256. doi: 10.1086/301214.

Frank C van den Bosch, Go Ogiya, Oliver Hahn, and Andreas Burkert. Disruption of dark matter substructure: fact or fiction? *Monthly Notices of the Royal Astronomical Society*, 474:3043–3066, 3 2018. ISSN 0035-8711. doi: 10.1093/mnras/stx2956.

Pauli Virtanen, Ralf Gommers, Travis E. Oliphant, Matt Haberland, Tyler Reddy, David Cournapeau, Evgeni Burovski, Pearu Peterson, Warren Weckesser, Jonathan Bright, Stéfan J. van der Walt, Matthew Brett, Joshua Wilson, K. Jarrod Millman, Nikolay Mayorov, Andrew R. J. Nelson, Eric Jones, Robert Kern, Eric Larson, C J Carey, İlhan Polat, Yu Feng, Eric W. Moore, Jake VanderPlas, Denis Laxalde, Josef Perktold, Robert Cimrman, Ian Henriksen, E. A. Quintero, Charles R. Harris, Anne M. Archibald, Antônio H. Ribeiro, Fabian Pedregosa, Paul van Mulbregt, and SciPy 1.0 Contributors. SciPy 1.0: Fundamental Algorithms for Scientific Computing in Python. *Nature Methods*, 17:261–272, 2020. doi: 10.1038/s41592-019-0686-2.

Maya Vitvitska, Anatoly A. Klypin, Andrey V. Kravtsov, Risa H. Wechsler, Joel R. Primack, and James S. Bullock. The origin of angular momentum in dark matter halos. *ApJ*, 581(2):799–809, December 2002. doi: 10.1086/344361.

M. Vogelsberger, S. Genel, V. Springel, P. Torrey, D. Sijacki, D. Xu, G. Snyder, S. Bird, D. Nelson, and L. Hernquist. Properties of galaxies reproduced by a hydrodynamic simulation. *Nature*, 509(7499):177–182, May 2014a. doi: 10.1038/nature13316.

Mark Vogelsberger, Shy Genel, Debora Sijacki, Paul Torrey, Volker Springel, and Lars Hernquist. A model for cosmological simulations of galaxy formation physics. *MNRAS*, 436(4):3031–3067, December 2013. doi: 10.1093/mnras/stt1789.

Mark Vogelsberger, Shy Genel, Volker Springel, Paul Torrey, Debora Sijacki, Dandan Xu, Greg Snyder, Dylan Nelson, and Lars Hernquist. Introducing the illustris project: simulating the coevolution of dark and visible matter in the universe. *MNRAS*, 444(2): 1518–1547, October 2014b. doi: 10.1093/mnras/stu1536.

B. Vollmer, J. Braine, B. Mazzilli-Ciraulo, and B. Schneider. Low star formation efficiency due to turbulent adiabatic compression in the taffy bridge. *åp*, 647:A138, March 2021. doi: 10.1051/0004-6361/202037887.

J. A. Vázquez-Mata, J. Loveday, S. D. Riggs, I. K. Baldry, L. J. M. Davies, A. S. G. Robotham, B. W. Holwerda, M. J. I. Brown, M. E. Cluver, L. Wang, M. Alpaslan, J. Bland-Hawthorn, S. Brough, S. P. Driver, A. M. Hopkins, E. N. Taylor, and A. H. Wright. Galaxy and mass assembly: luminosity and stellar mass functions in gama groups. *MNRAS*, 499(1):631–652, November 2020. doi: 10.1093/mnras/staa2889.

Liang Wang, Aaron A. Dutton, Gregory S. Stinson, Andrea V. Macciò, Camilla Penzo, Xi Kang, Ben W. Keller, and James Wadsley. Nihao project - i. reproducing the inefficiency of galaxy formation across cosmic time with a large sample of cosmological hydrodynamical simulations. *MNRAS*, 454(1):83–94, November 2015. doi: 10.1093/mnras/stv1937.

WenTing Wang, JiaXin Han, Marius Cautun, ZhaoZhou Li, and Miho N. Ishigaki. The mass of our milky way. *Science China Physics, Mechanics, and Astronomy*, 63(10):109801, May 2020. doi: 10.1007/s11433-019-1541-6.

Tracy Webb, Allison Noble, Andrew DeGroot, Gillian Wilson, Adam Muzzin, Nina Bonaventura, Mike Cooper, Anna Delahaye, Ryan Foltz, Chris Lidman, Jason Surace, H. K. C. Yee, Scott Chapman, Loretta Dunne, James Geach, Brian Hayden, Hendrik Hildebrandt, Jiasheng Huang, Alexandra Pope, Matthew W. L. Smith, Saul Perlmutter, and Alex Tudorica. An extreme starburst in the core of a rich galaxy cluster at z = 1.7. *ApJ*, 809(2):173, August 2015a. doi: 10.1088/0004-637X/809/2/173.

Tracy M. A. Webb, Adam Muzzin, Allison Noble, Nina Bonaventura, James Geach, Yashar Hezaveh, Chris Lidman, Gillian Wilson, H. K. C. Yee, Jason Surace, and David Shupe. The star formation history of bcgs to z = 1.8 from the sparcs/swire survey: Evidence for significant in situ star formation at high redshift. *ApJ*, 814(2):96, December 2015b. doi: 10.1088/0004-637X/814/2/96.

Risa H. Wechsler and Jeremy L. Tinker. The connection between galaxies and their dark matter halos. *ARA&A*, 56:435–487, September 2018. doi: 10.1146/annurev-astro-081817-051756.

Sachi Weerasooriya, Mia Sauda Bovill, Andrew Benson, Alexi M. Musick, and Massimo Ricotti. Devouring the milky way satellites: Modeling dwarf galaxies with galacticus. *The Astrophysical Journal*, 948:87, 5 2023. ISSN 0004-637X. doi: 10.3847/1538-4357/acc32b.

Martin D. Weinberg. Adiobatic invariants in stellar dynamics. i. basic concepts. *AJ*, 108: 1398, October 1994a. doi: 10.1086/117161.

Martin D. Weinberg. Adiabatic invariants in stellar dynamics. ii. gravitational shocking. *AJ*, 108:1403, October 1994b. doi: 10.1086/117162.

Rainer Weinberger, Volker Springel, Lars Hernquist, Annalisa Pillepich, Federico Marinacci, Rüdiger Pakmor, Dylan Nelson, Shy Genel, Mark Vogelsberger, Jill Naiman, and Paul Torrey. Simulating galaxy formation with black hole driven thermal and kinetic feedback. *MNRAS*, 465(3):3291–3308, March 2017. doi: 10.1093/mnras/stw2944.

Simone M. Weinmann, Thorsten Lisker, Qi Guo, Hagen T. Meyer, and Joachim Janz. Dwarf galaxy populations in present-day galaxy clusters - i. abundances and red fractions. *MNRAS*, 416(2):1197–1214, September 2011. doi: 10.1111/j.1365-2966.2011.19118.x.

Andrew R. Wetzel, Philip F. Hopkins, Ji-hoon Kim, Claude-André Faucher-Giguère, Dušan Kereš, and Eliot Quataert. Reconciling dwarf galaxies with ΛCDM cosmology: Simulating a realistic population of satellites around a Milky Way-mass galaxy. *ApJL*, 827(2):L23, August 2016. doi: 10.3847/2041-8205/827/2/L23.

Coral Wheeler, Jose Oñorbe, James S. Bullock, Michael Boylan-Kolchin, Oliver D. Elbert, Shea Garrison-Kimmel, Philip F. Hopkins, and Dušan Kereš. Sweating the small stuff: simulating dwarf galaxies, ultra-faint dwarf galaxies, and their own tiny satellites. *MNRAS*, 453(2):1305–1316, October 2015. doi: 10.1093/mnras/stv1691.

Coral Wheeler, Philip F. Hopkins, Andrew B. Pace, Shea Garrison-Kimmel, Michael Boylan-Kolchin, Andrew Wetzel, James S. Bullock, Dušan Kereš, Claude-André Faucher-Giguère, and Eliot Quataert. Be it therefore resolved: cosmological simulations of dwarf galaxies with 30 solar mass resolution. *MNRAS*, 490(3):4447–4463, December 2019. doi: 10.1093/mnras/stz2887.

S. D. M. White and M. J. Rees. Core condensation in heavy halos: a two-stage theory for galaxy formation and clustering. *MNRAS*, 183:341–358, May 1978. doi: 10.1093/mnras/183.3.341.

Simon D. M. White and Carlos S. Frenk. Galaxy formation through hierarchical clustering. *ApJ*, 379:52, September 1991. doi: 10.1086/170483.

Benjamin F. Williams, Robin Ciardullo, Patrick R. Durrell, Matt Vinciguerra, John J. Feldmeier, George H. Jacoby, Steinn Sigurdsson, Ted von Hippel, Henry C. Ferguson, Nial R. Tanvir, Magda Arnaboldi, Ortwin Gerhard, J. Alfonso L. Aguerri, and Ken Freeman. The metallicity distribution of intracluster stars in virgo. *ApJ*, 656(2):756–769, February 2007. doi: 10.1086/510149.

H. Yahagi and K. Bekki. Formation of intracluster globular clusters. *Monthly Notices of the Royal Astronomical Society: Letters*, 364(1):L86–L90, nov 2005. ISSN 1745-3925. doi: 10.1111/j.1745-3933.2005.00111.x. URL https://academic.oup.com/mnrasl/article-lookup/doi/10.1111/j.1745-3933.2005.00111.x.

Shengqi Yang, Xiaolong Du, Andrew J Benson, Anthony R Pullen, and Annika H G Peter. A new calibration method of sub-halo orbital evolution for semi-analytic models. *Monthly Notices of the Royal Astronomical Society*, 498:3902–3913, 9 2020. ISSN 0035-8711. doi: 10.1093/mnras/staa2496.

Andrew R. Zentner, Andreas A. Berlind, James S. Bullock, Andrey V. Kravtsov, and Risa H. Wechsler. The physics of galaxy clustering. i. a model for subhalo populations. *The Astrophysical Journal*, 624:505–525, 5 2005. ISSN 0004-637X. doi: 10.1086/428898.

Stefano Zibetti, Simon D. M. White, Donald P. Schneider, and Jon Brinkmann. Intergalactic stars in zåisebox-0.5ex 0.25 galaxy clusters: systematic properties from stacking of sloan digital sky survey imaging data. *MNRAS*, 358(3):949–967, April 2005. doi: 10.1111/j.1365-2966.2005.08817.x.

Adi Zolotov, Beth Willman, Alyson M. Brooks, Fabio Governato, Chris B. Brook, David W. Hogg, Tom Quinn, and Greg Stinson. The dual origin of stellar halos. *ApJ*, 702(2):1058–1067, September 2009. doi: 10.1088/0004-637X/702/2/1058.

Adi Zolotov, Alyson M. Brooks, Beth Willman, Fabio Governato, Andrew Pontzen, Charlotte Christensen, Avishai Dekel, Tom Quinn, Sijing Shen, and James Wadsley. Baryons matter: Why luminous satellite galaxies have reduced central masses. *The Astrophysical Journal*, 761:71, 12 2012. ISSN 0004-637X. doi: 10.1088/0004-637X/761/1/71.

F. Zwicky. On the masses of nebulae and of clusters of nebulae. *The Astrophysical Journal*, 86(2):217, oct 1937. ISSN 0004-637X. doi: 10.1086/143864. URL http://adsabs.harvard.edu/doi/10.1086/143864.

F. Zwicky. The coma cluster of galaxies. *Publications of the Astronomical Society of the Pacific*, 63(2):61, apr 1951. ISSN 0004-6280. doi: 10.1086/126318. URL http://iopscience.iop.org/article/10.1086/126318.

F. Zwicky. Luminous intergalactic matter. *Publications of the Astronomical Society of the Pacific*, 64(2):242, oct 1952. ISSN 0004-6280. doi: 10.1086/126484. URL http://iopscience.iop.org/article/10.1086/126484.

F. Zwicky. Non-uniformities in the apparent distribution of clusters of galaxies. *Publications of the Astronomical Society of the Pacific*, 69(2):518, dec 1957. ISSN 0004-6280. doi: 10.1086/127139. URL http://iopscience.iop.org/article/10.1086/127139.

Appendix A

Effect of ICL definition

As mentioned in section 2.4.1 there are various definitions of ICL in the literature. Here we examine the effect on the predicted ICL mass of adopting a few of these different definitions. The methods used to define ICL are as follows; considering stellar particles that do not belong to any subhalos in the range $0.15 \times r_{200} < r < r_{200}$ (shown by blue circles), compared to stars in $5 \times r_{h_*} < r < r_{200}$ where r_{h_*} is the stellar half mass radius of the central galaxy (shown by green circles), and stars in range $r_{25} < r < r_{200}$ where r_{25} is the radius where the surface brightness (SB) reaches 25 mag/arcsec^2 (results are shown by orange circles). The upper right panel of Fig. F.1 shows the mass in the ICL, while the upper left panel shows ICL fraction as a function of virial mass of the group for our sample of 39 halos in TNG50. The lower panels show the same quantities compared to the definition of ICL used in this paper. Our results suggest that, given the dispersion in the predicted ICL amount at a given virial mass, the changes in the definition will not significantly affect the results. All predicted fractions remain within approximately a factor of $\sim$2 of our adopted

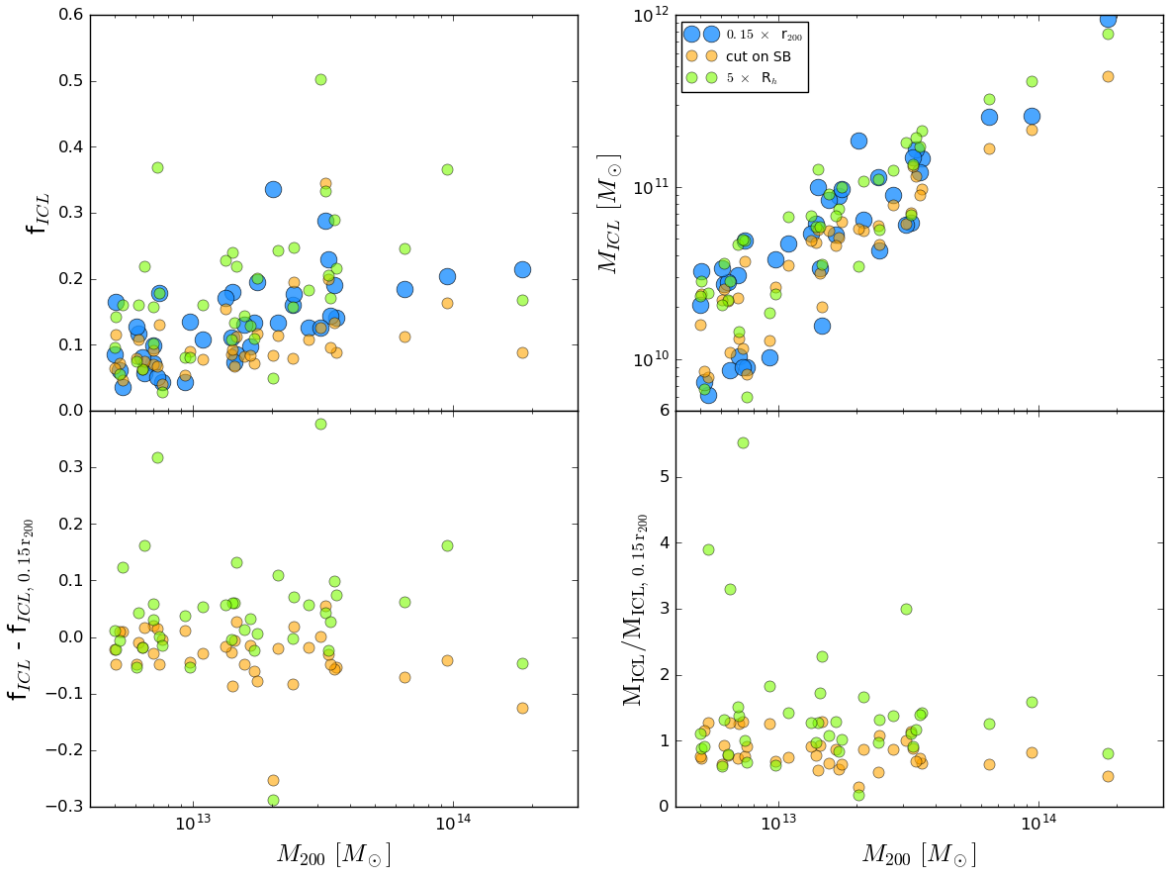

Figure A.1: Upper left panel: ICL fraction as a function of virial mass. Upper right panel: stellar mass content in the ICL as a function of virial mass. Lower left panel: alternative ICL fractions compared to the method used in this paper. Lower right panel: the fraction of stellar mass content in the ICL measured from alternative definitions to the mass content from the ICL definition method used in this paper. The different colors correspond to various definitions of ICL.

definition, with the SB-cut-based definition consistently yielding lower values, while the $5 \times r_{h*} < r < r_{200}$ definition tends to predict higher fractions than our adopted one.

Appendix B

The GC tagging technique

Below is a summary of the method introduced in Doppel et al. (2023) to tag GCs into the TNG50 simulations. We add GC particles to all selected galaxies in TNG50 that interact with the 39 most massive groups ($M_{200} > 5 \times 10^{12}$ $M_{\odot}$). The procedure is done at their time of infall, when we select the full set of DM particles that follow a given energy distribution. The energy distribution is calculated by assuming that the DM halos of the selected galaxies conform to an NFW profile (Navarro et al. 1996):

$$\rho_{\rm NFW}(r) = \frac{\rho^0_{\rm NFW}}{(r/r_{\rm NFW})(1 + r/r_{\rm NFW})^2}, \tag{B.1}$$

that is fit to each galaxy at infall following Lokas and Mamon (2001). We assume a scale radius, $r_{\rm NFW} = r_{\rm max}/\alpha$ where $r_{\rm max}$ is the radius of maximum circular velocity calculated from the dark matter particle distribution in the simulation and $\alpha = 2.1623$ (Bullock et al. 2001).

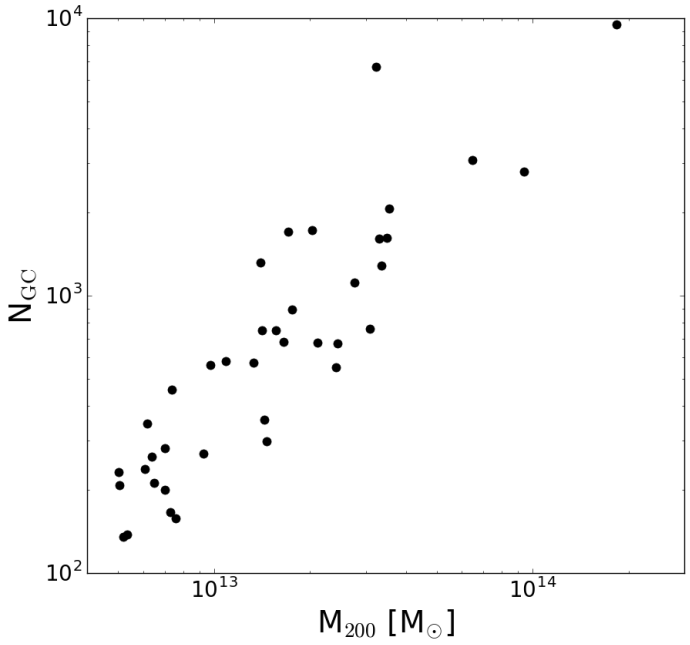

Figure B.1: Number of GCs in the ICL as a function of the virial mass of the halos.

Subsequently, GCs are assumed to follow a Hernquist profile (Hernquist 1990):

$$\rho_{\rm HQ}(r) = \frac{\rho^0_{\rm HQ}}{(r/r_{\rm HQ})(1+r/r_{\rm HQ})^3}. \tag{B.2}$$

with scale radius $r_{\rm HQ}$ is dependent upon whether the GC is "red" or "blue". The "red" component is intended to be representative of a more radially concentrated metal rich GCs, while a "blue" component refers to a more radially extended and metal poor population of GCs. Following (Ramos-Almendares et al. 2020), it is assumed that $r_{\rm HQ} = \beta r_{\rm NFW}$, where $\beta_{\rm red} = 0.5$ and $\beta_{\rm blue} = 3.0$. $\rho_{\rm HQ}$ is fit such that the number of GC candidates are maximized.

Next, the distribution function is calculated for the NFW halo, the blue GCs, and the red GCs following Binney and Tremaine (2008):

$$f_i(\epsilon) = \frac{1}{8\pi}\left[\int_0^\epsilon \frac{{\rm d}^2\rho_{\rm i}}{{\rm d}\psi^2}\frac{{\rm d}\psi}{\sqrt{\epsilon-\psi}} + \frac{1}{\sqrt{\epsilon}}\left(\frac{{\rm d}\rho_{\rm i}}{{\rm d}\psi}\right)\Big|_{\psi=0}\right], \tag{B.3}$$

where ρ_i is the density profile of i = (DM, Red GCs, Blue GCs), Ψ is the relative gravitational potential, and ϵ is the relative energy. In bins of relative energy, a fraction $f_{HQ,i}/f_{DM}$ of the DM particles are selected to be GCs, and the final set of GC candidates are defined to be within a cutoff radius of $r_h/3$, where r_h is the total half-mass radius of the galaxy, following Yahagi and Bekki (2005).

The method assumes a power-law relation between the total GC mass and the halo mass of each galaxy whose normalization is calibrated such that it reproduces the observed relation at the present-day (Harris et al. 2015). Only halos with $M_{200} > 10^{11}$ $M_\odot$ participate in the calibration process and properties of lower mass objects can be considered a prediction. More specifically, the resulting coefficients for the M_{GC} - M_{halo} relation at infall are:

$$M_{\mathrm{GC},z=0} = a M_{\mathrm{halo,z=0}}^{b}, \tag{B.4}$$

where $a = 2.6 \times 10^{-8}$ and 4.9×10^{-5} for red and blue GCs respectively, with b = 1.2 and 0.96 for red and blue GCs. Similarly to Harris et al. (2015), z = 0 halo masses are calculated assuming abundance matching parameters from Hudson et al. (2015).

The calibration for GC mass is made using the amount of GC stripping by z = 0: $f_{bound} = N_{candidates,z=0}/N_{candidates,infall}$. Where a GC candidate is considered (still) bound to a galaxy if its corresponding DM particles are identified as part of the galaxy via `SUBFIND`. Assuming that at infall, the relation between M_{GC} and M_{halo} still follows a power law:

$$M_{\mathrm{GC,inf}} = \frac{1}{f_{\mathrm{bound}}} M_{\mathrm{GC},z=0} = a_{\mathrm{inf}} M_{\mathrm{halo,inf}}^{b_{\mathrm{inf}}}, \tag{B.5}$$

with the coefficient and exponent found to be $a_{inf} = 2.6 \times 10^{-7}$ and 7.3×10^{-5} and $b_{inf} = 1.14$ and 0.98 for red and blue GCs respectively.

Finally, the number of all identified GC candidates with energy consistent with the distribution of red and blue GCs is in most cases larger than the observed number of GCs around such galaxies. Subsequently, the GC candidates at infall for each galaxy are subsampled to obtain a realistic number of GCs (Fig B.1 shows the number of GCs in the ICL for our sample of groups and clusters). For a given galaxy, we assume that the z-band luminosity function of GCs is Gaussian, centered on $L_{GC} = 2 \times 10^5$ $L_\odot$ with a dispersion that varies with galaxy luminosity (as found by Jordan et al. 2007). We select GC luminosities, converting them to masses assuming a z-band mass to light ratio of 1 $M_\odot/L_\odot$, until the total selected mass in GCs is consistent with the total GC mass assigned to the galaxy at infall. The resulting individual GC masses, m_{GC} are in the range 7×10^3 $M_\odot \leq m_{GC} \leq 5 \times 10^6$ $M_\odot$, consistent with observational constraints from Jordan et al. (2007).

Appendix C

Surface brightness profiles

In order to establish a fair comparison between observations and simulations, we randomly project our simulated groups and clusters generating their 2D surface brightness maps. The results are presented in Fig. C.1, where the solid black line represents the median surface brightness for our entire sample in circular radii bins. Because we span a range of host halo masses, we normalize the horizontal axis to the virial radius of each system. The shaded grey region illustrates the whole range of surface brightness covered by our entire sample. This variation in profile is given by two factors: object-to-object differences in assembly history and mass in the ICL and, also important, the range of host halo masses being included. For illustration, the median surface brightness including only the three most massive clusters with $M_{200} \sim 10^{14}\mathrm{M}_{\odot}$ is shown by the dashed black line, which is systematically ~ 1 magnitude brighter that considering the whole sample. The area being shaded by hatching for $R/r_{200} < 0.15$ separates the inner regions attributed to the BCG and not considered part of the ICL.

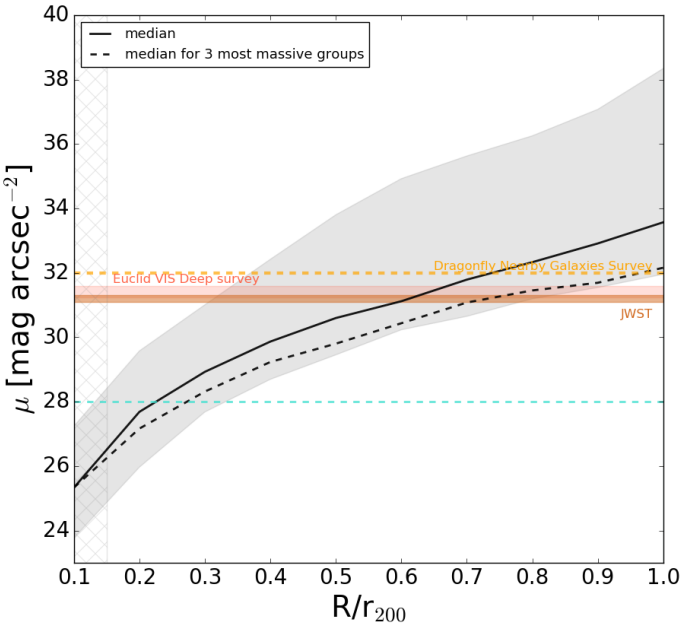

Figure C.1: Surface brightness profiles of our sample of groups and clusters. The black line represents the median profile for the entire sample, while the dashed black line corresponds to the median profile of the three most massive groups. The shaded region illustrates the dispersion across all groups in our sample. The gray hatched region indicates the extent of the BCG.

The turquoise horizontal dashed line indicates the 28 mag/arcsec^2 limit at which we measure the radius of each group. For comparison, we have included estimates of the surface brightness limits for the James Webb Space Telescope (based on the study of ICL in SMACS 0723 by Montes and Trujillo 2022[1]), the Euclide VIS Deep survey(Borlaff et al. 2022)[1], and the Dragonfly Telephoto Array's deep nearby galaxy survey (which provides g-band surface brightness profiles down to 31-32 mag/arcsec^2, see Merritt et al. (2016) for applications to stellar halo studies). We predict that observational campaigns in the future targeting $\sim$ 31 mag/arcsec^2 are a promising avenue to map the stellar diffuse component in groups and clusters out to at least half the virial radius.

[1]These limits correspond to a sky fluctuation of 3σ in an area of 10×10 arcsec^2.

Appendix D

Summary of Observations

In this section, we present the observational data utilized for the ICL fraction–halo mass relation. Although efforts were made to gather data from sources employing consistent definitions and methods, some studies included in this compilation used different techniques to identify the ICL. For instance, Spavone et al. (2020) studied the Fornax cluster and utilized multi-component fits[1] to distinguish the ICL component, revealing that approximately 34% of the total light in this cluster originates from the ICL. Another study by Da Rocha and Mendes de Oliveira (2005); Da Rocha et al. (2008) employed wavelet techniques[2] to measure the ICL in six objects from the Hickson Compact Group (HCG) catalog, resulting in a wide range of observed ICL fractions. The ICL fractions varied from no detected ICL in HCG 88 to approximately 33% for HCG 79 (the fraction representing the

[1]Using multiple equations to describe BCG + ICL (such as single or double Sérsic profiles and/or exponential profiles).

[2]The wavelet technique consists of deconvolving the signal into wavelet coefficients (since images are a 2D signal, each wavelet coefficient corresponds to a plane), identifying the objects representations in the wavelet space, defining the objects with a "multiscale vision model" (Bijaoui and Rué 1995) and reconstructing the detected objects (Da Rocha and Mendes de Oliveira 2005; Jiménez-Teja and Dupke 2016; Ellien et al. 2021).

ratio of ICL light to the total light of the group in the R band). Some studies have combined observational results with semi-analytical simulations to estimate the ICL fraction, such as the deep survey of the Virgo cluster conducted by Mihos et al. (2017), which estimated a range of 7-15% for the ICL fraction.

Furthermore, variations in the choice of observational bands used to infer the ICL fraction can be noticed. Different bands can yield different measurements of the ICL fraction. For example, Ragusa et al. (2021) investigated HCG 86 and found an ICL fraction of 14% in the r band and 19% in the g band, highlighting how the choice of band in observations can influence the measured amount of light attributed to the ICL.

An interesting outcome of these measurements is the dispersion observed in the ICL fraction at a given halo mass. Iodice et al. (2020) compared the ICL fractions of several different objects using the same method and demonstrated how features present in the ICL, outer envelope of the brightest cluster galaxy, and the presence of HI can indicate different evolutionary stages and mass assembly histories for different groups and clusters.

Additionally, some studies have linked the ICL fraction to the mean morphology of the group or cluster. Poliakov et al. (2021) measured the ICL fraction for multiple HCG objects and found that the mean surface brightness of the intra-group light correlates with the mean morphology of the group, with brighter intra-group light observed in groups with a larger fraction of early-type galaxies. It is important to note that the investigated groups in the TNG50 simulations exhibit various morphologies and formation histories, which may contribute to the wide variation in ICL fractions at a given mass.

Table D.1 below provides a summary of the observational results compiled from multiple sources.

Table D.1: Observational Data.

Object	**ref. for f_{ICL}**	f_{ICL}	M_{halo} [10^{13} $M_{\odot}$]	**Comments**
Fornax	Spavone et al. (2020)	34% (21.4% - 53.8%)	6.3	ref. for mass: Spavone et al. (2020); Ragusa et al. (2021); Montes (2022)
	Montes (2022)	34% (19% - 49%)		Observation was conducted in u,g,r,i bands (Spavone et al. 2020)
	Ragusa et al. (2021)	34±2%		
Virgo	Mihos et al. (2017)	7 -15%	31.6 (1)	ref. for mass(1): Ragusa et al. (2021); Spavone et al. (2020)
	Ragusa et al. (2021)	11±3%	14-40 (2)	ref. for mass(2): Weinmann et al. (2011)
				Observation was conducted in B and V bands (Mihos et al. 2017)
				Using results of simulations (Rudick et al. 2009), Mihos et al. (2017) estimated 5-10% of the ICL should be the form of coherent streams (the relatively high surface brightness tidal features that represent material most recently stripped from their host galaxies), which help them estimate the whole amount of ICL luminosity.
IC 1459	Iodice et al. (2020); Ragusa et al. (2021)	2±2%	3.7	ref. for mass: Iodice et al. (2020); Ragusa et al. (2021)
				Observation was conducted in g and r bands (Iodice et al. 2020)
NGC 5018	Spavone et al. (2018)	41%	0.68	ref. for mass: Ragusa et al. (2021); Iodice et al. (2020); Montes (2022)
	Ragusa et al. (2021)	40±5%		Observation was conducted in u,g,r bands (Spavone et al. 2018)
	Iodice et al. (2020)	41±5%		
NGC 1533	Ragusa et al. (2021); Iodice et al. (2020)	8±2%	0.49	ref. for mass: Ragusa et al. (2021); Iodice et al. (2020)
				Observation was conducted in g,r bands (Cattapan et al. 2019)

Continued on next page

Table D.1 – continued from previous page

Object	ref. for f_{ICL}	f_{ICL}	M_{halo} [10^{13} $M_\odot$]	Comments
HCG 8	Poliakov et al. (2021); Ragusa et al. (2021)	25.1%	5.29	ref. for mass: Montes (2022) Observation was conducted in r band (Poliakov et al. 2021)
HCG 15	Da Rocha et al. (2008); Iodice et al. (2020)	B: 16±3% [a,b] R: 18±4%[a,b]	5.3[b] (1)	ref. for mass(1): Da Rocha et al. (2008); Montes (2022) ref. for mass(2): Da Rocha et al. (2008); Ragusa et al. (2021); Iodice et al. (2020)
	Da Rocha et al. (2008); Ragusa et al. (2021)	B: 19±4% [a,c] R: 21±4%[a,c]	5.67[c] (2)	Observation was conducted in B and R bands (Da Rocha et al. 2008)
HCG 17	Poliakov et al. (2021)	16.3%		Observation was conducted in r band (Poliakov et al. 2021)
HCG 35	Da Rocha et al. (2008); Ragusa et al. (2021); Iodice et al. (2020)	B: 15±3% [a] R: 11±2%[a]	1.51 (1)	ref. for mass(1): Da Rocha et al. (2008); Ragusa et al. (2021); Iodice et al. (2020); Montes (2022) ref. for mass (2): Montes (2022)
	Poliakov et al. (2021)	12.8%	3.1 (2)	Observation was conducted in B and R bands (Da Rocha et al. 2008)
HCG 37	Poliakov et al. (2021); Ragusa et al. (2021)	12.7%	5.87 (1)	ref. for mass(1): Montes (2022) ref. for mass(2): Ragusa et al. (2021) Observation was conducted in r band (Poliakov et al. 2021)
			2.24 (2)	
HCG 51	Da Rocha et al. (2008); Iodice et al. (2020)	B: 26±5% [a,b] R: 24±5%[a,b]	3.59[b] (1)	ref. for mass(1): Da Rocha et al. (2008); Montes (2022) ref. for mass(2): Da Rocha et al. (2008)
	Da Rocha et al. (2008); Ragusa et al. (2021)	B: 31±6% [a,c] R: 28±5%[a,c]	0.74[c] (2)	Observation was conducted in B and R bands (Da Rocha et al. 2008)
HCG 74	Poliakov et al. (2021); Ragusa et al. (2021)	7.5%	28.65	ref. for mass: Montes (2022) Observation was conducted in r band (Poliakov et al. 2021)

Continued on next page

Table D.1 – continued from previous page

Object	ref. for f_{ICL}	f_{ICL}	M_{halo} [10^{13} $M_\odot$]	Comments
HCG 79	Da Rocha and Mendes de Oliveira (2005); Ragusa et al. (2021)	B: 46±11% [a] R: 33±11%[a]	1.04 (1)	ref. for mass(1): Montes (2022) ref. for mass(2): Ragusa et al. (2021); Iodice et al. (2020) Observation was conducted in B and R bands (Da Rocha and Mendes de Oliveira 2005)
	Iodice et al. (2020)	46±10%	3.98 (2)	
HCG 86	Ragusa et al. (2021)	Radius < 160kpc : g: 19±3% (35±5% [d]) r: 14±2% (29±6% [d]) Radius < 120kpc : g:16±3% (28±5% [d]) r: 11±2% (23±7% [d])	0.85	ref. for mass: Ragusa et al. (2021) Observation was conducted in g,r,i bands (Ragusa et al. 2021)
HCG 88	Da Rocha and Mendes de Oliveira (2005); Iodice et al. (2020)	0[a]	2.88 (1) 0.12 (2)	ref. for mass(1): Montes (2022) ref. for mass(2): Iodice et al. (2020) Observation was conducted in B and R bands (Da Rocha and Mendes de Oliveira 2005)
HCG 90	Ragusa et al. (2021); Iodice et al. (2020)	38±3%	1.17	ref. for mass: Ragusa et al. (2021); Iodice et al. (2020)
HCG 95	Da Rocha and Mendes de Oliveira (2005); Ragusa et al. (2021)	B: 11±26% [a] R: 12±10%[a]	2.14	ref. for mass: Ragusa et al. (2021); Montes (2022) Observation was conducted in B and R bands (Ragusa et al. 2021) (Poliakov et al. 2021)

[a] ICL fractions are measured using wavelet technique

[b] corresponding to sextet configuration

[c] corresponding to quintet configuration

[d] Measured ICL fraction with respect to mass of the BCG

Appendix E

Physical conditions for star formation

In this section we provide additional information on the gas density and temperature as physical conditions related to the rate of star formation. We show in Fig. E.1 the distribution of gas density (left panel) and temperature (right panel) of star-forming gas in different environments: ICL (blue) and satellites in our clusters (gray). The classification of cells as either belonging to the ICL or to satellites has been done consistent with the classification of stars, following membership of cells as assigned by SUBFIND and "cleaning" the ICL from particles close in distance to surviving satellites (see Sec. 3.3.1). Fig. E.1 below shows that the star formation in the ICL occurs with densities slightly biased low with respect to the star formation in the ISM of galaxies, but there is considerable overlap in the distributions. For completeness, we also show the temperature distributions on the right panel, which suggest a similar trend as in the density. However, it should be kept

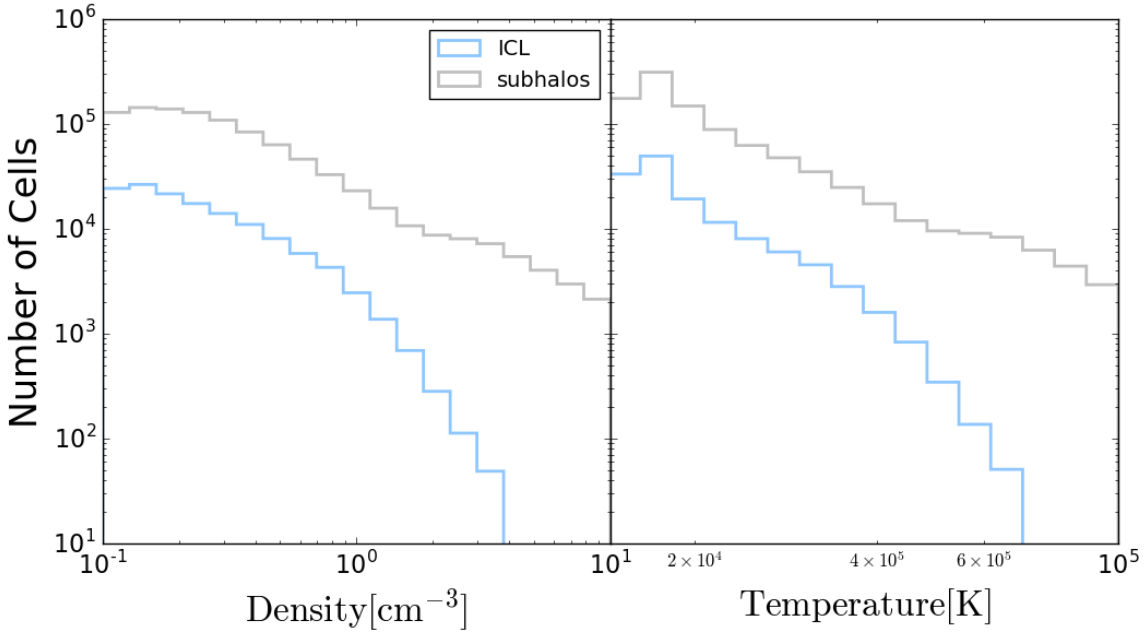

Figure E.1: Left panel: histogram of density of star-forming gas cells that belong to the ICL (shown by the blue line) and massive subhalos (shown by the gray line). Right panel: histogram of temperature of star-forming gas cells shown using the same color for the same components from the right panel.

in mind that in baryonic treatments based on the Springel and Hernquist (2003) model, temperature is not an independent variable, but instead computed from the density of cells above the threshold for star formation are placed on an effective equation of state T $\propto \rho^{\gamma}$.

Appendix F

Effect of resolution on predictions for star formation

To assess the impact of resolution on the star formation rates found within the ICL regions in our studied groups in TNG50, we turn our attention to the results obtained from TNG100 and TNG50-2. TNG100-1, part of the same suite of cosmological hydrodynamical simulations, represents a larger baryonic run with a volume of $110.7\,\mathrm{Mpc}^3$ and 2×1820^3 resolution elements (lower resolution compared to TNG50, which features 2×2160^3 resolution elements). In this run, the baryon and dark matter particle masses are $1.4 \times 10^6 \mathrm{M}_\odot$and $7.5 \times 10^6 \mathrm{M}_\odot$, respectively. TNG50-2 has the exact same volume as TNG50 but simulated at the resolution of TNG100.

For the comparison, we exclusively consider groups with virial masses similar to those examined in our study ($M_{200} \gtrapprox 6.5 \times 10^{13}$), resulting in a subset of 26 groups in TNG100 and 3 groups in TNG50-2.

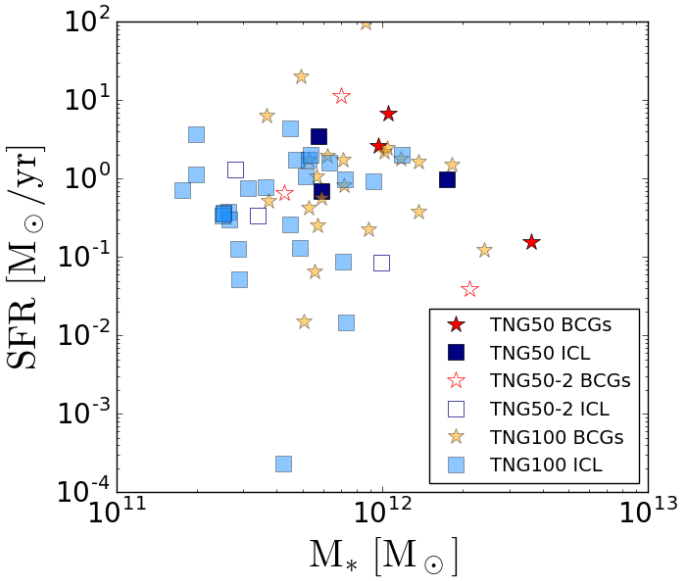

Figure F.1: Star formation rate (SFR) plotted against stellar mass for different groups in TNG100, TNG50, and TNG50-2 simulations. Results for central galaxies are represented by stars, with orange denoting centrals in TNG100, red for TNG50, and unfilled red stars for TNG50-2. The ICL component is illustrated by squares, with light blue indicating ICL in TNG100, navy blue for TNG50, and unfilled navy blue representing TNG50-2.

In Fig. F.1, we juxtapose the star formation rates in TNG50 and TNG100 for both central and ICL regions. The results of TNG50 seem within the scatter of those for the larger sample of TNG100 groups, perhaps slightly biased to the upper half of the SFR distribution. For a more direct comparison, we also show the 3 most massive groups in the TNG50-2 run, close in resolution to TNG100. These comparisons suggests a weak dependence of the results with numerical resolution which is in line with the resolution trends found in the formation of clouds in Nelson et al. (2020): better resolved runs seem more prone to form clouds and also will result in a larger chance to have star-forming gas in them.

Appendix G

Details on constraining Galacticus model

In this work, we utilize a model similar to that recently proposed by Weerasooriya et al. (2023), but with some differences which result from the recalibration of our model after including the physics described in §4.3. Here we outline the parameters that need adjustment.

Cooling rate: We follow White and Frenk (1991) to account for the cooling rates based on the following expression.

$$\dot{M}_{\rm cool} = \begin{cases} 4\pi r_{\rm infall}^2 \rho(r_{\rm infall}) \dot{r}_{\rm infall} & \text{if } r_{\rm infall} < r_{\rm hot,outer} \\ M_{\rm hot}/\tau_{\rm halo,dynamical} & \text{if } r_{\rm infall} \geq r_{\rm hot,outer} \end{cases}, \tag{G.1}$$

where $r_{\rm infall}$ is the infall radius in the hot halo and $\rho(r)$ is the density profile of the hot halo.

Feedback: We adopt a power-law model to parameterize the stellar feedback, treating the disk and spheroidal components separately. The outflow rate is calculated using the following equation:

$$\dot{M}_{\rm outflow} = \left(\frac{V_{\rm outflow}}{V}\right)^{\alpha_{\rm outflow}} \frac{\dot{E}}{E_{\rm canonical}}. \tag{G.2}$$

Here, $V_{\rm outflow}$ is the characteristic velocity, set to 250 km/s and 100 km/s for the disk and spheroid components, respectively. The tunable exponent $\alpha_{\rm outflow}$ is set to 2 for both components. E is the rate of energy input from the stellar populations and $E_{\rm canonical}$ is the total energy input by a canonical stellar population, normalized to $1 M_\odot$ after infinite time.

Reionization model: Our reionization model employs a methodology similar to that introduced by Benson (2020). Specifically, we assume that the intergalactic medium is instantaneously and fully reionized at redshift z = 9.97, as determined by Hinshaw et al. (2013). This instantaneous reionization results in a rapid photoheating of the IGM to T = 3×10^4 K, followed by a cooling such that the temperature at redshift z = 0 drops to T = 1×10^3 K, resulting in an electron scattering optical depth of 0.0633 in this model[1].

Accretion mode: Accretion of baryonic component into halos is computed using the filtering mass prescription of Naoz and Barkana (2007). In this prescription, it is assumed that the gas mass content of the halos is given by:

$$M_{\rm g}(M_{\rm 200b}, M_{\rm F}) = (\Omega_{\rm b}/\Omega_{\rm M}) f(M_{\rm 200b}/M_{\rm F}) M_{\rm 200b}, \tag{G.3}$$

[1]We would like to note that the electron scattering optical depth utilized in this study slightly deviates from the assumptions of FG20 model, but remains within 1.3σ of their results. The Planck 2018 (Planck Collaboration et al. 2020) results were employed in their analysis for this purpose.

where $M_{\rm F}$ is the filtering mass, as first introduced by Gnedin (2000) (here defined following Naoz and Barkana 2007), $M_{\rm 200b}$ is the halo mass defined by a density threshold of 200 times the mean background density, and $\Omega_{\rm b}$ and $\Omega_{\rm M}$ are baryon and total matter densities as a fraction of the critical density, and

$$f(x) = [1 - (2^{1/3} - 1)x^{-1}]^{-3}. \tag{G.4}$$

The accretion rate onto the halo is therefore assumed to be

$$\dot{M}_{\rm g} = \frac{\Omega_{\rm b}}{\Omega_{\rm M}} \frac{\rm d}{{\rm d}M_{\rm 200b}} \left[f(M_{\rm 200b}/M_{\rm F}) M_{\rm 200b} \right] \dot{M}_{\rm total}. \tag{G.5}$$

However, in practice, three assumptions are violated. Firstly, the filtering mass is not constant in time; secondly, $M_{\rm total}$ does not always correspond to $M_{\rm 200b}$; and thirdly, the growth of halos occurs through both smooth accretion and merging of smaller halos. As a result, the mass fraction in the halo will differ from $f(M_{\rm 200b}/M_{\rm F})$. To address this issue, it is additionally assumed that mass flows from the hot halo reservoir to an "unaccreted" mass reservoir[2] at a rate:

$$\dot{M}_{\rm hot} = -\frac{\alpha_{\rm adjust}}{\tau_{\rm dyn}} [M_{\rm hot} + M_{\rm unaccreted}][f_{\rm accreted} - f(M_{\rm 200b}/M_{\rm F})], \tag{G.6}$$

where $\alpha_{\rm adjust} = 0.3$ is chosen to ensure that the relation between gas mass and halo mass in equation G.3 is approximately maintained, $\tau_{\rm dyn}$ is the dynamical timescale, $M_{\rm unaccreted}$ is the mass in the unaccreted reservoir, and $f_{\rm accreted}$. By making these adjustments in the model, the effects of the increased gas pressure in the IGM on accretion into the CGM are accounted for.

[2]This "unaccreted" reservoir represents gas in the vicinity of the halo which has been unable to accrete due to thermal pressure.

Angular momentum: To track the angular momentum content of halos (and their constituent gas) we adopt the random-walk model first proposed by Vitvitska et al. (2002) and developed further by Benson et al. (2020, readers are encouraged to consult this paper for more detailed information) which predicts the spins of dark matter halos from their merger histories. According to this model, the acquisition of angular momentum by halos occurs through the cumulative effects of subhalo accretion. By incorporating this angular momentum prescription, we can effectively reproduce the distribution of spin parameters observed in N-body simulations (Benson et al. 2020). This approach is advantageous in accounting for the intricate processes associated with halo formation and evolution (specifically for the lower mass objects), thereby providing a more accurate representation of the dynamics and properties of the simulated halos.

In Benson et al. (2020) the model was applied only to very well-resolved halos. Since, in this work, we want to explore galaxy formation in very low-mass halos—much closer to the resolution limit of the merger trees—it becomes imperative to consider the unresolved mass accretion into the halos and the corresponding alterations in angular momentum, particularly for the lower mass range. Therefore, we include an additional stochastic contribution to the angular momentum from unresolved accretion. This represents the fact that the angular momentum vector of a halo will diffuse away from zero in a random walk even if the mean angular momentum contributed by unresolved accretion is zero. The three components of the angular momentum vector of unresolved accretion are treated as independent Wiener processes with time-dependent variance that scales as the characteristic angular momentum of the halo. Specifically, each component of the angular momentum

vector obeys:

$$J_{\rm i}(t_2) = J_{\rm i}(t_1) + \sigma\sqrt{\Delta J_{\rm v}^2}N(0,1) \tag{G.7}$$

where $\Delta J_{\rm v}^2$ represents the change in (the square of) the characteristic angular momentum of the halo, $J_{\rm v} = M_{\rm v}(t)V_{\rm v}(t)R_{\rm v}(t)$, due to unresolved accretion. Here $M_{\rm v}(t)$, $V_{\rm v}(t)$, and $R_{\rm v}(t)$ are the virial mass, velocity, and radius respectively, σ^2 represents the variance in angular momentum per unit increase in $J_{\rm v}^2$, and $N(0,1)$ is a random variable distributed as a standard normal.

Making the approximation that the characteristic angular momentum scales in proportion to mass[3] we can write

$$\Delta J_{\rm v}^2 \approx J_{\rm v}^2(t_2) - J_{\rm v}^2(t_1)\left\{\frac{M(t_1)+M_{\rm r}}{M(t_1)}\right\}^2 = J_{\rm v}^2(t_2) - J_{\rm v}^2(t_1)\left\{\frac{M(t_2)-M_{\rm u}}{M(t_1)}\right\}^2 \tag{G.8}$$

where $M_{\rm r}$ and $M_{\rm u}$ are the resolved and unresolved mass accreted between times t_1 and t_2 respectively.

This model captures the idea that the increase in angular momentum from a merging event should be of order $\Delta M V_{\rm v}(t)R_{\rm v}(t)$ (since merging halos have velocities which scale with $V_{\rm v}(t)$ and occur at separation $R_{\rm v}(t)$). Additionally, because this is a Wiener process the resulting distribution of $J_{\rm i}(t)$ at any given time is independent of the number of steps used to get from $t = 0$ to that time. (That is, the results are independent of how finely we sample the mass accretion history of each halo.) We find that $\sigma^2 = 0.001$ results in reasonably good agreement between predicted and observed galaxy sizes (as discussed in more detail in §4.4.2).

[3]In detail this is not correct, as there is also some dependence on the change in redshift across the timestep due to the dependence of virial densities on redshift. In practice, we ignore this dependence and absorb such effects into the parameter σ.

G.1 Dark Matter halo evolution in Galacticus

Unlike the approach taken by Weerasooriya et al. (2023), who utilized merger trees extracted from N-body simulations, this study utilizes the Galacticus framework for the evolution of both the DM and baryonic components within the halos. Here, we provide a brief overview of this process. Galacticus constructs merger trees for dark matter halos backwards in time using the algorithm of Cole et al. (2000), along with the modified merger rates found by Benson (2017), which were constrained to match the progenitor mass functions in the MultiDark (Klypin et al. 2016) N-body simulation suite (see here). It then evolves the properties of the halos forward in time. When halos merge, the more massive one becomes the host, while the smaller one becomes a subhalo orbiting within it. Subhalos are initialized at the host's virial radius, positioned isotropically at random, with velocities drawn from distributions predicted by cosmological simulations. In this work, we adopt parameters from Jiang et al. (2015) and best-fit values from Benson et al. (2020). The positions and densities of subhalos are tracked over time, accounting for dynamical friction, tidal stripping, and tidal heating until specified disruption criteria are met (Pullen et al. 2014; Yang et al. 2020). To enable rapid simulation, interactions between subhalos are ignored (see Penarrubia and Benson (2005) for a justification of this approximation), and subhalos are disrupted if their bound mass falls below $10^7 M_\odot$ or they pass within a distance from the host halo center equal to 1% of the host's virial radius. For a more comprehensive explanation, refer to Yang et al. (2020); we also refer the reader to the recent comparison between Galacticus predictions and Symphony simulations in Nadler et al. (2023b).

Here we explain further the nonlinear dynamical processes that govern the subhalo orbital evolution within the host halo.

Dynamical friction: causes a subhalo to decelerate as it traverses the dark matter particles of the host halo. This is modeled using the Chandrasekhar formula (Chandrasekhar 1943), assuming a Maxwell–Boltzmann distribution of host particles (see eq. (1) in Yang et al. 2020). Which introduce our first free parameter, the "Coulomb logarithm ($\ln \Lambda$)".

Tidal stripping: removes mass from the subhalo that lies beyond the tidal radius (King 1962; van den Bosch et al. 2018), where the tidal force from the host exceeds the subhalo's self-gravity. This is modeled following Zentner et al. (2005), with mass being removed outside the tidal radius over an orbital timescale (see eq. (5) in Yang et al. 2020). Our second free parameter, α, controls the strength of tidal stripping.

Tidal heating: injects energy into the subhalo through rapidly varying tidal forces, causing it to expand. This is modeled using the impulse approximation with an adiabatic correction factor and a tidal tensor time integral decay term (see eq. (8) in Yang et al. 2020). The exponent γ controls the adiabatic correction term, as discussed by Gnedin and Ostriker (1999). The value of γ is somewhat uncertain, with Gnedin and Ostriker (1999) finding $\gamma = 2.5$ (which was used by Pullen et al. 2014), while theoretical considerations predict $\gamma = 1.5$ in the slow-shock regime (Gnedin and Ostriker 1999; Weinberg 1994a,b). The heating coefficient, $\epsilon_{\rm h}$, which accounts for the higher order heating effects, is treated as a free parameter. This model was later improved by incorporating second-order terms in the impulse approximation for tidal heating (see eq. (4) in Benson and Du 2022), allowing

for an accurate match to the tidal tracks observed in high-resolution N-body simulations (refer to Benson and Du (2022) for further details).

An initial calibration of these free parameters was performed by Yang et al. (2020) using an MCMC fitting workflow to thoroughly explore the parameter space with high efficiency. For the purpose of this study, we adopt $\ln \Lambda = 1.35$, $\epsilon_{\rm h} = 2.70$, and $\alpha = 2.95$. We approximate these values for the choice of $\gamma = 1.5$ (as used in the updated tidal heating model of Benson and Du 2022) by interpolating between the cases of $\gamma = 0.0$ and 2.5, using the Caterpillar simulations as calibration target.

Appendix H

Occupation fraction – comparison with hydrodynamical simulations

Fig. H.1 shows a comparison of our occupation fraction predictions to those from several hydrodynamical simulations. At face value, our model predicts the occupation of substantially lower-mass halos compared to simulations. The solid black line with gray shading indicates our preferred model, while lines in blue hues represent predictions from hydrodynamical simulations from Sawala et al. (2016b), Benitez-Llambay and Frenk (2020) and Munshi et al. (2021) (see legends). However, there are two main factors that complicate this comparison. First, the physics included (and its implementation) vary substantially from model to model. We have checked in detail the different physics being implemented in Galacticus compared to these other simulations and conclude that the inclusion of H_2 cooling, likely accounts for the majority of the difference between our predictions and those of some hydrodynamical simulations. We show in the dashed black line how our

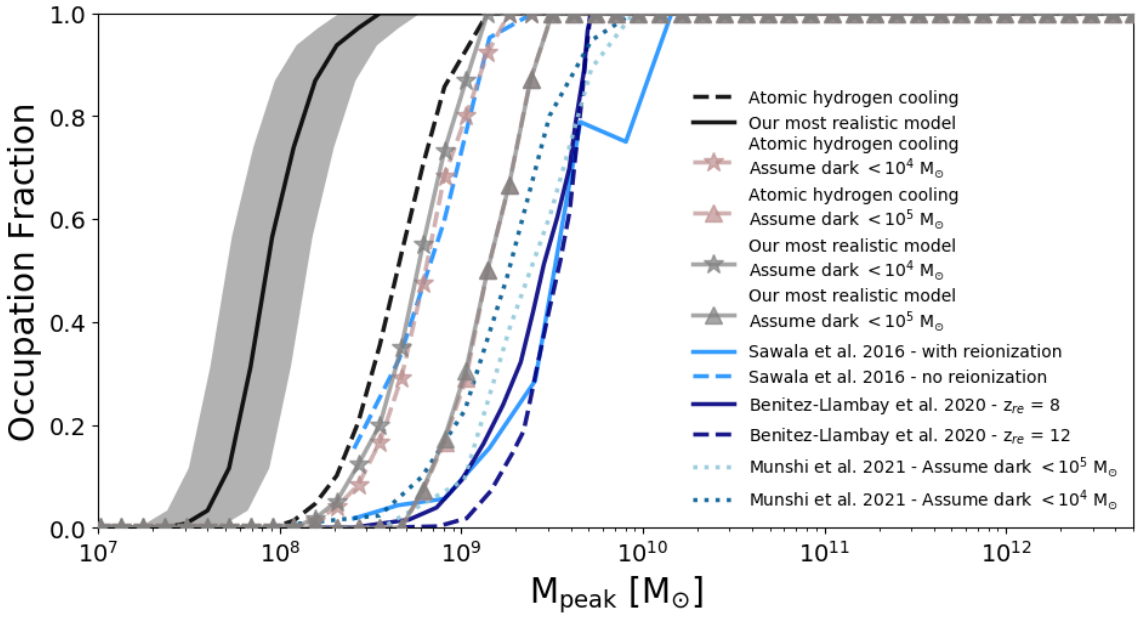

Figure H.1: Comparison to occupation fractions predicted by hydrodynamical simulations. Solid black line with gray shading shows the result of our preferred model, while the long-dashed thick black curve indicates the median occupation fraction when not including H_2 cooling. Results from Sawala et al. (2016b) and Benitez-Llambay and Frenk (2020) are presented with blue and light-blue curves. Dotted lines with blue hues illustrate results from Munshi et al. (2021). For all hydrodynamical simulations, the resolution to call a halo "dark" varies between $M_* < 10^4 - 10^5$ $M_\odot$, as indicated by the labels. To imitate resolution effects from simulations, we apply further cuts to our preferred and no-H_2 cooling models considering as "dark" galaxies with $M_* < 10^4$ $M_\odot$ (starred symbols) and $M_* < 10^5$ $M_\odot$ (triangle symbols). Including resolution cuts, in particular $M_* < 10^5$ $M_\odot$, brings our model in closer agreement with prediction from other simulations. However, we still predict a higher occupation fraction than these models.

predictions would change if only atomic hydrogen cooling was included. As expected, it lowers the occupation fraction of low mass halos, bringing our model into closer agreement with simulations, although it still shows a somewhat higher fraction of halos with a luminous component compared to hydrodynamical simulations.

The second factor complicating the comparison between our model and simulations is numerical resolution. In simulations, the particle mass and force resolution impose a limit in the formation of "luminous" galaxies, which tend to occur in higher mass halos than those resolved in our semi-analytical model. For instance, Munshi et al. (2021) clearly shows that the occupation fraction, defined as the halo mass where 50% of halos hosts a luminous component, might change by up to 1 dex in halo mass by varying the minimum $M_\star$ resolved. To examine this behavior, we impose two cuts to our preferred and no-H_2 cooling models: i) consider as dark all halos with a stellar mass below $M_\star < 10^4$ $M_\odot$ (curve with triangle symbols) and, ii) $M_\star < 10^5$ $M_\odot$ (curve with starred symbols). Interestingly, when applying these relatively "bright" cuts, the difference between models with and without H_2 cooling disappears. This highlights that the physics of molecular hydrogen cooling is only important when modeling the low mass end of the ultra-faint galaxies, or galaxies with $M_\star < 10^4$ $M_\odot$. It is also worth highlighting that imposing these cuts to mimic resolution effects brings our predicted occupation fractions into much closer agreement with simulations, suggesting that hydrodynamical results may be affected by the definition of the occupation fraction, which in turn is limited by resolution in these studies.

Appendix I

Comparison to other SAMs

Previous studies of the MW satellite galaxies in the context of the CDM cosmology have been made using other, similar SAM frameworks. Earlier studies by Benson et al. (2002); Somerville (2002); Kravtsov et al. (2004) only compared with the "classical" satellite population of dwarfs around MW (down to M_V = -8.8) due to the lack of resolution. More recent studies have pushed this limit further by using N-body simulations with better resolution as benchmarks for the formation and evolution of the subhalos that are used by SAMs to host the MW and its satellite population.

One of the N-body simulations used is the Via Lactea II simulation, which was adopted by Busha et al. (2010) to explore the effects of inhomogeneous reionization on the population of MW satellites. The availability of larger and smaller volume (lower and higher resolutions) realizations of the simulation allowed these authors to assess spatial variations in the epoch of reionization. Their galaxy evolution model was much more simplistic than that employed in this work in general, but their luminosity function predictions seem to

qualitatively agree with our simplest model (i.e. the model including atomic hydrogen cooling and assuming a reionization redshift of ∼10). A similar N-body simulation was used by Muñoz et al. (2009) who adopted a slightly more involved approach to account for star formation at different times. They found agreement with the observed satellite luminosity function (those discovered prior to SDSS and the ultra-faint sample found in the SDSS DR5) and showed that molecular hydrogen cooling is important for producing the correct abundance of low-luminosity satellites, although their molecular hydrogen cooling model is different from the one used in our study and the effect of which is stopped at $z = 20$ when they assume molecular hydrogen to be dissociated.

Another N-body simulation frequently used for the study of MW-analogs via SAMs is the Aquarius simulation. Macciò et al. (2010) compares results from three different semi-analytic models of galaxy formation (SAMs by Kang 2008; Somerville et al. 2008, and MORGANA first presented in Monaco et al. 2007) applied to high-resolution N-body simulations (Aquarius). The subhalo information was *not* used to determine the evolution of satellite galaxies (e.g. to determine merging timescales). To add a suitable reionization-induced suppression of galaxy formation, the Gnedin (2000) filtering mass prescription is added to each model, with a reionization history taken from Kravtsov et al. (2004). They found that all three models can achieve a reasonable match to the observed satellite luminosity function with a reionization epoch of $z = 7.5$. However, they note that the original filtering mass prescription overestimates the suppressing effects of reionization. Adopting the currently favored suppression (which becomes effective in haloes with characteristic velocities below ∼30 km/s), they found that a higher redshift, $z = 11$, of reionization is

required to restore a good match to the data. Macciò et al. (2010) explored the roles of various physical ingredients in their models in achieving this match. In particular, they found that the inclusion of supernova feedback is crucially important—without it far too many luminous galaxies are formed. The Aquarius simulation was also used in the study of Li et al. (2010) where they apply an updated version of the "Munich model" described by De Lucia and Blaizot (2007) (with updates to the reionization and feedback prescriptions) to study MW satellites. The cooling model used in this study is similar to that used in this work (White and Frenk 1991). It is important to note that cooling via molecular hydrogen was not included, under the assumption that H_2 is efficiently photodissociated. Given this difference they are still able to reproduce the luminosity function for MW satellites, but their mass-metallicity relation does not seem to predict the plateau observed at the lower mass end. Although not directly stated in their results, we can infer from their Fig. 15 a threshold of peak halo mass above which all of their subhalos are luminous (this threshold is $\sim 10^9$ $M_\odot$) which approximately agrees with our model where we include only atomic hydrogen cooling (as expected), but is clearly not able to produce the occupation fractions inferred from observation by recent studies (see results from Nadler et al. 2020).

The work conducted by Font et al. (2011) using the GALFORM model is closest to our approach in terms of the range of physics modelled and the detail of the treatment, e.g., inclusion of H_2 cooling and the evolution of the IGM is essentially that described in Benson et al. (2006), inclusion of UV background radiation by Haardt and Madau (2001) (note that all the analogous models employed in this study have undergone substantial revisions). However, they introduce a simplistic model to account for the impacts of local photoheating

from local sources which appears to overestimate the contribution of local photons to the suppression of low-mass satellites (by pushing the temperature rise in the local IGM to significantly earlier epochs, leading to a more substantial suppression of gas accretion). Notably, our model does not directly encompass photoheating; rather, its effect is encapsulated through the incorporation of our reionization model and a filtering mass within our model for accretion of IGM gas into halos, thereby regulating the post-reionization temperature of the intergalactic medium. Interestingly their model foresees a distinct plateau in the mass-metallicity relation, a prediction that resonates with our model's outcomes and aligns with the current observational inferences.

Overall, Galacticus employs the extended Press-Schechter formalism to construct merger trees, allowing it to transcend resolution limitations associated with N-body simulations (although it has the capacity to utilize merger trees derived from N-body simulations). It is important to note that for the purpose of this study we are resolving progenitor halos down to 10^7 $M_\odot$, which, as briefly discussed in Appendix J, gives us sufficient resolution. Additionally, the H_2 cooling model along with the FG20 UV background radiation introduced in section 4.3 are updated versions of ones utilized in previous studies. Additionally, we have explored the effects of inclusion of an IGM metallicity model. It is worth noting that different SAMs, adopting various models for these key physical processes, yield comparable outcomes through minor calibrational adjustments (specifically evident in studies on luminosity function, which tend to align with observations). This might suggest the presence of degeneracies in the way in which different physical processes can affect the predictions of each model (as also suggested by Font et al. 2011). However, a comprehensive

analysis of multiple observables rather than a singular property observed in the galaxy populations under scrutiny could potentially untangle these degeneracies. This is what we aim to accomplish in this paper by presenting a range of models and discerning differences across various observables such as the luminosity function, mass-metallicity relation, size-mass relation, and velocity dispersion-mass relation, in addition to exploring inferred theoretical properties such as the SMHM relation and occupation fraction.

Appendix J

Resolution study in our CDM model

In this section, we conducted tests to evaluate the performance of our model at different resolutions. We specifically assessed the impact of resolution on the prediction of the occupation fraction. Our results demonstrate that the accuracy of the occupation fraction predictions is not hindered by the resolution of 10^7 $M_\odot$ used in this study (illustrated by the black curve, with the corresponding dispersion indicated by the grey shaded region in Fig. J.1). To show this, we investigated higher resolutions, including $5 \times 10^6 M_\odot$ (illustrated by the dashed grey curve) and $10^6 M_\odot$ (depicted by the double-dotted-dashed grey curve[1]), revealing consistent occupation fraction predictions within the statistical uncertainty of our results. However, it should be noted that our model predicts that only a fraction of our

[1]Due to computational limitations, these results are derived from simulations with only four merger trees, sampled from the same mass range as other cases. Given the negligible predicted scatter for the halo-to-halo cases, we anticipate minimal impact on the calculated median occupation fraction.

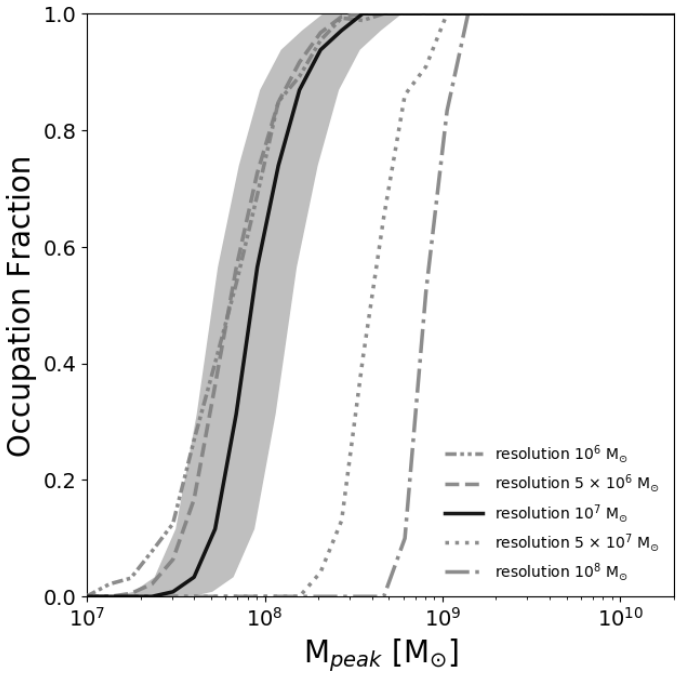

Figure J.1: Impact of resolution on the predicted occupation fraction as a function of the peak halo mass. Line types depict different resolutions, with the grey double-dotted-dashed, dashed, dotted, and dashed-dotted lines corresponding to resolutions of 10^6, 5×10^6, 5×10^7 and $10^8 M_\odot$, respectively. The black solid line represents our fiducial $10^7 M_\odot$ resolution, along with the uncertainty of the peak mass measurements from our results, which is depicted by the gray shaded region.

subhalos with masses below $\sim 2 \times 10^8\,M_\odot$ host a luminous component. As a result, going above a resolution of $10^7\,M_\odot$ (such as resolutions of $5\times10^7 M_\odot$ and $10^8\,M_\odot$ depicted by the dotted and dashed-dotted lines on the plot) would significantly impact the results.

We also examined the influence of resolution on the predicted metallicity of the satellites. As depicted in Fig. J.2, at higher stellar masses for the subhalos, we did not observe substantial differences resulting from resolution changes. However, at the lower mass range, altering the resolution introduced some variations in the metallicity predictions. These discrepancies could be attributed to the effects of bias in selecting the low stellar

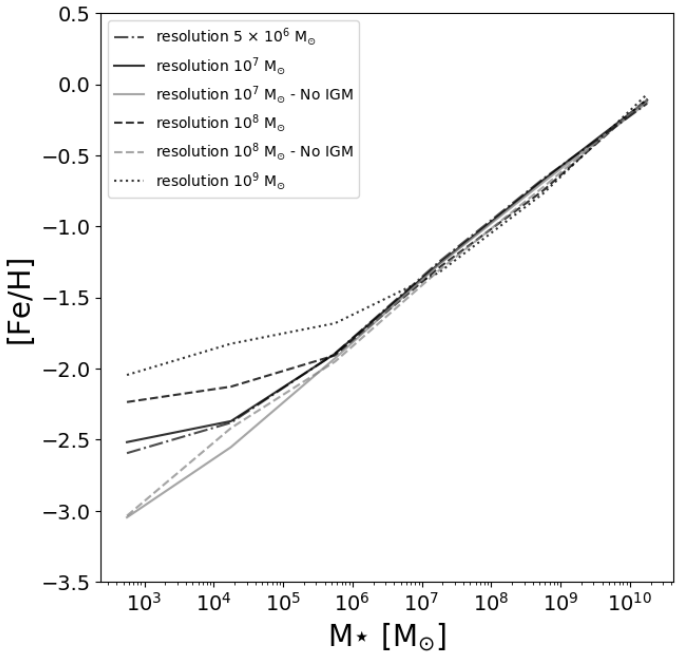

Figure J.2: Effect of resolution on the mass – metallicity relation. The mass-metallicity relation is shown with various black line styles representing different resolutions. Resolution $10^7 M_\odot$ is represented by the solid black line, while resolutions 5×10^6, 10^8 and $10^9 M_\odot$ are depicted by the dotted-dashed, dashed and dotted black lines, respectively. Additionally, the corresponding models without the inclusion of IGM metallicity are shown with gray lines, with solid and dotted lines representing resolutions 10^7 and $10^8 M_\odot$, respectively.

mass population due to the sharp resolution-induced cutoff in the SMHM relation within our results. In such cases, lower resolution would lead to a subhalo population with biased higher stellar masses (due to the resolution cutoff), which can statistically shift the median metallicity towards larger values. Additionally, we excluded the IGM metallicity from our model and compared its impact. The results demonstrated a similar behavior with slightly reduced significance.